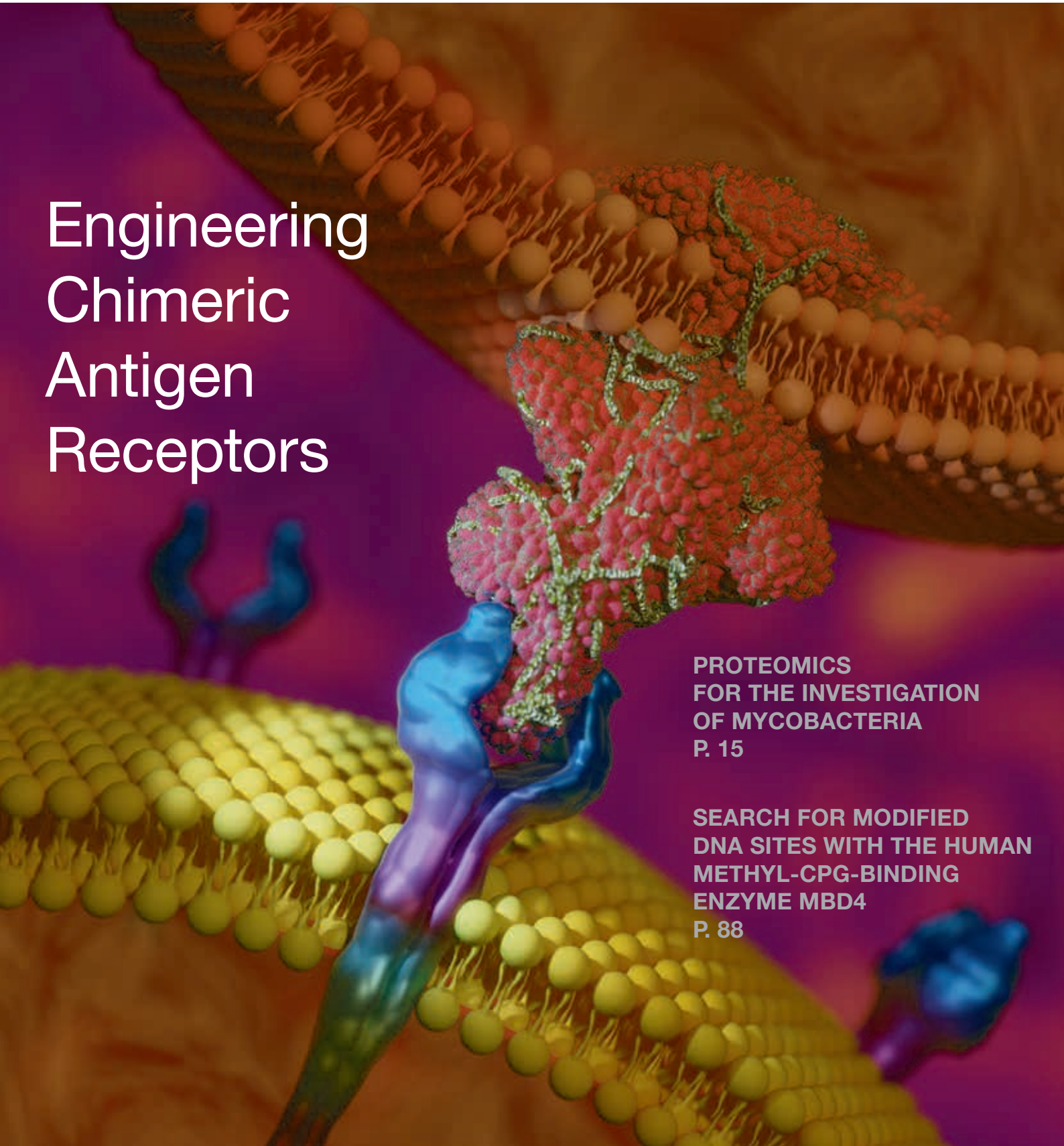


Acta Naturae

Engineering
Chimeric
Antigen
Receptors



PROTEOMICS
FOR THE INVESTIGATION
OF MYCOBACTERIA
P. 15

SEARCH FOR MODIFIED
DNA SITES WITH THE HUMAN
METHYL-CPG-BINDING
ENZYME MBD4
P. 88



НИАРМЕДИК

НИАРМЕДИК - российская фармацевтическая, биотехнологическая и медицинская компания, основанная в 1989 году. Все направления деятельности ГК НИАРМЕДИК нацелены на улучшения качества здравоохранения в России.

НИАРМЕДИК занимается развитием диагностического, фармацевтического и медицинского бизнеса на основе собственных исследований и переноса передовых зарубежных технологий.

ДИАГНОСТИЧЕСКИЕ НАБОРЫ И ЛАБОРАТОРНОЕ ОБОРУДОВАНИЕ


- Исследования и разработка
- Производство
- Продажи
- Оборудование для медицинских лабораторий

ФАРМАЦЕВТИКА

- Исследования и разработка
- Производство
- Продвижение
- Продажи

Дополнительную информацию можно получить по тел: +7(495)741-49-89
или на сайте www.nearmedic.ru

Letter from the Editors



Dear readers of *Acta Naturae*,
Having entered the new season, we
are delighted to bring you the first issue
of *Acta Naturae* in 2017.

As always, we did our best to make this issue as versatile and interesting for our wide audience as possible.

The issue opens with three reviews focused on the topical problems of modern life sciences: the review by S.V. Kulemzin et al. devoted to the design of chimeric antigen receptors; the review by Yu.A. Bespyatykh et al. on proteomic approaches for studying mycobacteria; and the review by A.M. Petrov et al. devoted to the role of cholesterol in the synaptic dysfunction and pathogenesis of neurodegenerative diseases. These reviews

clearly lie within the scope of the cutting-edge areas of biology.

This issue also contains eight experimental articles and two short communications. We believe that we have managed to maintain a balance between fundamental research and studies directly related to medicine.

So we continue our work. We are sorry to admit that there are some clouds on journal's horizons, but we hope that these clouds will soon clear out through our joint efforts (including the aid of our readers). We are grateful to the Niarmedic company for their support in publishing this issue of the journal.

We hope you enjoy your reading! ●

The Editorial Board

INNOVATION RUSSIA

Discussion club

We create a dialogue between all socially active groups of people: students, scientists, lecturers, businessmen, managers, innovators, investors, designers, art critics, architects, photographers.

Learn more
at WWW.STRF.RU

Everyone with something to say and
ideas to share is welcome to visit
our events

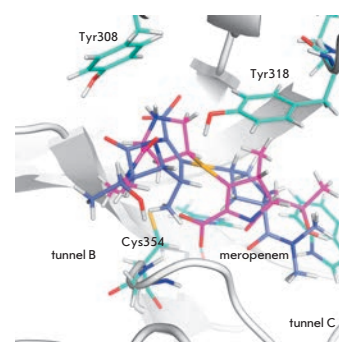


Tel.: +7 (495) 930-87-07, 930-88-50
E-mail: seminar@strf.ru

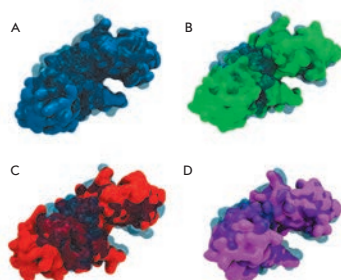
Building a Full-Atom Model Of L,D-Transpeptidase 2 From *Mycobacterium Tuberculosis* for Screening New Inhibitors

S.M. Baldin, N.M. Misiura, V.K. Švedas

L,D-transpeptidase 2 from *Mycobacterium tuberculosis* plays a key role in the formation of the cell wall of a pathogen and catalyzes the cross-linking of growing peptidoglycan chains by non-classical 3-3 bonds, which causes resistance to a broad spectrum of penicillins. Molecular modeling of enzyme interactions with the N- and C-terminal tetrapeptide fragments of growing peptidoglycan chains has been performed for the first time and has allowed to highlight the peculiarities of their binding at the formation of 3-3 cross-linkages, as well as to build a full-atom model of L,D-transpeptidase 2 for the screening and optimizing of inhibitors' structures.



Localization of β -lactam antibiotics in the LdtMt2 active site



Surface modeling of the phiKZ gp144 mutants compared to the native form

Dual Active Site in the Endolytic Transglycosylase gp144 of Bacteriophage phiKZ

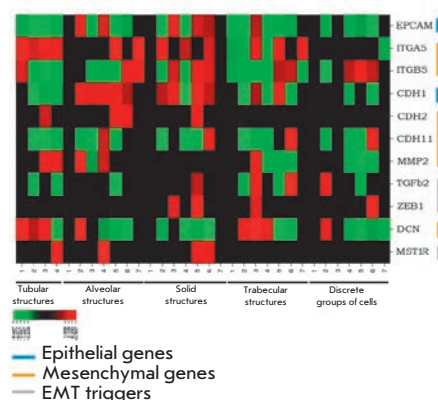
O.V. Chertkov, G.A. Armeev, I.V. Uporov, S.A. Legotsky, N.N. Sykilinda, A.K. Shaytan, N.L. Klyachko, and K.A. Miroshnikov

Lytic transglycosylases are abundant peptidoglycan lysing enzymes that degrade heteropolymers of bacterial cell walls in metabolic process or in the course of bacteriophage infection. The findings confirm the hypothesis of two active sites of phiKZ gp144 and clarify the conventional catalytic mechanism of this enzyme.

Intratumoral Morphological Heterogeneity of Breast Cancer as an Indicator of the Metastatic Potential and Tumor Chemosensitivity

T.S. Gerashchenko, M.V. Zavyalova, E.V. Denisov, N.V. Krakhmal, D.N. Pautova, N.V. Litviakov, S.V. Vtorushin, N.V. Cherdyntseva, V.M. Perelmuter

Breast cancer (BC) demonstrates considerable intratumoral morphological heterogeneity. Intratumoral morphological heterogeneity of BC may serve an indicator of the metastatic potential and tumor chemosensitivity.



Expression of EMT genes in different morphological structures of breast tumors

Founders

Ministry of Education and
Science of the Russian Federation,
Lomonosov Moscow State University,
Park Media Ltd

Editorial Council

Chairman: A.I. Grigoriev
Editors-in-Chief: A.G. Gabibov, S.N. Kochetkov

V.V. Vlassov, P.G. Georgiev, M.P. Kirpichnikov,
A.A. Makarov, A.I. Miroshnikov, V.A. Tkachuk,
M.V. Ugryumov

Editorial Board

Managing Editor: V.D. Knorre
Publisher: K.V. Kiselev

K.V. Anokhin (Moscow, Russia)
I. Bezprozvanny (Dallas, Texas, USA)
I.P. Bilenkina (Moscow, Russia)
M. Blackburn (Sheffield, England)
S.M. Deyev (Moscow, Russia)
V.M. Govorun (Moscow, Russia)
O.A. Dontsova (Moscow, Russia)
K. Drauz (Hanau-Wolfgang, Germany)
A. Friboulet (Paris, France)
M. Issagouliants (Stockholm, Sweden)
A.L. Konov (Moscow, Russia)
M. Lukic (Abu Dhabi, United Arab Emirates)
P. Masson (La Tronche, France)
K. Nierhaus (Berlin, Germany)
V.O. Popov (Moscow, Russia)
I.A. Tikhonovich (Moscow, Russia)
A. Tramontano (Davis, California, USA)
V.K. Švedas (Moscow, Russia)
J.-R. Wu (Shanghai, China)
N.K. Yankovsky (Moscow, Russia)
M. Zouali (Paris, France)

Project Head: N.V. Soboleva

Editor: N.Yu. Deeva

Designer: K.K. Oparin

Art and Layout: K. Shnaider

Copy Chief: Daniel M. Medjo

Address: 119234 Moscow, Russia, Leninskiye Gory, Nauchny
Park MGU, vlad.1, stroeniye 75G.
Phone/Fax: +7 (495) 727 38 60

E-mail: vera.knorre@gmail.com, actanaturae@gmail.com

Reprinting is by permission only.

© ACTA NATURAE, 2017

Номер подписан в печать 24 марта 2017 г.

Тираж 200 экз. Цена свободная.

Отпечатано в типографии «МИГ ПРИНТ»

CONTENTS

Letter from the Editors 1

REVIEWS

S. V. Kulemzin, V. V. Kuznetsova,
M. Mamonkin, A. V. Taranin, A. A. Gorchakov
Engineering Chimeric Antigen Receptors 6

J. A. Bespyatykh, E. A. Shitikov, E. N. Ilina
**Proteomics for the Investigation
of Mycobacteria 15**

A. M. Petrov, M. R. Kasimov, A. L. Zefirov
**Cholesterol in the Pathogenesis of Alzheimer's,
Parkinson's Diseases and Autism: Link
to Synaptic Dysfunction 26**

RESEARCH ARTICLES

I. V. Balalaeva, E. A. Sokolova,
A. D. Puzhikhina, A. A. Brilkina, S. M. Deyev
**Spheroids of HER2-Positive Breast
Adenocarcinoma for Studying Anticancer
Immunotoxins *In vitro* 38**

S.M. Baldin, N.M. Misiura, V.K. Švedas
**Building a Full-atom Model of
L,D-Transpeptidase 2 from *Mycobacterium
tuberculosis* for Screening New Inhibitors . . . 44**

N. S. Bondarenko, A. N. Shneiderman,
A. A. Guseva, B. A. Umarova
**Prolyl-glycyl-proline (PGP) Peptide
Prevents an Increase in Vascular Permeability
in Inflammation 52**

T.S. Gerashchenko, M.V. Zavyalova, E.V. Denisov, N.V. Krakhmal, D.N. Pautova, N.V. Litviakov, S.V. Vtorushin, N.V. Cherdyntseva, V.M. Perelmuter Intratumoral Morphological Heterogeneity of Breast Cancer as an Indicator of the Metastatic Potential and Tumor Chemosensitivity.....	E.A. Novoselova, O.B. Riabova, I.A. Leneva, V.G. Nesterenko, R.N. Bolgarin, V.A. Makarov Antiretroviral Activity Of a Novel Pyrimidyl-Di(Diazaspiroalkane) Derivative	56	105
E. S. Philonenko, M. V. Shutova, E. A. Khomyakova, E. M. Vassina, O. S. Lebedeva, S. L. Kiselev, M. A. Lagarkova Differentiation of Human Pluripotent Stem Cells into Mesodermal and Ectodermal Derivatives Is Independent of the Type of Isogenic Reprogrammed Somatic Cells ...	Guidelines for Authors.....	68	108
E.A. Tsvetkov, N.N. Potatieva, K.V. Bolshakov Voltage-Dependent Interaction of Capsaicine and Protons on TRPV1-Receptors		75	
O.V. Chertkov, G.A. Armeev, I.V. Uporov, S.A. Legotsky, N.N. Sykilinda, A.K. Shaytan, N.L. Klyachko, and K.A. Miroshnikov Dual Active Site in the Endolytic Transglycosylase gp144 of Bacteriophage phiKZ		81	
D. A. Yakovlev, A. A. Kuznetsova, O. S. Fedorova and N. A. Kuznetsov Search for Modified DNA Sites with the Human Methyl-CpG-Binding Enzyme MBD4.....		88	
SHORT REPORTS			
L. S. Melnikova, E. A. Pomerantseva, V.V. Molodina, P. G. Georgiev Mapping the <i>D.melanogaster</i> En1A Enhancer Modules Responsible for Transcription Activation and Long-Distance Enhancer-Promoter Interactions.....		99	

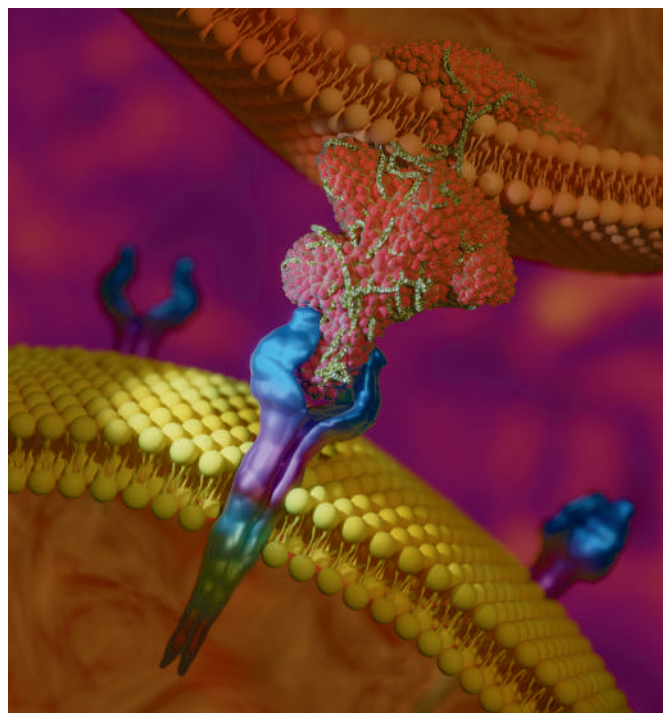


IMAGE ON THE COVER PAGE, courtesy of Grant Borodin
(see the article by Kulemzin *et al.*)

Engineering Chimeric Antigen Receptors

S. V. Kulemzin^{1#}, V. V. Kuznetsova^{1#}, M. Mamonkin³, A. V. Taranin^{1,2}, A. A. Gorchakov^{1,2*}

¹Institute of Molecular and Cellular Biology, SB RAS, Lavrentiev Ave. 8/2, Novosibirsk, 630090, Russia

²Novosibirsk State University, Pirogova str. 2, Novosibirsk, 630090, Russia

³Center for Cell and Gene Therapy, Baylor College of Medicine, Texas Children's Hospital and Houston Methodist Hospital, Houston, TX, USA

#equal contribution

*E-mail: gorchakov@mcb.nsc.ru

Received June 23, 2016; in final form, November 17, 2016

Copyright © 2017 Park-media, Ltd. This is an open access article distributed under the Creative Commons Attribution License, which permits unrestricted use, distribution, and reproduction in any medium, provided the original work is properly cited.

ABSTRACT Chimeric antigen receptors (CARs) are recombinant protein molecules that redirect cytotoxic lymphocytes toward malignant and other target cells. The high feasibility of manufacturing CAR-modified lymphocytes for the therapy of cancer has spurred the development and optimization of new CAR T cells directed against a broad range of target antigens. In this review, we describe the main structural and functional elements constituting a CAR, discuss the roles of these elements in modulating the anti-tumor activity of CAR T cells, and highlight alternative approaches to CAR engineering.

KEYWORDS adoptive immunotherapy, cancer, chimeric antigen receptor, T cells.

ABBREVIATIONS CAR – chimeric antigen receptor; TCR – T-cell receptor; mAb – monoclonal antibody; scFv – single-chain variable fragment; scFv-CAR – scFv-based CAR; DARPin – designed ankyrin repeat protein; FITC – fluorescein isothiocyanate; VHH – camelid single-domain antibody (nanobody); VLR – lamprey variable lymphocyte receptor; MHC – major histocompatibility complex proteins; ITAM – immunoreceptor tyrosine-based activation motif.

INTRODUCTION

Modern methods for re-targeting immune cells open unprecedented opportunities for the treatment of cancer and autoimmune diseases. Chimeric Antigen Receptors (CARs) represent one of the recent advances in this field. CARs are recombinant molecules that mediate cell activation upon encounter with the target antigen. The antigen-recognition domain of a CAR is typically derived from the sequences of monoclonal antibodies (mAbs). This domain functions to interact with tumor epitopes in an MHC-unrestricted manner. Cell activation is ensured by the signaling motifs in the intracellular portion of a CAR. At the moment, T cells are the most frequently used CAR “drivers” (CAR T cells), and this review focuses on the structural features of CARs, specifically in the context of T cells, although alternative cellular platforms exist, including NK cells, iNKT cells, and $\gamma\delta$ T cells.

The outline of CAR T-cell therapy is shown in *Fig. 1*. First, a CAR-encoding DNA cassette is delivered into primary T cells collected from a patient. Next, transgenic CAR T cells are expanded *ex vivo* and re-infused into the patient, where they encounter target tumor cells. Tumor recognition is mediated by the antigen-recognition domain of a CAR, while its intracellular part induces T cell activation, which

results in the destruction of tumor cells and proliferation of CAR T cells. Hence, this approach combines the selectivity of antibodies and the cytotoxic potential of T cells.

Although CAR T-cell therapy has only relatively recently transitioned from research laboratories into clinical trials, it has already shown highly promising results. Complete or partial remissions have been achieved in > 50% of leukemia patients that proved resistant to all other lines of therapy [1]. Meanwhile, the issues associated with the insufficient selectivity of CARs have also become apparent [2].

CAR STRUCTURE

The CARs engineered in the mid-1980s encompassed variable fragments of antibodies fused with the constant regions of TCR α and β chains [3]. In 1993, Z. Eshhar and colleagues refined this design by using scFvs as antigen-recognition domains, whereas the transmembrane and signaling sequences were derived from CD3 ζ or FcR γ ; importantly, the entire chimeric receptor consisted of a single polypeptide chain [4]. Subsequent generations of CARs had an overall similar structure but also carried additional signaling modules for enhancing T-cell activity. The key structural components of CARs are discussed below.

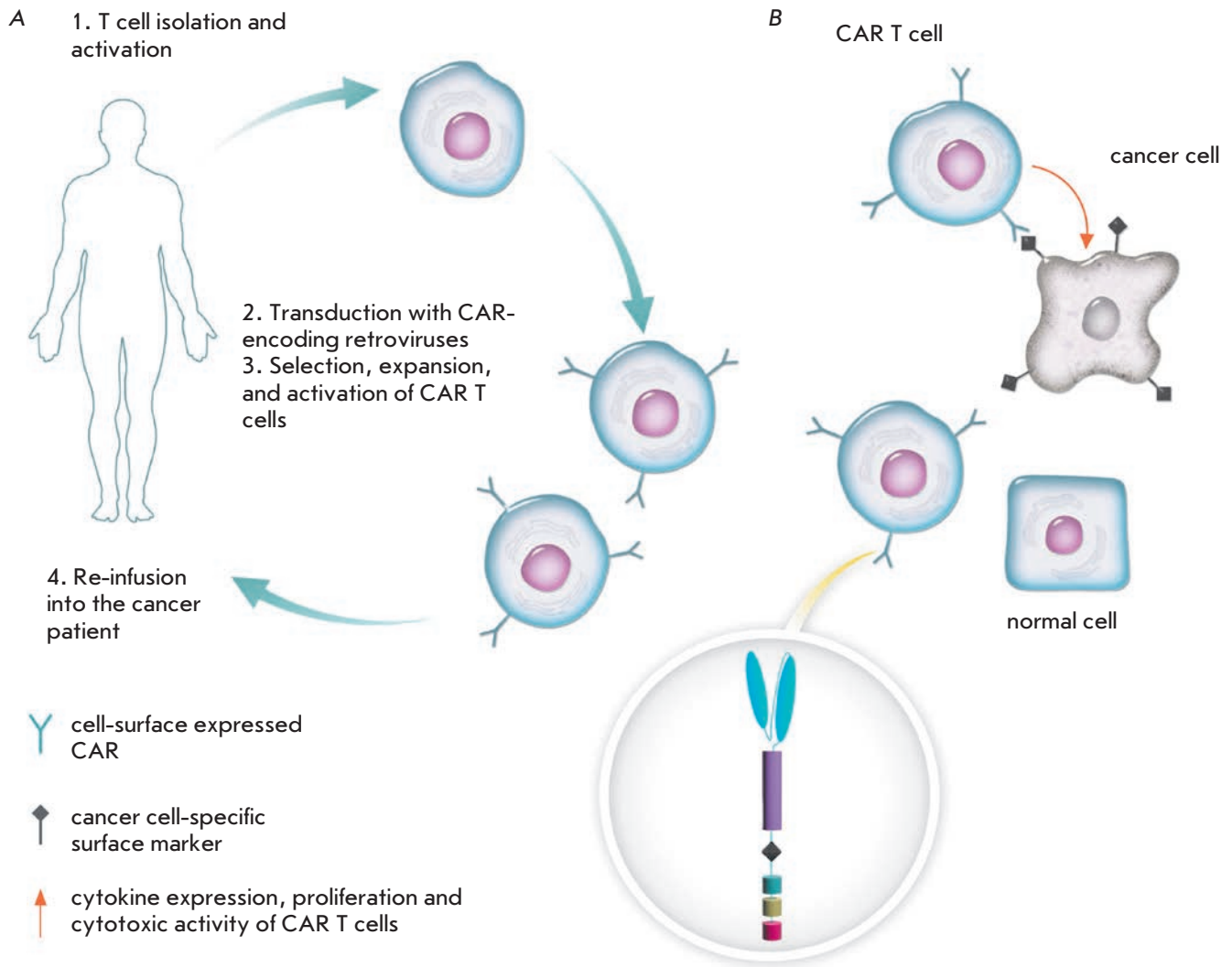


Fig. 1. Adoptive cell transfer therapy with CAR T cells. Peripheral blood leukocytes are collected from a cancer patient in a process called leukapheresis. These cells are then stimulated *ex vivo* prior to transduction with CAR-encoding lenti- or retroviruses. Following this step, the transduced cells are selected, expanded, activated, and reinfused back into the patient (A). Upon encountering target cancer cells, CAR T cells become activated: they secrete cytokines, proliferate, and destroy cancer cells (B).

THE ANTIGEN-RECOGNITION DOMAIN OF CAR

The scFv format

The vast majority of CARs use scFvs as antigen-binding modules [5] (Fig. 2). It is a convenient format, since the mAbs used for scFv design are typically well-characterized in preclinical models or have been approved for clinical use. Hence, the risk of unexpected cross-reaction between CAR T cells and healthy tissues is much lower although not absent when using CARs based on the previously tested scFvs. In addition, structural data are also frequently available for these antibodies,

making it possible to change the affinity of scFv-based CARs in either direction in a targeted manner. However, the drawbacks of using scFvs as antigen-recognition domains in CARs include the risk of developing an immune response against the murine and linker sequences within scFv [6] and the difficulties in designing polyspecific scFv-based CARs because of their large size and the requirement for structure stabilization via disulfide bonds [7]. Furthermore, the framework sequences of antibodies within scFvs have been reported to induce ligand-independent CAR clustering, which results in tonic signaling, nonspecific activation, and,

Cancer cell-associated targets recognized by CARs

Clinical stage:

BCMA, CD19, CD20, CD22, CD30, CD33, CD123, CD133, CEA, EGFR, EGFRvIII, EphA2, ErbB family, GPC3, HER2 (ERBB2), FAP, FR α , GD2, Ig κ , IL13R α 2, Mesothelin, Muc1, PSMA, ROR1, VEGFR2

Pre-clinical stage:

B7-H3 (CD276), B7H6 (NCR3LG1), CD5, CD23, CD70, CSPG4, EpCAM, GD3, HLA-A1+MAGE, IL11R α , Lewis-Y, Muc16, NKG2D ligands, PSCA, TAG72

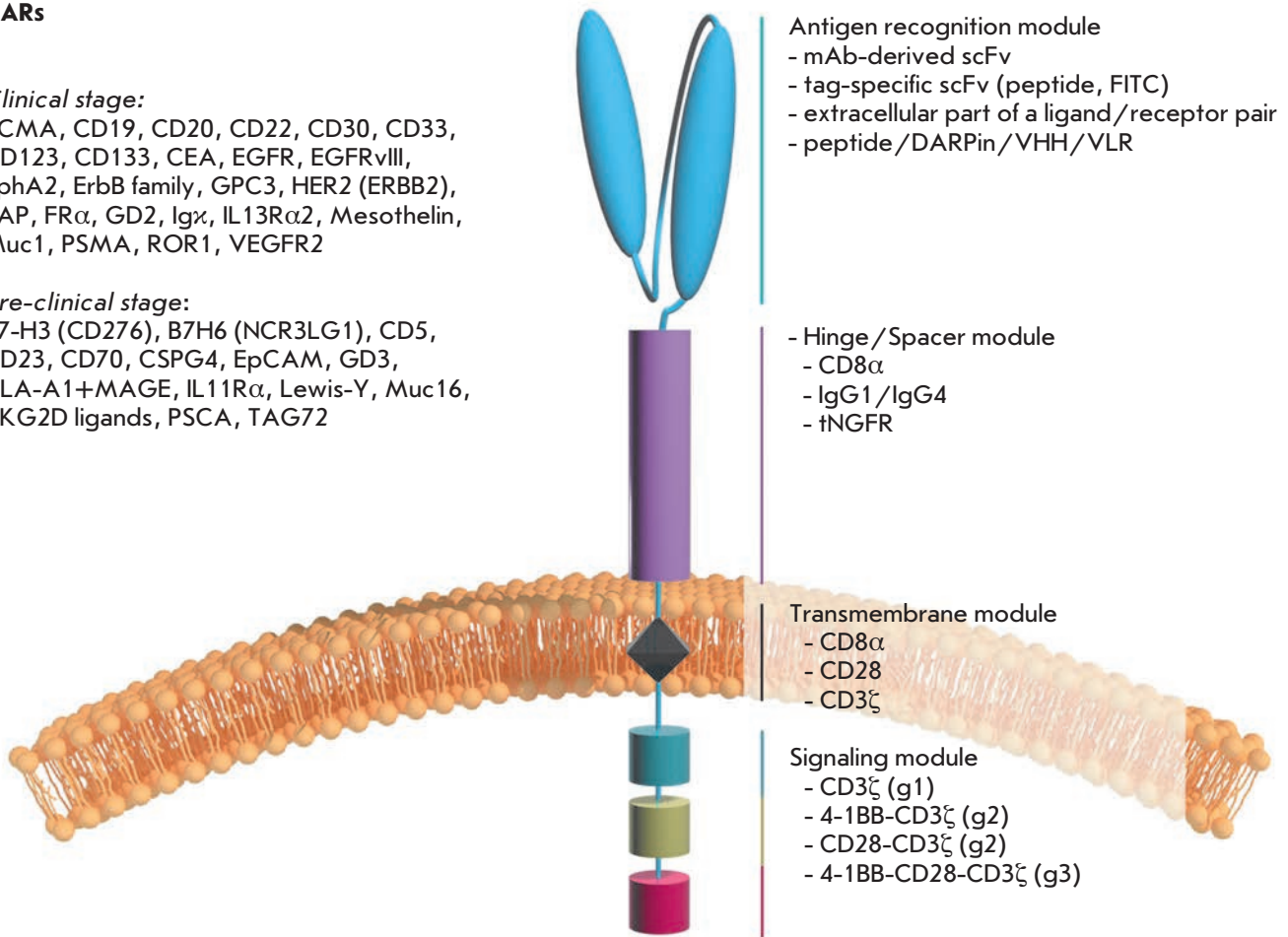


Fig. 2. CAR structure (monomeric layout). First- (g1), second- (g2), and third- (g3) generation CARs differ in the number of costimulatory domains.

ultimately, premature exhaustion and loss of activity by CAR T cells. A. Long and colleagues tested several scFv-based CARs (targeting CD19, GD2, CD22, and HER2) for ligand-independent signaling and showed that only the CD19-specific CAR completely lacked this unwanted feature [8].

Natural ligand–receptor pairs

Most clinically tested CARs encompass non-humanized murine scFv sequences. This is associated with the risk of an immune response against CAR T cells and anaphylactic reactions [9] and may, thereby, compromise the efficacy of the CAR therapy. It is partially for this reason that alternative designs of the antigen-recognition moieties of CARs are being actively explored based on natural human ligand–receptor pairs. For example, the expression of an IL13 receptor, IL13R α 2, is often increased on the surface of glioblastoma, ovar-

ian, and pancreatic cancer cells [10, 11]. Using this information, IL13-based CARs exhibiting specific recognition of IL13R α 2 were designed, although they were later found to recognize IL13 α 1 as well. [12–15]. Antigen-recognition domains of CARs specific to NKG2D ligands and CD70 have been designed using the extracellular domains NKG2D and CD27, respectively [16–18]. CARs recognizing HER3 (ErbB3) and HER4 (ErbB4) have been successfully produced by grafting the extracellular sequences from neuregulin 1 α and 1 β [19, 20]. Finally, CARs containing sequences from CD4 [21–23], VEGF [24], and NKp30 [25], as antigen-recognition domains (specific for HIV gp120, VEGFR2, and B7H6, respectively), have been engineered.

It should be mentioned that, in general, CARs based on the ligand–receptor interplay have the same shortcomings as scFv-based CARs: the targets of these receptors are not entirely tumor-specific and are pres-

ent, although at lower levels, on the surface of normal cells. Moreover, it is becoming progressively clear that receptors and ligands rarely have a single partner: usually there are several. Therefore, to eliminate the possibility of an unintended activation of CAR T cells after their encounter with cells expressing such off-target molecules, significant optimization of the CAR structure and function may be needed.

Peptide ligands

Peptide ligands have been successfully used as antigen-recognition domains in CARs. Despite their potential immunogenicity, peptides have an overall lower risk of triggering an immune response than much larger scFvs. D.M. Davies and colleagues designed the CAR containing peptide ligand T1E as an extracellular domain which recognizes target cells with surface expression of ErbB receptors [26]. Pameijer and colleagues showed that the 12-meric BPEP peptide within CAR enables successful recognition and destruction of target ovarian cancer cells expressing $\alpha\beta6$ integrin [27]. A similar design has successfully been tested for the pair IL11R α /nonapeptide IL11 (IL11R α is typically overexpressed on osteosarcoma, gastric, intestinal, breast, and prostate cancer cells) [28]. At present, such peptide-based CARs are still in the proof of concept stage or undergoing preclinical validation.

A related approach is to use CARs whose antigen-recognition domain consists of designed ankryrin repeat proteins (DARPin) [29, 30], nanoantibodies (VHH) [31–34], or variable lymphocyte receptors (VLRs) [35]. DARPins are compact and stable protein modules selected for high-affinity binding to one or several targets. For instance, it has been shown that HER2-specific DARPin-CARs function (i.e., induce activation and cytotoxic reaction) comparably to “conventional” scFv-CARs against the same target. The functionality of VHHs and VLRs as antigen-recognition domains in CARs has also been described. The key advantages of this system include the modularity and smaller size of DARPins/VHHs/VLRs compared to that of scFvs, which in turn opens an exciting opportunity to design polyspecific and/or polyvalent CARs that can simultaneously recognize several targets. Nevertheless, the declared low immunogenicity of DARPin/VHH/VLR-CARs still remains to be demonstrated. This may lead to complications in the translation of such platforms into a clinical setting.

Universal antigen-recognition modules

Tumor cells are known to be typically quite heterogeneous with respect to surface markers, and so CAR T cells can recognize them with different efficiencies: CAR T cells will likely ignore cells that have downreg-

ulated or silenced the expression of the target surface molecule. Hence, it is tempting to design CAR T cells whose activity can be relatively easily re-targeted using an extensive toolbox of the available mAbs. Three design variants of the so-called universal antigen-recognition modules of CARs have been reported thus far.

The first variant uses the dimeric form of chicken avidin, the protein known to have high-affinity binding to biotin and biotinylated molecules, as an antigen-recognition domain of a CAR [36]. Infusion of these universal CAR (uCAR) T cells, along with biotinylated mAbs recognizing target tumor cells, results in efficient and specific eradication of tumor cells in mice. Furthermore, sequential infusion of biotinylated mAbs against other targets results in appropriate retargeting of uCAR T cells. Interestingly, free biotin, which is invariably present in blood plasma, does not appear to compromise this effect, nor does it cause nonspecific autoactivation of uCAR T cells. Likewise, the use of scFv-based CARs against a neoepitope peptide in combination with target-specific antibodies containing this neoepitope [37] allows one to obtain functional uCAR T cells.

The second variant of uCARs was based on the use of FITC-specific scFvs. The principle by which anti-FITC-CAR T cells function is similar to that described above: these cells recognize FITC-conjugated mAbs or scFvs, and therefore start recognizing and destroying the cells tagged with these molecules [38, 39].

Finally, the effect of CAR T cells mimicking NK cells, which can exhibit potent ADCC against malignant or infected cells, was used in the third system of universal CARs. As soon as an antibody binds to the surface of the target cell, its Fc region is recognized by CD16a (Fc γ RIIIA). Approximately 40% of people are known to carry the F158V polymorphism in CD16a, which significantly increases the affinity of this receptor to antibodies [41, 42]. The use of the extracellular domain of this receptor as the antigen-recognition domain made it possible to design uCARs that can re-target the cytotoxic activity of T cells according to the antitumor antibodies being infused [43–45]. This approach is potentially complicated by the presence of an excess of free antibodies present in the serum that may outcompete the administered mAbs in binding to CD16-CAR T cells. The results of clinical trials of CD16-CAR T cells, in combination with rituximab (anti-CD20 mAbs) in patients with CD20-positive non-Hodgkin’s lymphomas and chronic lymphocytic leukemia, will demonstrate whether this is, indeed, the case.

Hence, the above-described “universal” solution has two key benefits: (i) it is convenient to control uCAR CAR T cell specificity (i.e., to change it if necessary or to simultaneously infuse several antibodies against differ-

ent targets) and (ii) these cells can be easily “switched off” by simply discontinuing the infusion of antibodies.

On the other hand, the potential immunogenicity of avidin, neoepitope peptides, and FITC may impede the smooth clinical translation of these CARs. This may be not too much of an issue, as many cancer patients are typically heavily immunosuppressed. Another problem is associated with the limited penetration of mAbs into organs and tissues, which may considerably reduce their effective concentration in solid tumors. In other words, these systems seem to suffer from the same drawbacks in the context of solid tumors as mAb-based therapies.

The hinge module of CARs

When a T cell interacts with an antigen-presenting cell, an immunological synapse with an intermembrane distance of ~15 nm is formed [46]. This distance is dictated by the architecture of TCR and the peptide–MHC complex. It determines the closed structure of the synapse and ensures physical exclusion of molecules that have extracellular domains longer than 15 nm. It turned out that this spatial separation is important for effective triggering of the phosphorylation cascade and T-cell activation [47, 48]. Thus, CD45 phosphatase has a bulky extracellular domain. When artificially shortened, this protein gets a chance to stay within the synapse, resulting in the suppression of activation signals [49, 50]. The distance between a CAR T cell and a tumor cell may be crucial in ensuring adequate activation of effector functions. Since mutual arrangement of the epitope on the target molecule and the antigen-recognition domain of the CAR in the context of the CAR T cell specifies the size of the synapse being formed, it becomes clear why this design feature can determine whether or not the CAR will be functional [51, 52]. For example, A.A. Hombach and colleagues demonstrated that CAR T cells recognizing the membrane-distal epitope of carcinoembryonic antigen (CEA) were moderately activated, while the same antigen transferred into a more proximal position resulted in much stronger CAR T cell activation [53]. Similarly, CAR T cells with the scFv recognizing a membrane-proximal epitope of CD22 (the antigen abundantly present on normal and malignant B cells) had high antileukemic activity, as opposed to the CAR T cells targeted against the membrane-distal epitope [54, 55]. These and some other examples [56, 57] indicate that membrane-distal epitopes in general tend to form synapses larger than the optimal 15 nm, and so this becomes compatible with the inclusion of CD45 and CD148 phosphatases, which in turn may attenuate the activation signaling.

Hence, given that the position of the epitope recognized by a specific scFv on the target cell surface is al-

ways fixed, the length and rigidity of the extracellular spacer (the hinge module) in the CAR needs to be adjusted empirically to ensure maximum steric compatibility with the scFv and the formation of a compact synapse.

CD8a, CD28, and IgG1/IgG4 (hinge-Fc part) sequences (in single studies, CD4, CD7, and IgD) are used most commonly as a spacer [58–61], review [62]. This choice is based on the fact that these sequences are relatively neutral, flexible, and have been well-characterized structurally. Nevertheless, the CD8a hinge has been reported to perform poorly in the context of certain scFv-based CARs, whereas the Fc-fragment of IgGs is far from biologically inert, and this has become apparent in *in vivo* studies. It was demonstrated that mutual recognition of cells with IgG-containing chimeric receptors and cells expressing Fc receptors (macrophages, monocytes, and NK cells) takes place. Specifically, IgG-CAR T cells become nonspecifically activated in the absence of the target antigen and attack FcR γ + cells, which in their turn are activated and destroy IgG-CAR T cells, thereby influencing therapy efficacy and safety [63, 64]. One of the ways to address this problem is to use mutant IgG hinge variants that do not bind Fc receptors (with either a CH2-domain deletion or mutations in the key amino acid residues responsible for FcR binding) [63–66].

Interestingly, all the spacer variants being used in CARs are sequences prone to homo- or heterodimerization; so, it is presently unclear whether the tonic/ligand-independent signaling from these receptors helps or hinders CAR T cells. By default, dimerization is believed to contribute to the better surface retention of CARs [67]. *In vitro* data available demonstrate that CAR dimerization has little effect on the activation of CAR T cells [14, 68, 69], whereas *in vivo* experiments are needed to accurately compare the functionality of dimerizing and monomeric CARs. It must be noted that a CAR encompassing a spacer region derived from NGFR/p75 has been reported [70]: such a CAR will likely be ignored by nontarget cells and remain monomeric. Furthermore, the NGFR spacer can function as a convenient epitope, which may simplify the selection and expansion of CAR T cells, as well as help promptly destroy these CAR T cells in the patient’s body, once needed.

Transmembrane module

The transmembrane module functions to anchor the receptor on the cell surface. This domain usually includes the transmembrane sequences of CD3 ζ , CD28, CD8, FcRI γ and less frequently, of CD4, CD7, OX40, and MHC(H2-Kb), the exact choice largely depending on the neighboring spacer and intracellular sequences [71]. It was demonstrated that the transmembrane

modules based on CD3 ζ and FcRI γ ensure efficient incorporation of CAR into endogenous TCR. This trans-signaling allows CARs lacking ITAMs or signaling sequences altogether to remain functional [69, 72–74]. Hence, CAR designs that mediate CAR inclusion or exclusion from TCR, as well as the recruitment of additional co-receptors, will likely result in the activation of quantitatively and qualitatively distinct signaling pathways, which requires further research.

The signaling (intracellular) module

The role of the signaling module of CARs is to transduce the activation signal to a T cell as soon as the extracellular domain has recognized the antigen. In normal T-cells, activation begins with the phosphorylation of ITAMs in the cytoplasmic portion of the CD3 ζ subunit of the TCR complex [75]. Thus, in most CAR designs implemented to date, signaling sequences from CD3 ζ are used as a module that triggers cell lytic activity. The ITAM-containing domains of other signaling subunits (e.g., FcR γ) were earlier tested for this role [4]; however, they proved to be less efficient in activating the cytotoxic function of CAR T cells [76, 77]. Induction of activating signaling in native T cells involves several steps. First, activated LCK kinase phosphorylates ITAM motifs in the cytoplasmic tail of CD3 ζ , thereby activating ZAP-70 kinase, which simultaneously triggers several signaling cascades. These events are known as “signal 1.” Yet, to achieve complete T-cell activation, “signal 2” is also needed [78]. Signal 2 is typically provided by costimulatory receptors, such as CD28, whose binding to CD80/CD86 activates PI3K and triggers the PI3K-dependent signaling pathway. This, in turn, initiates the mTOR cascade and launches T cell proliferation.

Hence, in experiment, first-generation CARs, which contained the CD3 ζ chain only, sent exclusively signal 1 to the cell. This led to a cytotoxic reaction against tumor cells [79] but did not provide enhanced proliferation of activated CAR T cells. In principle, signal 2 could potentially be provided by the native co-receptors present in the CAR T cells; however, many tumors do not express the corresponding ligands. In 1998, H.M. Finney and coauthors proposed the design of so-called second-generation CARs with a cytoplasmic domain additionally containing the costimulatory CD28 domain, fused together with CD3 ζ , to overcome this difficulty. This CAR design provides both signal 1 and signal 2 to the T cell; as a result, the cell is activated, it destroys the target, and proliferates [58, 80, 81]. Besides CD28, signaling sequences from costimulatory receptors, such as CD134 (TNFRSF4, OX40), CD154 (CD40L), CD137 (4-1BB), ICOS (CD278), CD27, CD244 (2B4), etc., were successfully tested in CARs [82–88]. The nature of the

costimulatory sequences (whether they are members of the IgSF or TNFRSF subfamilies) used directly influenced the phenotype and activity of CAR T cells [82, 89]. Further progress in the design of CAR signaling domains was based on combining two or more costimulatory sequences (4-1BB-CD28-CD3 ζ being the most frequent one). These receptors, known as third-generation CARs, secrete a broader range of cytokines (including TNF α , GM-CSF, and IFN γ), are less susceptible to activation-induced cell death, and show higher efficacy in tumor elimination in mouse models [90–92]. Despite these promising pre-clinical findings, whether third-generation CARs are similarly more active in clinical conditions remains to be shown [93].

Second-generation CARs with the CD28-CD3 ζ or 4-1BB-CD3 ζ sequence still remain the most frequent CAR formats used in clinical practice [94–97]. Clinical and preclinical studies have demonstrated that CD28-CD3 ζ -based CARs provide explosive expansion of CAR T cells *in vivo*, although this is also accompanied by CAR T cell exhaustion and terminal differentiation. In turn, this may lead to their limited persistence and a lack of antitumor effect [8, 98]. The dynamics of proliferation of 4-1BB-CD3 ζ -containing CAR T cells is smoother: the 4-1BB-domain triggers a different activation pathway and alleviates the effect of a premature exhaustion of CAR T cells. Therefore, 4-1BB-CD3 ζ CAR T cells persist in the organism for much longer, thereby providing a more durable and potent tumor control [87, 89, 99, 100]. Interestingly, Z. Zhao and coauthors have recently reported that providing 4-1BB-mediated co-stimulation in the context of CD28-CD3 ζ -CARs (via co-expression of 4-1BB ligand) combines the advantages of both pathways and outperforms the conventional CAR designs, including third-generation 4-1BB-CD28-CD3 ζ -containing CARs [101]. A similar approach based on the small-molecule controlled costimulatory switch to enhance the functionality of CAR T cells is used in the GoCAR-T-technology (Bellicum Pharmaceuticals). According to the data reported by the company, co-expression of the iMyD88-CD40 (iMC) hybrid molecule and the first-generation CAR engages a broader range of activation mechanisms, which results in more vigorous proliferation of GoCAR-T-cells that eliminate tumor cells both *in vitro* and *in vivo*.

It seems that there is no “one-size-fits-all” solution to CAR engineering, since different combinations of signaling and costimulatory modules are optimal for treating different types of cancers and these CAR variants are usually identified through trial and error. In this regard, the study by Australian researchers is notable: they have constructed a combinatorial library of the cytoplasmic domains of CAR using 14 signaling modules (CD3 ζ , CD28, 4-1BB, CD27, DAP10, etc.)

assembled in-frame. This library of CARs having an identical antigen-recognition moiety yet distinct signaling sequences was expressed in Jurkat T cells, and so CAR variants inducing the most potent cell activation were screened for. As a result, an unusual combination of the signaling sequences DAP10-CD3 ζ -CD27 was identified, which was more effective *in vitro* than the CD28-CD3 ζ [102]. L. Alvarez-Vallina and colleagues proposed a conceptually similar approach for identifying the optimal/novel antigen-recognition domains within CARs. They developed a lymphocyte display platform wherein scFv libraries are directly screened in the context of CAR T cells [103]. In this case, the scFv library in the CAR format is cloned into a lentiviral vector and expressed on the T-cell surface following viral transduction. The resulting library of scFv-CAR T cells is incubated with cells carrying the desired target, and T cells whose CARs are specific enough to recognize that target are collected and analyzed following several rounds of activation/selection and counter-selection. Selection of such CAR T cells is performed based on the activation markers that appear on the cell surface after CAR engagement (they become CD69-positive). In this approach, scFvs can be selected according to their ability to induce the activation and proliferation of scFv-CAR T cells rather than according to their affinity to the target. Hence, a key advantage of CAR T cell display is that CARs are selected right in the context of the synapse between the CAR T cell and the target cell, which may turn out to be more straightforward compared to the standard *in vitro* selection of high-affinity antigen-recognition binders, inevitably followed by their optimization and structural modification in the context of CAR T cells. Yet, one should bear in mind that CAR T cell display is associated with an important engineering constraint: namely, the significant decrease in the complexity of the CAR library

amenable for screening (below 10^6 – 10^7). These studies show that assays that recapitulate the *in vivo* situation as close as possible should be used for testing CAR designs early on, since the CARs shown to perform well *in vitro* do not necessarily work in mice, nor do they by any means guarantee the same will be observed in a clinical setting. For this reason, it is currently believed that designing and testing the broadest range of CAR variants possible may be the only way to ultimately bring, at least, one of them to patients.

CONCLUSIONS

The clear translational potential of the CAR T-cell platform has attracted interest to this field and prompted the development of various CAR designs. Nonetheless, the available experimental, and especially clinical, data that explore how the CAR structure affects its *in vivo* properties and which modifications ensure the maximum clinical effectiveness of CAR T-cell therapy remain scarce. Impressive results in the CAR T-cell therapy of rALL patients have stimulated attempts to adapt this platform to the treatment of solid cancers, and the first results indicate that further technological improvements are needed. Clearly, the widespread use of this platform will require additional systematic research and a more thorough understanding of the entire spectrum of the mechanisms that contribute to the establishment and maintenance of antitumor immunity.

The authors are thankful to A.V. Kharkevich for his assistance in preparing the illustrations.

This work was supported by the Russian Science Foundation (grant no. 16-14-10237). A.V. Tarantin received support from the Basic Research Program (discipline code 0310-2015-0006).

REFERENCES

- Gill S., June C.H. // Immunol. Rev. 2015. V. 263. № 1. P. 68–89.
- Morgan R.A., Yang J.C., Kitano M., Dudley M.E., Laurencot C.M., Rosenberg S.A. // Mol. Ther. 2010. V. 18. № 4. P. 843–851.
- Kuwana Y., Asakura Y., Utsunomiya N., Nakanishi M., Arata Y., Itoh S., Nagase F., Kurosawa Y. // Biochem. Biophys. Res. Commun. 1987. V. 149. № 3. P. 960–968.
- Eshhar Z., Waks T., Gross G., Schindler D.G. // Proc. Natl. Acad. Sci. USA. 1993. V. 90. № 2. P. 720–724.
- Bird R.E., Hardman K.D., Jacobson J.W., Johnson S., Kaufman B.M., Lee S.M., Lee T., Pope S.H., Riordan G.S., Whitlow M. // Science. 1988. V. 242. № 4877. P. 423–426.
- Kershaw M.H., Westwood J.A., Parker L.L., Wang G., Eshhar Z., Mavroukakis S.A., White D.E., Wunderlich J.R., Canevari S., Rogers-Freezer L., et al. // Clin. Cancer Res. 2006. V. 12. № 20. Pt 1. P. 6106–6115.
- Worn A., Pluckthun A. // J. Mol. Biol. 2001. V. 305. № 5. P. 989–1010.
- Long A.H., Haso W.M., Shern J.F., Wanhainen K.M., Murgai M., Ingaramo M., Smith J.P., Walker A.J., Kohler M.E., Venkateshwar V.R., et al. // Nat. Med. 2015. V. 21. № 6. P. 581–590.
- Maus M.V., Haas A.R., Beatty G.L., Albelda S.M., Levine B.L., Liu X., Zhao Y., Kalos M., June C.H. // Cancer Immunol. Res. 2013. V. 1. № 1. P. 26–31.
- Mintz A., Gibo D.M., Slagle-Webb B., Christensen N.D., Debinski W. // Neoplasia. 2002. V. 4. № 5. P. 388–399.
- Kioi M., Kawakami M., Shimamura T., Husain S.R., Puri R.K. // Cancer. 2006. V. 107. № 6. P. 1407–1418.
- Krenciute G., Krebs S., Torres D., Wu M.F., Liu H., Dotti G., Li X.N., Lesniak M.S., Balyasnikova I.V., Gottschalk S. // Mol. Ther. 2015. V. 24. № 2. P. 354–363.

13. Kahlon K.S., Brown C., Cooper L.J., Raubitschek A., Forman S.J., Jensen M.C. // *Cancer Res.* 2004. V. 64. № 24. P. 9160–9166.
14. Kong S., Sengupta S., Tyler B., Bais A.J., Ma Q., Doucette S., Zhou J., Sahin A., Carter B.S., Brem H., et al. // *Clin. Cancer Res.* 2012. V. 18. № 21. P. 5949–5960.
15. Krebs S., Chow K.K., Yi Z., Rodriguez-Cruz T., Hegde M., Gerken C., Ahmed N., Gottschalk S. // *Cytotherapy.* 2014. V. 16. № 8. P. 1121–1131.
16. Zhang T., Lemoi B.A., Sentman C.L. // *Blood.* 2005. V. 106. № 5. P. 1544–1551.
17. Shaffer D.R., Savoldo B., Yi Z., Chow K.K., Kakarla S., Spencer D.M., Dotti G., Wu M.F., Liu H., Kenney S., et al. // *Blood.* 2011. V. 117. № 16. P. 4304–4314.
18. Barber A., Zhang T., Megli C.J., Wu J., Meehan K.R., Sentman C.L. // *Exp. Hematol.* 2008. V. 36. № 10. P. 1318–1328.
19. Altenschmidt U., Kahl R., Moritz D., Schnierle B.S., Gerstmayr B., Wels W., Groner B. // *Clin. Cancer Res.* 1996. V. 2. № 6. P. 1001–1008.
20. Muniappan A., Banapour B., Lebkowski J., Talib S. // *Cancer Gene Ther.* 2000. V. 7. № 1. P. 128–134.
21. Roberts M.R., Qin L., Zhang D., Smith D.H., Tran A.C., Dull T.J., Groopman J.E., Capon D.J., Byrn R.A., Finer M.H. // *Blood.* 1994. V. 84. № 9. P. 2878–2889.
22. Yang O.O., Tran A.C., Kalams S.A., Johnson R.P., Roberts M.R., Walker B.D. // *Proc. Natl. Acad. Sci. USA.* 1997. V. 94. № 21. P. 11478–11483.
23. Romeo C., Seed B. // *Cell.* 1991. V. 64. № 5. P. 1037–1046.
24. Niederman T.M., Ghogawala Z., Carter B.S., Tompkins H.S., Russell M.M., Mulligan R.C. // *Proc. Natl. Acad. Sci. USA.* 2002. V. 99. № 10. P. 7009–7014.
25. Zhang T., Wu M.R., Sentman C.L. // *J. Immunol.* 2012. V. 189. № 5. P. 2290–2299.
26. Davies D.M., Foster J., van der Stegen S.J., Parente-Pereira A.C., Chiapero-Stanke L., Delinassios G.J., Burbridge S.E., Kao V., Liu Z., Bosshard-Carter L., et al. // *Mol. Med.* 2012. V. 18. P. 565–576.
27. Pameijer C.R., Navanjo A., Meechoovet B., Wagner J.R., Aguilar B., Wright C.L., Chang W.C., Brown C.E., Jensen M.C. // *Cancer Gene Ther.* 2007. V. 14. № 1. P. 91–97.
28. Huang G., Yu L., Cooper L.J., Hollomon M., Huls H., Kleinerman E.S. // *Cancer Res.* 2012. V. 72. № 1. P. 271–281.
29. Binz H.K., Stumpf M.T., Forrer P., Amstutz P., Pluckthun A. // *J. Mol. Biol.* 2003. V. 332. № 2. P. 489–503.
30. Hammill J.A., VanSeggelen H., Helsen C.W., Denisova G.F., Eveleigh C., Tantalò D.G., Bassett J.D., Bramson J.L. // *J. Immunother. Cancer.* 2015. V. 3. P. 55.
31. Jamnani F.R., Rahbarizadeh F., Shokrgozar M.A., Mahboudi F., Ahmadvand D., Sharifzadeh Z., Parhamifar L., Moghimi S.M. // *Biochim. Biophys. Acta.* 2014. V. 1840. № 1. P. 378–386.
32. Sharifzadeh Z., Rahbarizadeh F., Shokrgozar M.A., Ahmadvand D., Mahboudi F., Jamnani F.R., Moghimi S.M. // *Cancer Lett.* 2013. V. 334. № 2. P. 237–244.
33. Zhang G., Liu R., Zhu X., Wang L., Ma J., Han H., Wang X., Zhang G., He W., Wang W., et al. // *Immunol. Cell Biol.* 2013. V. 91. № 10. P. 615–624.
34. Zhang G., Wang L., Cui H., Wang X., Zhang G., Ma J., Han H., He W., Wang W., Zhao Y., et al. // *Sci. Rep.* 2014. V. 4. P. 3571.
35. Moot R., Raikar S.S., Fleischer L., Tylawsky D.E., Nakahara H., Doering C.B., Spencer H.T. // *Mol. Ther. Oncolytics.* 2016. V. 3. P. 16026.
36. Urbanska K., Lanitis E., Poussin M., Lynn R.C., Gavin B.P., Kelderman S., Yu J., Scholler N., Powell D.J., Jr. // *Cancer Res.* 2012. V. 72. № 7. P. 1844–1852.
37. Rodgers D.T., Mazagova M., Hampton E.N., Cao Y., Ramadoss N.S., Hardy I.R., Schulman A., Du J., Wang F., Singer O., et al. // *Proc. Natl. Acad. Sci. USA.* 2016. V. 113. № 4. P. E459–E468.
38. Tamada K., Geng D., Sakoda Y., Bansal N., Srivastava R., Li Z., Davila E. // *Clin. Cancer Res.* 2012. V. 18. № 23. P. 6436–6445.
39. Ma J.S., Kim J.Y., Kazane S.A., Choi S.H., Yun H.Y., Kim M.S., Rodgers D.T., Pugh H.M., Singer O., Sun S.B., et al. // *Proc. Natl. Acad. Sci. USA.* 2016. V. 113. № 4. P. E450–E458.
40. Wu J., Edberg J.C., Redecha P.B., Bansal V., Guyre P.M., Coleman K., Salmon J.E., Kimberly R.P. // *J. Clin. Invest.* 1997. V. 100. № 5. P. 1059–1070.
41. Koene H.R., Kleijer M., Algra J., Roos D., von dem Borne A.E., de Haas M. // *Blood.* 1997. V. 90. № 3. P. 1109–1114.
42. Musolino A., Naldi N., Bortesi B., Pezzuolo D., Capelletti M., Missale G., Laccabue D., Zerbini A., Camisa R., Bisagni G., et al. // *J. Clin. Oncol.* 2008. V. 26. № 11. P. 1789–1796.
43. Clemenceau B., Congy-Jolivet N., Gallot G., Vivien R., Gaschet J., Thibault G., Vie H. // *Blood.* 2006. V. 107. № 12. P. 4669–4677.
44. Kudo K., Imai C., Lorenzini P., Kamiya T., Kono K., Davidoff A.M., Chng W.J., Campana D. // *Cancer Res.* 2014. V. 74. № 1. P. 93–103.
45. D’Aloia M.M., Caratelli S., Palumbo C., Battella S., Arriga R., Lauro D., Palmieri G., Sconocchia G., Alimandi M. // *Cytotherapy.* 2016. V. 18. № 2. P. 278–290.
46. Dustin M.L., Shaw A.S. // *Science.* 1999. V. 283. № 5402. P. 649–650.
47. Grakoui A., Bromley S.K., Sumen C., Davis M.M., Shaw A.S., Allen P.M., Dustin M.L. // *Science.* 1999. V. 285. № 5425. P. 221–227.
48. Grakoui A., Bromley S.K., Sumen C., Davis M.M., Shaw A.S., Allen P.M., Dustin M.L. // *J. Immunol.* 2015. V. 194. № 9. P. 4066–4072.
49. Irls C., Symons A., Michel F., Bakker T.R., van der Merwe P.A., Acuto O. // *Nat. Immunol.* 2003. V. 4. № 2. P. 189–197.
50. Cordoba S.P., Choudhuri K., Zhang H., Bridge M., Basat A.B., Dustin M.L., van der Merwe P.A. // *Blood.* 2013. V. 121. № 21. P. 4295–4302.
51. Moritz D., Groner B. // *Gene Ther.* 1995. V. 2. № 8. P. 539–546.
52. Dotti G., Gottschalk S., Savoldo B., Brenner M.K. // *Immunol. Rev.* 2014. V. 257. № 1. P. 107–126.
53. Hombach A.A., Schildgen V., Heuser C., Finfern R., Gilham D.E., Abken H. // *J. Immunol.* 2007. V. 178. № 7. P. 4650–4657.
54. James S.E., Greenberg P.D., Jensen M.C., Lin Y., Wang J., Till B.G., Raubitschek A.A., Forman S.J., Press O.W. // *J. Immunol.* 2008. V. 180. № 10. P. 7028–7038.
55. Haso W., Lee D.W., Shah N.N., Stetler-Stevenson M., Yuan C.M., Pastan I.H., Dimitrov D.S., Morgan R.A., Fitzgerald D.J., Barrett D.M., et al. // *Blood.* 2013. V. 121. № 7. P. 1165–1174.
56. Guest R.D., Hawkins R.E., Kirillova N., Cheadle E.J., Arnold J., O’Neill A., Irlam J., Chester K.A., Kemshead J.T., Shaw D.M., et al. // *J. Immunother.* 2005. V. 28. № 3. P. 203–211.
57. Long A.H., Haso W.M., Orentas R.J. // *Oncoimmunology.* 2013. V. 2. № 4. P. e23621.
58. Finney H.M., Lawson A.D., Bebbington C.R., Weir A.N. // *J. Immunol.* 1998. V. 161. № 6. P. 2791–2797.

59. Moritz D., Wels W., Mattern J., Groner B. // *Proc. Natl. Acad. Sci. USA*. 1994. V. 91. № 10. P. 4318–4322.
60. Wilkie S., Picco G., Foster J., Davies D.M., Julien S., Cooper L., Arif S., Mather S.J., Taylor-Papadimitriou J., Burchell J.M., et al. // *J. Immunol.* 2008. V. 180. № 7. P. 4901–4909.
61. Patel S.D., Moskalenko M., Smith D., Maske B., Finer M.H., McArthur J.G. // *Gene Ther.* 1999. V. 6. № 3. P. 412–419.
62. Sadelain M., Brentjens R., Riviere I. // *Curr. Opin. Immunol.* 2009. V. 21. № 2. P. 215–223.
63. Almasbak H., Walseng E., Kristian A., Myhre M.R., Suso E.M., Munthe L.A., Andersen J.T., Wang M.Y., Kvalheim G., Gaudernack G., et al. // *Gene Ther.* 2015. V. 22. № 5. P. 391–403.
64. Hudecek M., Sommermeyer D., Kosasih P.L., Silva-Benedict A., Liu L., Rader C., Jensen M.C., Riddell S.R. // *Cancer Immunol. Res.* 2015. V. 3. № 2. P. 125–135.
65. Jonnalagadda M., Mardiros A., Urak R., Wang X., Hoffman L.J., Bernanke A., Chang W.C., Bretzlaff W., Starr R., Priceman S., et al. // *Mol. Ther.* 2015. V. 23. № 4. P. 757–768.
66. Hombach A., Hombach A.A., Abken H. // *Gene Ther.* 2010. V. 17. № 10. P. 1206–1213.
67. Riddell S.R., Protzer U. // *Gene Ther.* 2010. V. 17. № 10. P. 1191–1192.
68. Fitzer-Attas C.J., Schindler D.G., Waks T., Eshhar Z. // *J. Immunol.* 1998. V. 160. № 1. P. 145–154.
69. Bridgeman J.S., Hawkins R.E., Bagley S., Blaylock M., Holland M., Gilham D.E. // *J. Immunol.* 2010. V. 184. № 12. P. 6938–6949.
70. Zhao Y., Wang Q.J., Yang S., Kochenderfer J.N., Zheng Z., Zhong X., Sadelain M., Eshhar Z., Rosenberg S.A., Morgan R.A. // *J. Immunol.* 2009. V. 183. № 9. P. 5563–5574.
71. Shi H., Sun M., Liu L., Wang Z. // *Mol. Cancer*. 2014. V. 13. P. 219.
72. Gosse J.A., Wagenknecht-Wiesner A., Holowka D., Baird B. // *J. Immunol.* 2005. V. 175. № 4. P. 2123–2131.
73. Annenkov A.E., Moyes S.P., Eshhar Z., Mageed R.A., Chernajovskiy Y. // *J. Immunol.* 1998. V. 161. № 12. P. 6604–6613.
74. Bridgeman J.S., Ladell K., Sheard V.E., Miners K., Hawkins R.E., Price D.A., Gilham D.E. // *Clin. Exp. Immunol.* 2014. V. 175. № 2. P. 258–267.
75. Irving B.A., Weiss A. // *Cell*. 1991. V. 64. № 5. P. 891–901.
76. Haynes N.M., Snook M.B., Trapani J.A., Cerruti L., Jane S.M., Smyth M.J., Darcy P.K. // *J. Immunol.* 2001. V. 166. № 1. P. 182–187.
77. Roberts M.R., Cooke K.S., Tran A.C., Smith K.A., Lin W.Y., Wang M., Dull T.J., Farson D., Zsebo K.M., Finer M.H. // *J. Immunol.* 1998. V. 161. № 1. P. 375–384.
78. Lenschow D.J., Walunas T.L., Bluestone J.A. // *Annu. Rev. Immunol.* 1996. V. 14. № 1. P. 233–258.
79. Gong M.C., Latouche J.B., Krause A., Heston W.D., Bander N.H., Sadelain M. // *Neoplasia*. 1999. V. 1. № 2. P. 123–127.
80. Hombach A., Wiczarkowicz A., Marquardt T., Heuser C., Usai L., Pohl C., Seliger B., Abken H. // *J. Immunol.* 2001. V. 167. № 11. P. 6123–6131.
81. Maher J., Brentjens R.J., Gunset G., Riviere I., Sadelain M. // *Nat. Biotechnol.* 2002. V. 20. № 1. P. 70–75.
82. Brentjens R.J., Santos E., Nikhamin Y., Yeh R., Matsu-shita M., La Perle K., Quintas-Cardama A., Larson S.M., Sadelain M. // *Clin. Cancer Res.* 2007. V. 13. № 18. Pt 1. P. 5426–5435.
83. Altvater B., Landmeier S., Pscherer S., Temme J., Juergens H., Pule M., Rossig C. // *Cancer Immunol. Immunother.* 2009. V. 58. № 12. P. 1991–2001.
84. Wang J., Jensen M., Lin Y., Sui X., Chen E., Lindgren C.G., Till B., Raubitschek A., Forman S.J., Qian X., et al. // *Hum. Gene Ther.* 2007. V. 18. № 8. P. 712–725.
85. Pule M.A., Straathof K.C., Dotti G., Heslop H.E., Rooney C.M., Brenner M.K. // *Mol. Ther.* 2005. V. 12. № 5. P. 933–941.
86. Song D.G., Ye Q., Poussin M., Harms G.M., Figini M., Powell D.J., Jr. // *Blood*. 2012. V. 119. № 3. P. 696–706.
87. Imai C., Mihara K., Andreansky M., Nicholson I.C., Pui C.H., Geiger T.L., Campana D. // *Leukemia*. 2004. V. 18. № 4. P. 676–684.
88. Finney H.M., Akbar A.N., Lawson A.D. // *J. Immunol.* 2004. V. 172. № 1. P. 104–113.
89. Milone M.C., Fish J.D., Carpenito C., Carroll R.G., Binder G.K., Teachey D., Samanta M., Lakhai M., Gloss B., Danet-Desnoyers G., et al. // *Mol. Ther.* 2009. V. 17. № 8. P. 1453–1464.
90. Zhong X.S., Matsushita M., Plotkin J., Riviere I., Sadelain M. // *Mol. Ther.* 2010. V. 18. № 2. P. 413–420.
91. Carpenito C., Milone M.C., Hassan R., Simonet J.C., Lakhai M., Suhoski M.M., Varela-Rohena A., Haines K.M., Heitjan D.F., Albelda S.M., et al. // *Proc. Natl. Acad. Sci. USA*. 2009. V. 106. № 9. P. 3360–3365.
92. Karlsson H., Svensson E., Gigg C., Jarvius M., Olsson-Stromberg U., Savoldo B., Dotti G., Loskog A. // *PLoS One*. 2015. V. 10. № 12. P. e0144787.
93. Till B.G., Jensen M.C., Wang J., Qian X., Gopal A.K., Maloney D.G., Lindgren C.G., Lin Y., Pagel J.M., Budde L.E., et al. // *Blood*. 2012. V. 119. № 17. P. 3940–3950.
94. Savoldo B., Ramos C.A., Liu E., Mims M.P., Keating M.J., Carrum G., Kamble R.T., Bollard C.M., Gee A.P., Mei Z., et al. // *J. Clin. Invest.* 2011. V. 121. № 5. P. 1822–1826.
95. Brentjens R.J., Davila M.L., Riviere I., Park J., Wang X., Cowell L.G., Bartido S., Stefanski J., Taylor C., Olszewska M., et al. // *Sci. Transl. Med.* 2013. V. 5. № 177. P. 177ra138.
96. Grupp S.A., Kalos M., Barrett D., Aplenc R., Porter D.L., Rheingold S.R., Teachey D.T., Chew A., Hauck B., Wright J.F., et al. // *N. Engl. J. Med.* 2013. V. 368. № 16. P. 1509–1518.
97. Kochenderfer J.N., Dudley M.E., Feldman S.A., Wilson W.H., Spaner D.E., Maric I., Stetler-Stevenson M., Phan G.Q., Hughes M.S., Sherry R.M., et al. // *Blood*. 2012. V. 119. № 12. P. 2709–2720.
98. Lee D.W., Kochenderfer J.N., Stetler-Stevenson M., Cui Y.K., Delbrook C., Feldman S.A., Fry T.J., Orentas R., Sabatino M., Shah N.N., et al. // *Lancet*. 2015. V. 385. № 9967. P. 517–528.
99. Maude S.L., Frey N., Shaw P.A., Aplenc R., Barrett D.M., Bunin N.J., Chew A., Gonzalez V.E., Zheng Z., Lacey S.F., et al. // *N. Engl. J. Med.* 2014. V. 371. № 16. P. 1507–1517.
100. van der Stegen S.J., Hamieh M., Sadelain M. // *Nat. Rev. Drug Discov.* 2015. V. 14. № 7. P. 499–509.
101. Zhao Z., Condomines M., van der Stegen S.J., Perna F., Kloss C.C., Gunset G., Plotkin J., Sadelain M. // *Cancer Cell*. 2015. V. 28. № 4. P. 415–428.
102. Duong C.P., Westwood J.A., Yong C.S., Murphy A., Devaud C., John L.B., Darcy P.K., Kershaw M.H. // *PLoS One*. 2013. V. 8. № 5. P. e63037.
103. Alonso-Camino V., Sanchez-Martin D., Compte M., Nunez-Prado N., Diaz R.M., Vile R., Alvarez-Vallina L. // *Mol. Ther. Nucl. Acids*. 2013. V. 2. P. e93.

Proteomics for the Investigation of Mycobacteria

J. A. Bespyatykh*, E. A. Shitikov, E. N. Ilina

Federal Research and Clinical Center of Physical-Chemical Medicine of Federal Medical Biological Agency, Malaya Pirogovskaya str. 1a, Moscow, 119435, Russia

*E-mail: JuliaBespyatykh@gmail.com

Received March 17, 2016; in final form, October 10, 2016

Copyright © 2017 Park-media, Ltd. This is an open access article distributed under the Creative Commons Attribution License, which permits unrestricted use, distribution, and reproduction in any medium, provided the original work is properly cited.

ABSTRACT The physiology of *Mycobacterium tuberculosis*, the causative agent of tuberculosis, is being studied with intensity. However, despite the genomic and transcriptomic data available today, the pathogenic potential of these bacteria remains poorly understood. Therefore, proteomic approaches seem relevant in studying mycobacteria. This review covers the main stages in the proteomic analysis methods used to study mycobacteria. The main achievements in the area of *M. tuberculosis* proteomics are described in general. Special attention is paid to the proteomic features of the Beijing family, which is widespread in Russia. Considering that the proteome is a set of all the proteins in the cell, post-translational modifications of mycobacterium proteins are also described.

KEYWORDS *Mycobacterium tuberculosis*, proteins, proteome, proteomics, tuberculosis.

ABBREVIATIONS MS – mass-spectrometry; HPLC – high-performance liquid chromatography; MRM – multiple reaction monitoring; PTM – post-translational modifications; ORF – open reading frame; TB – tuberculosis

INTRODUCTION

The systems biology of prokaryotes seeks to understand how the physical and chemical properties and the nature of the interaction between biomolecules are related to the formation of the phenotypic properties of microorganisms. Nowadays, the nucleotide sequence of a prokaryotic genome can be deciphered within hours. Nevertheless, despite the fact that the genome encodes, either directly or indirectly, key cell biomolecules such as RNA and proteins, it remains impossible to characterize their functional properties based on information regarding the genomic sequence. Accurate and reproducible methods for the quantification of all components under various conditions are needed to study the structure, function, and molecular mechanisms of regulation in these molecular systems. To date, these assessments have become common for RNA [1–4]. However, they still lag behind in sensitivity and representativeness due to technical limitations at the protein level.

Clinically relevant microorganisms, in particular mycobacteria, have been studied most intensely using systems biology methods. To date, 213 mycobacterial species have been described, many of which are associated with infectious processes in humans or animals [5]. These species include *Mycobacterium tuberculosis*, *M. leprae*, and *M. ulcerans*, which cause tuberculosis, leprosy, and Buruli ulcer, respectively. According to international statistics, approximately one-third of the

world's population is infected with tuberculosis; approximately 1.3 million deaths from the disease were registered in 2015 [6]. Not surprisingly, the features of the physiology and molecular organization of *M. tuberculosis* are of the greatest interest.

Until recently, major efforts have focused on the features of the genomic organization of the tuberculosis pathogen. Today, genomic sequencing data for more than 10,000 *M. tuberculosis* strains with different phenotypes and genotypes are available. However, the experience of applying the whole genome sequencing technology with subsequent comparative analysis reveals the limited applicability of the approach for a complete description of the causes behind drug resistance and pathogenicity [7]. Thus, the majority of the point mutations that distinguish groups of strains have been found in the promoter regions of the genes and/or regions encoding proteins with a hypothetical function and playing an unknown role in the physiology of mycobacteria. In this context, a functional analysis of the information enciphered in the pathogen genome performed using proteomic testing, including quantitative proteomics, becomes relevant.

It is worth noting that isolation of DNA and RNA from mycobacteria and further manipulations have been described in a large number of protocols [8–10] which are applied in various laboratories [11–16]. The situation with protein isolation, especially isolation of the total protein fraction required to obtain the pro-

teome, is quite the opposite. The features of organization of the cell wall, which is resistant to environmental factors, acids and alkalis, make *M. tuberculosis* a rather complex target for a proteomic analysis. This, in its turn, requires the development of unique conditions for protein extraction. The implemented protocols of proteomic analysis of *M. tuberculosis* should also be sufficiently effective, taking into account the complexity of accumulation of a large bacterial mass due to the extremely slow culture growth.

This review looks into the development of tools for the proteomic analysis of mycobacteria in the chronological aspect of increasing their informative value and the accuracy of assessments.

PROTEOMIC APPROACHES FOR MYCOBACTERIAL STUDIES

Development of the methods of proteomic analysis of mycobacteria

Mark Wilkins was the first to introduce the term “proteome” in 1986, which combined two words: “PROTEIn” and “genOME” [17]. Proteome is the set of all proteins in the cell, including the changes that occur over time or under some factors. In 1997, the term “proteomics” appeared by analogy with genomics, which studies genes and their functions [18].

Proteomics studies the set of proteins synthesized by an organism/cell in a specific environment and at a particular stage of the cell cycle. It describes the qualitative composition of proteins, their relative representation, interaction with other macromolecules, and post-translational modifications (PTM) [19–21].

Proteomics still lags behind genomics and transcriptomics due to instrumental problems and the insufficient sensitivity of the existing methods. However, the number of works that utilize proteomic methods for studying infectious agents is on the increase.

R. Aebersold et al. made the most significant contribution to the development of the proteomics of mycobacteria [22, 23]. The main studies on mycobacterial proteins are presented in *table*.

The early studies in the field of *M. tuberculosis* proteomics conducted at the end of the 20th century relied on the strategy of the so-called top-down proteomics, the main principle of which is sorting the intact proteins isolated from a biological sample based on their physical and chemical properties (using gel electrophoresis and gel filtration) and subsequently identifying them using mass spectrometric (MS) methods (*Fig. 1*). This approach enabled the identification and quantification of about 100 mycobacterial proteins [24], which does not exceed 3% of the total proteome of *M. tuberculosis*.

Further development of the tools of a proteomic analysis opened up new ways for exploring tuberculosis and facilitated the study of many complex issues, including the interactions between a bacterium and the host cell. The technologies that implement the strategy of the so-called bottom-up proteomics are considered to be most effective for obtaining the total proteome [20, 21]. These technologies are based on the fact that the total set of proteins isolated from a biological object is first proteolytically cleaved into peptides, which are then continuously analyzed by high-performance liquid chromatography coupled with tandem mass spectrometry (HPLC-MS/MS) (*Fig. 1*). The variety of bottom-up methods at the stage of MS experiment can be divided into (1) exploratory or panoramic (shotgun proteomics) and (2) confirming (target) ones (*Fig. 2*). The first ones are aimed at identifying and quantifying as many proteins as possible and allow one to identify up to 1,000 *M. tuberculosis* proteins in a single MS run [25]. The latter methods are developed for tracking a relatively small set of proteins/peptides, which is defined prior to an experiment, in numerous samples with the highest sensitivity, accuracy, reproducibility and capacity available for the method (e.g., multiple reaction monitoring, MRM).

The most accurate results in a quantitative comparison of samples using the panoramic approach are achieved by isotopic labeling of one of the analytes [38]. In particular, stable isotope labeling by amino acids in a cell culture (SILAC) is based on the incorporation of essential amino acids containing stable isotopes (usually ¹³C/¹⁵N arginine and/or lysine) in the protein structure [39, 40]. It is assumed that the analyzed cells do not synthesize lysine and arginine but utilize only the labeled amino acids present in the medium. However, *M. tuberculosis* is capable of endogenously synthesizing lysine, which immediately limits the possibilities of this approach. The main emphasis in the quantitative proteomics of mycobacteria has since recently been placed on using non-labeling methods for the MS quantification of proteins that are characterized by greater sensitivity and performance [31, 41].

New approaches to the accumulation and processing of mass spectra, e.g., SWATH™ designed by ABSciEX, combine the panoramic (data-independent acquisition, DIA) and confirming (data-dependent acquisition, DDA) techniques aimed at minimizing the limitations of each one of them [42]. Moreover, SWATH™ does not require the selection of individual parent ions, while precursor ions are skipped by large windows (e.g., of about 25 Da). Thus, SWATH™ allows one to identify and quantify a large set of proteins, similarly to the conventional panoramic approach but with a precision and reproducibility typical of that of MMP for a larger number of samples.

Table. The major studies that have contributed to the development of mycobacterial proteomics

Year	Title	Number of identified proteins	Reference
1997	Definition of <i>Mycobacterium tuberculosis</i> culture filtrate proteins by two-dimensional polyacrylamide gel electrophoresis, N-terminal amino acid sequencing, and electrospray mass spectrometry	32	M.G. Sonnenberg and J.T. Belisle [26]
1999	Comparative proteome analysis of <i>Mycobacterium tuberculosis</i> and <i>Mycobacterium bovis</i> BCG strains: toward functional genomics of microbial pathogens	107	P.R. Jungblut <i>et al.</i> [27]
2000	Toward the proteome of <i>Mycobacterium tuberculosis</i>	167	I. Rosenkrands <i>et al.</i> [24]
2003	Comprehensive proteomic profiling of the membrane constituents of a <i>Mycobacterium tuberculosis</i> strain	739	S. Gu <i>et al.</i> [28]
2004	Complementary analysis of the <i>Mycobacterium tuberculosis</i> proteome by two-dimensional electrophoresis and isotope-coded affinity tag technology	361	F. Schmidt <i>et al.</i> [29]
2005	<i>Mycobacterium tuberculosis</i> functional network analysis by global subcellular protein profiling	1044	K.G. Mawuenyega <i>et al.</i> [30]
2010	Using a label-free proteomics method to identify differentially abundant proteins in closely related hypo- and hypervirulent clinical <i>Mycobacterium tuberculosis</i> Beijing isolates	1668	G.A. de Souza <i>et al.</i> [31]
2011	Comparison of membrane proteins of <i>Mycobacterium tuberculosis</i> H37Rv and H37Ra strains	1578	H. Malen <i>et al.</i> [32]
2011	Characterization of the <i>Mycobacterium tuberculosis</i> proteome by liquid chromatography mass spectrometry-based proteomics techniques: a comprehensive resource for tuberculosis research	1051	C. Bell <i>et al.</i> [33]
2011	Proteogenomic analysis of <i>Mycobacterium tuberculosis</i> by high resolution mass spectrometry	3176	D.S. Kelkar <i>et al.</i> [34]
2013	The Mtb Proteome Library: A resource of assays to quantify the complete proteome of <i>Mycobacterium tuberculosis</i>	3894	O.T. Schubert <i>et al.</i> [23]
2014	Disclosure of selective advantages in the “modern” sublineage of the <i>Mycobacterium tuberculosis</i> Beijing genotype family by quantitative proteomics.	2392	J. de Keijzer <i>et al.</i> [35]
2015	Quantitative proteomic analysis of <i>M. tuberculosis</i> cluster Beijing B0/W148 strains	1868	J. Bespyatykh <i>et al.</i> [36, 37]

PROTEOMIC FEATURES OF CERTAIN MYCOBACTERIAL GROUPS

Proteomic characterization of the *M. tuberculosis* H37Rv strain

M. tuberculosis H37Rv is now the most well-studied mycobacterial strain. The genomic sequence of this strain was completely deciphered in 1998 [43]. It is not surprising that it is also the proteome of this strain that has been studied as thoroughly as possible. The existence of 97% out of 4,012 annotated proteins has been confirmed by genomic sequences using comprehensive proteomic approaches [23]. Pools of cell wall and membrane proteins [32, 44], cytosolic proteins [25, 30, 45], and secreted proteins detected in a culture filtrate [46] have been described.

An analysis of the proteins of DosR regulon, which is associated with the anaerobic survival of *M. tuberculosis*, revealed changes in their representation in a strain H37Rv bacterial culture under hypoxic conditions [29]. In particular, representation of the HspX protein increased 340-fold during hypoxia compared to that in the culture under normal conditions. It is worth noting that this regulon had earlier been studied only at the level of transcripts [47, 48].

Of special interest are the studies focused on a simulation of the infectious process and assessment of the protein profile of *M. tuberculosis* under conditions maximally similar to the existence of bacterial cells in a living organism. Cho *et al.* [49] conducted a comparative proteomic analysis of the proteins of a latent H37Rv strain at the exponential, logarithmic, and stationary

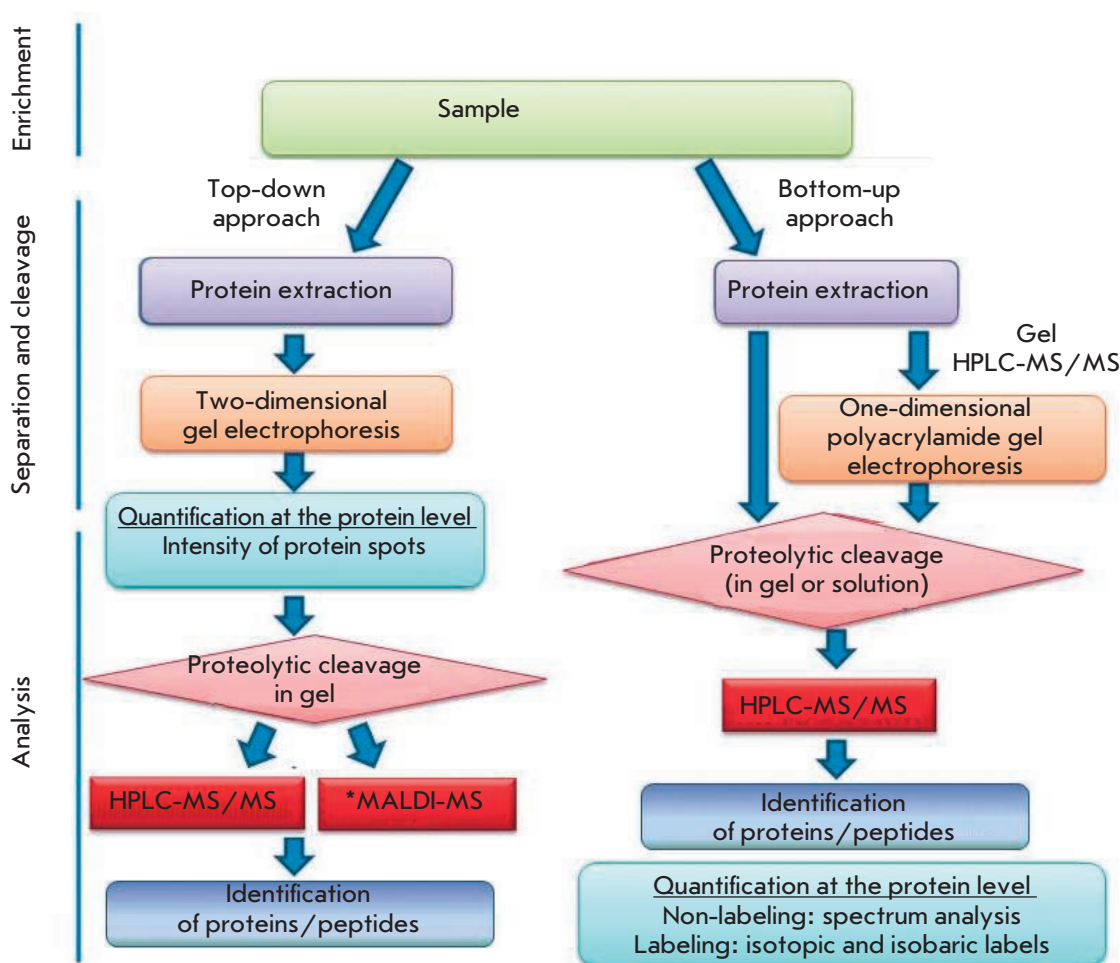


Fig. 1. Main proteomic approaches: top-down and bottom-up. Adapted from [118] with modifications.

*MALDI MS – matrix-assisted laser desorption/ionization combined with mass spectrometry

growth phases using the technique of site-specific labeling of cysteine residues (isotope-coded affinity tags, ICAT) based on covalent labeling of the cysteine residue in the polypeptide chain by chemically identical but isotopically different reagents [22, 29]. The results allowed them to identify highly enriched proteins typical of the exponential and stationary phases: 193 and 241 proteins, respectively. Most of these systems were associated with the pathways of protein degradation and energetic metabolism.

The differences in the proteomic profiles of a virulent H37Rv strain and avirulent mycobacteria (*M. tuberculosis* H37Ra, *M. bovis* BCG) were evaluated in order to study the virulence factors of *M. tuberculosis* and to identify potential candidates for designing vaccines. A similar representation of the majority of membrane proteins was found in the strains H37Rv and H37Ra, while the representation of 121 proteins in these strains varied more than fivefold. Further re-

search into membrane lipoproteins and data on their regulation suggested that the change in the metabolic state might play some role in the increased virulence [32]. The study of Esat-6 proteins and ESAT-6-like proteins, which are found in H37Rv strains but not in the H37Ra strain, showed mutations in the genes of five ESAT-6-like proteins in the strain H37Ra. It is worth mentioning that the 6 kDa antigen (Esat-6) forms a heterodimeric complex with the CFP-10 protein [50]. Therefore, the ESAT-6/CFP-10 system is believed to be associated with *M. tuberculosis* and inhibit the fusion of phagosome and lysosome in host macrophages, thereby preventing the destruction of mycobacterial cells [51].

Although H37Rv and *M. bovis* BCG share more than 99.9% homology at the genomic level, 294 proteins that differ statistically significantly between the two strains have been identified [41]. A lack in certain regions of difference (RD) was previously established in the BCG

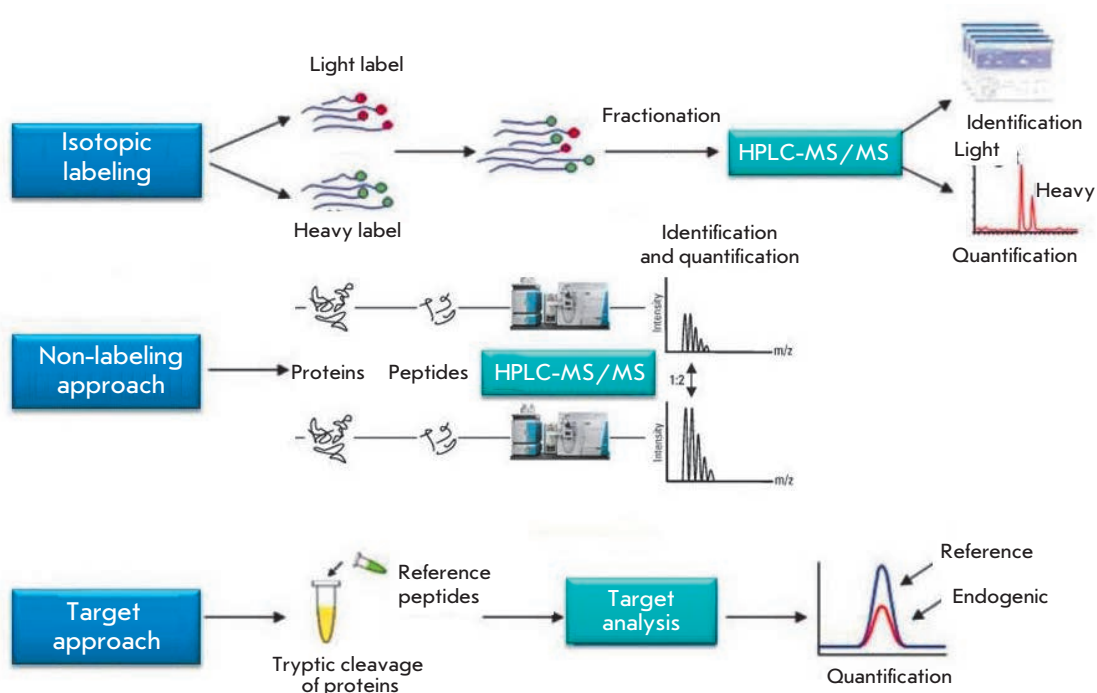


Fig. 2. Methods of proteomic analysis implementing the bottom-up approaches

genome using a comparative genomic analysis of these strains; the lack of pathogenicity was associated with a loss of the corresponding genes [52]. Hence, a series of different proteins corresponded to the described RDs [41, 53, 54]. Among them, special attention was paid to the ESAT-6 system, the proteins of which had been previously suggested as candidates for designing a new vaccine [55]. In addition, 22 differentially expressed proteins, such as acetyl-CoA acetyltransferase (Rv0243) and several Esat-6-like proteins (Rv1198, Rv1793), were proposed for designing diagnostic and vaccine agents [54].

Proteomic characterization of strains of the Beijing *M. tuberculosis* family

As noted above, most studies have focused on the proteome of the laboratory *M. tuberculosis* H37Rv strain, while data on the proteomic characteristics of other genetic families is very scarce.

According to the most elaborate classification, *M. tuberculosis* strains are divided into seven genetic lines [56]. From a clinical point of view, the Beijing family is of undoubted interest. The strains of this family belong to the phylogenetic line 2 and are represented in the largest number of countries globally: 13% of the global amount of isolates [57]. In addition, they are characterized by an association with the development of drug resistance [58] and greater virulence compared to other families [59].

A comparison of the proteomes of the Beijing and H37Rv strains showed significant differences between them. Representation of the proteins Rv0129c, Rv0831c, Rv1096, Rv3117, and Rv3804c, which belong to known virulence factors [60], was higher in the Beijing strains than in H37Rv. Meanwhile, the content of proteins Hsp65 (Rv0440), Pst1 (Rv0934), and Rv1886c, which are basic antigens whose reduced production may contribute to the avoidance of the host's immune response by mycobacteria [61, 62], was decreased. Furthermore, proteins of the efflux pumps Rv0341, Rv2688c, and Rv3728 were found only in the Beijing strains [35].

However, we found only two papers [31, 35] that focused on the variety of proteins in the Beijing strains. In the first study, de Souza et al. compared the proteomes of the hypo- and hypervirulent strains of the family and described about 50 proteins that are highly represented in each group, while a total of 1,668 proteins have been identified [31]. Representation of the ESAT-6 protein was shown to be lower in hypervirulent strains than that in hypovirulent strains. Moreover, this result was additionally confirmed by a comparative assessment of the expression of the corresponding gene at the transcriptional level. The increase in the relative representation of the ESAT-6 protein was previously regarded as a characteristic of virulent strains [51, 55]. This ambiguous result proves that the role of ESAT-6 secretion pathways in the pathogenic-

1. Automated annotation



2. Comparison with experimental peptides



3. Refining annotation

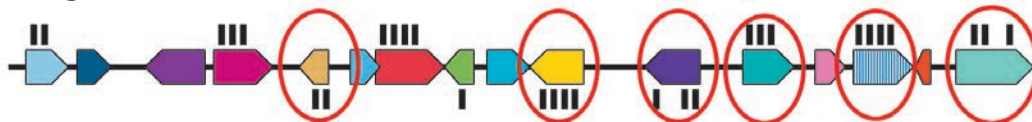


Fig. 3. Refining annotation using mass spectrometry data

ity of *M. tuberculosis* is rather complex. This can be an additional argument for the phenotypic differences between the strains of the Beijing and H37Rv families.

Another study by de Keijzer et al. was devoted to comparing the proteins of the *M. tuberculosis* strains that belong to ancient (atypical) and modern (typical) sublineages of the Beijing family [35]. Isotope labeling of amino acids in cell culture combined with HPLC-MS/MS enabled the identification and quantification of 2,392 proteins. Despite the fact that the protein profiles of both sublineages turned out to be very similar, differences in the representation of four proteins were found: MmpL4 (Rv0450c), Rv3137, Rv1269c, and SseA (Rv3283). Among these proteins, the representation of MmpL4 (Rv0450c) and Rv3137 in the group of typical strains was significantly higher than that in the atypical ones. The SseA (Rv3283) protein is among the underrepresented proteins of the modern Beijing family; its transcriptional level was also reduced.

It is worth noting that Beijing family strains hold a dominant position (50–80%) in the population structure of the tuberculosis pathogen in Russia [63, 64]. The members of this family can be divided into several types based on a VNTR analysis [65, 66]. Types M2 and M11 are most widespread in Russia and comprise about 80% of all detected isolates [66, 67]. After exploring Beijing strains B0/W148 belonging to the M11 type, we confirmed their association with the development of multidrug resistance, found new potential ways of formation of anti-TB drug resistance, and described their unique genomic rearrangement [15].

In turn, we performed a comparative proteomic analysis of Beijing B0/W148 cluster strains and the H37Rv strain [37]. A total of 1,868 proteins of B0/W148 cluster strains and 1,560 proteins of the strain H37Rv have been identified. Among them, a group of 266 dif-

ferentially represented proteins was isolated. The representation of 41 proteins in Beijing B0/W148 cluster strains was higher than in strain H37Rv, while the representation of 225 proteins was lower. We evaluated the potential biological effect of these differences on the basis of an enrichment of the functional categories of the proteins during a Gene Ontology (GO) analysis and recruitment of the gene regulatory network [68]. We assumed that some of the aforementioned features of the B0/W148 cluster representatives contribute to increased virulence and successful dissemination of these strains. In particular, we observed an increased representation of the enzymes responsible for the biosynthesis of long-chain fatty acids along with reduced representation of the proteins responsible for their degradation. Mycobacteria utilize long-chain fatty acids to obtain mycothiol acids and various lipids, which are considered to be the major virulence factors of *M. tuberculosis* manifesting themselves at the initial stages of infection when bacteria penetrate a macrophage. We have also noted an increase in the representation of the HsaA protein involved in the degradation of steroids. *M. tuberculosis* was shown to utilize extracellular cholesterol as a source of energy and to biosynthesize cell wall lipids. These observations may argue for the increased survival of mycobacteria in macrophages, which is a known characteristic of Beijing B0/W148 cluster strains [69, 70]. In addition, we found a very low level of the SseA protein in B0/W148 strains, which may possibly lead to the accumulation of reactive oxygen species and, as a result, DNA damage. This, in turn, can yield a wide spectrum of genetic variants that contribute to the survival of the bacterial cell under selection, in particular during drug therapy.

Studies in the field of proteomics of drug-resistant *M. tuberculosis* strains are also worth our attention

[71–73]. For example, a comparison of the resistant and susceptible strains revealed five proteins (Rv0491, Rv1446c, Rv2145, Rv2971, and Rv3028c) with increased representation in isoniazid-resistant strains [72]. These are membrane proteins that can potentially serve as targets for new therapeutic agents. An analysis of the aminoglycoside-resistant strains revealed an increased representation of the proteins Rv0685, Rv1876, and Rv3841, which are associated with iron metabolism [73]. Assimilation and utilization of iron play an important role in the growth, virulence, and formation of latent *M. tuberculosis* species. Pandey and Rodriguez have suggested that ferritin (Rv3841) is required for maintaining iron homeostasis in mycobacterial cells, while its lack renders bacteria more susceptible to antibiotics [74]. Increased representation of the Rv1876 and Rv3224 proteins involved in iron metabolism was also mentioned in a similar study, and their possible role in the development of resistance to second-line anti-TB drugs was suggested [71]. A comprehensive comparison of sensitive strains and multidrug-resistant strains revealed such virulence factors in resistant strains as catalase/peroxidase (Rv1908c), which is activated in phagosomes [50]. It was demonstrated previously that catalase/peroxidase activity is required for cell growth and persistence in mice, guinea pigs [75], and human peripheral blood monocytes [76]. In addition, the proteins Rv0036, Rv2032c, Rv0635, Rv1827, and Rv2896c, which partake in cellular metabolism and contribute to intracellular survival, have been identified. In one of the recent studies, the proteins Rv2031c, Rv3692, and Rv0444c were suggested for use as biomarkers for effective serodiagnosis of resistant mycobacterium strains [77].

Analysis of post-translational modifications

The advance in proteomic analysis techniques makes it possible to draw up an inventory of proteins, compare their representation, and identify the known post-translational modifications (PTM).

Today, PTMs of *M. tuberculosis* proteins such as O-glycosylation [33, 78–84], phosphorylation [85, 86], methylation [87], acetylation [88], lipidation [33, 81, 82, 89–93], deamidation [94], N-formylation [95, 96], and ubiquitination [94, 97–102] have been described.

In particular, a characterization of the ubiquitin-like protein Rv2111c of *M. tuberculosis* made it the first described ubiquitin-like bacterial system [101]. Ubiquitination (attachment of a several-molecules-long chain of the short protein ubiquitin to the protein) is a universal PTM in eukaryotes, acting as a signal for the protein's cleavage by proteasome. It is difficult to identify the corresponding proteins, since they are quickly eliminated. Ubiquitination sites were initially found in 41 *M.*

tuberculosis proteins [103]. A total of 602 ubiquitin-like mycobacterial proteins have been described to date. However, modification sites have been experimentally identified only in 55 of them [102].

Phosphorylation is another common PTM. A total of 516 sites of serine/threonine phosphorylation by kinases were found in 301 *M. tuberculosis* proteins. This data was used to search for potential motifs to explain phosphorylation by kinases. Remarkably, six out of eight tested kinases contained conserved motifs, thus indicating that there is a high level of redundancy of kinase function in *M. tuberculosis* [86].

The lipoproteins exported through the general secretory pathway and processed by signal peptidase II are modified by acylation of N-terminal cysteine. In mycobacteria, these modifications have not yet been fully characterized. Some lipoproteins can also be O-glycosylated near the N-terminus. This region often contains several threonine residues that act as a target for the aforescribed modifications. The role of these modifications is still unknown. However, there is speculation that they protect proteins from proteolytic cleavage. At least some lipoproteins are exported to the bacterial cell surface [104, 105] using a lipid tail anchored in the outer membrane [106]. Therefore, the N-terminal regions of the polypeptide chain are susceptible to proteolytic cleavage and many lipoproteins, slightly truncated and in the soluble form, can be found in culture supernatants. The glycosylated lipoproteins MPT 83 [107] and SodC [82] are currently the best characterized. O-mannosylation (a special type of glycosylation), as shown in a mouse model, reduces the pathogenic potential of *M. tuberculosis* [108]. More than 40 O-glycosylated proteins were found in the supernatant of a *M. tuberculosis* culture using proteomic approaches [83, 109]. Only one glycosylated protein not belonging to lipoproteins is known: MPT 32, or Apa [78]. Apa is one of the most common extracellular proteins secreted via the general secretory pathway [110].

Finally, detection of the TB antigen, a surface heparin-binding hemagglutinin that is considered to be a component in the design of a new vaccine, arouses interest [111, 112]. The uniqueness of this protein holds in that several lysine residues are methylated [87]. These methylated lysine residues apparently have an immunological significance and comprise T-cell epitopes in heparin-binding hemagglutinin [113]. There is ample evidence that many post-translational modifications are significant for the immune system and for protecting the organism against tuberculosis.

The lifetime of cellular proteins, their interaction with other proteins, and enzymatic activity are regulated via PTMs. The PTMs of many eukaryotic proteins comprise the necessary stage of protein maturation.

Proteins not subjected to PTMs turn out to be functionally inactive [114]. The role of the PTMs of mycobacterial proteins still remains poorly understood.

Proteogenomic analysis

All the studies we have described show that the genomic variability of mycobacterial strains is reflected at the proteomic level; hence, the data of comparative proteomics may be helpful in understanding the phenotypic differences of different groups of bacteria, such as the degree of drug sensitivity and virulence. On the other hand, proteomic studies facilitate the correct deciphering of genomic information.

Most mass spectrometric techniques rely on databases containing annotated amino acid sequences of the protein. However, a comparative analysis has shown that annotation based on genomic data is often incomplete and contains errors. For example, the genomic sequence of the *M. tuberculosis* strain H37Rv was fully deciphered at the Sanger Institute in 1998 [43] and shown to contain 3,924 open-reading frames (ORF). However, a few years later, the authors reported an increase in ORF to 3,995 [115]. The annotated version of *M. tuberculosis* H37Rv (the 27th version according to the TubercuList database) currently contains 4,018 protein-coding genes, 26% of which belong to the class of proteins with a hypothetical function. Moreover, proteomic studies have largely facilitated the processing of genomic annotation by presenting experimental evidence for a series of genes that had not been previously annotated or genes whose transcription initiation sites had been incorrectly identified, as well as by simply confirming the existing ORF (Fig. 3). Kelkar et al. identified 3,176 proteins of *M. tuberculosis* H37Rv and 250 peptides not corresponding to the existing annotation based on the data of a MS/MS analysis in 2011. As a result, the annotation was supplemented with 41 proteins and the transcription initiation sites of 33 genes were specified [34]. The same year, Norwegian researchers refined the annotation of 24 genes of the

H37Rv strain using the MS approaches [116]. In general, several large proteogenomic studies of *M. tuberculosis* have been conducted over the past few years, where each of the studies described between 20 and 40 unannotated proteins, and existing genome annotations have been refined [23, 34, 116, 117].

CONCLUSION

The advances in proteomics have opened up new approaches in studying tuberculosis by making it easier to find solutions to many complex problems, including the interactions between bacteria and the host cell. Despite the fact that proteomics lags behind genomics and transcriptomics due to limitations in instruments and insufficient sensitivity, an increasing number of studies involving proteomic approaches for the investigation of infectious agents are being published. For example, virulence factors and their mechanisms of action, host and pathogen response to the infectious process have been described using a proteomic analysis. Proteomics has made it possible to describe the unique features of various *M. tuberculosis* strains more thoroughly.

Studying the tuberculosis pathogen at the proteomic level can contribute to the identification of the metabolic and physiological characteristics necessary for a successful course of infection, as well as the virulence mechanisms that allow *M. tuberculosis* to modulate the host's immune response. The proteins synthesized during the entry of mycobacteria into the host's cells are important for their survival under these conditions: so they are considered as potential targets for developed drugs. Designing new drugs and treatment regimens is especially topical today, when strains of multiple types and extensive drug resistance continue to spread. Hence, studying the complete proteomic profile of mycobacteria may contribute to a better understanding of pathogen physiology and even tuberculosis treatment.

This study was supported by the Russian Science Foundation (№ 14-15-00689).

REFERENCES

1. Azhikina T., Skvortsov T., Radaeva T., Mardanov A., Ravin N., Apt A., Sverdlov E. // *Biotechniques*. 2010. V. 48. № 2. P. 139–144.
2. Tailleux L., Waddell S.J., Pelizzola M., Mortellaro A., Withers M., Tanne A., Castagnoli P.R., Gicquel B., Stoker N.G., Butcher P.D., et al. // *PLoS One*. 2008. V. 3. № 1. P. e1403.
3. Talaat A.M., Lyons R., Howard S.T., Johnston S.A. // *Proc. Natl. Acad. Sci. USA*. 2004. V. 101. № 13. P. 4602–4607.
4. Talaat A.M., Ward S.K., Wu C.W., Rondon E., Tavano C., Bannantine J.P., Lyons R., Johnston S.A. // *J. Bacteriol.* 2007. V. 189. № 11. P. 4265–4274.
5. Tortoli E. // *FEMS Immunol. Med. Microbiol.* 2006. V. 48. № 2. P. 159–178.
6. WHO. World Health Statistic. 2015.
7. Warner D.F., Mizrahi V. // *Nat. Genet.* 2013. V. 45. № 10. P. 1107–1108.
8. Akhtar S., Sarkar S., Mishra A., Sarkar D. // *Anal. Biochem.* 2011. V. 417. № 2. P. 286–288.
9. Ghodbane R., Asmar S., Betzner M., Linet M., Pierquin J., Raoult D., Drancourt M. // *J. Clin. Microbiol.* 2015. V. 53. № 8. P. 2693–2696.
10. Tyler A.D., Christianson S., Knox N.C., Mabon P., Wolfe J., van Domselaar G., Graham M.R., Sharma M.K. // *PLoS One*. 2016. V. 11. № 2. P. e0148676.
11. Bespyatykh J.A., Zimenkov D.V., Shitikov E.A., Kulagina E.V., Lapa S.A., Gryadunov D.A., Ilina E.N., Govorun V.M. // *Infect. Genet. Evol.* 2014. V. 26. P. 41–46.

12. Chernyaeva E.N., Shulgina M.V., Rotkevich M.S., Dobrynin P.V., Simonov S.A., Shitikov E.A., Ischenko D.S., Karpova I.Y., Kostryukova E.S., Ilina E.N., et al. // *BMC Genomics*. 2014. V. 15. P. 308.
13. Ilina E.N., Shitikov E.A., Ikryannikova L.N., Alekseev D.G., Kamashev D.E., Malakhova M.V., Parfenova T.V., Afanas'ev M.V., Ischenko D.S., Bazaleev N.A., et al. // *PLoS One*. 2013. V. 8. № 2. P. e56577.
14. Shitikov E., Ilina E., Chernousova L., Borovskaya A., Rukin I., Afanas'ev M., Smirnova T., Vorobyeva A., Larionova E., Andreevskaya S., et al. // *Infect. Genet. Evol.* 2012. V. 12. № 4. P. 838–845.
15. Shitikov E.A., Bespyatykh J.A., Ischenko D.S., Alexeev D.G., Karpova I.Y., Kostryukova E.S., Isaeva Y.D., Nosova E.Y., Mokrousov I.V., Vyazovaya A.A., et al. // *PLoS One*. 2014. V. 9. № 1. P. e84971.
16. Sotnikova E.A., Shitikov E.A., Malakhova M.V., Kostryukova E.S., Ilina E.N., Atrashevskaya A.V., Ignatyev G.M., Vinokurova N.V., Gorbachyov V.Y. // *Genome Announc.* 2016. V. 4. № 2. P. e00182–00116.
17. Wilkins M.R., Pasquali C., Appel R.D., Ou K., Golaz O., Sanchez J.C., Yan J.X., Gooley A.A., Hughes G., Humphery-Smith I., et al. // *Biotechnology (N.Y.)*. 1996. V. 14. № 1. P. 61–65.
18. James P. // *Q. Rev. Biophys.* 1997. V. 30. № 4. P. 279–331.
19. Hakkinen L., Uitto V.J., Larjava H. // *Periodontol.* 2000. V. 24. P. 127–152.
20. Molloy M.P., Witzmann F.A. // *Brief Funct. Genomic Proteomic.* 2002. V. 1. № 1. P. 23–39.
21. Monteoliva L., Albar J.P. // *Brief Funct. Genomic Proteomic.* 2004. V. 3. № 3. P. 220–239.
22. Gygi S.P., Rist B., Gerber S.A., Turecek F., Gelb M.H., Aebersold R. // *Nat. Biotechnol.* 1999. V. 17. № 10. P. 994–999.
23. Schubert O.T., Mouritsen J., Ludwig C., Rost H.L., Rosenberger G., Arthur P.K., Claassen M., Campbell D.S., Sun Z., Farrah T., et al. // *Cell Host Microbe*. 2013. V. 13. № 5. P. 602–612.
24. Rosenkrands I., King A., Weldingh K., Moniatte M., Moertz E., Andersen P. // *Electrophoresis*. 2000. V. 21. № 17. P. 3740–3756.
25. Mehaffy C., Hess A., Prenni J.E., Mathema B., Kreiswirth B., Dobos K.M. // *Proteomics*. 2010. V. 10. № 10. P. 1966–1984.
26. Sonnenberg M.G., Belisle J.T. // *Infect. Immun.* 1997. V. 65. № 11. P. 4515–4524.
27. Jungblut P.R., Schaible U.E., Mollenkopf H.J., Zimny-Arndt U., Raupach B., Mattow J., Halada P., Lamer S., Hagens K., Kaufmann S.H. // *Mol. Microbiol.* 1999. V. 33. № 6. P. 1103–1117.
28. Gu S., Chen J., Dobos K.M., Bradbury E.M., Belisle J.T., Chen X. // *Mol. Cell Proteomics*. 2003. V. 2. № 12. P. 1284–1296.
29. Schmidt F., Donahoe S., Hagens K., Mattow J., Schaible U.E., Kaufmann S.H., Aebersold R., Jungblut P.R. // *Mol. Cell Proteomics*. 2004. V. 3. № 1. P. 24–42.
30. Mawuenyega K.G., Forst C.V., Dobos K.M., Belisle J.T., Chen J., Bradbury E.M., Bradbury A.R., Chen X. // *Mol. Biol. Cell*. 2005. V. 16. № 1. P. 396–404.
31. de Souza G.A., Fortuin S., Aguilar D., Pando R.H., McEvoy C.R., van Helden P.D., Koehler C.J., Thiede B., Warren R.M., Wiker H.G. // *Mol. Cell Proteomics*. 2010. V. 9. № 11. P. 2414–2423.
32. Malen H., de Souza G.A., Pathak S., Softeland T., Wiker H.G. // *BMC Microbiol.* 2011. V. 11. P. 18.
33. Bell C., Smith G.T., Sweredoski M.J., Hess S. // *J. Proteome Res.* 2012. V. 11. № 1. P. 119–130.
34. Kelkar D.S., Kumar D., Kumar P., Balakrishnan L., Muthusamy B., Yadav A.K., Shrivastava P., Marimuthu A., Anand S., Sundaram H., et al. // *Mol. Cell Proteomics*. 2011. V. 10. № 12. P. M111.011627.
35. de Keijzer J., de Haas P.E., de Ru A.H., van Veelen P.A., van Soolingen D. // *Mol. Cell Proteomics*. 2014. V. 13. № 10. P. 2632–2645.
36. Bespyatykh J., Shitikov E., Altukhov I., Butenko I., Alexeev D., Melnikova N., Zhuravlev V., Ilina E. // *ProkaGenomics*. 2015. V. P GLOB 06. P. 117.
37. Bespyatykh J., Shitikov E., Butenko I., Altukhov I., Alexeev D., Mokrousov I., Dogonadze M., Zhuravlev V., Yablonsky P., Ilina E., et al. // *Sci. Rep.* 2016. V. 6. P. 28985.
38. Treumann A., Thiede B. // *Expert Rev. Proteomics*. 2010. V. 7. № 5. P. 647–653.
39. Ong S.E., Blagojev B., Kratchmarova I., Kristensen D.B., Steen H., Pandey A., Mann M. // *Mol. Cell Proteomics*. 2002. V. 1. № 5. P. 376–386.
40. Wang H., Dong D., Tang S., Chen X., Gao Q. // *J. Proteome Res.* 2013. V. 12. № 5. P. 2055–2066.
41. Gunawardena H.P., Feltcher M.E., Wrobel J.A., Gu S., Braunstein M., Chen X. // *J. Proteome Res.* 2013. V. 12. № 12. P. 5463–5474.
42. Gillet L.C., Navarro P., Tate S., Rost H., Selevsek N., Reiter L., Bonner R., Aebersold R. // *Mol. Cell Proteomics*. 2012. V. 11. № 6. P. O111.016717.
43. Cole S.T., Brosch R., Parkhill J., Garnier T., Churcher C., Harris D., Gordon S.V., Eiglmeier K., Gas S., Barry C.E., 3rd, et al. // *Nature*. 1998. V. 393. № 6685. P. 537–544.
44. Xiong Y., Chalmers M.J., Gao F.P., Cross T.A., Marshall A.G. // *J. Proteome Res.* 2005. V. 4. № 3. P. 855–861.
45. Covert B.A., Spencer J.S., Orme I.M., Belisle J.T. // *Proteomics*. 2001. V. 1. № 4. P. 574–586.
46. Samanich K.M., Belisle J.T., Sonnenberg M.G., Keen M.A., Zolla-Pazner S., Laal S. // *J. Infect. Dis.* 1998. V. 178. № 5. P. 1534–1538.
47. Park H.D., Guinn K.M., Harrell M.I., Liao R., Voskuil M.I., Tompa M., Schoolnik G.K., Sherman D.R. // *Mol. Microbiol.* 2003. V. 48. № 3. P. 833–843.
48. Rodriguez J.G., Hernandez A.C., Helguera-Repetto C., Aguilar Ayala D., Guadarrama-Medina R., Anzola J.M., Bustos J.R., Zambrano M.M., Gonzalez Y.M.J., Garcia M.J., et al. // *MBio*. 2014. V. 5. № 3. P. e01125–01114.
49. Cho S.H., Goodlett D., Franzblau S. // *Tuberculosis (Edinb.)*. 2006. V. 86. № 6. P. 445–460.
50. Singhal N., Sharma P., Kumar M., Joshi B., Bisht D. // *Proteome Sci.* 2012. V. 10. № 1. P. 14.
51. Tan T., Lee W.L., Alexander D.C., Grinstein S., Liu J. // *Cell Microbiol.* 2006. V. 8. № 9. P. 1417–1429.
52. Brosch R., Pym A.S., Gordon S.V., Cole S.T. // *Trends Microbiol.* 2001. V. 9. № 9. P. 452–458.
53. Mattow J., Jungblut P.R., Schaible U.E., Mollenkopf H.J., Lamer S., Zimny-Arndt U., Hagens K., Muller E.C., Kaufmann S.H. // *Electrophoresis*. 2001. V. 22. № 14. P. 2936–2946.
54. Mattow J., Schaible U.E., Schmidt F., Hagens K., Siejak F., Brestrich G., Haeselbarth G., Muller E.C., Jungblut P.R., Kaufmann S.H. // *Electrophoresis*. 2003. V. 24. № 19–20. P. 3405–3420.
55. He X.Y., Zhuang Y.H., Zhang X.G., Li G.L. // *Microbes Infect.* 2003. V. 5. № 10. P. 851–856.
56. Comas I., Coscolla M., Luo T., Borrell S., Holt K.E., Kato-Maeda M., Parkhill J., Malla B., Berg S., Thwaites G., et al. // *Nat. Genet.* 2013. V. 45. № 10. P. 1176–1182.

57. Parwati I., van Crevel R., van Soolingen D. // *Lancet Infect Dis.* 2010. V. 10. № 2. P. 103–111
58. Hanekom M., Gey van Pittius N.C., McEvoy C., Victor T.C., van Helden P.D., Warren R.M. // *Tuberculosis (Edinb.)*. 2011. V. 91. № 6. P. 510–523.
59. Dormans J., Burger M., Aguilar D., Hernandez-Pando R., Kremer K., Roholl P., Arend S.M., van Soolingen D. // *Clin. Exp. Immunol.* 2004. V. 137. № 3. P. 460–468.
60. Pheiffer C., Betts J.C., Flynn H.R., Lukey P.T., van Helden P. // *Microbiology*. 2005. V. 151. Pt 4. P. 1139–1150.
61. Monahan I.M., Betts J., Banerjee D.K., Butcher P.D. // *Microbiology*. 2001. V. 147. Pt2. P. 459–471.
62. Sherman D.R., Voskuil M., Schnappinger D., Liao R., Harrell M.I., Schoolnik G.K. // *Proc. Natl. Acad. Sci. USA.* 2001. V. 98. № 13. P. 7534–7539.
63. Mokrousov I., Otten T., Vyazovaya A., Limeschenko E., Filipenko M.L., Sola C., Rastogi N., Steklova L., Vyshnevskiy B., Narvskaya O. // *Eur. J. Clin. Microbiol. Infect. Dis.* 2003. V. 22. № 6. P. 342–348.
64. Norkina O.V., Kinsht V.N., Mokrousov I.V., Kurunov Yu.N., Krasnov V.A. // *Molecular Genetics, Microbiology and Virology*. 2003. № 3. P. 9–18.
65. Mokrousov I., Narvskaya O., Vyazovaya A., Millet J., Otten T., Vishnevsky B., Rastogi N. // *J. Clin. Microbiol.* 2008. V. 46. № 11. P. 3576–3584.
66. Surikova O.V., Voitech D.S., Kuzmicheva G., Tatkov S.I., Mokrousov I.V., Narvskaya O.V., Rot M.A., van Soolingen D., Filipenko M.L. // *Eur. J. Epidemiol.* 2005. V. 20. № 11. P. 963–974.
67. Drobniowski F., Balabanova Y., Nikolayevsky V., Ruddy M., Kuznetsov S., Zakharova S., Melentyev A., Fedorin I. // *Jama.* 2005. V. 293. № 22. P. 2726–2731.
68. Peterson E.J., Reiss D.J., Turkarslan S., Minch K.J., Rustad T., Plaisier C.L., Longabaugh W.J., Sherman D.R., Baliga N.S. // *Nucl. Acids Res.* 2014. V. 42. № 18. P. 11291–11303.
69. Lasunskaja E., Ribeiro S.C., Manicheva O., Gomes L.L., Suffys P.N., Mokrousov I., Ferrazoli L., Andrade M.R., Kritski A., Otten T., et al. // *Microbes Infect.* 2010. V. 12. № 6. P. 467–475.
70. Pardini M., Niemann S., Varaine F., Iona E., Meacci F., Orru G., Yesilkaya H., Jarosz T., Andrew P., Barer M., et al. // *Tuberculosis (Edinb.)*. 2009. V. 89. № 4. P. 317–324.
71. Kumar B., Sharma D., Sharma P., Katoch V.M., Venkatesan K., Bisht D. // *J. Proteomics*. 2013. V. 94. P. 68–77.
72. Mattow J., Siejak F., Hagens K., Becher D., Albrecht D., Krah A., Schmidt F., Jungblut P.R., Kaufmann S.H., Schai-ble U.E. // *Proteomics*. 2006. V. 6. № 8. P. 2485–2494.
73. Sharma D., Kumar B., Lata M., Joshi B., Venkatesan K., Shukla S., Bisht D. // *PLoS One*. 2015. V. 10. № 10. P. e0139414.
74. Pandey R., Rodriguez G.M. // *Infect. Immun.* 2012. V. 80. № 10. P. 3650–3659.
75. Li Z., Kelley C., Collins F., Rouse D., Morris S. // *J. Infect. Dis.* 1998. V. 177. № 4. P. 1030–1035.
76. Manca C., Paul S., Barry C.E., 3rd, Freedman V.H., Kaplan G. // *Infect. Immun.* 1999. V. 67. № 1. P. 74–79.
77. Zhang L., Wang Q., Wang W., Liu Y., Wang J., Yue J., Xu Y., Xu W., Cui Z., Zhang X., et al. // *Proteome Sci.* 2012. V. 10. P. 12.
78. Dobos K.M., Khoo K.H., Swiderek K.M., Brennan P.J., Belisle J.T. // *J. Bacteriol.* 1996. V. 178. № 9. P. 2498–2506.
79. Espitia C., Mancilla R. // *Clin. Exp. Immunol.* 1989. V. 77. № 3. P. 378–383.
80. Herrmann J.L., Delahay R., Gallagher A., Robertson B., Young D. // *FEBS Lett.* 2000. V. 473. № 3. P. 358–362.
81. Herrmann J.L., O’Gaora P., Gallagher A., Thole J.E., Young D.B. // *EMBO J.* 1996. V. 15. № 14. P. 3547–3554.
82. Sartain M.J., Belisle J.T. // *Glycobiology*. 2009. V. 19. № 1. P. 38–51.
83. Smith G.T., Sweredoski M.J., Hess S. // *J. Proteomics*. 2014. V. 97. P. 296–306.
84. VanderVen B.C., Harder J.D., Crick D.C., Belisle J.T. // *Science*. 2005. V. 309. № 5736. P. 941–943.
85. Kusebauch U., Ortega C., Ollodart A., Rogers R.S., Sherman D.R., Moritz R.L., Grundner C. // *Proc. Natl. Acad. Sci. USA.* 2014. V. 111. № 25. P. 9265–9270.
86. Priscic S., Dankwa S., Schwartz D., Chou M.F., Locasale J.W., Kang C.M., Bemis G., Church G.M., Steen H., Husson R.N. // *Proc. Natl. Acad. Sci. USA.* 2010. V. 107. № 16. P. 7521–7526.
87. Pethe K., Bifani P., Drobecq H., Sergheraert C., Debric A.S., Loch C., Menozzi F.D. // *Proc. Natl. Acad. Sci. USA.* 2002. V. 99. № 16. P. 10759–10764.
88. Okkels L.M., Muller E.C., Schmid M., Rosenkrands I., Kaufmann S.H., Andersen P., Jungblut P.R. // *Proteomics*. 2004. V. 4. № 10. P. 2954–2960.
89. Lancioni C.L., Li Q., Thomas J.J., Ding X., Thiel B., Drage M.G., Pecora N.D., Ziady A.G., Shank S., Harding C.V., et al. // *Infect. Immun.* 2011. V. 79. № 2. P. 663–673.
90. Okuda S., Tokuda H. // *Annu. Rev. Microbiol.* 2011. V. 65. P. 239–259.
91. Sanchez A., Espinosa P., Esparza M.A., Colon M., Bernal G., Mancilla R. // *Scand. J. Immunol.* 2009. V. 69. № 1. P. 20–28.
92. Sanchez A., Espinosa P., Garcia T., Mancilla R. // *Clin. Dev. Immunol.* 2012. V. 2012. P. 950503.
93. Sutcliffe I.C., Harrington D.J. // *FEMS Microbiol. Rev.* 2004. V. 28. № 5. P. 645–659.
94. Striebel F., Imkamp F., Sutter M., Steiner M., Mamedov A., Weber-Ban E. // *Nat. Struct. Mol. Biol.* 2009. V. 16. № 6. P. 647–651.
95. Chun T., Serbina N.V., Nolt D., Wang B., Chiu N.M., Flynn J.L., Wang C.R. // *J. Exp. Med.* 2001. V. 193. № 10. P. 1213–1220.
96. Doi T., Yamada H., Yajima T., Wajjwalku W., Hara T., Yoshikai Y. // *J. Immunol.* 2007. V. 178. № 6. P. 3806–3813.
97. Barandun J., Delley C.L., Weber-Ban E. // *BMC Biol.* 2012. V. 10. P. 95.
98. Burns K.E., Cerda-Maira F.A., Wang T., Li H., Bishai W.R., Darwin K.H. // *Mol. Cell.* 2010. V. 39. № 5. P. 821–827.
99. Burns K.E., Pearce M.J., Darwin K.H. // *J. Bacteriol.* 2010. V. 192. № 11. P. 2933–2935.
100. Cerda-Maira F.A., Pearce M.J., Fuortes M., Bishai W.R., Hubbard S.R., Darwin K.H. // *Mol. Microbiol.* 2010. V. 77. № 5. P. 1123–1135.
101. Pearce M.J., Mintseris J., Ferreyra J., Gygi S.P., Darwin K.H. // *Science*. 2008. V. 322. № 5904. P. 1104–1107.
102. Tung C.W. // *BMC Bioinformatics*. 2012. V. 13. P. 40.
103. Poulsen C., Akhter Y., Jeon A.H., Schmitt-Ulms G., Meyer H.E., Stefanski A., Stuhler K., Wilmanns M., Song Y.H. // *Mol. Syst. Biol.* 2010. V. 6. № 386. P. 10.1038/msb.2010.1039.
104. Braibant M., Lefevre P., de Wit L., Peirs P., Ooms J., Huygen K., Andersen A.B., Content J. // *Gene*. 1996. V. 176. № 1–2. P. 171–176.
105. Harboe M., Wiker H.G., Ulvund G., Lund-Pedersen B., Andersen A.B., Hewinson R.G., Nagai S. // *Infect. Immun.* 1998. V. 66. № 1. P. 289–296.
106. Young D.B., Garbe T.R. // *Res. Microbiol.* 1991. V. 142. № 1. P. 55–65.

107. Michell S.L., Whelan A.O., Wheeler P.R., Panico M., Easton R.L., Etienne A.T., Haslam S.M., Dell A., Morris H.R., Reason A.J., et al. // *J. Biol. Chem.* 2003. V. 278. № 18. P. 16423–16432.
108. Liu C.F., Tonini L., Malaga W., Beau M., Stella A., Bouyssié D., Jackson M.C., Nigou J., Puzo G., Guilhot C., et al. // *Proc. Natl. Acad. Sci. USA.* 2013. V. 110. № 16. P. 6560–6565.
109. Gonzalez-Zamorano M., Mendoza-Hernandez G., Xolalpa W., Parada C., Vallecillo A.J., Bigi F., Espitia C. // *J. Proteome Res.* 2009. V. 8. № 2. P. 721–733.
110. Nagai S., Wiker H.G., Harboe M., Kinomoto M. // *Infect. Immun.* 1991. V. 59. № 1. P. 372–382.
111. Guerrero G.G., Debrie A.S., Loch C. // *Vaccine.* 2010. V. 28. № 27. P. 4340–4347.
112. Vidal Pessolani M.C., Marques M.A., Reddy V.M., Loch C., Menozzi F.D. // *Microbes Infect.* 2003. V. 5. № 7. P. 677–684.
113. Temmerman S., Pethe K., Parra M., Alonso S., Rouanet C., Pickett T., Drowart A., Debrie A.S., Delogu G., Menozzi F.D., et al. // *Nat. Med.* 2004. V. 10. № 9. P. 935–941.
114. Jensen O.N. // *Nat. Rev. Mol. Cell Biol.* 2006. V. 7. № 6. P. 391–403.
115. Camus J.C., Pryor M.J., Medigue C., Cole S.T. // *Microbiology.* 2002. V. 148. Pt 10. P. 2967–2973.
116. de Souza G.A., Arntzen M.O., Fortuin S., Schurch A.C., Malen H., McEvoy C.R., van Soolingen D., Thiede B., Warren R.M., Wiker H.G. // *Mol. Cell Proteomics.* 2011. V. 10. № 1. P. M110.002527.
117. de Souza G.A., Malen H., Softeland T., Saelensminde G., Prasad S., Jonassen I., Wiker H.G. // *BMC Genomics.* 2008. V. 9. P. 316.
118. Yadeta K.A., Elmore J.M., Coaker G. // *Front Plant Sci.* 2013. V. 4 P. 10.3389/fpls.2013.00086.

Cholesterol in the Pathogenesis of Alzheimer's, Parkinson's Diseases and Autism: Link to Synaptic Dysfunction

A. M. Petrov*, M. R. Kasimov, A. L. Zefirov

Kazan State Medical University, Normal Physiology department, Butlerova str. 49, Kazan, 420012, Russia

*E-mail: fysio@rambler.ru

Received April 22, 2016; in final form, November 28, 2016

Copyright © 2017 Park-media, Ltd. This is an open access article distributed under the Creative Commons Attribution License, which permits unrestricted use, distribution, and reproduction in any medium, provided the original work is properly cited.

ABSTRACT In our previous review, we described brain cholesterol metabolism in control conditions and in the case of some rare neurological pathologies linked to defects in the genes which are directly involved in the synthesis and/or traffic of cholesterol. Here, we have analyzed disruptions in cholesterol homeostasis in widespread neurodegenerative diseases (Alzheimer's and Parkinson's diseases) and autism spectrum disorders. We particularly focused on the synaptic dysfunctions that could arise from changes in both membrane cholesterol availability and oxysterol production. Notably, alterations in the brain cholesterol metabolism and neurotransmission occur in the early stages of these pathologies and the polymorphism of the genes associated with cholesterol homeostasis and synaptic communication affects the risk of onset and severity of these diseases. In addition, pharmacological and genetic manipulations of brain cholesterol homeostasis in animal models frequently have marked effects on the progression of neurodegenerative diseases. Thus, the development of Alzheimer's, Parkinson's and autism spectrum disorders may be partially associated with an imbalance of cholesterol homeostasis that leads to changes in the membrane cholesterol and oxysterol levels that, in turn, modulates key steps in the synaptic transmission.

KEYWORDS cholesterol, oxysterols, lipid rafts, neurodegenerative disease, synaptic transmission.

ABBREVIATIONS A β – amyloid peptide β ; ABC – ATP-binding cassette transporters; ApoE – apolipoprotein E; AD – Alzheimer's disease; PD – Parkinson's disease; OH-Ch – hydroxycholesterol; BBB – blood-brain barrier; LRP – LDL-receptor related protein; LX-receptor – Liver X receptor; ASD – autism spectrum disorders; CYP46A1 – cholesterol 24-hydroxylase; CYP7B1 – oxysterol 7 α -hydrolase; ER – endoplasmic reticulum.

INTRODUCTION

Previously, we described changes in cholesterol metabolism in rare hereditary pathologies of the central nervous system caused by mutations in the genes which are directly involved in the biosynthesis of cholesterol (Smith-Lemli-Opitz syndrome) or its intracellular traffic (Niemann-Pick type C disease) and synthesis regulation (Huntington disease) [1]. In this review, we analyze the relationships between such common neurodegenerative diseases as Alzheimer's and Parkinson's and autism spectrum disorders and cholesterol homeostasis and synaptic dysfunction.

ALZHEIMER'S DISEASE (AD)

Alzheimer's disease is the most widespread neurodegenerative disease. It usually affects older people and manifests itself as a deterioration of memory and cognitive abilities. It involves the deposition of amyloid peptide β (A β) into amyloid plaques in the extracellular

space of the brain and neurofilament bundles of the hyperphosphorylated tau protein inside cells. An accumulation of A β and death of neurons, especially in the hippocampus, are considered the main manifestations of AD. The accumulation of A β reflects the imbalance between its production and its elimination from the brain. A β is formed in a two-step cleavage of the transmembrane protein APP (amyloid precursor protein) by proteases called secretases. The APP is first cleaved by either secretase α or β , and then by γ . The cleavage of APP by α -secretase results in a nonamyloidogenic product, sAPP α , which does not cause the disease. Moreover, sAPP α has neuroprotective effects and enhances long-term potentiation and learning ability. APP is cleaved by β -secretase (BACE1) to release the soluble fragment sAPP β (involved in the elimination of synapses and apoptosis) and a C-terminal fragment (β CTF) which is subsequently cut by γ -secretase (a complex of several proteins comprising presenilin 1

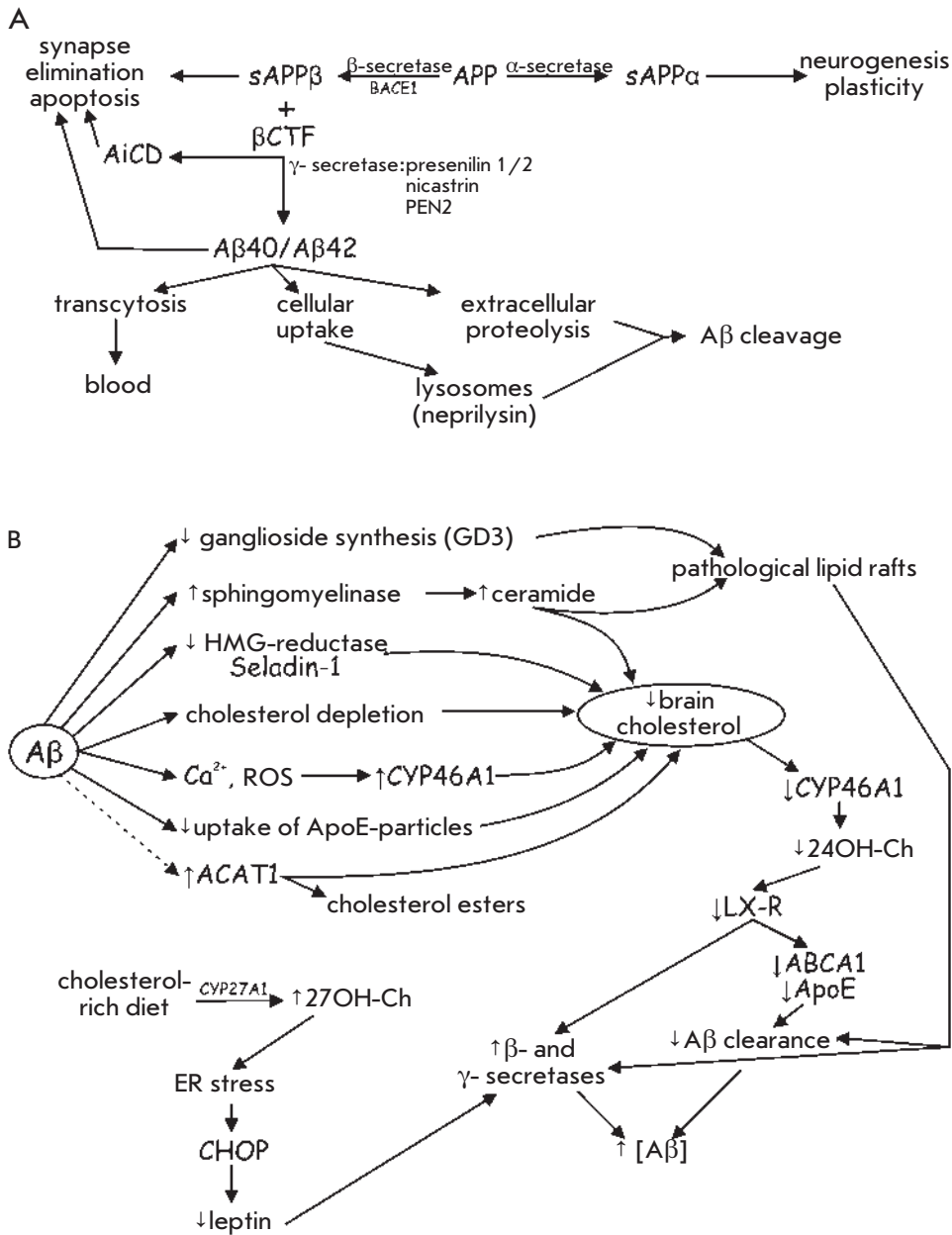


Fig. 1. Synthesis of amyloid peptide and brain level of cholesterol. A – Amyloid precursor protein (APP) processing: involvement of α -, β - and γ -secretases. B – Links between amyloid peptide β ($A\beta$) production and brain cholesterol metabolism. Impact of cholesterol-rich diet. See text for details.

or 2, APH, nicastrin and PEN2) with the formation of toxic $A\beta$ containing 40 or 42 (more toxic) amino acid residues. In addition, β CTF proteolysis by γ -secretase results in the release of the intracellular APP domain (AICD), which, in cooperation with Fe65 and TIP60, can trigger the transcription of genes which accelerate cell death and disrupt neurogenesis [2]. $A\beta$ in the brain interstitial fluid can be removed via several mechanisms: transfer through the BBB, uptake by cells for degradation in the lysosomes, and cleavage by specific proteases (Fig. 1A). Lysosomes contain a specific $A\beta$ -degrading protease, neprilysin, whereas outside the cell $A\beta$ clearance is performed by an insulin-de-

grading enzyme (IDE) which is secreted by astrocytes and microglia [3]. There are two forms of AD: with early (5–10%) and late (90–95%) onset in which the disease symptoms appear before and after 65 years of age, respectively. The early form is strictly hereditary and is associated with excessive production of $A\beta$. Patients with a late onset type of AD usually have inefficient $A\beta$ clearance rather than an enhanced production [4, 5].

The levels of cholesterol in the brain and blood plasma: correlations with AD, role of oxysterols

Experimental data support the significant contribution of changes in cholesterol metabolism to the patho-

genesis of AD (*Fig. 1B*). However, it is unclear whether the disruption in cholesterol homeostasis is a cause or a consequence of the disease. An earlier work revealed A β accumulation in the brain of rabbits receiving a cholesterol-rich diet [6]. Later research showed that cholesterol intake increases tau phosphorylation, causes oxidative stress and cognitive defects, but does not change the level of cholesterol in a rabbit's brain [7]. Several epidemiological studies (but not all of them) found an increased risk of AD in individuals with elevated plasma cholesterol, especially in mid-life [2, 8]. There is a confirmed correlation between high (or low) cholesterol content in low (high) density lipoproteins and A β levels in the brain of patients in early stages of AD [9]. However, the relationship between cholesterol levels in plasma and AD may be mediated by changes in the vascular tone and inflammatory responses rather than by direct influence on the brain cholesterol. Chronic cerebral hypoperfusion in rats and mice with AD increases BACE1 expression, A β concentration, and cognitive defects [10]. Hypoperfusion and inflammation, high levels of cholesterol in the plasma can cause AD-promoting vascular dysfunction and changes in oxysterol production.

In AD, the concentration of 24S-hydroxycholesterol (24OH-Ch) decreases in the brain. However, in patients at the initial stages of AD the level of 24OH-Ch transiently increases in the plasma and cerebrospinal fluid [11]. Individuals with elevated plasma 24OH-Ch have a higher probability of developing cognitive impairment over the next 8 years [12]. The excessive production of 24OH-Ch may be an indication of an attempt to compensate for the nascent dysfunction [1]. Elevated expression of the 24OH-Ch-synthesizing enzyme CYP46A1 (using adenoviral therapy) in the brain of APP23-mice significantly reduces A β accumulation, gliosis, and cognitive defects [13]. The effect of CYP46A1 activation may be mediated by 24OH-Ch that stimulates LX α and β -receptors, which, in turn, increases the expression of the genes involved in cholesterol synthesis and traffic [1]. Deletion of LX α or β -receptor genes causes age-related neurodegenerative disorders [14]. Conversely, activation of LX-receptors increases A β clearance and reverses the memory deficit in transgenic APP/PS1 and APP23 mice, probably by upregulating the levels of ApoE and ABCA1 in the brain [15]. ABCA1 can quickly remove the excess A β from the membrane into the extracellular space that protects neurons from the toxic effect of A β accumulation [16]. In the endothelial cells of brain capillaries, 24OH-Ch increases A β clearance, enhancing the expression of ABCA1, and reduces A β production, altering secretase expression [17].

The level of 27OH-Ch in the brain is significantly higher in AD [18]. In rabbits receiving a diet rich in

cholesterol, the levels of 24OH-Ch and 27OH-Ch in the plasma increase, whereas the ratio of 24OH-Ch to 27OH-Ch in the brain is lower, which may exacerbate the risk of neurodegeneration. It is assumed that an increased influx of 27OH-Ch into the brain and/or increased extrusion of 24OH-Ch from the brain may underlie the association between a high level of cholesterol in the plasma and AD [11, 19]. Studies of organotypical brain slices from adult animals have shown that 27OH-Ch increases the levels of A β and phosphorylated tau, whereas 24OH-Ch promotes nonamyloidogenic APP processing. Moreover, 24OH-Ch inhibits the toxic effects of 27OH-Ch when these oxysterols are co-applied. 27OH-Ch can cause ER stress, resulting in the activation of the transcription factor CHOP (C/EBP α homologous protein), which suppresses the leptin synthesis that normally reduces BACE1 expression, A β production, and tau phosphorylation [19].

Although early studies indicated that the level of brain cholesterol is elevated in patients with AD, other researchers have found that brain cholesterol synthesis and the total pool of cholesterol in the brain decrease [8] (*Fig. 1B*). In AD, the level of cholesterol is reduced in the temporal gyrus, hippocampus, lipid raft fraction in the whole brain, and white matter [20–22]. However, the cholesterol content is increased in the cores of mature amyloid plaques and the nerve terminals enriched with amyloid aggregates [23]. These observations suggest the existence of an A β -dependent mechanism of cholesterol removal from the nerve terminal membrane. Other ways of lowering brain cholesterol availability in patients with AD can be associated with: APP/A β -dependent suppression of cholesterol synthesis by inhibition of 3-hydroxy-3-methylglutaryl-CoA reductase (HMG-reductase) [24]; decrease in the uptake of cholesterol-loaded ApoE-particles under the influence of A β [15]; increase in cholesterol oxidation due to enhanced CYP46A1 activity [11]; A β -induced modification of lipid rafts [1, 25]. The increase in CYP46A1 activity may be caused by A β -induced alterations in Ca²⁺ homeostasis and oxidative stress [11, 26]. The aging process is accompanied by a reduction in the cholesterol content, especially noticeable in regions susceptible to AD, which may be related to an increased CYP46A1 expression/activity and decreased cholesterol synthesis/traffic [26, 27].

The brain biopsies of AD patients revealed an accumulation of cholesterol ester-rich lipid drops in A β -positive neurons, and the higher the number of such drops, the greater the concentration of A β [28]. Inhibition of the synthesis of cholesterol esters (acetyl-CoA-cholesterol acyltransferase/ACAT1) was accompanied by an increase in 24-OH Ch concentration and a markedly reduced generation of A β , plaque formation, and

cognitive defects in an animal model of AD [29]. It is possible that the early stages of AD involve an increase in the synthesis of the enzymes responsible for the formation of cholesterol esters [30]. One way to stimulate cholesterol esterification may be by increased production of 25-OH Ch, which is caused by inflammation. In addition, the expression of the CYP7B1 enzyme that metabolizes 25- and 27-OH Ch is downregulated in AD [31].

The brain level of sphingomyelin is reduced in AD patients, and the concentration of ceramides, products of sphingomyelin hydrolysis by sphingomyelinases, is increased. Consequently, normal lipid rafts “dissolve,” cholesterol is released from the membranes, and ceramides aggregate to form large ceramide-enriched lipid platforms, which are involved in the initiation of cell death. Sphingomyelinase activation may occur in the early stages of AD in response to A β [32, 33]. The brain concentration of gangliosides (lipid raft components) decreases with aging, but patients with AD show a steeper reduction. A β and AICD can inhibit and reduce the expression of the enzymes required for the synthesis of several gangliosides. However, the content of the gangliosides GM1 and GM2 involved in A β aggregation increases in the AD brain [21]. The imbalance in ganglioside composition can contribute to the conversion of A β into a highly toxic oligomeric form [1, 33].

A β synthesis and cholesterol

The extracellular N-terminal fragment of APP contains a cholesterol-binding site [34], but most APP molecules are located outside lipid rafts. Secretases β and γ , which are involved in A β synthesis, are both residents of lipid rafts. Expression of the scaffold protein RanBP9 (increased in APP-mice) promotes targeting of the APP to lipid rafts, which contain BACE1 [35]. The activation of β -secretase requires lipid raft-dependent dimerization and stabilization steps. In the presence of elevated levels of cholesterol and sphingolipids, raft-associated γ -secretase produces a more toxic form, A β 42. However, the synthesis of A β (~ 70%) mainly occurs within a cell [28]. Therefore, it first requires the stage of raft-dependent endocytosis, in which APP, β -, and γ -secretases uptake into a vesicle and are then delivered to endosomes/lysosomes. A β is generated in the endolysosomes under acidic conditions that favor BACE1 activity. Subsequently, a portion of A β is released into the extracellular space by exocytosis (e.g., as a content of synaptic vesicles) [3] (*Fig. 2A*). A β aggregation into toxic oligomers is enhanced by zinc ions from synaptic vesicles [36]. It should be noted that non-amyloidogenic cleavage of APP by α -secretase occurs on the cell surface [3].

The toxic effects of A β may depend on its binding to membrane components. In the fibroblasts of AD pa-

tients, A β interacts with the plasma membrane more actively when the cholesterol level is low, while high levels of cholesterol prevent A β -induced generation of reactive oxygen species and lipid oxidation [37]. On the other hand, A β -mediated disruption of long-term synaptic potentiation and increased synaptic depression may be caused by its binding to PrP (in this case, metabotropic glutamate receptor 5 and LRP1 act as co-receptors) and the subsequent activation of tyrosine kinase Fyn, which phosphorylates the tau protein. A reduced integrity of rafts due to cholesterol removal disrupts the complex of PrP-metabotropic glutamate receptor 5-LRP1, attenuating the interaction of A β with the postsynaptic membranes [8, 38] (*Fig. 2A*).

From one point of view, the increase in membrane cholesterol promotes the association of APP, β -, and γ -secretases within the lipid rafts and increases A β production, while other authors suggest that APP and the secretases are distributed into different rafts [3, 34, 39]. A decreased membrane cholesterol content increases APP cleavage by α -secretase, reducing the formation of toxic A β [3]. However, activation of the plasminogen into the plasmin, which cuts A β , occurs on the surface of the lipid rafts and, therefore, raft disruption can reduce the rate of A β degradation [39]. Upon loss of raft integrity, their components, in particular β - and γ -secretases, can diffuse into the liquid-disordered membrane phase, where APP is mainly distributed, and, therefore, A β production may increase [32]. AD is associated with a reduced expression of seladin-1 (selective Alzheimer disease indicator 1), a gene that encodes an enzyme converting desmosterol to cholesterol. Deletion of seladin-1 leads to a lower cholesterol level, disorganization of lipid rafts, and A β accumulation. Conversely, overexpression of seladin-1 (for example, in response to estrogen administration) accelerates cholesterol metabolism in the brain and increases neurons' resistance to A β [40]. Interestingly, caveolin 1 gene knockout (caveolin 1 stabilizes the membrane rafts) leads to a pathology, similar to that observed in AD, which is accompanied by A β accumulation and neurodegeneration. The level of caveolin 1 in neurons reduces with aging, whereas the fluidity of the synaptosomal membranes increases [41]. A low expression of caveolin 1 reduces membrane cholesterol availability, since caveolin 1 is involved in the delivery of newly synthesized cholesterol to the plasma membrane [42].

Some studies indicate that pharmacological strategies for lowering the level of cholesterol in cells, having its initial normal baseline level, inhibit A β synthesis when APP is overexpressed. However, it is unclear how this conclusion can be extrapolated to the disease or the process of normal aging, especially if we con-

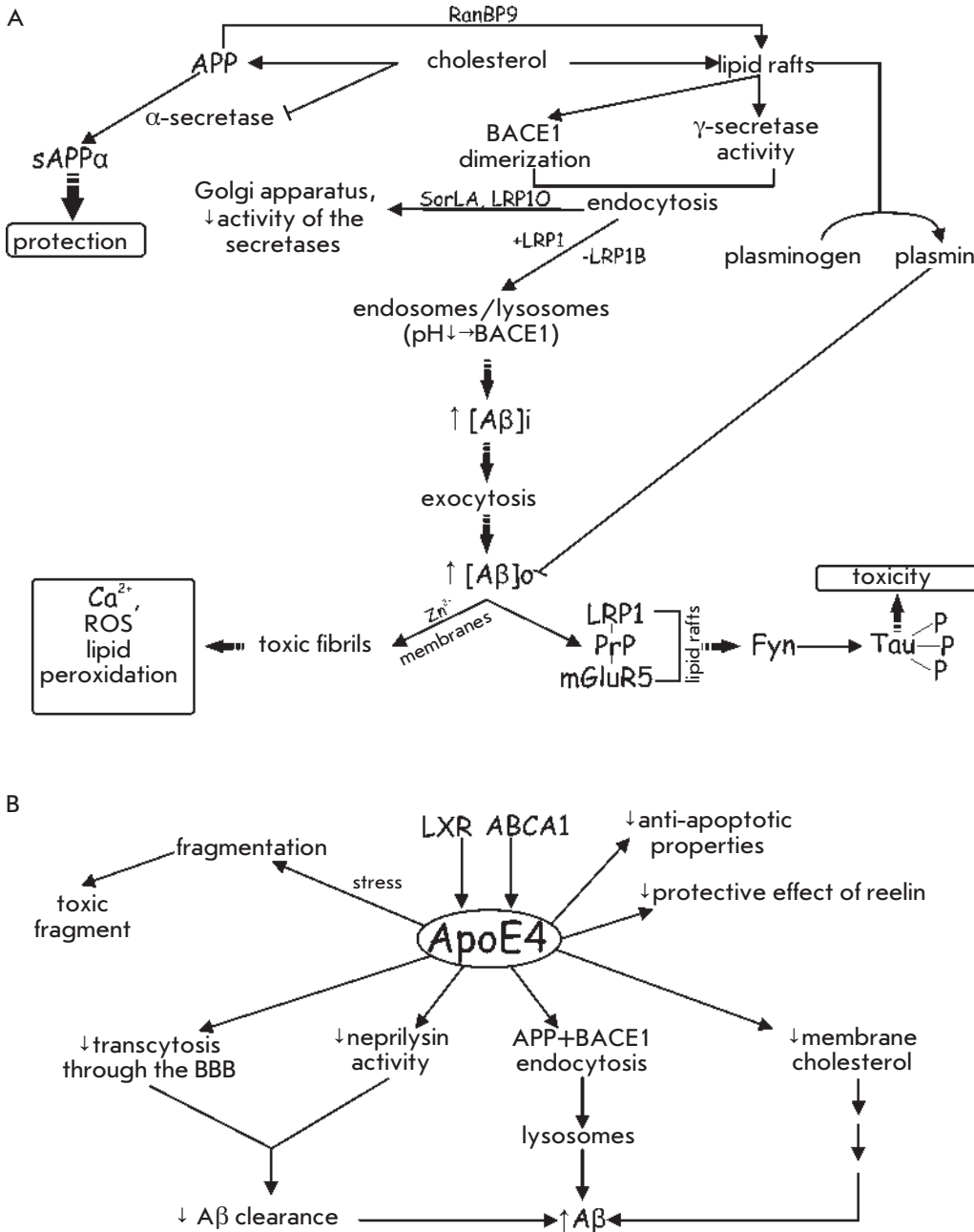


Fig. 2. Cholesterol, lipid rafts and ApoE4 in the amyloid peptide β (Aβ) turnover. A – Role of cholesterol and lipid rafts in the production and toxicity of Aβ. B – Influence of ApoE4 on the Aβ synthesis/clearance balance and neuron survival. See text for details.

consider the lowering of cholesterol levels in a normal and pathological (in AD) aging brain [8]. A more likely scenario is the one in which a decreased cholesterol level in neuronal membranes, coupled with an increased Aβ production, a reduced Aβ degradation, and an enhanced inflammatory response, contributes to the progression of AD [22, 39]. It should be noted that treatment with statins has no significant beneficial effect in AD, even though statins significantly reduce plasma cholesterol levels [43]. Moreover, several studies have found cognitive deficits in response to statin

treatments [44]; so, in January 2014 the U.S. Food and Drug Administration (FDA) issued a recommendation on the risks of statins. A promising finding is the use of phytosterols in AD, which suppress Aβ production *in vitro* by inhibiting both the activity and expression of β- and γ-secretases, and BACE1 internalization into endosomes. The effect of phytosterols on Aβ processing may be associated with their stimulatory action on LX-receptors or the ability to accumulate in lipid rafts; the latter facilitates the re-localization of APP and presenilin to a non-raft phase [45].

ApoE and AD

Low levels of ApoE-particles in the brain correlate with an increase in the risk of AD, but it is unclear whether this is associated with cholesterol transport. By interacting with receptors, ApoE triggers anti-apoptotic signaling pathways. ApoE binds to A β , then the complex passes through the BBB with the help of LRP, thereby lowering the concentration of A β in the brain. A β interaction with ApoE-particles is potentiated by sulfated derivatives of galactocerebrosides, the concentration of which in the brain is lower in AD [2, 46, 47]. An agonist of the nuclear retinoid X receptor rapidly increases the production of ApoE and promotes A β degradation, decreasing the formation of A β -plaques [48]. Oxysterol (24-OH Ch), which promotes the expression of ApoE, ABCA1, and ABCG1 via the stimulation of LX-receptors, has similar effects [1, 30].

There are three known human ApoE isoforms, which differ from each other only by one amino acid residue. The most common allele is *ApoE3*, while *ApoE4* is detected only in 15–20% of the population and is considered a risk factor for AD with late onset. The probability of AD in individuals with one copy of *ApoE4* is 4 times, and with two copies, 12–20 times higher than in carriers of the *ApoE3* allele. The presence of *ApoE2*, conversely, hinders the progression of AD. Why *ApoE4* provokes the disease has not yet been established [2, 8]. There are several possibilities [2, 5, 48–51]: 1) ApoE4 binding to A β is weaker, causing less efficient clearance; 2) ApoE4 is produced in smaller quantities, quickly decomposes, and does not form dimers that promote A β degradation; in contrast, A β in a complex with ApoE4 becomes resistant to degradation by neprilysin; 3) ApoE4 is less effective in maintaining axonal growth and the survival of neurons; 4) ApoE4 promotes the endocytosis of APP and BACE1 and their targeting to early endosomes, thereby increasing A β synthesis; 5) ApoE4 reduces the expression of reelin receptors in synapses, blocking its protective properties (*Fig. 2B*).

In AD, the C-terminal fragment of ApoE that promotes the accumulation of neurofibrillary bundles may appear in the brain. Cellular stress *in vitro* can trigger the fragmentation of ApoE with production of the toxic fragment. ApoE4 is more susceptible to cleavage, and expression of truncated ApoE4 leads to AD-like neurodegeneration [8, 52].

Variations in the other genes involved in the cholesterol metabolism are also risk factors for AD: for example, polymorphism of lipoprotein receptors (LRP1, LRP10, SorLA, ApoER2) and transporters (ABCA1, ABCA7, clusterin) genes [2]. LRP1 is involved in A β uptake and elimination, and a decrease in its expression contributes to A β accumulation. However, LRP1 increases the rate of endocytosis and directs APP into

the lysosomes, which may upregulate A β synthesis [53]. A lower rate of endocytosis is typical for LRP1B; therefore, LRP1B inhibits the formation of A β [2]. SorLA/LR11, the level of which decreases in the late forms of AD, interacts with APP monomers, preventing their dimerization. This reduces APP cleavage by the γ - and β -secretases that prefer to use APP dimers as a substrate [54]. LRP10 and SorLA enhance APP traffic to the Golgi complex, where the secretases are less active [55]. Weak ABCA1 activity may contribute to AD, whereas its overexpression reduces the accumulation of A β . ABCA1 deficiency leads to the production of lipid-poor ApoE particles and a decrease in the amount of ApoE (by ~ 80%); additionally, cholesterol esters accumulate in the peripheral tissues [56].

Synaptic pathology in AD

Synaptic dysfunctions in AD represent the earliest events leading to cognitive deficit. At the early stages of AD, a decrease in glutamatergic transmission occurs in the cortex and hippocampus. The presynaptic events are the first to change, and the impairment of postsynaptic processes is recorded later. Long before the amyloid plaque formation, elimination of synapses and neuronal death, the synthesis of the key proteins of exo-endocytotic machinery (SNAP-25, synaptophysin, AP-2, AP-180, dynamin 1, synaptotagmin) decreases in the prefrontal cortex, and the first cognitive defects are observed [8, 57–59]. Despite the variety of the effects of ApoE4 gene variants – changes in the APP processing, decrease in A β clearance, synaptic plasticity interruptions – there is a common pathway for ApoE4 action associated with changes in endocytic recycling, probably through the reduction in the expression and activity of endocytotic proteins [51]. In patients with AD, early endosomes are 32 times larger in volume and the enlargement of endosomes begins before the manifestation of clinical symptoms in ApoE4 carriers [60]. Levetiracetam, acting on the SV2A protein of synaptic vesicles, reverses the ApoE4-induced changes both in endosomal traffic and A β processing [51].

High neuronal activity increases the production of A β in normal and pathological conditions (e.g., epilepsy). This is partly due to intense synaptic vesicle endocytosis, whereby APP molecules are captured in endosomes and are cleaved therein [61]. Also, soon after a burst of synaptic activity the early gene *Arc* is expressed and the *Arc* protein then increases the association of γ -secretase with APP in endosomes [62]. During vesicular exocytosis, the generated A β is released into the synaptic cleft, where it can regulate both neurotransmitter release and reception (*Fig. 3*). Synaptic activity can reduce the intraneuronal accumulation of A β by increasing the activity of neprily-

sin [63]. It is assumed that APP and A β are elements of “physiological” feedback, which controls synaptic transmission. Blocking A β production in young mice reduces their performance in memory tests [64]. Overproduction of A β may be caused by excessive/impaired synaptic activity. Individuals who carry mutations in presenilin 1 show an increased activation of the hippocampus 15 years before the onset of AD [65]. Enhanced expression/activity of ryanodine receptors in nerve terminals, causing an increased cytosolic Ca²⁺ and exocytosis, may occur before manifestations of histological and cognitive defects [59]. ApoE4 changes the brain activity in the early period: carriers of the *ApoE4* allele have a higher activation of the hippocampus at rest and when performing memory tests [66]. ApoE4 interferes with reelin-dependent signaling, which is involved in the migration, maturation, survival of neuronal cells, and synaptic plasticity [2, 8]. ApoE4 suppresses the effects of reelin, because it decreases the number of available ApoE-receptors by preventing the return of the receptors to the plasma membrane after the endocytosis induced by binding to reelin and ApoE [50]. In addition, reelin signaling becomes susceptible to the toxic action of A β . A β via a mechanism involving mitochondrial dysfunction may activate caspase 3, which (1) stimulates calcineurin (phosphatase PP2B) and (2) cleaves the protein kinase Akt. Subsequently, PP2B dephosphorylates NMDA-receptors in the sites for Fyn phosphorylation and loss of Akt leads to disinhibition of GSK3 β -kinase [67]. As a result, the long-term potentiation in response to the activation of ApoE receptors by reelin, which normally causes activation of Fyn and inhibition of GSK3 β -kinase, is suppressed in the hippocampus [50]. Hyperactivity of GSK3 β -kinase may be a factor that contributes to excessive phosphorylation of the tau protein, leading to the formation of neurofibrillary bundles, which disconnect from microtubules and may diffuse throughout the neuron [8, 67].

The effects of the extra- and intracellular A β on synaptic transmission

In synapses with weak activity, A β ([pM]) can activate presynaptic α 7-nicotinic cholinergic receptors, promoting an increase in cytosolic Ca²⁺ and the release of a neurotransmitter. In high doses, A β ([nM]) can enhance the internalization of postsynaptic NMDA- and AMPA-receptors and long-term depression [58, 68]. By blocking the reuptake of glutamate, the elevated levels of A β lead to a decrease in the quantum size and a persistent increase in glutamate concentration in the synaptic cleft. Thus, postsynaptic NMDA-receptors become desensitized from the excessive stimulation while presynaptic NMDA and metabotropic glutamate receptors are still activated, causing long-term depression [57]. A β binds

to presynaptically located P/Q-type calcium channels leading to the inhibition of the neurotransmitter release [69]. A β can form a Ca²⁺-pore, the entry of Ca²⁺ through which activates protease calpain that cuts endocytotic protein dynamin 1 [70]. The level of Cu²⁺ increases in AD, A β in a complex with Cu²⁺ acquires the ability to convert cholesterol into 4-cholesten-3-one, and its concentration is increased in AD [36]. The accumulation of 4-cholest-3-one can inhibit synaptic Ca²⁺-ATP-ase, disrupt the stability of lipid rafts, and depress neurotransmission [71]. A β may be involved in establishing the balance between silent and active synapses: “low activity” synapses increase their “job” in response to A β , while highly active synapses reduce it (*Fig. 3*). It is worth noting that nerve terminals in old animals are more susceptible to the negative effect of A β . These nerve terminals are characterized by a smaller total synaptic vesicle pool, weak mitochondria activity, and antioxidant capacity. Under these conditions, the inhibition of synaptic vesicle recycling induced by A β is substantially lower in the presence of exogenous antioxidants [72].

The severity of AD correlates with the presence of A β 42 in neurons (especially in the neocortex), and the suppression of neurotransmission coincides with the accumulation of A β inside the nerve terminal, long before the appearance of extracellular plaques [28]. A β is trapped inside the endocytosed vesicles, and the presence of A β 42 in these vesicles activates casein kinase 2, which by phosphorylation of dynamin and synaptophysin promotes the inhibition of endocytosis and exhaustion of synaptic vesicle pools after the synaptic activity [73]. A β absorbed into vesicles directly interacts with synaptophysin and disrupts the formation of a complex between synaptophysin and VAMP2, thereby increasing the number of primed vesicles and enhancing exocytosis [74]. However, after intensive exocytosis, endocytosis is weak, since the interaction of synaptophysin/VAMP2 is required for efficient endocytosis. Chronic administration of A β in non-toxic concentrations inhibits the glutamate release in the hippocampal nerve terminals by reducing the size of readily releasable and recycling pools [75]. Perhaps that also can be attributed to the fact that A β 42 in endosomes are moved by axonal transport from nerve terminals to cell bodies, where A β 42 suppresses the expression of exocytotic and endocytotic proteins: SNAP-25, synaptotagmin, synaptophysin, dynamin 1, and amphiphysin 1 [57, 58]. After endocytosis, A β can be directed towards multivesicular bodies, where A β forms fibrils that perforate the membranes, causing neuronal death. These fibrils subsequently form plaques [76]. In general, many studies indicate that endocytosis is the key event which is associated with the formation, elimination, and toxicity of A β .

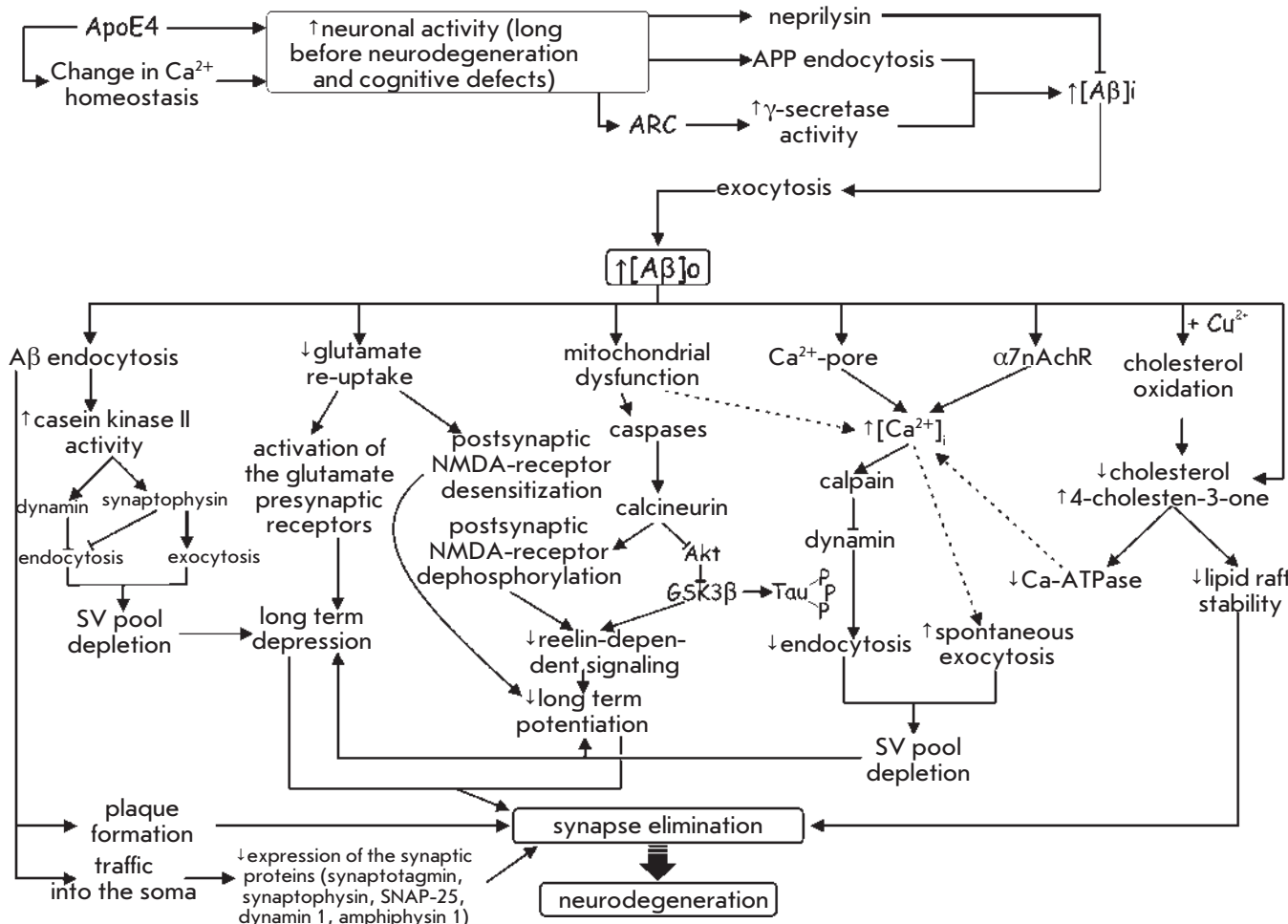


Fig. 3. Pathways of amyloid peptide β ($A\beta$) action on synaptic transmission and plasticity. Role of neuronal activity in $A\beta$ accumulation. See text for details.

PARKINSON'S DISEASE (PD)

Parkinson's disease (PD) is the second-most common neurodegenerative disease, which is characterized by tremor, slowed movements, rigidity, and cognitive impairment. As with AD, significantly fewer cases of PD are associated with mutations in specific genes, such as α -synuclein, parkin, LRRK2, PINK1, DJ-1, and ATP13A2. A peculiar feature of PD is the accumulation of α -synuclein in neurons as a part of protein inclusions, the so-called Lewy bodies. It affects dopaminergic neurons in the substantia nigra of the midbrain. It is worth noting that contemporary studies have revealed that 60% of patients with AD have deposits of α -synuclein in the amygdala, and that some patients with PD have an accumulation of $A\beta$ in the brain [8, 19, 30, 77]. This suggests that specific pathways leading to the development of PD or AD converge, causing the appearance of common signs.

The role of cholesterol in PD remains controversial (Fig. 4). A study of lipid rafts isolated from the frontal

cortex of subjects with early-stage PD showed a decrease in polyunsaturated fatty acids without changes in the content of cholesterol and sphingomyelin [78]. However, α -synuclein comprises two cholesterol-binding domains and membrane cholesterol affects its aggregation [41]. Theoretically, synuclein can disrupt the lipid raft integrity, by interacting with cholesterol [1]. Cholesterol depletion (using methyl- β -cyclodextrin) reduces the α -synuclein level in the membrane and its accumulation in neuronal bodies and synapses. Statins inhibit the aggregation of α -synuclein in a neuronal culture and the addition of exogenous cholesterol increases α -synuclein aggregation, which suppresses the growth of neurons [79]. Food deprivation (on the model of 3D5-cells) causes the aggregation of α -synuclein and apoptosis, which is associated with ER stress and SREBP1 activation, followed by an increase in cholesterol synthesis [80]. In PD, the concentration of some oxysterols increases in the brain in response to the overproduction of reactive oxygen species [81]. A cho-

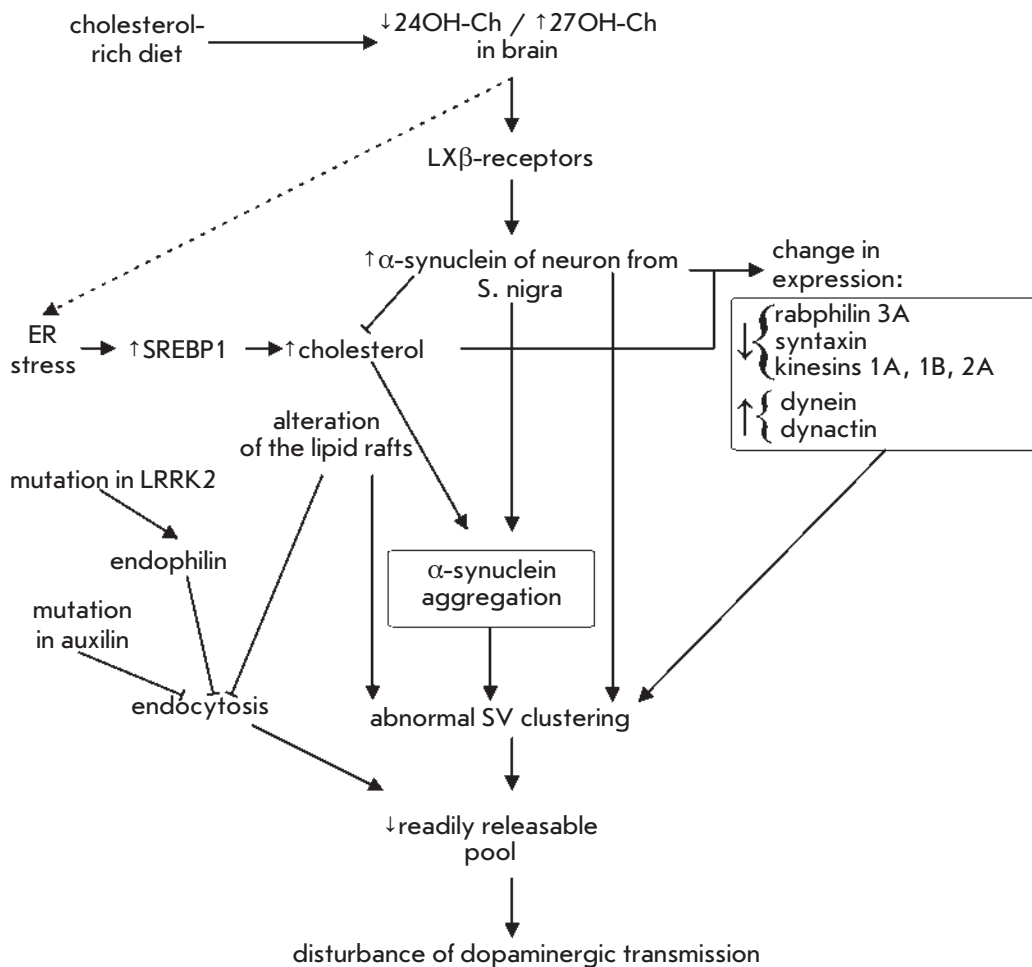


Fig. 4. Relation between cholesterol, α -synuclein, and alterations in pre-synaptic events with dopaminergic neuron dysfunction in Parkinson's disease. See text for details.

lesterol-rich diet reduces the ratio of 24OH-Ch : 27OH-Ch in the brain and increases the level of α -synuclein in substantia nigra without altering the cerebral cholesterol level. 27OH-Ch promotes and 24OH-Ch prevents an increase in α -synuclein concentration in a SH-SY5Y human neuroblastoma cell line. Moreover, 27OH-Ch exerts this effect through the activation of the LX β -receptors that bind to the promoter of the α -synuclein gene [19].

Long before the neuronal death, the dopamine release is suppressed at the early stage of PD. Mutations and duplications/triplication of the α -synuclein gene causes PD with an early onset. α -Synuclein is concentrated in nerve terminals and binds to synaptic vesicles. Normally, synuclein is important for the clustering of vesicles in the proximity of the active zone, since it simultaneously interacts with the synaptobrevin 2 of one vesicle and the phospholipids of another vesicle, acting as a bridge. Mutation in the α -synuclein gene may reduce its vesicle-clustering ability, and its overexpression causes massive aggregation of synaptic vesicles, and eventually both lead to a decrease in the size of the readily releasable pool

[82]. Overexpression of α -synuclein contributes to its intensive interaction with the membranes of synaptic vesicles and multivesicular bodies and disruption of their functioning [83]. Overexpression of mutant α -synuclein significantly alters the levels of the proteins involved in vesicular traffic and exocytosis (reduced quantities of rabphilin 3A, syntaxin, kinesins 1A, 1B, 2A, increased levels of dynein, dynactin 1) in the substantia nigra and the striatum [82]. A significant reduction in transcript levels (dynamin 2, AP-2, syntaxin-2, VAMP A, VAMP 4), implicated in vesicular cycling, was detected in the peripheral blood of patients at the first stage of PD [84].

In the case of hereditary PD, associated with a mutation in the *LRRK2* gene (kinase containing leucine rich repeat), the traffic of synaptic vesicles is disrupted at the beginning of the disease. *LRRK2* normally phosphorylates endophilin, thereby inhibiting its association with the membrane. At the same time excessive or insufficient activity of *LRRK2* hinders synaptic vesicle endocytosis [85]. The juvenile form of PD is caused by mutations in the auxilin which participates in the uncoating of synaptic clathrin-coated vesicles.

AUTISM SPECTRUM DISORDERS (ASD)

Autism spectrum disorders (ASD) are characterized by significant abnormalities in social interaction, difficulty in communication, and stereotypical behavioral patterns. These disorders may arise from genetic alterations, prenatal exposure to viruses and toxins, and interactions of the mother's and fetus' immune systems [30]. ASD are often associated with hereditary diseases, such as the Rett and fragile X syndromes, neurofibromatosis type 1, tuberous sclerosis, phenylketonuria, and the Smith-Opitz-Lemley syndrome.

Recently, new details have emerged concerning a relationship between cholesterol metabolism and the pathogenesis of some ASD. The Rett syndrome, which affects mainly women (1/10,000), is often associated with mutations in the X-linked gene of methyl-CpG-binding protein 2 (MeCP2). MeCP2 interacts with methylated DNA in the nucleus and recruits various transcription factors that regulate gene transcription, including those involved in cholesterol homeostasis. In the Rett syndrome, the levels of total cholesterol, the high- and low-density lipoproteins are increased, and the expression of scavenger receptor B1, responsible for the uptake of cholesterol, is reduced [86]. Expression of the genes involved in cholesterol metabolism was found to be slightly elevated in the brains of one-month-old mice with a mutation in *Mecp2/Y*. At the age of 2 months, these mice had an increased level of total cholesterol in the brain, but the production of cholesterol was suppressed, probably due to the activation of a negative feedback. As a result, by day 70 of postnatal development, the cholesterol concentration returned to its normal range. Reducing the production of cholesterol (mediated by a mutation in the gene *Sqle/squalene epoxidase* or by statins) in the mutant *Mecp2/Y* mice prevented a progression of the disease [87]. Treatment of women with the Rett syndrome with statins also improves their mental state. Therefore, early abnormalities of cholesterol metabolism in the Rett syndrome may contribute to the behavioral phenotype and a decrease in the survival rate [86]. It should be noted that statins also inhibit the synthesis of isoprenoid intermediaries (farnesyl pyrophosphate and ubiquinones), affecting such protein modifications as prenylation, which is important for the functioning of signaling proteins, such as Ras [88].

Statins are effective in the fragile X syndrome and type 1 neurofibromatosis [88]. The fragile X syndrome is one of the known causes (1/4,000) of mental retardation and autism. This syndrome occurs due to the expansion of CCG triplet repeats (greater than 200 repeats, full mutation) in the promoter of the *FMR1* gene (fragile X mental retardation 1), which leads to hypermethylation and suppression of *FMR1* gene

transcription [30]. Reduced production of the FMR protein (RNA-binding protein that inhibits the translation induced by the activation of several receptors in dendrites) enhances the synthesis of some proteins involved in neurotransmission. Studies of animal models of the fragile X syndrome revealed an abnormally high activity of group I metabotropic glutamate receptors (mGR-I). Caveolin 1 and membrane cholesterol availability can regulate the traffic and signaling of these receptors [42]. The signaling mediated by mGR-I is attenuated in the neurons of mutant mice treated with statins. Additionally, such treatment reduces the abnormally increased protein synthesis and long-term depression in the hippocampus, audiogenic seizures, and visual cortex hyperexcitability.

ASD are closely related to synaptic dysfunction. Signs of ASD usually manifest themselves in early childhood, when sensory experiences modify and tune the excitation/inhibition balance; therefore, it is assumed that disruption of the glutamate/GABAergic transmission ratio may contribute to ASD. The synaptic theory of ASD began with the identification of a mutation leading to the disease in the gene for neuroligin, a postsynaptic cell-adhesion molecule. Then, it was found that many genes associated with predisposition to autism encode synaptic proteins [90]. Mutations in presynaptic cell-adhesion molecules, neurexins, inhibit synaptic vesicle exocytosis in the hippocampus and cause social behavioral anomalies. Dysfunction of the CASP2 protein, which regulates the release of electron-dense granules with neuropeptides (neurotrophin-3, brain-derived neurotrophic factor) and monoamines, increases the risk of autism [91]. Mutations in the *Mecp2* gene reduce the levels of synaptic proteins, including synapsins, and the vesicular glutamate transporter. There is also a decrease in the expression of the GABA-synthesizing enzyme GAD and the size of the neurotransmitter quantum in GABA synapses [92]. The fragile X syndrome involves downregulation of the GABA-A receptor $\alpha 5$ - and γ -subunits and tonic currents through receptors composed of these subunits. Mice without reelin (normally expressed in cortical interneurons) exhibit a ASD phenotype and decreased GABA spillover [93]. Genetic polymorphism of exocytotic protein SNAP-25, mutations in presynaptic synapsin 1, 2, and the active zone protein RIMS3, which affect the neurotransmitter release, are associated with the probability of ASD. Mutations in the postsynaptic proteins IL-1RAPL1 and SynGAP1 involved in synapse formation are also related to ASD [91].

This work was supported by a RFBR grant (№ 17-04-00046), and partly by RFBR (№ 16-34-00127) and RNF (№ 14-15-00847).

REFERENCES

1. Petrov A.M., Kasimov M.R., Zefirov A.L. // *Acta Naturae*. 2016. V. 8. № 1. P. 58–73.
2. Bu G. // *Nat. Rev. Neurosci.* 2009. V. 10. № 5. P. 333–344.
3. Di Paolo G., Kim T.W. // *Nat. Rev. Neurosci.* 2011. V. 12. № 5. P. 284–296.
4. Mawuenyega K.G., Sigurdson W., Ovod V., Munsell L., Kasten T., Morris J.C., Yarasheski K.E., Bateman R.J. // *Science*. 2010. V. 330. № 6012. P. 1774.
5. Nalivaeva N., Belyaev N.D., Kerridge C., Turner A.J. // *Front. Aging Neurosci.* 2014. V. 6. A.235.
6. Sparks D.L., Scheff S.W., Hunsaker J.C. 3rd, Liu H., Landers T., Gross D.R. // *Exp. Neurol.* 1994. V. 126. № 1. P. 88–94.
7. Ghribi O., Larsen B., Schrag M., Herman M.M. // *Exp. Neurol.* 2006. V. 200. № 2. P. 460–467.
8. Martin M.G., Ahmed T., Korovaichuk A., Venero C., Menchón S.A., Salas I., Munck S., Herreras O., Balschun D., Dotti C.G. // *EMBO Mol. Med.* 2014. V. 6. № 7. P. 902–917.
9. Reed B., Villeneuve S., Mack W., DeCarli C., Chui H.C., Jagust W. // *JAMA Neurol.* 2014. V. 71. № 2. P. 195–200.
10. Kitaguchi H., Tomimoto H., Ihara M., Shibata M., Uemura K., Kalara R.N., Kihara T., Asada-Utsugi M., Kinoshita A., Takahashi R. // *Brain Res.* 2009. V. 1294. P. 202–210.
11. Leoni V., Caccia C. // *Biochimie*. 2013. V. 95. № 3. P. 595–612.
12. Hughes T.M., Kuller L.H., Lopez O.L., Becker J.T., Evans R.W., Sutton-Tyrrell K., Rosano C. // *J. Alzheimers Dis.* 2012. V. 30. № 1. P. 53–61.
13. Hudry E., van Dam D., Kulik W., De Deyn P.P., Stet F.S., Ahouansou O., Benraiss A., Delacourte A., Bougnères P., Aubourg P. // *Mol. Ther.* 2010. V. 18. № 1. P. 44–53.
14. Wang L., Schuster G.U., Hultenby K., Zhang Q., Andersson S., Gustafsson J.A. // *Proc. Natl. Acad. Sci. USA.* 2002. V. 99. № 21. P. 13878–13883.
15. Fitz N.F., Castranio E.L., Carter A.Y., Kodali R., Lefterov I., Koldamova R. // *J. Alzheimers Dis.* 2014. V. 41. № 2. P. 535–549.
16. Matsuda A., Nagao K., Matsuo M., Kioka N., Ueda K. // *J. Neurochem.* 2013. V. 126. № 1. P. 93–101.
17. Gosselet F., Saint-Pol J., Fenart L. // *Biochem. Biophys. Res. Commun.* 2014. V. 446. № 3. P. 687–691.
18. Heverin M., Bogdanovic N., Lütjohann D., Bayer T., Pikuleva I., Bretillon L., Diczfalusy U., Winblad B., Björkhem I. // *J. Lipid Res.* 2004. V. 45. № 1. P. 186–193.
19. Marwarha G., Ghribi O. // *Exp. Gerontol.* 2014. pii: S0531-5565(14)00270-8.
20. Mason R.P., Shoemaker W.J., Shajenko L., Chambers T.E., Herbet L.G. // *Neurobiol. Aging.* 1992. V. 13. № 3. P. 413–419.
21. Molander-Melin M., Blennow K., Bogdanovic N., Dellheden B., Månsson J.E., Fredman P. // *J. Neurochem.* 2005. V. 92. № 1. P. 171–182.
22. Abad-Rodríguez J., Ledesma M.D., Craessaerts K., Perga S., Medina M., Delacourte A., Dingwall C., De Strooper B., Dotti C.G. // *J. Cell Biol.* 2004. V. 167. № 5. P. 953–960.
23. Gylys K.H., Fein J.A., Yang F., Miller C.A., Cole G.M. // *Neurobiol. Aging.* 2007. V. 28. № 1. P. 8–17.
24. Pierrot N., Tyteca D., D'auria L., Dewachter I., Gailly P., Hendrickx A., Tasiaux B., Haylani L.E., Muls N., N'kuli F. // *EMBO Mol. Med.* 2013. V. 5. № 4. P. 608–625.
25. Evangelisti E., Zampagni M., Cascella R., Becatti M., Fiorillo C., Caselli A., Bagnoli S., Nacmias B., Cecchi C. // *J. Alzheimers Dis.* 2014. V. 41. № 1. P. 289–300.
26. Sodero A.O., Vriens J., Ghosh D., Stegner D., Brachet A., Pallotto M., Sassoè-Pognetto M., Brouwers J.F., Helms J.B., Nieswandt B. // *EMBO J.* 2012. V. 31. № 7. P. 1764–1773.
27. Sodero A.O., Weissmann C., Ledesma M.D., Dotti C.G. // *Neurobiol. Aging.* 2011. V. 32. № 6. P. 1043–1053.
28. Gómez-Ramos P., Asunción Morán M. // *J. Alzheimers Dis.* 2007. V. 11. № 1. P. 53–59.
29. Bryleva E.Y., Rogers M.A., Chang C.C., Buen F., Harris B.T., Rousselet E., Seidah N.G., Oddo S., LaFerla F.M., Spencer T.A., et al. // *Proc. Natl. Acad. Sci. USA.* 2010. V. 107. P. 3081–3086.
30. Anchisi L., Dessi S., Pani A., Mandas A. // *Front Physiol.* 2013. V. 3. P. 1–12.
31. Lathe R., Sapronova A., Kotelevtsev Y. // *BMC Geriatrics.* 2014. V. 14. A. 36.
32. Rushworth J.V., Hooper N.M. // *Int. J. Alzheimers Dis.* 2011. P. 603052.
33. Matsuzaki K. // *Int. J. Alzheimers Dis.* 2011. V. 2011. P. 956104.
34. Barrett P.J., Song Y., van Horn W.D., Hustedt E.J., Schafer J.M., Hadziselimovic A., Beel A.J., Sanders C.R. // *Science*. 2012. V. 336. P. 1168–1171.
35. Woo J.A., Roh S.E., Lakshmana M.K., Kang D.E. // *FASEB J.* 2012. V. 26. № 4. P. 1672–1681.
36. Puglielli L., Friedlich A.L., Setchell K.D., Nagano S., Opazo C., Cherny R.A., Barnham K.J., Wade J.D., Melov S., Kovacs D.M., Bush A.I. // *J. Clin. Invest.* 2005. V. 115. № 9. P. 2556–2563.
37. Pensalfini A., Zampagni M., Liguri G., Becatti M., Evangelisti E., Fiorillo C., Bagnoli S., Cellini E., Nacmias B., Sorbi S., Cecchi C. // *Neurobiol. Aging.* 2011. V. 32. № 2. P. 210–222.
38. Rushworth J.V., Griffiths H.H., Watt N.T., Hooper N.M. // *J. Biol. Chem.* 2013. V. 288. № 13. P. 8935–8951.
39. Ledesma M.D., Abad-Rodríguez J., Galvan C., Biondi E., Navarro P., Delacourte A., Dingwall C., Dotti C.G. // *EMBO Rep.* 2003. V. 4. № 12. P. 1190–1196.
40. Sarajärvi T., Haapasalo A., Viswanathan J., Mäkinen P., Laitinen M., Soininen H., Hiltunen M. // *J. Biol. Chem.* 2009. V. 284. № 49. P. 34433–34443.
41. Head B.P., Peart J.N., Panneerselvam M., Yokoyama T., Pearn M.L., Niesman I.R., Bonds J.A., Schilling J.M., Miyanojara A., Headrick J. // *PLoS One.* 2010. V. 5. № 12. P. e15697.
42. Stary C.M., Tsutsumi Y.M., Patel P.M., Head B.P., Patel H.H., Roth D.M. // *Front. Physiol.* 2012. V. 3. P. 393.
43. Sano M., Bell K.L., Galasko D., Galvin J.E., Thomas R.G., van Dyck C.H., Aisen P.S. // *Neurology.* 2011. V. 77. P. 556–563.
44. Schilling J.M., Cui W., Godoy J.C., Risbrough V.B., Niesman I.R., Roth D.M., Patel P.M., Drummond J.C., Patel H.H., Zemljic-Harpf A.E., Head B.P. // *Behav. Brain Res.* 2014. V. 267. P. 6–11.
45. Burg V.K., Grimm H.S., Rothhaar T.L., Grösgen S., Hundsdoerfer B., Haupenthal V.J., Zimmer V.C., Mett J., Weingärtner O., Laufs U. // *J. Neurosci.* 2013. V. 33. № 41. P. 16072–16087.
46. Vance J.E. // *Disease Models Mechanisms.* 2012. V. 5. P. 746–755.
47. Lane-Donovan C., Philips G.T., Herz J. // *Neuron.* 2014. V. 83. № 4. P. 771–787.
48. Cramer P.E., Cirrito J.R., Wesson D.W., Lee C.Y., Karlo J.C., Zinn A.E., Casali B.T., Restivo J.L., Goebel W.D., James M.J., et al. // *Science.* 2012. V. 335. P. 1503–1506.

49. Hayashi H. // *Biol. Pharm. Bull.* 2011. V. 34. № 4. P. 453–461.
50. Durakogluligil M.S., Chen Y., White C.L., Kavalali E.T., Herz J. // *Proc. Natl. Acad. Sci. USA.* 2009. V. 106. № 37. P. 15938–15943.
51. Rhinn H., Fujita R., Qiang L., Cheng R., Lee J.H., Abelio- vich A. // *Nature.* 2013. V. 500. № 7460. P. 45–50.
52. Harris F.M., Brecht W.J., Xu Q., Tesseur I., Kekonius L., Wyss-Coray T., Fish J.D., Masliah E., Hopkins P.C., Scarce-Levie K. // *Proc. Natl. Acad. Sci. USA.* 2003. V. 100. № 19. P. 10966–10971.
53. Liu Q., Trotter J., Zhang J., Peters M.M., Cheng H., Bao J., Han X., Weeber E.J., Bu G. // *J. Neurosci.* 2010. V. 30. № 50. P. 17068–17078.
54. Schmidt V., Baum K., Lao A., Rateitschak K., Schmitz Y., Teichmann A., Wiesner B., Petersen C.M., Nykjaer A., Wolf J. // *EMBO J.* 2012. V. 31. № 1. P. 187–200.
55. Brodeur J., Thériault C., Lessard-Beaudoin M., Marcil A., Dahan S., Lavoie C. // *Mol. Neurodegener.* 2012. V. 7. P. 31.
56. Karasinska J.M., de Haan W., Franciosi S., Ruddle P., Fan J., Kruit J.K., Stukas S., Lütjohann D., Gutmann D.H., Wellington C.L. // *Neurobiol. Dis.* 2013. V. 54. P. 445–455.
57. Palop J.J., Mucke L. // *Nat. Neurosci.* 2010. V. 13. № 7. P. 812–818.
58. Sheng M., Sabatini B.L., Südhof T.C. // *Cold Spring Harb. Perspect. Biol.* 2012. V. 4. № 5. pii: a005777.
59. Chakroborty S., Kim J., Schneider C., Jacobson C., Molgó J., Stutzmann G.E. // *J. Neurosci.* 2012. V. 32. № 24. P. 8341–8353.
60. Israel M.A., Yuan S.H., Bardy C., Reyna S.M., Mu Y., Herrera C., Hefferan M.P., van Gorp S., Nazor K.L., Boscolo F.S. // *Nature.* 2012. V. 482. № 7384. P. 216–220.
61. Cataldo A.M., Barnett J.L., Pieroni C., Nixon R.A. // *J. Neurosci.* 1997. V. 17. № 16. P. 6142–6151.
62. Wu J., Petralia R.S., Kurushima H., Patel H., Jung M.Y., Volk L., Chowdhury S., Shepherd J.D., Dehoff M., Li Y. // *Cell.* 2011. V. 147. № 3. P. 615–628.
63. Tampellini D., Rahman N., Gallo E.F., Huang Z., Dumont M., Capetillo-Zarate E., Ma T., Zheng R., Lu B., Nanus D.M. // *J. Neurosci.* 2009. V. 29. № 31. P. 9704–9713.
64. Puzzo D., Privitera L., Fa' M., Staniszewski A., Hashimoto G., Aziz F., Sakurai M., Ribe E.M., Troy C.M., Mercken M. // *Ann. Neurol.* 2011. V. 69. № 5. P. 819–830.
65. Quiroz Y.T., Budson A.E., Celone K., Ruiz A., Newmark R., Castrillón G., Lopera F., Stern C.E. // *Ann. Neurol.* 2010. V. 68. № 6. P. 865–875.
66. Dean D.C. 3rd1, Jerskey B.A., Chen K., Protas H., Thiyyagura P., Roontiva A., O'Muircheartaigh J., Dirks H., Waskiewicz N., Lehman K., Siniard A.L. // *JAMA Neurol.* 2014. V. 71. № 1. P. 11–22.
67. Jo J., Whitcomb D.J., Olsen K.M., Kerrigan T.L., Lo S.C., Bru-Mercier G., Dickinson B., Scullion S., Sheng M., Collingridge G., Cho K. // *Nat. Neurosci.* 2011. V. 14. № 5. P. 545–547.
68. Bezprozvanny I.B. // *Acta Naturae.* 2010. V. 2. № 1(4). P. 72–80.
69. Nimrich V., Grimm C., Draguhn A., Barghorn S., Lehmann A., Schoemaker H., Hillen H., Gross G., Ebert U., Bruehl C. // *J. Neurosci.* 2008. V. 28. № 4. P. 788–797.
70. Sinjoanu R.C., Kleinschmidt S., Bitner R.S., Brioni J.D., Moeller A., Ferreira A. // *Neurochem. Int.* 2008. V. 53. № 3–4. P. 79–88.
71. Kasimov M.R., Giniatullin A.R., Zefirov A.L., Petrov A.M. // *Biochim. Biophys. Acta.* 2015. V. 1851. № 5. P. 674–685.
72. Quiroz-Baez R., Flores-Domínguez D., Arias C. // *Curr. Alzheimer Res.* 2013. V. 10. № 3. P. 324–331.
73. Moreno H., Yu E., Pigino G., Hernandez A.I., Kim N., Moreira J.E., Sugimori M., Llinás R.R. // *Proc. Natl. Acad. Sci. USA.* 2009. V. 106. № 14. P. 5901–5906.
74. Russell C.L., Semerdjieva S., Empson R.M., Austen B.M., Beesley P.W., Alifragis P. // *PLoS One.* 2012. V. 7. № 8. P. e43201.
75. Parodi J., Sepúlveda F.J., Roa J., Opazo C., Inestrosa N.C., Aguayo L.G. // *J. Biol. Chem.* 2010. V. 285. № 4. P. 2506–2514.
76. Friedrich R.P., Tepper K., Rönicke R., Soom M., Westermann M., Reymann K., Kaether C., Fändrich M. // *Proc. Natl. Acad. Sci. USA.* 2010. V. 107. № 5. P. 1942–1947.
77. Ugrumov M.V., Khaindrava V.G., Kozina E.A., Kucheryanu V.G., Bocharov E.V., Kryzhanovsky G.N., Kudrin V.S., Narkevich V.B., Klodt P.M., Rayevsky K.S., Pronina T.S. // *Neuroscience.* 2011. V. 181. P. 175–188.
78. Fabelo N., Martín V., Santpere G., Marín R., Torrent L., Ferrer I., Díaz M. // *Mol. Med.* 2011. V. 17. № 9–10. P. 1107–1118.
79. Bar-On P., Crews L., Koob A. O., Mizuno H., Adame A., Spencer B., Masliah E. // *J. Neurochem.* 2008. V. 105. P. 1656–1667.
80. Jiang P., Gan M., Lin W.L., Yen S.H. // *Front. Aging Neurosci.* 2014. V. 6. P. 1–12.
81. Brown A.J., Jessup W. // *Mol. Aspects Med.* 2009. V. 30. № 3. P. 111–122.
82. Diao J., Burré J., Vivona S., Cipriano D.J., Sharma M., Kyoung M., Südhof T.C., Brunger A.T. // *Elife.* 2013. V. 2. P. e00592.
83. Boassa D., Berlanga M.L., Yang M.A., Terada M., Hu J., Bushong E.A., Hwang M., Masliah E., George J.M., Ellisman M.H. // *J. Neurosci.* 2013. V. 33. № 6. P. 2605–2615.
84. Alieva A.Kh., Shadrina M.I., Filatova E.V., Karabanov A.V., Illarioshkin S.N., Limborska S.A., Slominsky P.A. // *Biomed. Res. Int.* 2014. Article ID 718732.
85. Matta S., van Kolen K., da Cunha R., van den Bogaart G., Mandemakers W., Miskiewicz K., De Bock P.J., Morais V.A., Vilain S., Haddad D. // *Neuron.* 2012. V. 75. № 6. P. 1008–1021.
86. Nagy G., Ackerman S.L. // *Nat. Genet.* 2013. V. 45. № 9. P. 965–967.
87. Buchovecky C.M., Turley S.D., Brown H.M., Kyle S.M., McDonald J.G., Liu B., Pieper A.A., Huang W., Katz D.M., Russell D.W., Shendure J. // *Nat. Genet.* 2013. V. 45. № 9. P. 1013–1020.
88. Osterweil E.K., Chuang S.C., Chubykin A.A., Sidorov M., Bianchi R., Wong R.K., Bear M.F. // *Neuron.* 2013. V. 77. № 2. P. 243–250.
89. Berry-Kravis E., Levin R., Shah H., Mathur S., Darnell J.C., Ouyang B. // *Am. J. Med. Genet. A.* 2015. V. 167A. № 2. P. 379–384.
90. Qiu S., Aldinger K.A., Levitt P. // *Dev. Neurosci.* 2012. V. 34. № 2–3. P. 88–100.
91. Shinoda Y., Sadakata T., Furuichi T. // *Exp. Anim.* 2013. V. 62. № 2. P. 71–78.
92. Nguyen M.V., Du F., Felice C.A., Shan X., Nigam A., Mandel G., Robinson J.K., Ballas N. // *J. Neurosci.* 2012. V. 32. № 29. P. 10021–10034.
93. Cea-Del Rio C.A., Huntsman M.M. // *Front Cell Neurosci.* 2014. V. 8. P. 245.

Spheroids of HER2-Positive Breast Adenocarcinoma for Studying Anticancer Immunotoxins *In Vitro*

I. V. Balalaeva^{1,2*}, E. A. Sokolova^{1,2}, A. D. Puzhikhina¹, A. A. Brilkina¹, S. M. Deyev^{1,2,3}

¹Lobachevsky State University of Nizhny Novgorod, Gagarin Ave., 23, Nizhny Novgorod, 603950, Russia

²Shemyakin–Ovchinnikov Institute of Bioorganic Chemistry, Russian Academy of Sciences, Miklukho–Maklaya Str., 16/10, Moscow, 117997, Russia

³National Research Tomsk Polytechnic University, Lenin Ave., 30, Tomsk, 634050, Russia

*E-mail: irin-b@mail.ru

Received August 22, 2016; in final form, November 18, 2016

Copyright © 2017 Park-media, Ltd. This is an open access article distributed under the Creative Commons Attribution License, which permits unrestricted use, distribution, and reproduction in any medium, provided the original work is properly cited.

ABSTRACT Tumor response to therapeutic treatment is largely determined by its heterogeneity and the presence of intercellular junctions, hindering the penetration of large molecules deep into the three-dimensional structure of the tumor. In that context, 3D *in vitro* tumor models such as cancer cell spheroids are becoming increasingly popular. We obtained spheroids of human breast adenocarcinoma SKBR-3 overexpressing the HER2 cancer marker. The toxicity of HER2-targeted immunotoxin 4D5scFv-PE40 against spheroids was shown to be several orders of magnitude lower compared to a monolayer cell culture. The significant difference in the severity of the immunotoxin effect can be explained by the fact that it ineffectively penetrates the spheroid and predominantly influences the cells of the outer layers. The resulting tumor spheroid model can be used in development of drugs for targeted therapy as well as to study ways to improve the efficiency of anticancer agents by targeting cell–cell contacts.

KEYWORDS 4D5scFv-PE40 immunotoxin, cancer marker HER2, drug penetration into tumor, spheroids, targeted therapy.

ABBREVIATIONS HER2 – human epidermal growth factor receptor 2; scFv – single-chain variable fragment; PE40 – 40 kDa fragment of *Pseudomonas* exotoxin A; DMSO – dimethyl sulfoxide; MTT – 3-(4,5-dimethylthiazol-2-yl)-2,5-diphenyltetrazolium bromide; PAG – polyacrylamide gel.

INTRODUCTION

The complex structure of solid tumors *in vivo* causes serious difficulties in *in vitro* studies of tumor development and when evaluating the therapeutic potential of anticancer drugs. A monolayer cell culture, despite its widest distribution, fails to reflect a number of features of the real tumor, especially its 3D organization. The 3D structure of a tumor implies numerous cell–cell contacts and considerable gradients of gases, nutrients, and catabolites throughout the tumor volume, resulting in the formation of a specific microenvironment for the cells of different layers. In turn, this leads to a heterogeneity of tumor cell populations that manifests itself as a variation of gene expression profiles and metabolism. A tumor's heterogeneity largely determines its response to a therapeutic treatment. Furthermore, cell–cell contacts hinder the penetration of large molecules into the tumor, whereby the efficiency of drugs is strongly impacted by their ability to diffuse through

the tumor mass [1]. In this regard, 3D *in vitro* tumor models, such as cancer cell spheroids, are becoming increasingly popular. Multicellular tumor spheroids are compact conglomerates of cancer cells that represent the avascular stage of tumor node development: a small primary tumor and early metastasis or the tumor zone located away from the vessel. The structural similarity between the spheroid and a real tumor increases the relevance of such a model, enabling a more accurate evaluation of potential anticancer agents under *in vitro* conditions [2, 3]. Taking into account the rapid development of targeted (directed) therapy [4], it is of particular interest to produce and employ cell spheroids that express the molecular targets that determine the specificity of a targeted agent.

We obtained spheroids of human breast adenocarcinoma SKBR-3 overexpressing the HER2 cancer marker and demonstrated that this model is informative in the assessment of the penetration depth and anticancer

efficiency of HER2-targeted immunotoxin 4D5scFv-PE40.

EXPERIMENTAL

Production of spheroids of human breast adenocarcinoma

HER2-overexpressing human breast adenocarcinoma cells, SKBR-3 (ATCC number HTB-30), were used [5]. The cells were cultured in a McCoy's 5A medium with 1.5 mM L-glutamine (HyClone, USA) supplemented with 10% (v/v) fetal calf serum (HyClone, USA) at 37°C in 5% CO₂. For passaging, the cells were carefully detached using a Versene solution (PanEco, Russia).

The spheroids were produced following three protocols. For the first one, we used 96-well culture plates with the standard adhesive surface (Corning, USA) pre-coated with 1% agarose (AppliChem, Germany) in distilled water (50 µl per well). For the second and third protocols, we used 96-well Ultra-Low-Attachment Microplates (Corning, USA) with a round or flat bottom, respectively. In all cases 200 cells were seeded per well.

The images of the spheroids were captured by phase contrast microscopy on an Axiovert 200 inverted microscope with an EC Plan-Neofluar 10 × /0.3 objective lens (Carl Zeiss, Germany). The volume of a spheroid (V, mm³) was calculated according to the equation: $V = a \times b^2 / 2$, where *a* is the larger diameter (µm) and *b* is the smaller diameter (µm).

Production of 4D5scFv-PE40 immunotoxin

Recombinant immunotoxin 4D5scFv-PE40 [6] was produced in *Escherichia coli* cells, strain BL21(DE3), transformed with the plasmid pSD-4D5scFv-PE40 containing the gene of the protein under *lac*-promoter control. The protein was purified successively by metal-chelate affinity chromatography using a HisTrap FF 1 ml column (GE Healthcare, USA) and ion exchange chromatography on a QSepharose FF 1 ml column (GE Healthcare, USA) according to the manufacturer's instructions. Fractions containing the desired protein were analyzed by electrophoresis in 12% PAG under denaturing conditions according to the standard protocol.

Analysis of the cytotoxicity of 4D5scFv-PE40 immunotoxin against a SKBR-3 monolayer culture and spheroids

For the cytotoxicity study on a monolayer culture, the SKBR-3 cells were seeded in a 96-well plate (Corning, USA), 2,000 cells per well, and grown overnight. The medium was then replaced with a fresh one containing 4D5scFv-PE40 at various concentrations (10⁻⁵–10² nM), and the cells were incubated for 72 h. Cell viability was

estimated using a MTT assay [7]. The medium was replaced with a fresh one containing 0.5 mg/ml MTT (Alfa Aesar, Great Britain), followed by incubation for 4 h. The formed formazan crystals were solved in DMSO (PanEco, Russia), and the optical density at 570 nm was measured on a Synergy MX microplate reader (BioTek, USA). The spheroids were produced as described above using 96-well round bottom ultra-low-attachment plates and cultured overnight. The cytotoxicity of the 4D5scFv-PE40 immunotoxin against the spheroids was studied in the same way with the incubation time increased up to 168 h.

Relative cell viability was represented as a percentage of the average optical density in the wells with treated cells to the average optical density in the wells with untreated cells. The cytotoxicity of the immunotoxin against the spheroids was also evaluated according to a spheroid's volume on the final day of incubation in the presence of immunotoxin: relative cell viability was in this case calculated as a percentage of the mean volumes of treated to untreated spheroids. Data were processed using the GraphPad Prism 6 software (GraphPad Software). The IC₅₀ was calculated by nonlinear regression using the four-parameter dose-response model.

Assessment of immunotoxin 4D5scFv-PE40 penetration of spheroids

In order to visualize the penetration of 4D5scFv-PE40 into a spheroid, the immunotoxin was conjugated with a low-molecular-weight fluorescent dye, DyLight650. For the reaction, the protein was exchanged into borate buffer (400 mM H₃BO₃, 70 mM Na₂B₄O₇, pH 8.0) by gel filtration on a PD SpinTrap G-25 column (GE Healthcare, USA). N-Hydroxysuccinimide derivative DyLight650 NHS Ester (Thermo Fisher Scientific, USA) that ensures dye conjugation to the protein primary amino groups was used. The protein was incubated with a sevenfold molar excess of DyLight650 NHS Ester diluted in DMSO for 1 h at room temperature in the dark in accordance with the manufacturer's recommendations. Unbound dye was removed by gel filtration on a PD SpinTrap G-25 column equilibrated with phosphate buffered saline (PBS), pH 7.4 (PanEco, Russia).

SKBR-3 cells were seeded in a 96-well ultra-low-attachment round-bottom plate, 1,000 cells per well, and grown overnight to produce spheroids. The formed spheroids were incubated in a medium containing fluorescent conjugates of 4D5scFv-PE40 for 2 h at 37°C. The spheroids were then washed twice with PBS and fixed with 10% formalin in PBS for 15 min in the dark. The images of the spheroids were obtained using an Axio Observer Z1 LSM 710 NLO/Duo confocal micro-

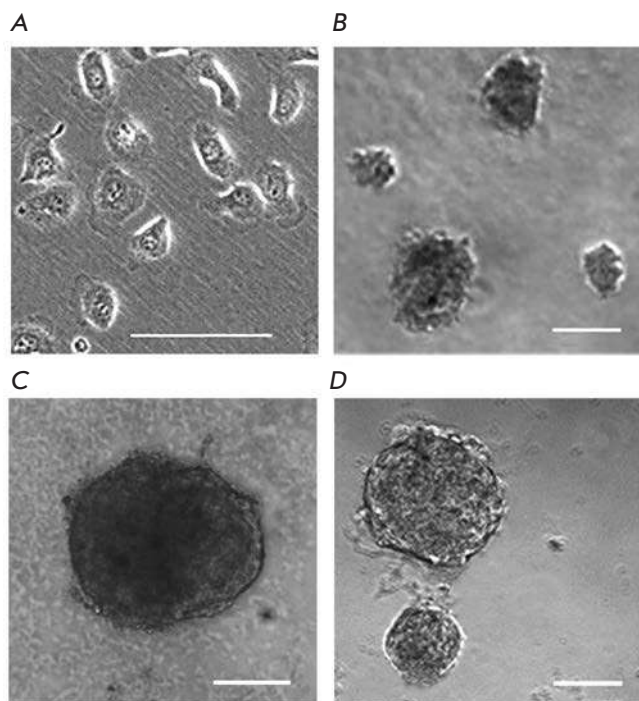


Fig. 1. Morphology of SKBR-3 cells in a monolayer culture (A) and after culturing for 8 days under non-attachment conditions: agarose (B) and ultra-low attachment plates with round (C) or flat (D) bottom. Bar, 50 μm (A) or 100 μm (B, C, D).

scope (Carl Zeiss, Germany) equipped with a EC Plan-Neofluar 20 \times /0.50 objective lens. DyLight650 fluorescence was excited at 633 nm with a helium-neon laser. The signal was registered in the range of 643–735 nm.

RESULTS AND DISCUSSION

Cancer cells, including a number of human breast cancer cell lines, are generally known to show a strong tendency toward forming spheroids in a culture [8–12]. However, the difficulties associated with obtaining well-shaped cell spheroids of SKBR-3 cells were encountered in several studies in a wide range of culture conditions, including when extracellular matrix components (Matrigel) were added into the growth medium or the medium viscosity was increased by adding methylcellulose [9, 10].

Culturing SKBR-3 cells under various conditions that prevent the formation of a monolayer culture (Fig. 1A) revealed their significant impact on the spheroid-formation ability of a cell culture. The cells grown on agarose formed loose aggregates of irregular shape that greatly varied in size and had jagged edges. The diameter of the largest aggregates was 30–100 μm on

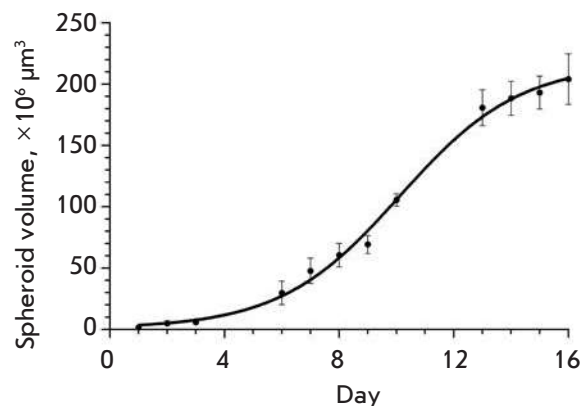


Fig. 2. The growth curve of SKBR-3 spheroids in ultra-low attachment round-bottom plates. Mean \pm SEM, $n = 5$. The cells were seeded in the plates on day 0.

the 2nd day after cell seeding and reached 60–140 μm within 8 days of culturing (Fig. 1B).

Utilization of the ultra-low-attachment plates was more successful. A single spheroid was formed in each well of the round-bottom plate after culturing for one day; it was a tight round-shaped conglomerate of cells with a diameter of about 160–200 μm and a clearly defined edge. By day 8 of culturing, the spheroids had reached 250–560 μm in diameter (Fig. 1C). When cultured in flat-bottom plates, 20–30 round-shaped spheroids were formed per well, mostly with a clear smooth edge and size of 30–60 and 130–360 μm on culturing days 2 and 8, respectively (Fig. 1D).

With allowance for the features of formation of the 3D structures by SKBR-3 cells under various culturing conditions, the round-bottom ultra-low-attachment plate was acknowledged as the optimal one and was further used. The growth dynamics of the spheroids produced using this technique was shown to be complex: the initial exponential phase that lasted for about 10 days in our experiment gave way to a phase of slower growth (Fig. 2). A similar behavior described by the Gompertz function characterizes tumor growth *in vivo* [13]. The deceleration in spheroid growth can be attributed to the change in the ratio between different cell populations as its size rises and to the increasingly hindered supply of oxygen and nutrients deep into the spheroid: the increase in the proportion of non-dividing (resting) cells and/or death of resting cells accompanied by enlargement of the necrotic core [3, 14].

Overexpression of the HER2 receptor is one of the key features of the SKBR-3 cell line used for spheroid production. This receptor belongs to the epidermal growth factor receptor family and is an important com-

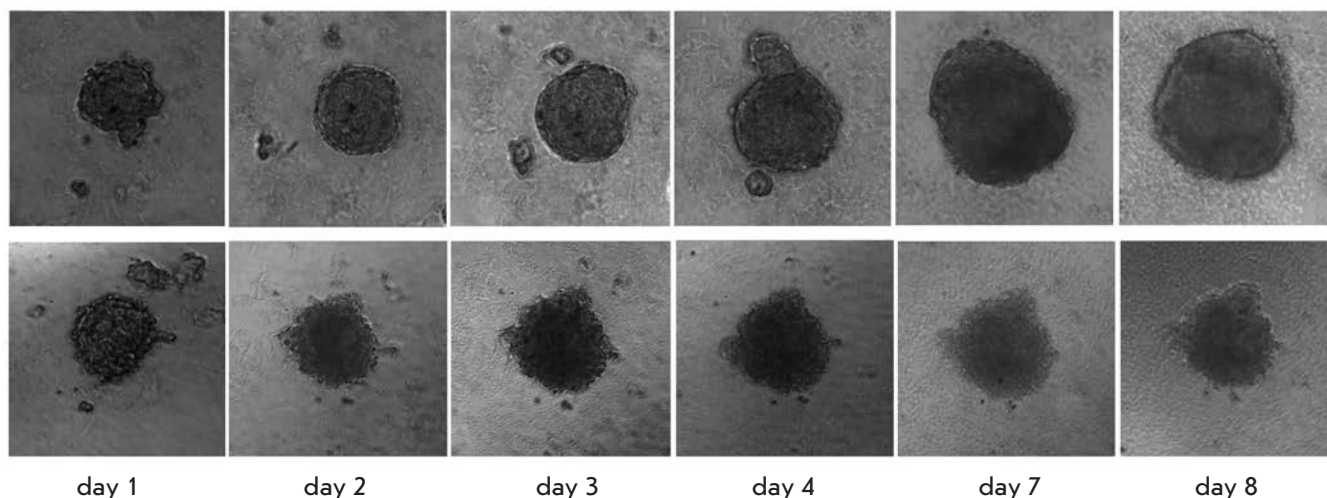


Fig. 3. Morphology of SKBR-3 spheroids on different days of growth in the control (*upper panel*) and in the presence of 100 nM 4D5scFv-PE40 (*lower panel*). Image size 400×400 μm .

ponent of the signal transduction network that controls cell proliferation, differentiation, and apoptosis [15]. The high level of HER2 expression that is typical of many types of tumors and its role in tumor pathogenesis make this receptor an advanced target for targeted anticancer drugs [16, 17]. Recombinant immunotoxins, fusion proteins comprising functionally independent targeting and toxic modules, are promising agents for targeted therapy. Antibody fragments or non-immunoglobulin polypeptides act as targeting modules that provide directed delivery of such molecular constructs to cancer cells, while the toxic effect is ensured by naturally modified toxin proteins of various origins [18]. We analyzed the growth of spheroids under the influence of the previously created recombinant immunotoxin 4D5scFv-PE40 that comprised HER2-specific antibody 4D5scFv as a targeting module and a 40 kDa fragment of *Pseudomonas* exotoxin A (PE40) as a toxic module [6].

The presence of 4D5scFv-PE40 in the growth medium significantly slowed down spheroid growth (*Fig. 3*). The impact of the immunotoxin on the spheroid size was dose-dependent (*Fig. 4*). Complete inhibition of spheroid growth was achieved at immunotoxin concentrations higher than 1 nM (*Fig. 3*, lower row). The immunotoxin also affected the spheroid morphology: in contrast to the control, the spheroids loosened and lost their characteristic shape as early as on day 2 of incubation with the immunotoxin (*Fig. 3*, lower row). Tight packing of cells in the spheroid structure is known to be made possible by an increased expression of cell junction proteins, in particular cadherins, and their accumulation on the cell surface [19, 20]. Since the

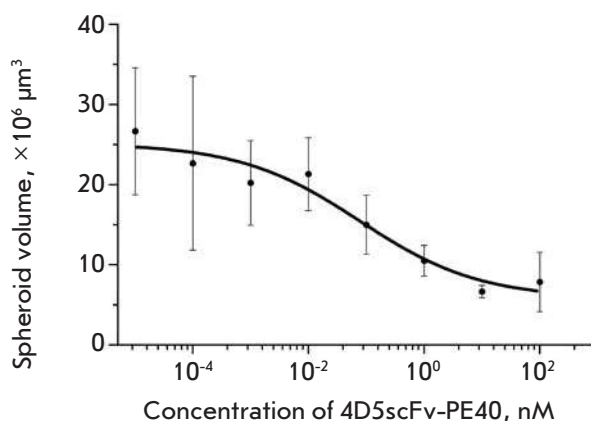


Fig. 4. Size of SKBR-3 spheroids after incubation for 7 days in the presence of 4D5scFv-PE40 at different concentrations. Mean \pm SEM, $n = 6$ for all experimental conditions.

toxic effect of *Pseudomonas* exotoxin A is a result of the blockage of protein synthesis in target cells [21], the observed effect of 4D5scFv-PE40 immunotoxin on the spheroid morphology may be due to a reduction in the amount of cell adhesion proteins in the cells.

A comparative analysis of 4D5scFv-PE40 cytotoxicity against SKBR-3 cells in the monolayer and spheroids estimated by a MTT assay showed significant resistance by the spheroids to this agent. Thus, the effect of 4D5scFv-PE40 against the monolayer culture was observed at concentrations ranging from 0.1 pM to 0.1 nM with IC_{50} of about 0.8 pM after 72 h of incu-

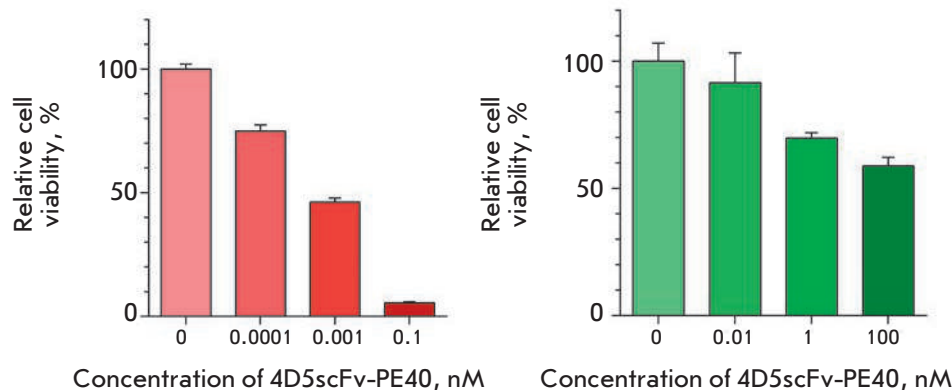


Fig. 5. Effect of 4D5scFv-PE40 on SKBR-3 culture growth. *Left-hand side:* the relative viability of the monolayer culture after incubation with immunotoxin for 72 h. *Right-hand side:* the relative viability of the spheroid cells 168 h after the immunotoxin was added into the medium. Mean \pm SEM, $n = 6$ for all experimental conditions.

bation (Fig. 5, left). This is consistent with the results obtained earlier for another HER2-overexpressing cell line, SKOV-3 [22]. However, the viability of the cells in the spheroids practically did not decrease under the same conditions. When the incubation time was increased to 168 h, the toxic effect of 4D5scFv-PE40 immunotoxin was observed only when its concentration was increased to 1 nM and IC_{50} was higher than 100 nM (Fig. 5, right).

The phenomenon of greater resistance shown by tumors *in vivo* to therapeutic agents compared to corresponding cancer cells in culture is well known [23, 24]. We have previously shown the toxic effect of the 4D5scFv-PE40 immunotoxin at picomolar concentrations on the HER2-overexpressing human ovarian adenocarcinoma cells SKOV-kat in culture, while its *in vivo* activity against SKOV-kat xenograft tumors becomes evident under its administration at nanomolar concentration [25]. The use of a monolayer culture of cancer cells obviously does not allow one to predict the effective range of concentrations of a tested agent in the whole organism.

Resistance usually depends on a combination of factors different in nature that represent both the tumor properties and the pharmacokinetics of the drug. One of these factors is insufficient drug accumulation in the tumor as a result of its poor penetration into the tumor mass, which in turn can arise from high interstitial fluid pressure, irregular arrangement of tumor blood vessels, numerous intercellular contacts, and/or the presence of extracellular matrix components. This is of particular importance for protein drugs: notably, recombinant immunotoxins, whose molecule size (50–70 kDa) results in a short blood circulation time (20–30 min) on the one hand, while on the other hand it slows down diffusion into tissues [26–28].

In order to estimate the depth of the immunotoxin penetration into the spheroid, we conjugated 4D5scFv-PE40 with the DyLight650 fluorescent dye. We dis-

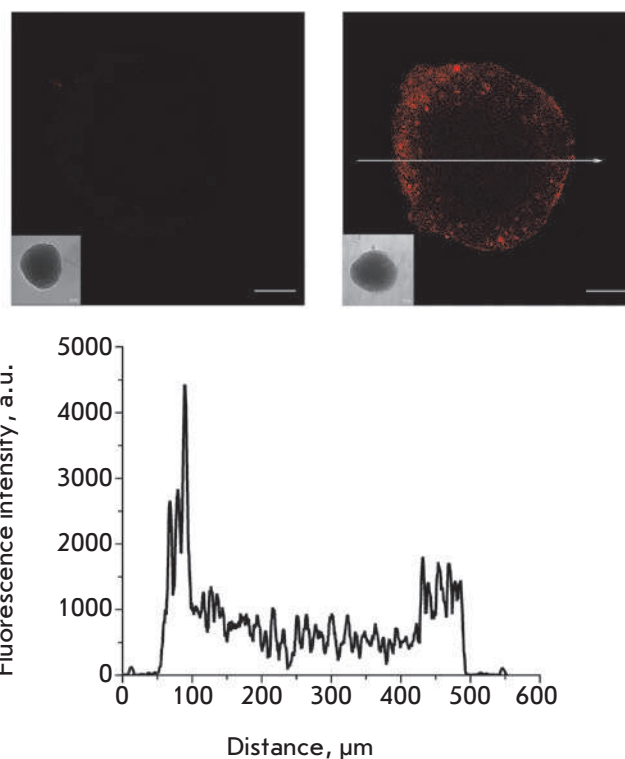


Fig. 6. Confocal images of an unstained SKBR-3 spheroid (*left*) and SKBR-3 spheroid stained for 2 h with 4D5scFv-PE40 conjugated with a DyLight650 fluorescent dye (*right*). Bar, 100 μ m. The insets show wide-field microscopy images of the same spheroids. Bottom: the fluorescence signal profile along the arrow shown in the right-hand side image.

covered that after incubation for 2 h, the 4D5scFv-PE40 immunotoxin labeled with the fluorescent dye had penetrated to a depth of about 80–100 μ m (into a spheroid 400–500 μ m in diameter), which corresponds to several surface cellular layers (Fig. 6). These results

are consistent with the data on the penetration of antibody Fab-fragments with a size lying in the same range (about 50 kDa) into the spheroids of human colon cancer [29].

CONCLUSION

Thus, the significant difference between the severity of the toxic effect of the 4D5scFv-PE40 immunotoxin on spheroids and on a monolayer of SKBR-3 cells can largely be attributed to its inefficient penetration into the depth of the spheroid and to its predominant impact on the cells of the outer layers. In this case, the use of spheroids consisting of tumor cells only enables an evaluation of the direct influence of cell-cell contacts on the test drug efficiency. In this regard, we believe that the obtained tumor spheroid model can be successfully used to study ways to improve the efficiency

of accumulation of anticancer agents in a tumor via the simultaneous influence on cell-cell contacts. This is of particular interest for designing and testing HER2-specific agents, since the HER2 receptor is usually hidden under cell adhesion proteins and may be unavailable for binding by the targeted agent [30, 31]. Such influence is possible for proteins that target intercellular tight junctions [32]. This approach was proposed several years ago and has proved to be effective when full-length therapeutic antibodies are used and appears to be of interest for the development of targeted cancer therapy.

This work was supported by the Ministry of Education and Science of the Russian Federation (project № 14.578.21.0051, unique identifier RFMEFI57814X0051).

REFERENCES

- Minchinton A.I., Tannock I.F. // *Nat. Rev. Cancer*. 2006. V. 6. № 8. P. 583–592.
- Antoni D., Burckel H., Josset E., Noel G. // *Int. J. Mol. Sci*. 2015. V. 16. №3. P. 5517–5527.
- Weiswald L.B., Bellet D., Dangles-Marie V. // *Neoplasia*. 2015. V. 17. № 1. P. 1–15.
- Deyev S.M., Lebedenko E.N., Petrovskaya L.E., Dolgikh D.A., Gabibov A.G., Kirpichnikov M.P. // *Russ. Chem. Rev.* 2015. V. 84. P. 1–26.
- Hynes N.E., Gerber H.A., Saurer S., Groner B. // *J. Cell Biochem*. 1989. V. 39. № 2. P. 167–173.
- Sokolova E.A., Zdobnova T.A., Stremovskiy O.A., Balalaeva I.V., Deyev S.M. // *Biochemistry (Mosc)*. 2014. V. 79. № 12. P. 1376–1381.
- Mosmann T. // *J. Immunol. Meth.* 1983. V. 65. № 1–2. P. 55–63.
- Glinsky V.V., Huflejt M.E., Glinsky G.V., Deutscher S.L., Quinn T.P. // *Cancer Res*. 2000. V. 60, № 10. P. 2584–2588.
- Ivascu A., Kubbies M. // *Int. J. Oncol*. 2007. V. 31. № 6. P. 1403–1413.
- Froehlich K., Haeger J.D., Heger J., Pastuschek J., Photini S.M., Yan Y., Lupp A., Pfarrer C., Mrowka R., Schleussner E., Markert U.R., Schmidt A. // *J. Mammary Gland Biol. Neoplasia*. 2016. V. 21. № 3–4. P. 89–98.
- Akasov R., Haq S., Haxho F., Samuel V., Burov S.V., Markvicheva E., Neufeld R.J., Szewczuk M.R. // *Oncotarget*. 2016. V. 7, № 40. P. 66119–66134.
- Debnath J., Brugge J.S. // *Nat. Rev. Cancer*. 2005. V. 5. № 9. P. 675–688.
- Hjelstuen M.H., Rasch-Halvorsen K., Brekken C., Bruland O., de L.D.C. // *Acta Oncol*. 1996. V. 35. № 3. P. 273–279.
- Lin R.Z., Chang H.Y. // *Biotechnol. J*. 2008. V. 3. № 9–10. P. 1172–1184.
- Polanovski O.L., Lebedenko E.N., Deyev S.M. // *Biochemistry*. 2012. V. 77. № 3. P. 227–245.
- Harari D., Yarden Y. // *Oncogene*. 2000. V. 19. № 53. P. 6102–6114.
- Yan M., Parker B.A., Schwab R., Kurzrock R. // *Cancer Treat Rev*. 2014. V. 40. № 6. P. 770–780.
- Kreitman R.J. // *Aaps J*. 2006. V. 8. № 3. P. E532–551.
- Mueller S., Cadenas E., Schonthal A.H. // *Cancer Res*. 2000. V. 60. № 1. P. 156–163.
- Xiang X., Phung Y., Feng M., Nagashima K., Zhang J., Broaddus V.C., Hassan R., Fitzgerald D., Ho M. // *PLoS One*. 2011. V. 6. № 1. P. e14640.
- Weldon J.E., Pastan I. // *FEBS J*. 2011. V. 278. № 23. P. 4683–4700.
- Sokolova E.A., Stremovskiy O.A., Zdobnova T.A., Balalaeva I.V., Deyev S.M. // *Acta Naturae*. 2015. V. 7. № 4. P. 93–96.
- Niero E.L., Rocha-Sales B., Lauand C., Cortez B.A., de Souza M.M., Rezende-Teixeira P., Urabayashi M.S., Martins A.A., Neves J.H., Machado-Santelli G.M. // *J. Exp. Clin. Cancer Res*. 2014. V. 33. P. 37.
- Fong E.L., Harrington D.A., Farach-Carson M.C., Yu H. // *Biomaterials*. 2016. V. 108. P. 197–213.
- Zdobnova T., Sokolova E., Stremovskiy O., Karpenko D., Telford W., Turchin I., Balalaeva I., Deyev S. // *Oncotarget*. 2015. V. 6. № 31. P. 30919–30928.
- Weldon J.E., Xiang L., Zhang J., Beers R., Walker D.A., Onda M., Hassan R., Pastan I. // *Mol. Cancer Ther*. 2013. V. 12. № 1. P. 48–57.
- Zielinski R., Lyakhov I., Hassan M., Kuban M., Shaffer-Weaver K., Gandjbakhche A., Capala J. // *Clin. Cancer Res*. 2011. V. 17. № 15. P. 5071–5081.
- Cao Y., Marks J.W., Liu Z., Cheung L.H., Hittelman W.N., Rosenblum M.G. // *Oncogene*. 2014. V. 33. № 4. P. 429–439.
- Sutherland R., Buchegger F., Schreyer M., Vacca A., Mach J.P. // *Cancer Res*. 1987. V. 47. № 6. P. 1627–1633.
- Choi I.K., Strauss R., Richter M., Yun C.O., Lieber A. // *Front. Oncol*. 2013. V. 3. P. 193.
- Beyer I., van Rensburg R., Lieber A. // *Tissue Barriers*. 2013. V. 1. № 1. P. e23647.
- Beyer I., van Rensburg R., Strauss R., Li Z., Wang H., Persson J., Yumul R., Feng Q., Song H., Bartek J., Fender P., Lieber A. // *Cancer Res*. 2011. V. 71. № 22. P. 7080–7090.

Building a Full-Atom Model of L,D-transpeptidase 2 from *Mycobacterium tuberculosis* for Screening New Inhibitors

S.M. Baldin^{1,2}, N.M. Misiura³, V.K. Švedas^{1,3*}

¹Belozersky Institute of Physicochemical Biology, Lomonosov Moscow State University, Leninskie gory 1, bldg. 40, Moscow, 119991, Russia

²Faculty of Chemistry, Lomonosov Moscow State University, Leninskie gory 1, bldg. 3, Moscow, 119991, Russia

³Faculty of Bioengineering and Bioinformatics, Lomonosov Moscow State University, Leninskie gory 1, bldg. 73, Moscow, 119991, Russia

*E-mail: vyfas@belozersky.msu.ru

Received September 03, 2016; in final form, November 15, 2016

Copyright © 2017 Park-media, Ltd. This is an open access article distributed under the Creative Commons Attribution License, which permits unrestricted use, distribution, and reproduction in any medium, provided the original work is properly cited.

ABSTRACT L,D-transpeptidase 2 from *Mycobacterium tuberculosis* plays a key role in the formation of the cell wall of a pathogen and catalyzes the cross-linking of growing peptidoglycan chains by non-classical 3-3 bonds, which causes resistance to a broad spectrum of penicillins. Molecular modeling of enzyme interactions with the N- and C-terminal tetrapeptide fragments of growing peptidoglycan chains has been performed for the first time and has allowed us to highlight the peculiarities of their binding at the formation of 3-3 cross-linkages, as well as to build a full-atom model of L,D-transpeptidase 2 for the screening and optimizing of inhibitors' structures.

KEYWORDS L,D-transpeptidase, *Mycobacterium tuberculosis*, catalytic mechanism, molecular docking, molecular dynamics simulations, inhibitors.

ABBREVIATIONS Ac – acetyl, WHO – World Health Organization, Ldt – L,D-transpeptidase, LdtMt1 and LdtMt2 – L,D-transpeptidase 1 & 2 from *Mycobacterium tuberculosis*, m-DAP – meso-diaminopimelic acid, IG – immunoglobulin, MD – molecular dynamics, PME – Particle Mesh Ewald

INTRODUCTION

The danger posed by tuberculosis continues to grow with the appearance of new multidrug-resistant strains of *M. tuberculosis*. According to the WHO report of 2015, approximately 10.4 million people contracted tuberculosis and 1.8 million people died from it [1]. There is an obvious need for new anti-TB drugs, as well as medical treatment technologies, not to mention the design of more effective antibiotics to suppress the infection. That is why new, heretofore unknown, molecular targets that are associated with the functioning and structural organization of the causative agents of tuberculosis are of particular interest.

One of the essential distinctive features of *Mycobacterium tuberculosis* is the structure of its cell wall. In most bacteria, a cell wall contains classical 4-3 cross-linkages of peptidoglycan chains (bonds between the meso-diaminopimelic acid (m-DAP) residue and D-Ala). At the same time, the cell wall of *M. tuberculosis* for the most part originates from the formation of non-classical 3-3 cross-linkages (up to approximately 80% of all bonds between m-DAP residues of different

peptidoglycan chains in the stationary phase). Once this was discovered, it became clear why β -lactam antibiotics capable of inactivating penicillin-binding enzymes such as D,D-transpeptidases that catalyze the formation of classical 4-3 cross-linkages [2] are ineffective in the treatment of tuberculosis. It was recently established that the formation of non-classical 3-3 cross-linkages is catalyzed by the earlier unknown enzymes L,D-transpeptidases (*Fig. 1*).

The genome of *M. tuberculosis* encodes five proteins which contain L,D-transpeptidase domains (sites Rv0116c, Rv0192, Rv0483, Rv1433 and Rv2518c) [5]. Rv2518c, which codes LdtMt2, is the most abundantly expressed gene. Loss of this gene leads to changes in colony morphology, suppresses the growth of bacteria, and increases sensitivity to classical antibiotics (amoxicillin used in combination with clavulanic acid) [3].

LdtMt2 is a lipoprotein that consists of 408 amino acid residues; its N-terminal region is located in a lipid bilayer. The polypeptide chain contains a short region exposed inside the cell, a transmembrane region, and

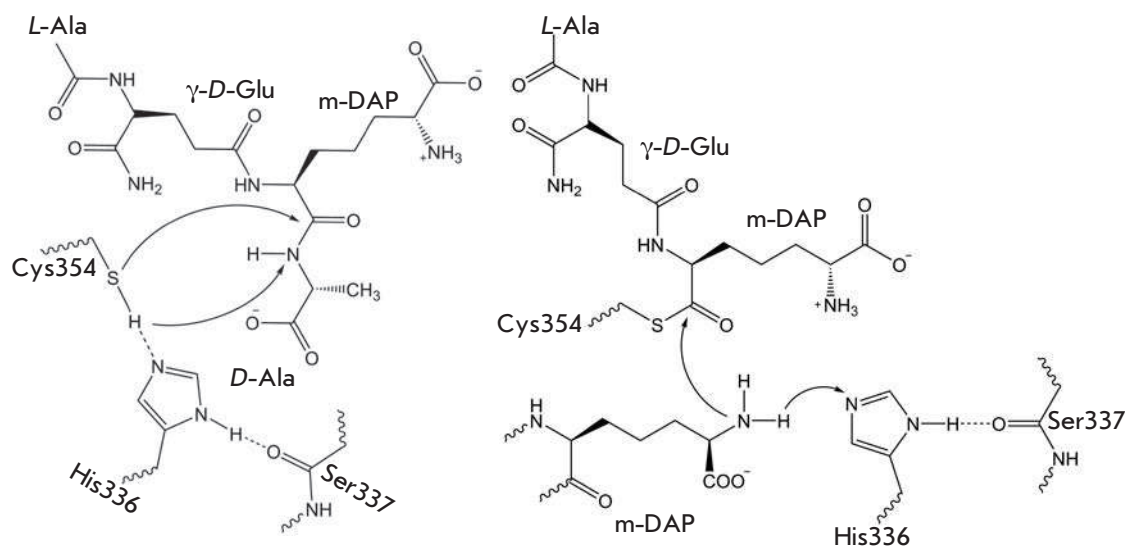


Fig. 1. Catalytic mechanism of the LdtMt2 is shown with the tripeptide analog of the natural substrate. Formation of the acyl enzyme is presented in the left part, the subsequent acyl transfer to the nucleophile and the formation of 3-3 cross-linkage of peptidoglycan is presented in the right part of the figure

a region exposed outside the membrane. The outside region can be divided into 3 domains: domains A and B, which are non-catalytic IG-like domains (comprising residues 55-146 and 149-250, respectively), and the C-terminal catalytic domain C (residues from 251 to 408) [6]. Residues Cys354, His336, and Ser337 play a key role in the catalysis and constitute a catalytic triad [6]. The active site of LdtMt2 is isolated from the solvent and hidden under the so-called active site lid (residues Tyr298-Trp324) that forms 3 tunnels, A, B & C, the last two being involved in a process of substrate delivery to the active site [7]. This element of secondary structure represents an antiparallel β -sheet with a disordered loop. Access of the substrate and solvent to the active site is limited by bulky Tyr308 and Tyr318 residues, which are part of the lid, as well as the Tyr330, Phe334, and Trp340 residues that are located at the entrance to the active site.

The full-atom structure of LdtMt2 remains unknown. However, the structures of the domains A&B and B&C (PDB, 4HU2 & 4HUC, respectively) are available [6]. Furthermore, the structures of the catalytic domain with the dipeptide fragment N- γ -D-glutamyl-m-DAP of peptidoglycan (PDB 3TUR) [5], as well as the covalent complexes of LdtMt2 with meropenem and LdtMt1 with imipenem, have been reported [7, 8]. Confusingly, there is a discrepancy between the presented structures: molecules of the same class of inhibitors (meropenem and imipenem) are located in different tunnels despite the high homology of the catalytic L,D-transpeptidase domains in LdtMt1 and LdtMt2 (Fig. 2).

Important information concerning the catalytic mechanism of LdtMt2 was obtained during QM/MM-modeling of the enzymatic reaction with the

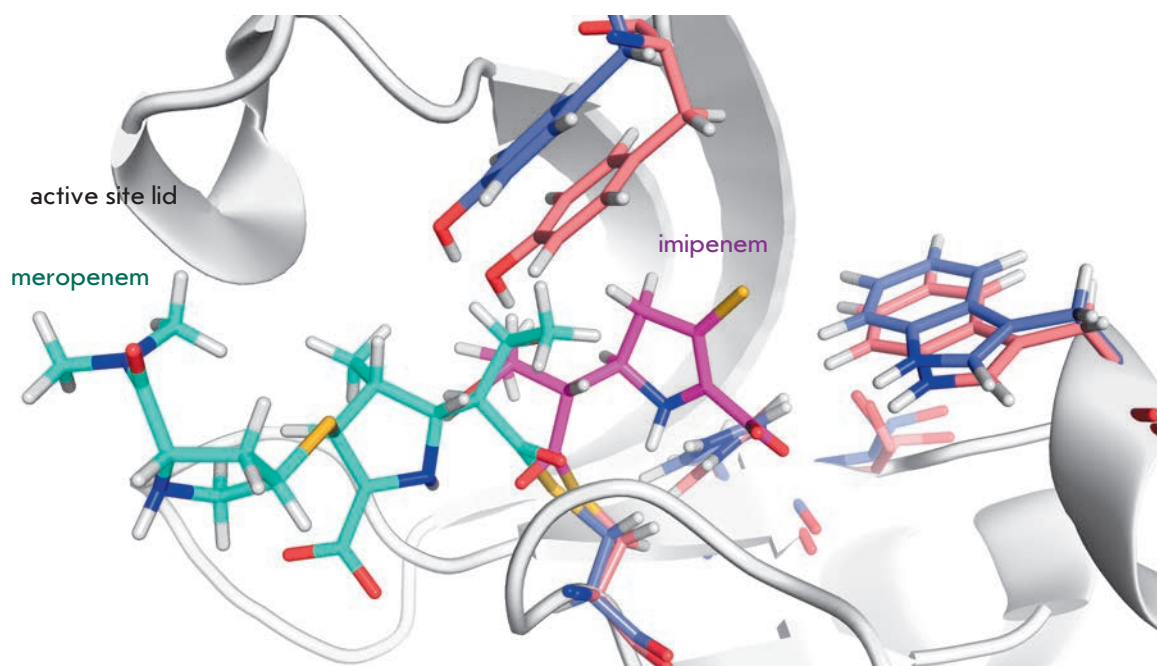
tripeptide fragment N- γ -D-Glu-m-DAP-D-Ala of peptidoglycan [9]. The authors identified the energy profiles for two reaction stages: the formation of the acyl enzyme and the consequent acyl (L-center of the first m-DAP residue) transfer to the nucleophile (D-center of the second m-DAP residue) that leads to the cross-linking of peptidoglycan chains (Fig. 1). Molecular modeling techniques may help identify the structural peculiarities in the active site organization of L,D-transpeptidases, their interaction with substrates, and facilitate the search for inhibitors. In order to achieve this, it is necessary to be in possession of adequate molecular models of the enzyme that can be used to screen libraries of potential inhibitors. The goal of this work was to perform a molecular modeling of enzyme binding with the tetrapeptide fragment of peptidoglycan, as well as with β -lactam compounds, and to build a full-atom model of LdtMt2 for the screening and optimization of inhibitors' structures.

EXPERIMENTAL SECTION

Software

Calculation of the ionization states of amino acid residues was performed by PROPKA 3.0 [10]. The starting structure preparation and trajectory analysis were performed using the AmberTools 16 program package, and energy minimization and molecular dynamics were calculated in Amber 14 [11]. Molecular docking was performed with AutoDock 4 [12]. The structures of the inhibitors and substrate fragment were built using ACD/ChemSketch (<http://www.acdlabs.com>). Geometry optimization and calculation of partial atomic charges were carried out with PC GAMESS/Firefly 8.1 [13] and the resp module of AmberTools 16, respective-

Fig. 2. Structural alignment of the enzyme-inhibitor complexes LdtMt2-meropenem (4GSU) and LdtMt1-imipenem (4JMX) demonstrates that residues of meropenem (blue) and imipenem (pink) are located in different tunnels



ly. Visualization and structure editing of enzyme-substrate complexes were performed by VMD 1.9.2 [14] and PyMol 1.8 [15]. Computation of molecular dynamics trajectories was performed using the MSU supercomputer “Lomonosov” [16].

Structure preparation

Two crystallographic structures were selected as starting models of the enzyme and enzyme-substrate complex: 4HU2 [6], which contains coordinates of the non-catalytic domains A and B; 3TUR [5], which contains coordinates of the catalytic domain C, as well as the non-catalytic domain B and the dipeptide fragment of peptidoglycan of the *M. tuberculosis* cell wall (γ -D-Glu-m-DAP). A full-atom model of the LdtMt2-substrate complex was built according to the following procedure: two structures were aligned via domain B and the chains were connected to form a three-domain structure of LdtMt2, then the missing amino acid residues D-Ala and L-Ala in a peptidoglycan fragment were added to the substrate's structure, and the N-acetyl group was attached to the L-Ala residue in order to neutralize the charge of the N-terminal amino group. Partial atom charges were determined as follows: the initial geometry of each amino acid residue was optimized at the MP2/6-31G* level of theory, then the electrostatic potential was calculated according to HF/6-31G*. The resulting structure of the enzyme-substrate complex was placed in a TIP3P water cell with a minimum distance of 10 Å from the edge of the cell. Calculation of molecular dynamics trajectories was performed with AMBER ff14SB [17]. The con-

stants of the force field for the substrate's bonds and angles were obtained from ff14SB and other missing parameters, from GAFF.

Energy minimization and molecular dynamics

Models of the enzyme and enzyme-substrate complex were equilibrated, and molecular dynamics' trajectories were calculated according to the following protocol: first, two steps of the energy minimization of the system were performed. The energy of the solvent residues was minimized by the steepest descent algorithm (2,000 steps), followed by a conjugate gradient algorithm (2,000 steps). Afterwards, the system was heated up at a constant volume from 0 to 310K over 50 ps and then equilibrated over 1,000 ps under constant pressure. The integration step was 0.002 ps. All simulations were performed using periodic boundaries and the Particle Mesh Ewald method (PME) to account for long-range Coulomb interactions. The radius of the cut-off disconnected Coulomb interactions was 8 Å.

Molecular docking

The LdtMt2 model to perform the molecular docking of different β -lactam compounds was prepared as follows: water molecules, sodium ions, and the substrate (fragment of peptidoglycan) were removed from the solvated structure of the enzyme-substrate complex taken from the molecular dynamics trajectories after energy minimization. Then, a map of potential interactions was calculated around the active site and the β -lactam inhibitors were docked using the Lamarckian genetic algorithm. A series of 50 to 100 independent

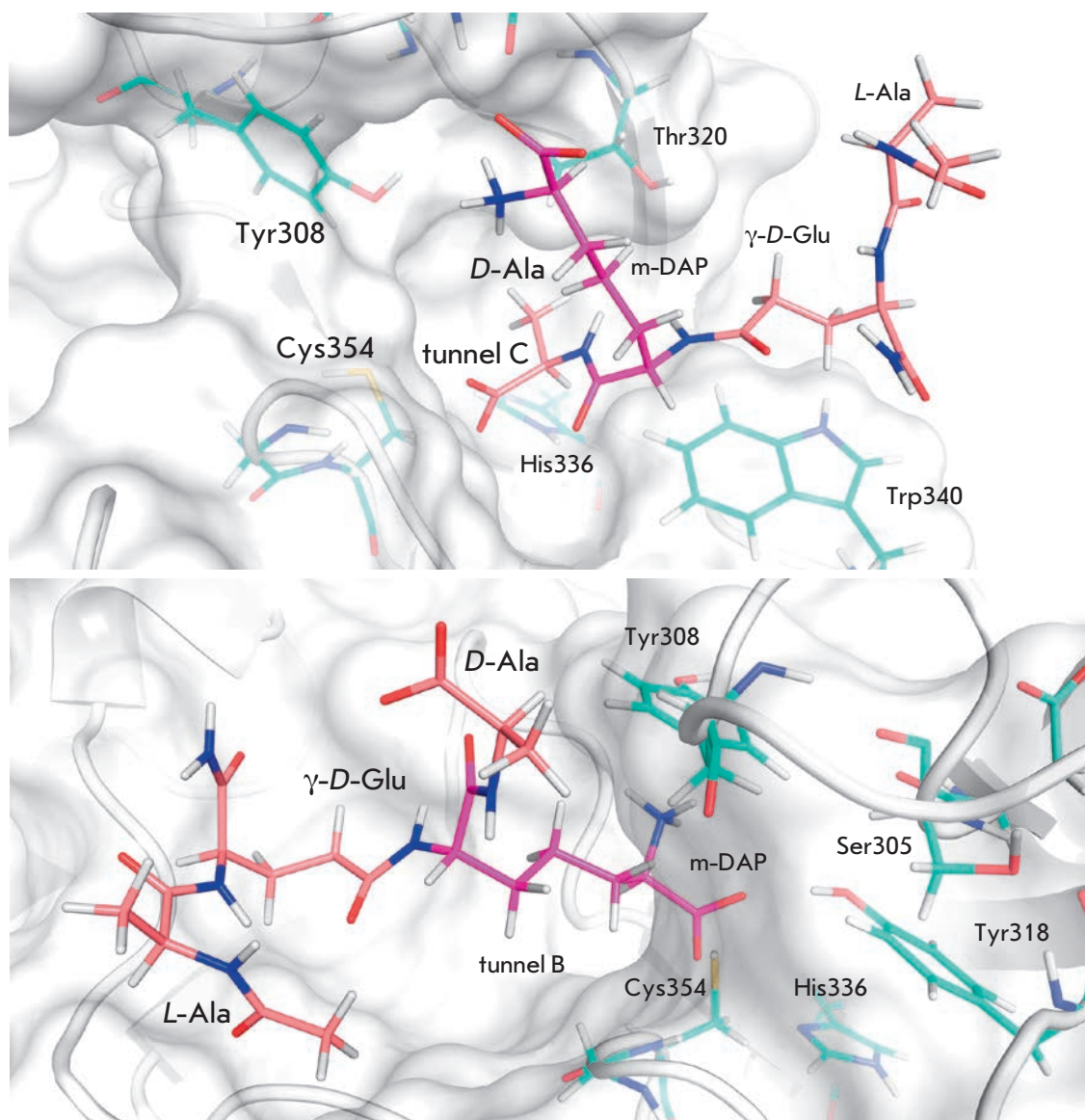


Fig.3. Interaction of the tetrapeptide fragment of peptidoglycan with the LdtMt2 active site residues at substrate binding in tunnel C (upper panel) and the tunnel B (lower panel)

docking runs was performed for each compound. The resulting enzyme-inhibitor complexes were clustered, and the peculiarities of the structural organization of the enzyme-inhibitor complexes in each cluster were analyzed. We considered the following indicators as a criterion of productive binding of an inhibitor in the enzyme active site that leads to a reactive enzyme-inhibitor complex and then the formation of a stable acyl enzyme:

1. The formation of hydrogen bonds between the inhibitor and the enzyme in the oxyanion hole (formation of hydrogen bonds between the N-atoms of the main chain formed by the residues Gly353 and Cys354 with the carbonyl oxygen of the β -lactam ring);
2. The distance between the attacking sulfur atom S^γ of catalytic cysteine Cys354 and the C atom of

the carbonyl group of the β -lactam ring does not exceed 5 Å.

RESULTS AND DISCUSSION

Molecular modeling of peptidoglycan binding in alternative site of LdtMt2

The difficulty in determining substrate localization in the L,D-transpeptidase active site is further compounded by the fact that binding of two molecules of the same compound should be considered. One molecule should bind as the acyl donor, which further leads to the formation of an acyl enzyme intermediate, whereas the other one should bind as a nucleophile, which leads to the formation of the acyl enzyme-nucleophile complex, followed by the acyl group trans-

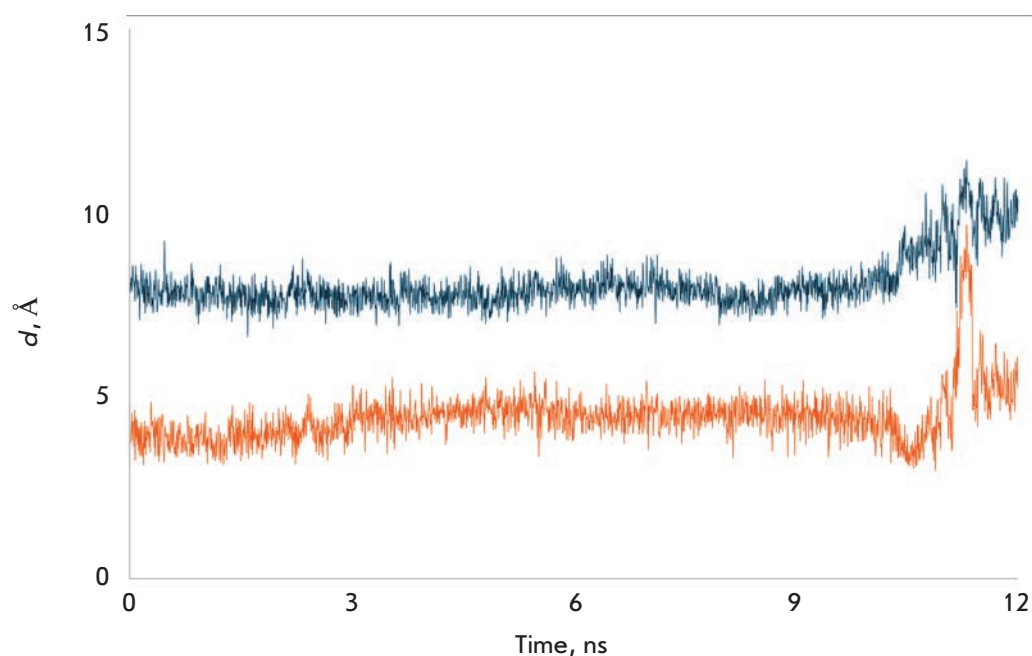


Fig.4. MD simulation of the tetrapeptide binding in the tunnel C of LdtMt2. Characteristic distances between the S^{γ} atom of Cys354 and the C atom of the carbonyl group of the peptide m-DAP-D-Ala (orange line), and the N-atom of the D-center of m-DAP (blue line)

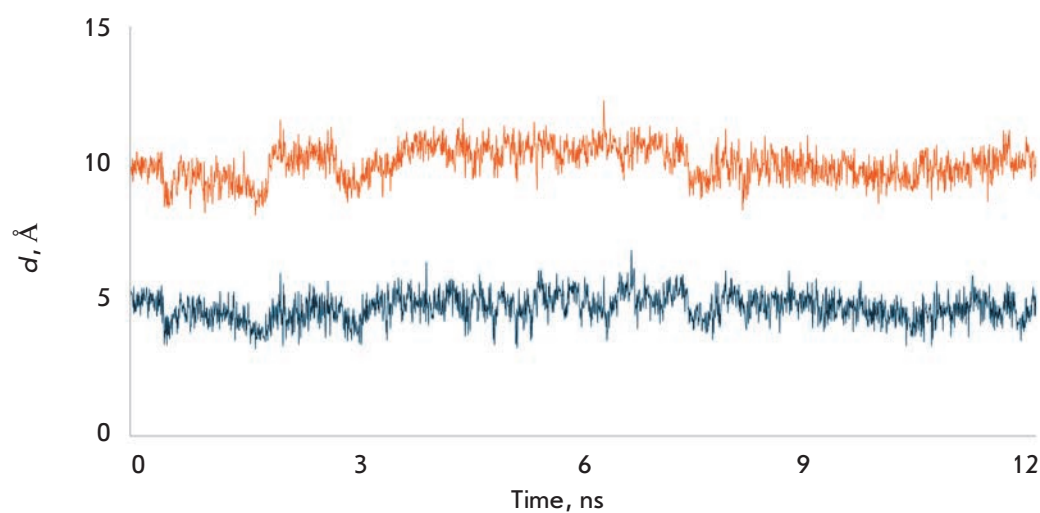


Fig.5. MD simulation of the tetrapeptide binding in the tunnel B of LdtMt2. Characteristic distances between the S^{γ} atom of Cys354 and the C atom of the carbonyl group of the peptide m-DAP-D-Ala (orange line), and the N-atom of the D-center of m-DAP (blue line)

fer to the nucleophile and 3-3 cross-linking of peptidoglycan of the cell wall. The discrepancy in earlier published results concerning the localization of substrate-like inhibitors in the active site of LdtMt2 and LdtMt1 can result from insufficient attention paid to the opportunities of two different ways of binding of the natural substrate. In order to search for an optimal structure of the covalent LdtMt2 inhibitors (such, for example, as β -lactam compounds carbapenems), it is necessary to proceed with an adequate structure of the enzyme-substrate complex, where the substrate molecule occupies the position of the acyl donor capable of forming the acyl enzyme. Models of alternative binding of the tetrapeptide fragment (N-Ac-L-Ala- γ -D-Glu-m-DAP-D-Ala) of the natural substrate in the LdtMt2

active site were built on the basis of the 3TUR structure, and molecular dynamics was applied to discriminate between two different ways of substrate binding in the active site. In the first model, the tetrapeptide N-Ac-L-Ala- γ -D-Glu-m-DAP-D-Ala was placed in tunnel C, whereas in the alternative model the tetrapeptide was located in tunnel B (Fig. 3).

At binding of the peptidoglycan fragment in tunnel B, the substrate hydrogen bonds are formed with the residues His352, Ser331, Tyr308 and Tyr318. In the model of the enzyme-substrate complex with the substrate positioned in tunnel C, labile hydrogen bonds form with the residues Asn356, Trp340, His352, and Tyr318, similarly to the binding of the shorter tripeptide analog of the natural peptidoglycan [9].

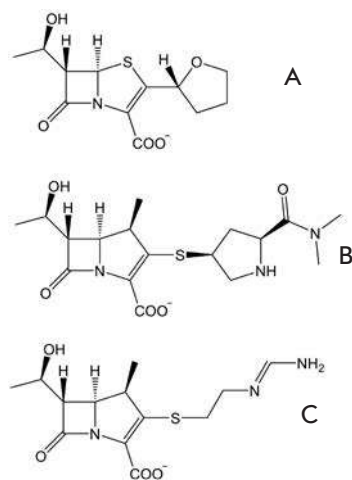


Fig. 6. Structures of β -lactam antibiotics that were docked in the active site of LdtMt2. [A] - faropenem, [B] - meropenem, [C] - imipenem

Our simulations show that the L-Ala residue in a tetrapeptide fragment of peptidoglycan does not play a key role in the substrate binding in both (B and C) tunnels, and it is exposed to the solvent most of the time during MD trajectories. However, it is capable of forming short-lived hydrogen bonds with the N- and O-atoms of a backbone formed by the residues Arg319 and Thr320. This fact allows us to suggest that the residues of N-acetylglucosamine and N-acetylmuramic acid next to L-Ala in a peptidoglycan structure do not participate (or play a minor role) in the recognition of the acyl donor by the enzyme.

At binding of the substrate in tunnel C, a reactive enzyme-substrate complex is formed: the S^{γ} -atom of the catalytic Cys354 residue is at a distance (3.5–5.7 Å) favorable for a nucleophilic attack of the C atom of the carbonyl group of the peptide bond m-DAP-D-Ala during the whole MD trajectory (Fig. 4, orange line). It should be noted that in a model of the enzyme-substrate complex when the peptidoglycan fragment is located in tunnel B, the substrate is positioned differently and is incapable of forming an acyl enzyme. The distance between the S^{γ} -atom of the catalytic Cys354 residue and the C atom of the carbonyl group of the peptide bond m-DAP-D-Ala during the whole MD trajectory (Fig. 5, orange line) varies in the range 8.1–12.3 Å, which excludes the possibility of this substrate molecule playing the role of acyl donor. At the same time, the orientation of the substrate molecule in tunnel B well corresponds to the role of the nucleophile at the formation of the 3-3 cross-linkage: the distance between the N-atom of the free amino group of m-DAP and the S^{γ} -atom of catalytic Cys354 is in the range 3.2–6.8 Å (Fig. 5, blue line). Simulations have shown that an alternative role for each substrate molecule

is impossible: the tetrapeptide positioned in tunnel C cannot serve as the nucleophile (Fig. 4, blue line), and the tetrapeptide bound in tunnel B cannot play the role of an acyl donor (Fig. 5, orange line). Establishment of this fact is important both for understanding the full catalytic cycle of the enzyme, and for searching for its inhibitors. Thus, at a structural optimization of β -lactam inhibitors capable of inactivating the enzyme due to the formation of a stable acyl enzyme, it is necessary to consider the binding of the inhibitor in tunnel C: i.e., in the location where binds the substrate molecule that plays the role of an acyl donor at the 3-3 cross-linking of the peptidoglycan chains.

Modeling of the interaction of LdtMt2 and β -lactam compounds

In two reported structures of acyl enzymes (4JMX formed at the inactivation of LdtMt1 by imipenem and 4GSU formed at the inactivation of LdtMt2 by meropenem), the residues of the inhibitors are located in different tunnels of the active site. The meropenem residue in the LdtMt2 active site is positioned at the entrance to tunnel B and mostly exposed to a solvent, whereas the thiazolidine ring of the imipenem residue in the active site of LdtMt1 is entirely immersed in tunnel C.

In this case, it is important to determine the primary location of the β -lactam ring in the active site, which could correspond to the reactive enzyme-inhibitor complex capable of forming the acyl enzyme. Based on the criteria of theoretical chemistry, the nucleophilic attack on the C atom of the carbonyl group of the β -lactam ring by the S^{γ} atom of the catalytic Cys354 residue of LdtMt2 may materialize only if the distance between these atoms is in the range 3.5–4.0 Å and if the carbonyl group of the β -lactam ring is located in the oxyanion hole. Basing on our molecular modeling results of enzyme binding with the tetrapeptide fragment of natural peptidoglycan, we performed the molecular docking of three β -lactam inhibitors known from the literature that were shown to form reactive enzyme-inhibitor complexes with LdtMt2 (Fig. 6). Like in the modeling of enzyme-substrate interactions, we considered the binding of inhibitors in both tunnel B and tunnel C.

At docking in tunnel B, we observed no formation of reactive enzyme complexes with any of the tested inhibitors: the distance between the S^{γ} atom of the catalytic Cys354 of LdtMt2 and the C atom of the carbonyl group of the β -lactam ring exceeded 5 Å. Binding in tunnel B also did not allow the carbonyl group of the β -lactam ring to form hydrogen bonds with the oxyanion hole residues (main chain N-atoms of Cys354 and Gly353). A typical example of the LdtMt2-meropenem complex is shown in Fig. 7 (left). Thus,

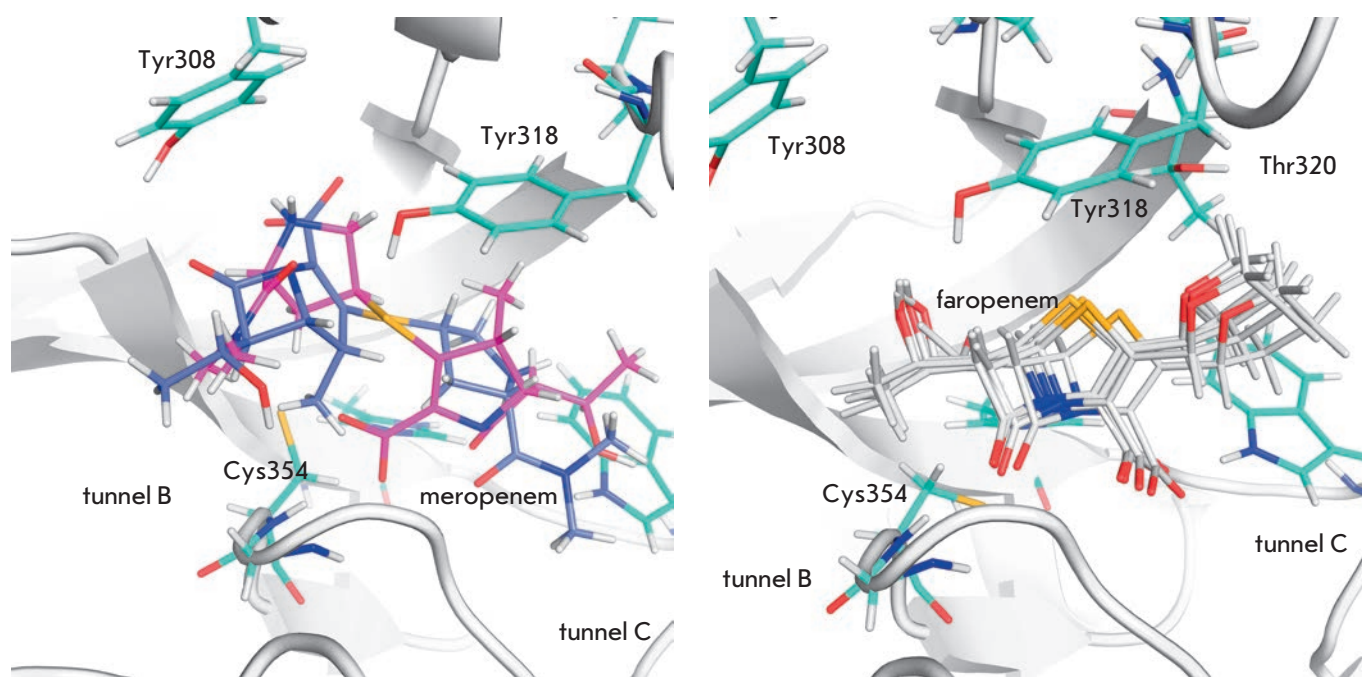


Fig.7. Localization of β -lactam antibiotics in the LdtMt2 active site at meropenem binding in the tunnel B (left panel) and faropenem binding in the tunnel C (right panel). In case of meropenem there is no accurate place for binding of the inhibitor and formation of the reactive enzyme-inhibitor complex, a distance between the S^{γ} -atom of the catalytic Cys354 and the C atom of the carbonyl group of β -lactam ring is not optimal for nucleophilic attack. At faropenem binding in the tunnel C (right panel) all docked structures form a single cluster that correspond to the reactive enzyme-inhibitor complex. The distance between the S^{γ} atom of the catalytic Cys354 and the C atom of the carbonyl group of β -lactam ring is optimal for nucleophilic attack and the carbonyl group of β -lactam ring can form hydrogen bonds with the oxyanion hole residues

we concluded that an inhibitor cannot form a reactive complex with the enzyme at binding in tunnel B.

CONCLUSIONS

The main goal of this work was to study binding of the tetrapeptide fragment of the natural substrate - cell wall peptidoglycan in the LdtMt2 active site and build a full-atom model of the enzyme-substrate complex which could allow one to search for new substrate-like irreversible inhibitors and to optimize their structure.

The conducted molecular dynamics simulations have shown that binding of the N- and C-terminal fragments of the growing peptidoglycan chain in different tunnels is responsible for the different steps of the catalytic mechanism at the formation of non-classical 3-3 cross-linkages in peptidoglycan. In order to simulate LdtMt2 interaction with β -lactam inhibitors capable of inactivating the enzyme through the formation of stable acyl enzymes, it is necessary to consider the binding of potential inhibitors in tunnel C of the active site.

REFERENCES

1. WHO. Global Tuberculosis Report; Geneva, 2016.
2. Fisher J.F., Meroueh S.O., Mobashery S. // *Chem. Rev.* 2005. V. 105. № 2. P. 395–424.
3. Gupta R., Lavollay M., Mainardi J., Arthur M., Bishai W., Lamichhane G. // *Nat. Med.* 2010. V. 16. № 4. P. 466–469.
4. Jankute M., Cox J.A., Harrison J., Besra G.S. // *Ann. Rev. Microbiol.* 2015. V. 69. P. 405–423.
5. Erdemli S., Gupta R., Bishai W.R., Lamichhane G., Amzel M., Bianchet M. // *Structure.* 2012. V. 20. № 12. P. 2103–2115.
6. Böhth D., Steiner E.M., Stadler D., Lindqvist Y., Schnell R., Schneider G. // *Acta Crystallogr. D Biol. Crystallogr.* 2013. V. 69. № 3. P. 432–441.
7. Kim H.S., Kim J., Im H.N., Yoon J.Y., An D.R., Yoon H.J., Kim J.Y., Min H.K., Kim S.J., Lee J.Y., et al. // *Acta Crystallogr. D Biol. Crystallogr.* 2013. V. 69. № 3. P. 420–431.
8. Correale S., Ruggiero A., Capparelli R., Pedone E., Berisio R. // *Acta Crystallogr. D Biol. Crystallogr.* 2013. V. 69. P. 1697–1706.
9. Silva J.R.A., Roitberg A.E., Alves C.N. // *J. Chem. Inf.*

- Model. 2014. V. 54. № 9. P. 2402–2410.
10. Li H., Robertson A.D., Jensen J.H. // *Proteins*. 2005. V. 61. № 4. P. 704–721.
11. Case D.A., Berryman J.T., Betz R.M., Cerutti D.S., Cheatham T.E., III, Darden T.A., Duke R.E., Giese T.J., Gohlke H., Goetz A.W., et al. // *AMBER 2015*, University of California, San Francisco, 2015.
12. Morris G.M., Huey R., Lindstrom W., Sanner M.F., Belew R.K., Goodsell D.S., Olson A.J. // *J. Comput. Chem.* 2009. V. 30. № 16. P. 2785–2791.
13. Granovsky A.A. Firefly version 8. <http://classic.chem.msu.su/gran/firefly/index.html>
14. Humphrey W., Dalke A., Schulten K. // *J. Mol. Graphics*. 1996. V. 14. P. 33–38.
15. The PyMOL Molecular Graphics System. Version 1.8 Schrödinger, LLC.
16. Voevodin V.V., Zhumatiy S., Sobolev S., Antonov A., Bryzgalov P., Nikitenko D., Stefanov K., Voevodin V. // *Open Systems J.* 2012. V. 7. P. 36–39.
17. Maier J.A., Martinez C., Kasavajhala K., Wickstrom L., Hauser K.E., Simmerling C. // *J. Chem. Theory Comput.* 2015. V. 11. № 8. P. 3696–3713.

Prolyl-glycyl-proline (PGP) Peptide Prevents an Increase in Vascular Permeability in Inflammation

N. S. Bondarenko¹, A. N. Shneiderman², A. A. Guseva³, B. A. Umarova³

¹Koltsov Institute of Developmental Biology, Vavilova str. 26, Moscow, 119334, Russia

²Institute of Carcinogenesis, Cancer Research Center of N.N. Blokhin, Kashirskoe sh. 24, Moscow, 115478, Russia

³Lomonosov Moscow State University, Leninskie Gory 1, Moscow, 119991, Russia

*E-mail: n.s.bondarenko@gmail.com

Received January 25, 2016; in final form, November 28, 2016

Copyright © 2017 Park-media, Ltd. This is an open access article distributed under the Creative Commons Attribution License, which permits unrestricted use, distribution, and reproduction in any medium, provided the original work is properly cited.

ABSTRACT This study was aimed at investigating the effect of prolyl-glycyl-proline (PGP) tripeptide on vascular permeability in rats with an inflammation. It was found that the peptide reduces the rat paw edema induced by a subcutaneous administration of histamine to the same extent as the conventional anti-inflammatory agent diclofenac. However, an assessment of the relative expression level of the *cox-2* gene at the inflammation focus using real-time PCR showed that, in contrast to diclofenac, PGP does not affect the *cox-2* gene expression. This is indicative of the fact that they have different mechanisms of action. We used the model of acute peritonitis induced by an intraperitoneal injection of thioglycolate to demonstrate that the inflammatory response of an organism is accompanied by increased vascular permeability in the tissues of the stomach and small intestine. Pre-administration (30 minutes before the induction of the inflammation) of PGP prevented this increase, whereby the level of vascular permeability, exudate volume in the peritoneal cavity, and the amount of the Evans Blue dye in this exudate remained at the control level. Therefore, these results suggest that the anti-inflammatory action of PGP is based on its ability to prevent an increase in vascular permeability.

KEYWORDS anti-inflammatory action, inflammation, prolyl-glycyl-proline (PGP), vascular permeability.

INTRODUCTION

Most pathological processes in the body are accompanied by the development of an inflammatory response. It is important to understand the role of endogenous regulatory systems in this process in order to restore the disturbed functions of the organism. Regulatory peptides that are formed in the inflammation focus as a result of a degradation of extracellular matrix proteins are of great interest. Prolyl-glycyl-proline (PGP) tripeptide, a typical representative of the glyprolines family, is one of such peptides [1]. To date, a wide range of properties attributed to this peptide that are indicative of its protective effect on the inflammation-related disorders of various body systems have been discovered. In particular, PGP and its metabolites have a protective and therapeutic effect on the gastric mucosa in ulcerogenesis of various etiologies [2] and reduce the number of neutrophils in the inflammation focus in rats with peritonitis induced by intraperitoneal injection of a 1% acetic acid solution [3]. In an experimental model of acute peritonitis (intraperitoneal injection of a 40% thioglycolate solution), we demonstrated that the peptide has a pronounced anti-inflammatory effect to a

certain degree mediated by mast cell stabilization [4, 5]. Mast cells are a source of many vasoactive mediators which increase vascular endothelial permeability [6], one of the first signs of an inflammatory response [7]. Based on this fact, we assumed that the PGP can affect the vascular permeability and, consequently, formation of edema in the inflammatory response. Our study focuses on an investigation of this issue.

EXPERIMENTAL

PGP peptide was synthesized at the Institute of Molecular Genetics, Russian Academy of Sciences, Moscow.

In this study, we used male albino rats weighing 180–220 g. The experiments complied with the ethical principles and regulations as recommended by the European Science Foundation (ESF) and the Declaration on the Humane Treatment of Animals.

A rat paw edema was induced by subcutaneous injection of 0.2 mg of histamine (Sigma, USA) in 0.1 ml of saline. The thickness and circumference of the paw was measured every hour for 4 hours.

Two hours after inflammation induction with histamine, the animals underwent excision of a tissue

sample from the inflammation focus under ether anesthesia; the sample was immediately placed into a RNAlater solution (Ambion).

RNA from the tissue samples was isolated using Tri-Reagent (Sigma, USA) according to the manufacturer's protocol.

Single-stranded cDNA was obtained by adding 80 pmol of random 9-mer primers to 2 µg of the pooled RNA pretreated with DNase I (Fermentas, USA) (1 unit of enzyme per 1 µg of RNA) and incubation for 5 min at 70°C. Then, 25 µl of RT-MIX (RT-Buf 10 × (Fermentas, USA)), 40 mM of dNTP, and 10 units of RNasin (Promega, USA) were added to the ice-cooled mixture and incubated for 5 min at 37°C. Further, 200 units of M-MuLV reverse transcriptase (Fermentas, USA) was added and reacted at 42°C for 1 hour. The reaction was stopped by heating the mixture at 70°C for 10 min. The sample was diluted to 200 µl with deionized water. Samples were stored at -20°C.

Real-time PCR was performed using an iCycler iQ5 thermocycler (BioRad Laboratories GmbH, Germany). cDNA was used as a PCR template. The reaction mixture contained 10 pmol of the 5'- and 3'-primers, 1.6 mM of MgCl₂, 0.25 mM of dNTP, 10 × amplification buffer with the intercalating fluorescent dye Eva Green (Synthol, Russia), and 1 unit of Taq-DNA polymerase (Synthol, Russia). The reaction mixture was pre-heated for 10 minutes at 95°C and then subjected to 40 cycles of denaturation (95°C), annealing (60°C), and polymerization (72°C), accompanied by an assessment of the amount of accumulated product using the fluorescence spectrum at the end of the elongation stage. Each reaction was performed in triplicates. We used the following primers:

cox-2 F-5'-CCATGTCAAACCGTGGTGAATG-3',
cox-2 R-5'-ATGGGAGTTGGGCAGTCATCAG-3',
gapdh RN F-5'-CTGACATGCCGCTGGAGAAA-3',
gapdh RN R-5'-TGGAAGAATGGGAGTTGCTGTTGA-3'.

The housekeeping gene *Gapdh* was used as a reference to adjust the amount of transcripts added to the reaction. The primers were selected using the VectorNTI program. The primer annealing temperature and the number of amplification cycles for each fragment were selected experimentally. Experimental results were processed, and the relative expression level was calculated using Bio-Rad iQ5 2.0 Standard Edition Opticaland and the REST 2005 software. The reaction efficiency coefficient was calculated using the LinReg-PCR program.

Acute experimental peritonitis was induced in the rats by intraperitoneal injection of a 40% thioglycolate solution (Fluka, Switzerland) at a dose of 4 g/kg, followed by measurement of the vascular permeability

in the stomach and small intestine. For this purpose, an Evans blue dye (Sigma, USA) was injected (50 mg/kg) into the jugular vein using a syringe. In 15 minutes, the animals were anesthetized, dissected, and fluid samples were collected. The animals were then transcardially perfused for 2–3 minutes with saline containing 20 units/ml heparin. The stomach and small intestine were isolated, fragmented, and weighed. The dye was extracted by soaking tissues in formamide (Scharlau Chemie SA) for 48 hours at 37°C. The samples were then centrifuged for 15 min at 2000 rpm. The amount of the dye was determined using a Multiscan EX spectrophotometer (Thermo Scientific) at $\lambda = 620$ nm and expressed in µg/g of tissue and in µg/ml of exudate.

The results were processed statistically using the non-parametric Mann-Whitney test in the STATISTICA 6 software. Threshold significance value was set to 0.05.

RESULTS AND DISCUSSION

In the first series of experiments, the animals were subcutaneously injected with 0.2 mg histamine in a paw at a volume of 100 microliters in order to induce the edema. The same paw was intramuscularly injected with PGP at a dose of 3.7 µmol/kg 30 min before the induction of the inflammation. Another group of experimental animals received diclofenac at a dose of 1 mg/kg (Hemopharm, Serbia). Control animals were injected with saline instead of peptide. The thickness and circumference of the paw were measured and expressed as a percentage with respect to the baseline (before drug administration). The results are shown in *Fig. 1*.

The thickness and circumference of the paw 30 minutes after administration of histamine increased on average by 20.5%. After pretreatment with peptide, paw swelling was significantly less pronounced. As early as in 1 hour, paw circumference decreased by 29.5% compared to the control; in 2 and 3 hours – by 38 and 47%, respectively. Two hours after induction of the inflammation, paw thickness was 38% lower than in the control; in 3 hours – 35% lower.

Thus, pre-treatment with PGP resulted in a reduced edema. This confirms the previously discovered anti-inflammatory effect of the peptide. When comparing the effects of PGP and NSAID diclofenac (*Fig. 1*), it was found that the peptide and diclofenac are characterized by a similar action. They both reduced the edema induced by histamine. This suggests a possible similarity in their mechanisms of action. It is known that diclofenac inhibits cyclooxygenase-2 (COX-2), one of the key enzymes in the chain of prostaglandin synthesis from arachidonic acid. For this reason, in the next series of experiments, we investigated the effect of PGP on the *cox-2* gene expression during an inflammation

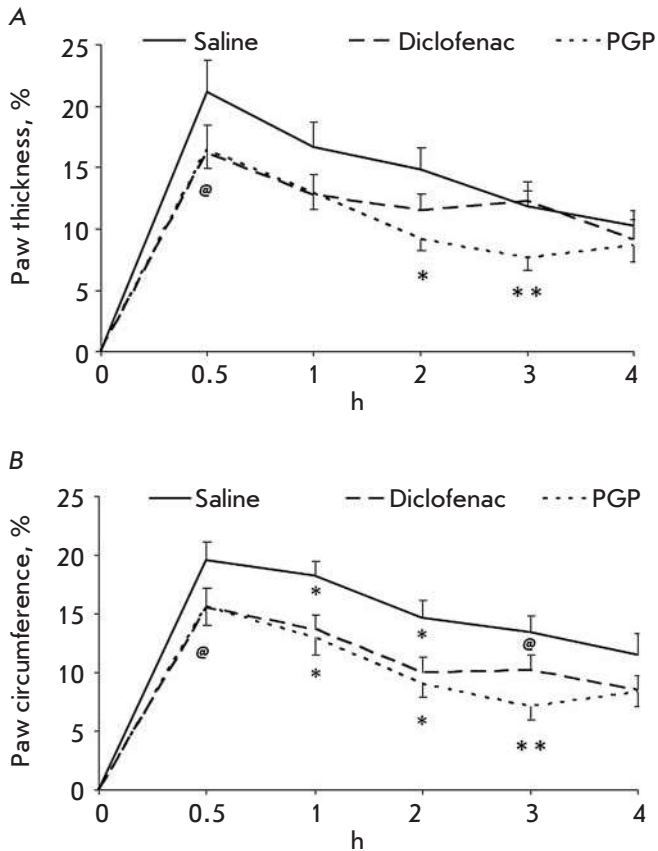


Fig. 1. The effect of PGP and diclofenac on the change in the thickness (A) and the circumference (B) of a rat paw in a histamine-induced inflammation. * – $p < 0.05$, ** – $p < 0.01$, @ – $p < 0.1$.

caused by subcutaneous administration of histamine in the paw. The results are shown in *Fig. 2*.

Subcutaneous injection of histamine resulted in an almost fivefold increase in *cox-2* gene expression 2 hours after the inflammation onset. Pretreatment with diclofenac decreased the level of expression of the investigated gene by 31%. However, injection of the peptide did not alter the level of gene expression and it remained the same as in the inflammation. This reflects differences in the antiedematous mechanisms of PGP and diclofenac.

Since the formation of an edema is caused by an increased permeability of the vascular endothelium, we evaluated the effect of PGP on the change in vascular permeability in the stomach and small intestine in rats with acute peritonitis.

The study group animals received an intramuscular injection of PGP at a dose of $3.7 \mu\text{mol/kg}$ 15 minutes before an intraperitoneal injection of thioglycolate. In the other group, the animals received saline instead of PGP. In the third group, the animals received saline

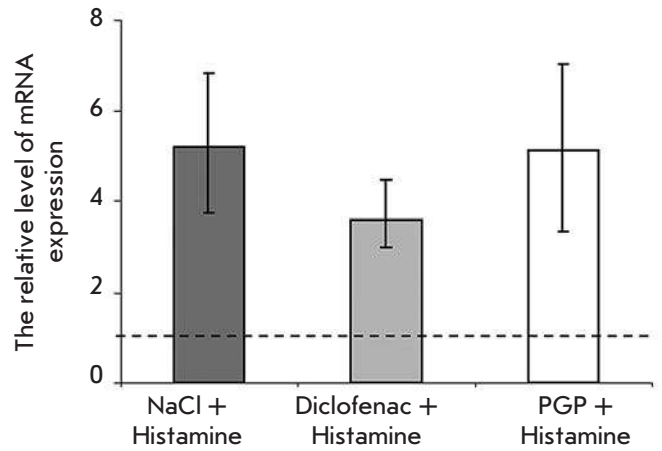


Fig. 2. The level of COX-2 mRNA expression. The dotted line shows the normal expression level.

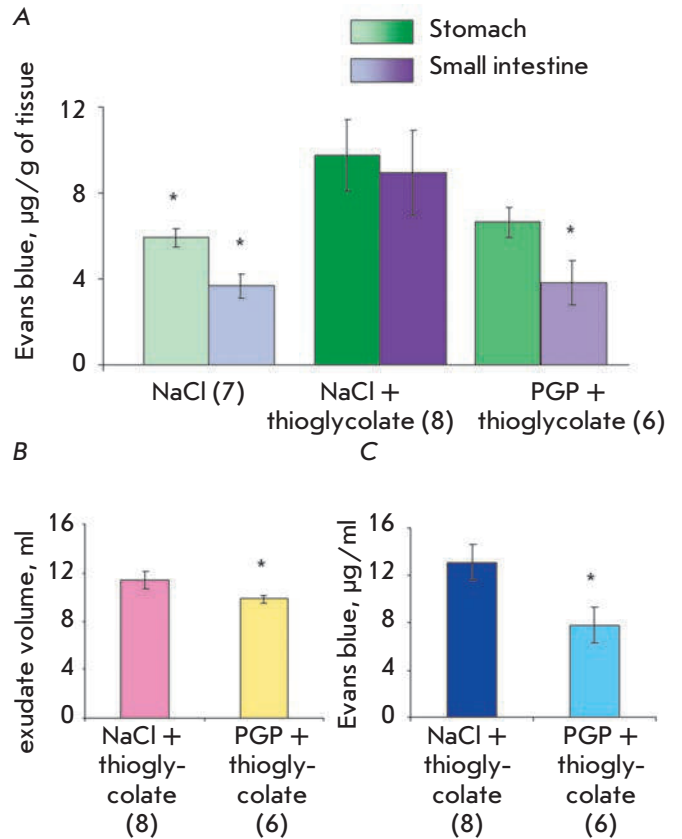


Fig. 3. Changes in the vascular permeability in the stomach and small intestine (A), peritoneal exudate volume (B), and the amount of Evans blue dye in the exudate (C) in rats with experimental acute peritonitis 30 minutes after thioglycolate administration. * – $p < 0.05$. The numbers in parentheses indicate the number of animals in each group.

without a subsequent induction of inflammation. The level of vascular permeability was assessed based on the amount of Evans blue dye in the exudate and tissue samples from the stomach and intestine.

The results are shown in *Fig. 3*. It is clear that the vascular permeability in the control (5.9 μg of dye per 1 g in the gastric tissue and 3.7 $\mu\text{g}/\text{g}$ in the intestinal tissue (*Fig. 3A*)) differs significantly from the vascular permeability during inflammation. Vascular permeability in the stomach increased on average by 66%, while in the intestines it increased 2.4-fold. Pre-administration of the peptide prevented an increase in vascular permeability in the stomach and intestines. Increased permeability after the administration of thioglycolate and the effect of peptide administration persisted for 2 hours.

Furthermore, the decrease in the vascular permeability is evidenced by the reduced amount of exudate in the peritoneal cavity by 14% and an almost two-fold lower amount of the dye in the exudate ($\mu\text{g}/\text{ml}$) (*Fig. 3B, C*).

Therefore, pre-administration of PGP prevents an increase in vascular permeability in the stomach and small intestine. The exudate volume and the amount of the dye in it also remain at the control level.

The ability of PGP to prevent an increase in the vascular endothelial permeability may be associated with both the direct action of the peptide on blood vessels [8] and its stabilizing effect on the mast cells [9], whose mediators are known to contribute much to the initiation and regulation of the vascular permeability. During our experiments, we found that the peptide cannot be considered as a conventional anti-inflammatory drug such as diclofenac, since, despite the formal similarity of the observed effects, the mechanisms of action are different.

The data on the participation of PGP in the regulation of the inflammatory process are contradictory.

On the one hand, the protective effect of glyprolines on various inflammation-related disorders was conclusively established. Thus, they not only have a protective effect on the gastric mucosa during the formation of ulcers, but also protect cells from oxidative stress and are involved in the regulation of the immune status of the organism [10].

On the other hand, PGP and its N-acetylated derivative (N-AcPGP) are chemoattractants for neutrophils [11]. This activity is mediated by an interaction with CXCR2 neutrophil receptors. These peptides attract neutrophils to the inflammation focus and thus prolong the process. However, CXCR2 receptors are ligand-selective, which can trigger signaling cascades both enhancing and limiting inflammation [12]. Furthermore, there is recent evidence showing that binding of N-AcPGP to the CXCR2 receptors of neutrophils, monocytes, and macrophages contributes to the therapeutic effect of this peptide in sepsis. It was found that administration of N-AcPGP to mice results in increased production of interferon- γ and IL-12, as well as an inhibition of the production of proinflammatory cytokines (TNF- α , IL-1 β , and IL-6) in the peritoneal fluid. N-AcPGP directly increased the *in-vitro* production of interferon- γ and decreased the lipopolysaccharide-stimulated production of TNF- α by murine spleen macrophages and human leukocytes [12]. These data indicate that the chemoattractant activity of the peptides does not preclude an ability to exhibit anti-inflammatory properties under certain conditions.

CONCLUSION

Our collection of data suggests that the anti-inflammatory action of the peptide is based on both a mast cell stabilization and its ability to prevent an increase in vascular permeability.

REFERENCES

- Ashmarin I.P., Karazeeva E.P., LA Lyapina L.A., Samonina G.E. // *Biochemistry (Mosc)*. 1998. V. 63. № 2. P. 119–124.
- Ashmarin I.P., Samonina G.E., Badmaeva K.E., Bakaeva Z.V., Vas'kovskii B.V., Zolotarev Iu.A. // *Uspekhi fiziologicheskikh nauk*. 2006. V. 37. № 2. P. 11–18.
- Bakaeva Z.V., Samonina G.E., Umarova B.A., Kopylova G.N., Goncharova E.L., Baglikova K.E. // *Cytokines and inflammation*. 2008. V. 7. № 2. P. 28–32.
- Umarova B.A., Lelekova T.V., Kopylova G.N., Samonina G.E., Bakaeva Z.V., Goncharova E.L., Bondarenko N.S. // *Cytokines and inflammation*. 2009. V. 8. № 3. P. 44–47.
- Umarova B.A., Bondarenko N.S., Kopylova G. N., Samonina G. E. // *Biochemistry (Moscow) supplement series A: membrane and cell biology*. 2011. V. 5. № 3. P. 237–241.
- Kumar P., Shen Q., Pivetti C.D., Lee E.S., Wu M.H., Yuan S.Y. // *Expert reviews in molecular medicine*. 2009. V. 11. P. e19.
- Kunder C.A., St John A.L., Abraham S.N. // *Blood*. 2011. V. 118. № 20. P. 5383–5393.
- Bakaeva Z.V., Badmaeva K.E., Sergeev I.Yu., Samonina G.E. // *Bulletin of experimental biology and medicine*. 2003. V. 135. № 4. P. 334–336.
- Bondarenko N.S., Kovalenko S.S., Kopylova G.N., Umarova B.A., Graevskaya E.E., Maksimov G.V. // *Biologicheskie Membrany*. 2013. V. 30. № 3. P. 199–205.
- Andreeva L.A., Mezentseva M.V., Nagaev I.Y., Shapoval I.M., Shcherbenko V.E., Potapova L.A., Russu L.I., Narovlyansky A.N., Ershov F.I., Myasoedov N.F. // *Doklady biological sciences*. 2010. V. 434. P. 300–303.
- Haddox J.L., Pfister R. R., Sommers C. I., Blalock J. E., Villain M. // *Investigative ophthalmology & visual science*. 1999. V. 40. № 10. P. 2427–2429.
- Kim S. D., Lee H. Y., Shim J. W., Kim H. J., Yoo Y. H., Park J. S., Bae, Y.-S. // *American journal of respiratory and critical care medicine*. 2011. V. 184. № 2. P. 243–251.

Intratumoral Morphological Heterogeneity of Breast Cancer As an Indicator of the Metastatic Potential and Tumor Chemosensitivity

T.S. Gerashchenko^{1,2}, M.V. Zavyalova^{1,2,3}, E.V. Denisov^{1,2*}, N.V. Krakhmal^{1,3}, D.N. Pautova², N.V. Litviakov^{1,2}, S.V. Vtorushin^{1,3}, N.V. Cherdyntseva^{1,2}, V.M. Perelmuter^{1,3}

¹Cancer Research Institute, Tomsk National Research Medical Center, Russian Academy of Sciences, Kooperativny per., 634050, Tomsk, Russia

²Tomsk State University, 36 Lenin Ave., Tomsk, 634050, Russia

³Siberian State Medical University, Moskovsky trakt 2, Tomsk, 634050, Russia

*E-mail: d_evgeniy@oncology.tomsk.ru

Received March 13, 2016; in final form, November 11, 2016

Copyright © 2017 Park-media, Ltd. This is an open access article distributed under the Creative Commons Attribution License, which permits unrestricted use, distribution, and reproduction in any medium, provided the original work is properly cited.

ABSTRACT Breast cancer (BC) demonstrates considerable intratumoral morphological heterogeneity. The aim of this work was to evaluate the relationship among different morphological structures, the rate of metastasis, and efficacy of neoadjuvant chemotherapy (NAC) in NAC-treated ($n = 427$) and NAC-naïve ($n = 249$) BC patients. We also studied the involvement of an epithelial-mesenchymal transition (EMT) in the development of the intratumoral morphological heterogeneity of BC. We found a significant association between the intratumoral morphological heterogeneity and the rate of BC metastasis and response to NAC, which, in most cases, correlated with the presence of alveolar and trabecular structures. In particular, the rate of lymph node metastasis in tumors containing alveolar and trabecular structures was higher compared to that in tumors lacking such structures. NAC-treated patients with alveolar and trabecular structures had a high distant metastasis rate and a low metastasis-free survival rate. Furthermore, alveolar and trabecular structures were found to be associated with a lack of response to NAC. Interestingly, the association between alveolar structures and a high distant metastasis rate was found only in NAC-unresponsive patients, whereas the association between trabecular structures and an increased distant metastasis was revealed in responders. Alveolar structures were associated with chemoresistance only in patients with lymph node metastases, whereas trabecular structures were associated with chemoresistance only in patients without lymph node metastases. In general, increased intratumoral morphological diversity correlated with considerable chemoresistance and a high metastasis rate of BC. We found variable expressions of epithelial (*EPCAM* and *CDH1*) and mesenchymal (*ITGA5*, *ITGB5*, *CDH2*, *CDH11*, *TGF β 2*, *ZEB1*, *MMP2*, *DCN*, *MST1R*) markers and, thus, different EMT manifestations in different morphological structures. Therefore, intratumoral morphological heterogeneity of BC may serve as an indicator of the metastatic potential and tumor chemosensitivity.

KEYWORDS intratumoral heterogeneity, invasion, metastasis, breast cancer, chemotherapy, epithelial-mesenchymal transition.

ABBREVIATIONS NAC – neoadjuvant chemotherapy; BC – breast cancer; EMT – epithelial-mesenchymal transition.

INTRODUCTION

One of the main characteristics of malignant tumors is the heterogeneity of their cell composition, or intratumoral heterogeneity. The heterogeneity of the cell shape and the morphology within the tumor was first described by Rudolf Virchow in the 19th century [1]. Since the time of Virchow's work, the concept of intratumoral heterogeneity has been greatly advanced.

Different cell populations are now known to be able to coexist in the tumor and specifically affect the tumor's biological behavior [2]. A high degree of intratumoral heterogeneity is associated with a poor clinical prognosis, and the presence of certain cell populations is associated with metastasis and the development of tumor drug resistance [3]. The investigation of various types of intratumoral heterogeneity and the features of its

impact on the clinical course of malignancies is one of the major challenges of modern oncology.

Breast tumors are characterized by a significant variability of the cell composition, as well as by histologic, expression, and genotypic heterogeneity [4]. The intratumoral morphological heterogeneity has been described in invasive breast carcinoma of no special type that is the most common histological type of BC (occurrence rate of up to 80%). According to the WHO classification, breast cancer cells can be arranged in cords, clusters, and trabeculae; in some tumors, a solid or syncytial cell component is prevalent [5]. Furthermore, breast tumors can include tubular, alveolar, glandular-papillary, and solid structures of tumor cells, as well as carcinoid-like areas or scirrhous foci [6]. In our previous studies, we primarily focused on the investigation of tubular, alveolar, solid, and trabecular structures, as well as discrete groups of tumor cells, their genetic and expression portrait, and their association with the rate of lymph node metastasis and the efficacy of neoadjuvant chemotherapy of BC [7–12].

Previously, we had assumed that different structures might be a morphological manifestation of an invasive growth of breast tumors [8, 13]. For example, individual and collective cell invasion patterns can be conventionally distinguished. They are represented by various patterns differing from each other in their form and mechanisms of cell migration. Individual migration can occur both as an amoeboid motion via actomyosin-driven contractions of the cytolemma and as a mesenchymal (fibroblast-like) motion associated with an elongation of the cell's shape, enhanced adhesion of cells to the extracellular matrix, and an increased proteolytic activity. Collective invasion occurs via a mesenchymal migration of tumor cell groups (clusters, solid structures, etc.) [13, 14]. The key mechanism of cell migration is a EMT-related transformation of epithelial cells into mesenchymal cells and the acquisition of a locomotor phenotype by the latter [15]. During EMT, epithelial cells lose cell-cell interactions and the apical-basal polarity and acquire an elongated shape and mobility, which enables them to detach from the primary tumor. These changes are regulated by the Snail, Twist, Slug, ZEB1, and ZEB2 transcription factors and are accompanied by a loss of cell-cell adhesion molecules (E-cadherin, EpCAM, etc.) and by the acquisition of mesenchymal features, such as the expression of N-cadherin, vimentin, etc. [14, 16–19]. Invasive growth is known to be closely related to the metastasis process and directly affect the development of resistance to drugs [15].

In this paper, we consider the relationship between the rate of lymph node and distant metastasis, as well as the efficacy of treatment and the different morpho-

logical structures present in a primary breast tumor. We analyze the expression patterns of EMT-associated genes in different morphological structures to understand the involvement of the invasion process in the development of the intratumoral morphological heterogeneity of BC.

MATERIALS AND METHODS

Morphological analysis and association studies

We analyzed two groups of BC patients treated at the Department of General Oncology of the Cancer Research Institute, Tomsk National Research Medical Center. The first group consisted of 427 patients with invasive breast carcinoma of no special type ($T_{1-4}N_{0-3}M_{0-1}$), aged 28 to 90 years (mean age, 49.9 ± 9.44 years), who received 2–4 NAC courses using CMX/CMF, CAX, FAC, and taxane regimens. The second group included 249 patients with invasive breast carcinoma of no special type ($T_{1-4}N_{0-3}M_{0-1}$), aged 21 to 85 (mean age, 56.02 ± 11.16 years), who did not receive NAC. The characteristics of the patients are presented in *Tables 1* and *2*.

Morphological structures were investigated in biopsy and surgical specimens from patients of both groups. Biopsy and surgical material, which was provided in two to six specimens of a breast tumor, was used to prepare two sections (5–6 μ m). The sections were stained with hematoxylin and eosin and examined by two or three pathologists for the presence of different morphological structures (tubular, alveolar, solid, and trabecular structures, as well as discrete groups of tumor cells) in accordance with [10].

The NAC efficacy was assessed based on the results of instrumental studies (ultrasound and mammography) using the RECIST scale [20]. Patients were classified into responders that show a response (complete or partial) to NAC and non-responders with a lack of response (a stable or progressive disease).

We performed association studies of the relationship between different morphological structures of tumors and the clinical parameters of the disease in both groups of patients, as well as the efficacy of chemotherapy in the NAC group. The obtained data were processed with the χ^2 test and Fisher's exact test using Statistica 8.0. Survival was evaluated using the Kaplan-Meier method. The results were considered significant at $p < 0.05$.

Expression analysis

Expression of the genes involved in EMT (*EPICAM*, *ITGA5*, *ITGB5*, *CDH1*, *CDH2*, *CDH11*, *TGF β 2*, *ZEB1*, *MMP2*, *DCN*, and *MST1R*) was analyzed in different morphological structures of the breast tumors by quan-

Table 1. Clinicopathological characteristics of NAC-treated patients

Clinicopathological parameter	Indicator	Number of cases, %
Age	≤ 50 years	230 (53.8)
	> 50 years	197 (46.2)
Menopause	Premenopausal	224 (52.4)
	Postmenopausal	203 (47.6)
Tumor size	T ₁	101 (23.7)
	T ₂	266 (62.3)
	T ₃	48 (11.2)
	T ₄	12 (2.8)
Lymph node metastases	N ₀	213 (49.9)
	N ₁	138 (32.3)
	N ₂	64 (15.0)
	N ₃	12 (2.8)
Distant metastases	M ₀	220 (51.5)
	M ₁	127 (29.7)
	No data	80 (18.8)
Expression of estrogen receptors	Yes	167 (39.1)
	No	158 (37.0)
	No data	102 (23.8)
Expression of progesterone receptors	Yes	154 (36.1)
	No	173 (40.5)
	No data	100 (23.4)
Expression of epidermal growth factor receptors (HER2)	–	160 (37.5)
	+	76 (17.9)
	++	26 (6.0)
	+++	8 (1.8)
	No data	157 (36.8)
Molecular subtype	Luminal	153 (35.8)
	Triple-negative	96 (22.5)
	HER2-positive	26 (6.1)
	No data	152 (35.6)
NAC regimen	CMX/CMP	165 (38.7)
	CAX	56 (13.1)
	Taxanes	31 (7.2)
	FAC	110 (25.8)
	No data	65 (15.2)
NAC efficacy	Complete response	27 (6.3)
	Partial response	183 (42.9)
	Stable disease	133 (31.2)
	Progressive disease	21 (4.9)
	No data	63 (14.7)

Notes: CMX – cyclophosphamide, methotrexate, and Xeloda; CMF – cyclophosphamide, methotrexate, and 5-fluorouracil; FAC – 5-fluorouracil, adriablastina, and cyclophosphamide; CAX – cyclophosphamide, adriablastina, and Xeloda; taxanes – docetaxel and paclitaxel.

Table 2. Clinicopathological characteristics of NAC-naive patients

Parameter	Indicator	Number of cases, %
Age	≤ 50 years	77 (31.0)
	> 50 years	172 (69.0)
Menopause	Premenopausal	169 (67.9)
	Postmenopausal	80 (32.1)
Tumor size	T ₁	145 (58.2)
	T ₂	95 (38.2)
	T ₃	8 (3.2)
	T ₄	1 (0.4)
Lymph node metastases	N ₀	146 (58.6)
	N ₁	65 (26.1)
	N ₂	26 (10.5)
	N ₃	12 (4.8)
Distant metastases	M ₀	222 (89.2)
	M ₁	27 (10.8)
Expression of estrogen receptors	Yes	184 (74.0)
	No	65 (26.0)
Expression of progesterone receptors	Yes	159 (63.9)
	No	90 (36.1)
Expression of epidermal growth factor receptors (HER2)	Yes	48 (19.3)
	No	201 (80.7)
Molecular subtype	Luminal	195 (78.3)
	Triple-negative	36 (14.5)
	HER2-positive	17 (6.8)
	No data	1 (0.4)

titative real-time PCR. We used frozen samples of tumor tissue obtained during surgery from seven patients with invasive breast carcinoma of no special type, luminal B molecular subtype (T₁₋₂N₀₋₃M₀), aged from 42 to 65 years (mean age, 56.42 ± 8.75 years), who did not receive NAC. Hematoxylin- and eosin-stained sections of freshly frozen breast tumor specimens were used to isolate five types of morphological structures (*Fig. 1*) using a PALM laser microdissection (Carl Zeiss, Germany) according to the previously published procedure [8, 21]. In particular, we obtained tubular, alveolar, and trabecular structures (90–120 samples, ~ 900–1,200 cells), solid structures (50–60 samples, up to 5,000 cells), and discrete groups of tumor cells (300–350 samples, ~ 400–600 cells). To prevent the occurrence of stromal components in the samples, laser microdissection was performed along the edge of the outer epithelial layer of the morphological structures. The microdissected samples were used to isolate total RNA (RNeasy Micro Plus Kit, Qiagen, USA). The RNA integrity (RIN) was assessed using the 2200 TapeStation instrument (Agilent, USA). The RNA was subjected to reverse transcription (cDNA), ligation, and whole transcriptome amplification (QuantiTect Whole Transcriptome Kit, Qiagen, USA). The amplified cDNA was used

for PCR according to [8]. The expression analysis results were evaluated relative to morphologically intact breast ducts that were also sampled during the laser microdissection of normal tissue adjacent to the tumor and the reference gene *ACTB* using the Pfaffl method [22].

RESULTS

Chemotherapy is well known to affect the structure of the tumor population. Chemotherapy-induced changes in tumor cells largely determine the further course of the disease: drug resistance, metastasis, and recurrence [23–25]. In this regard, we analyzed two independent samples of BC patients with and without NAC treatment.

The rate of lymph node and distant metastasis in NAC-naïve BC patients, depending on intratumoral morphological heterogeneity

The presence of either alveolar or trabecular structures in the tumors of NAC-naive patients was associated with a higher rate of lymph node metastasis of BC compared to tumors lacking those structures (47.8 vs. 23.2%, $p = 0.0004$; 43.0 vs. 30.0%, $p = 0.0012$, respectively; *Fig. 2A*). The absence of discrete groups of cells in

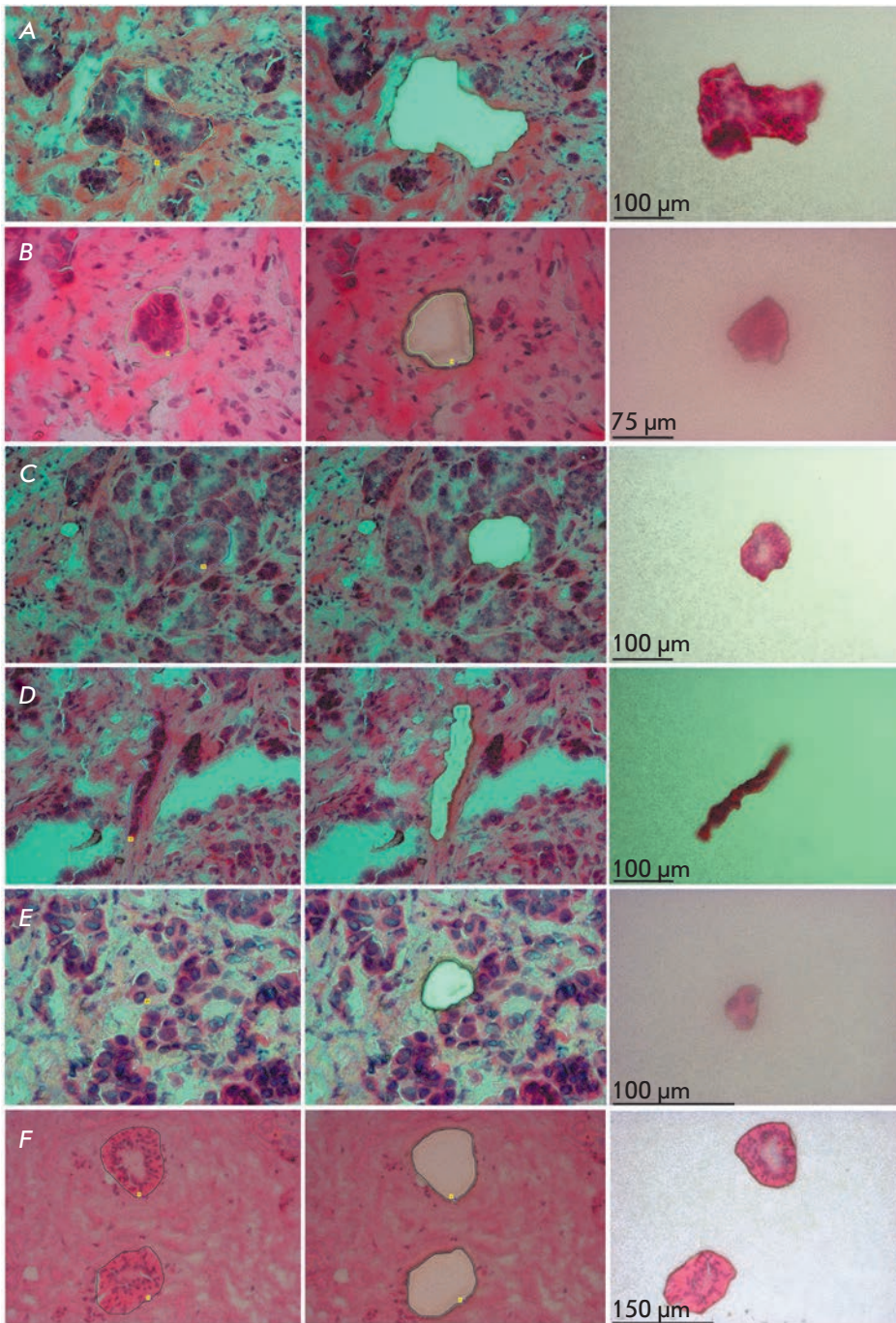


Fig. 1. Laser microdissection of different morphological structures and morphologically intact ducts from tumor and normal tissues of the breast, respectively. The figure shows sections before and after microdissection, as well as the microdissected structures on adhesive caps: *A* – solid structure, *B* – alveolar structure, *C* – tubular structure, *D* – trabecular structure, *E* – a discrete group of tumor cells, *F* – morphologically intact ducts. Hematoxylin and eosin staining

the tumors was associated with an increased rate of distant metastasis compared to the tumors containing the structures (16.9 vs. 8.2%, $p = 0.043$; *Fig. 2B*). These findings are in general consistent with the data, which were previously obtained in a smaller sample of patients, on the association between alveolar structures and the rate of lymph node metastasis [7, 10, 11], as well as the association between trabecular structures and the risk of lymph node metastasis [12].

The rate of lymph node metastasis in NAC-treated BC patients, depending on intratumoral morphological heterogeneity

In NAC-treated patients, the rate of lymph node metastasis of tumors containing alveolar or trabecular structures or discrete groups of cells was higher than that in tumors lacking these structures (64.2 vs. 33.0%, $p < 0.0001$; 57.7 vs. 36.8%, $p < 0.0001$; 59.3 vs. 41.4%, $p = 0.0002$, respectively; *Fig. 2B*). We previously de-

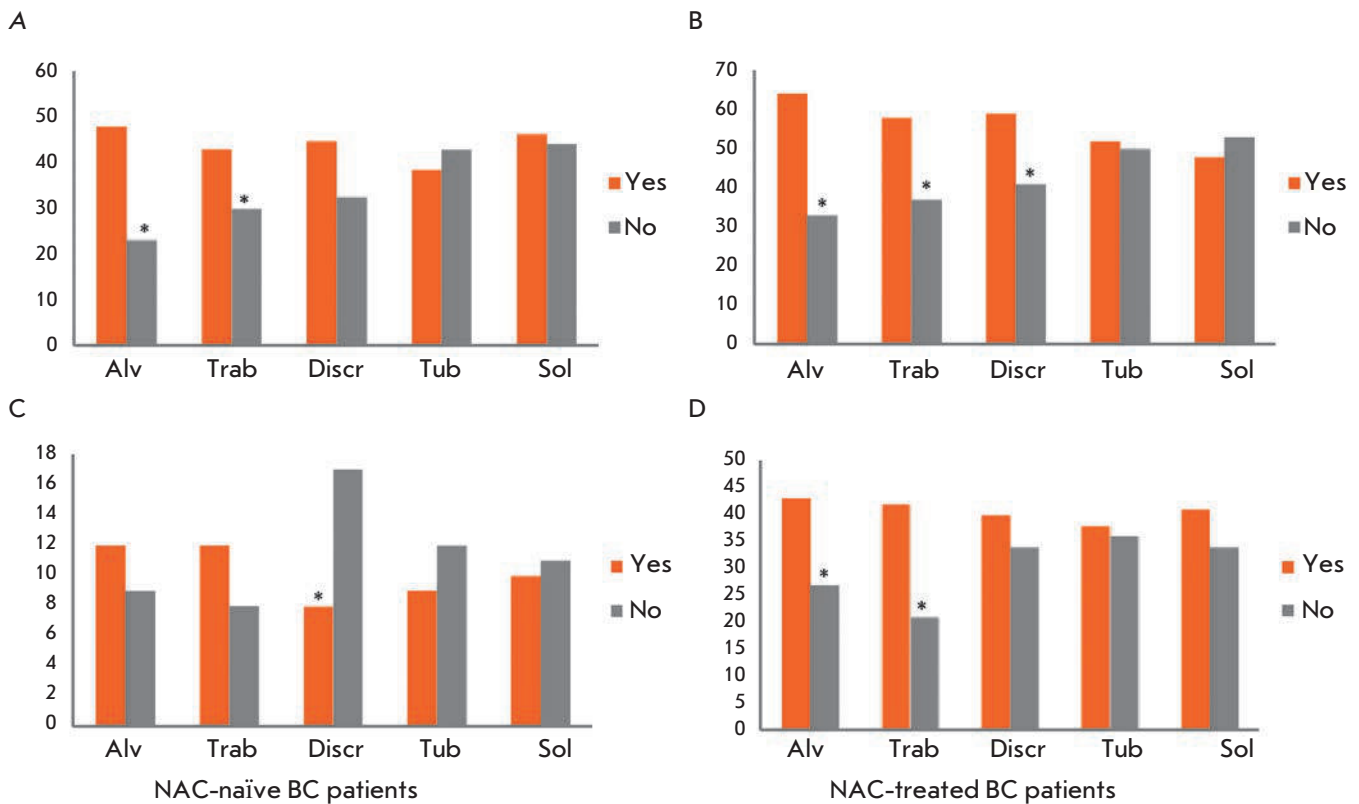


Fig. 2. The rate of lymph node (A, B) and distant (C, D) metastasis in BC patients, depending on the presence of different morphological structures in tumors. A – the rate (%) of lymph node metastasis in NAC-naïve patients. B – the rate (%) of lymph node metastasis in NAC-treated patients. C – the rate (%) of distant metastasis in NAC-naïve patients. D – the rate (%) of distant metastases in NAC-treated patients. Alv – alveolar structures; Trab – trabecular structures; Discr – discrete groups of tumor cells; Tub – tubular structures; Sol – solid structures. * – Statistically significant differences ($p < 0.05$)

scribed a relationship between alveolar structures in the tumors of NAC-treated patients and an increased risk of lymph node metastasis. However, the study group was small, and that relationship was observed only in postmenopausal patients [26]. In patients with alveolar or trabecular structures, the lymph node metastasis rate was higher, regardless of the efficacy of chemotherapy ($p = 0.0032$ and $p < 0.0001$; $p = 0.0004$ and $p = 0.0152$; Fig. 3A). On the contrary, in the group of responders, the rate of lymph node metastasis was higher in patients with discrete groups of cells in the tumor than in patients with tumors lacking such structures (53.8 vs. 34.0%, $p = 0.0041$, respectively; Fig. 3A).

The rate of distant metastasis in NAC-treated BC patients, depending on intratumoral morphological heterogeneity

In patients with alveolar or trabecular structures in tumors, the rate of distant metastasis was higher than that in patients with tumors lacking such structures

(42.8 vs. 27.3%, $p = 0.0036$; 41.9 vs. 20.7%, $p = 0.0005$; Fig. 2D). Furthermore, patients with alveolar or trabecular structures had a low metastasis-free survival rate compared to patients lacking these structures ($p = 0.0087$ and $p = 0.0073$, respectively; Fig. 4A, B). A relationship between alveolar structures and distant metastasis was found only in non-responders to chemotherapy (58.5 vs. 31.0%, $p = 0.0030$; Fig. 3B), whereas in the case of trabecular structures, this relationship was observed only in responders (34.3 vs. 9.3%, $p = 0.0011$; Fig. 3B). In addition, the relationship between morphological structures and distant metastasis depended on the menopausal status. For example, alveolar and solid structures were associated with a high rate of distant metastasis only in premenopausal patients (48.0 vs. 26.5%, $p = 0.0059$; 50.0 vs. 33.0%, $p = 0.028$, respectively; Fig. 3E), while trabecular structures were associated with a high risk of distant metastasis only in a subgroup of postmenopausal patients (41.4 vs. 9.7%, $p = 0.0002$; Fig. 3E).

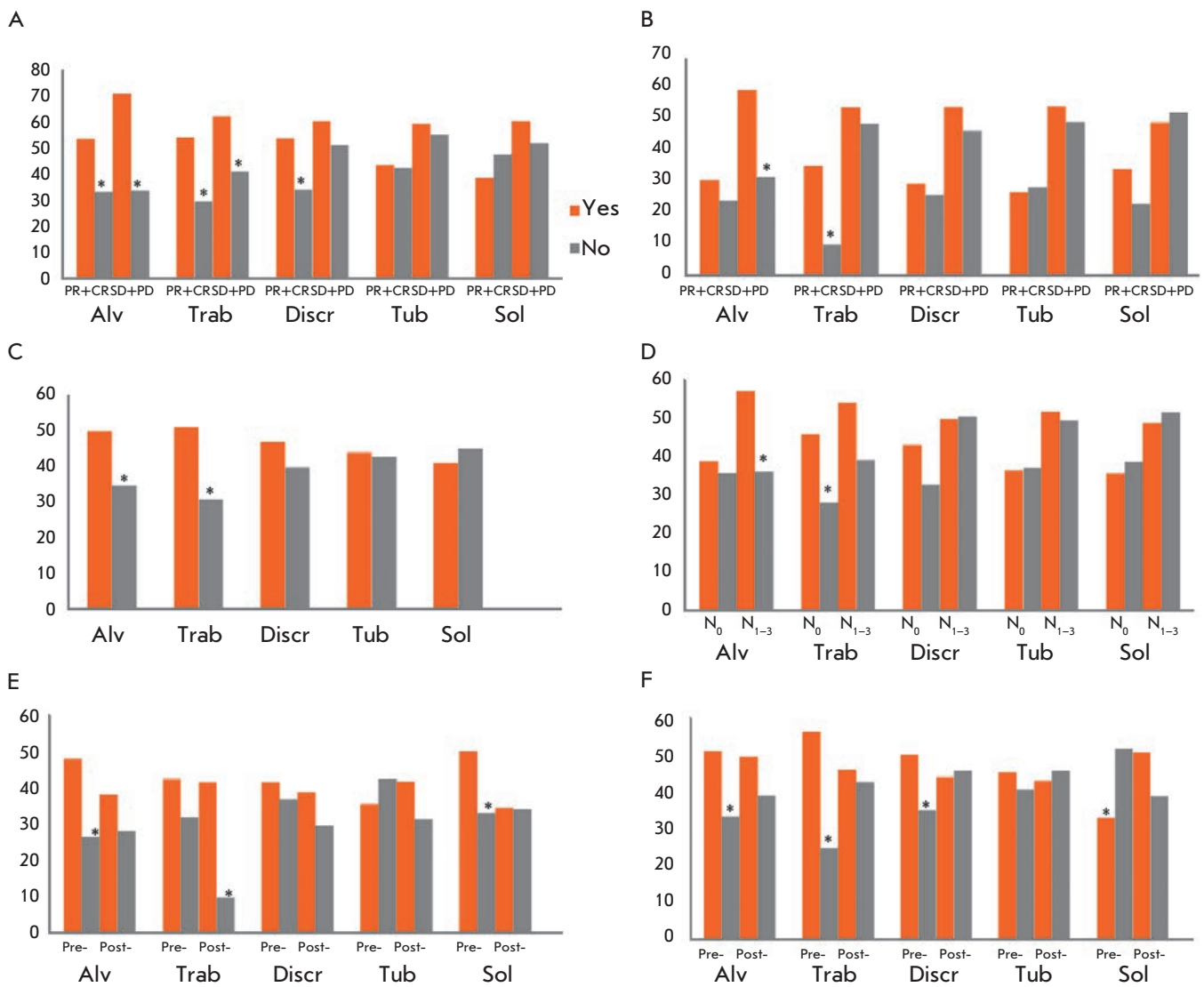


Fig. 3. The chemotherapy efficacy and metastasis rate in NAC-treated BC patients, depending on the presence of different morphological structures in tumors. *A, B* – the rate (%) of lymph node and distant metastasis in responders and nonresponders to neoadjuvant chemotherapy. *C* – the frequency (%) of a lack of response to neoadjuvant chemotherapy. *D* – the frequency (%) of a lack of response to neoadjuvant chemotherapy in patients with/without lymph node metastases. *E, F* – the rate (%) of distant metastasis and the frequency (%) of a lack of response to neoadjuvant chemotherapy in pre- and postmenopausal patients. Alv – alveolar structures; Trab – trabecular structures; Discr – discrete groups of tumor cells; Tub – tubular structures; Sol – solid structures; Pre- – premenopausal patients; Post- – postmenopausal patients; N₀ – negative lymph node status; N₁₋₃ – positive lymph node status; PR+CR – partial response and complete response; SD+PD – stable disease and progressive disease. * – Statistically significant differences ($p < 0.05$)

The dependence of the NAC efficacy on the intratumoral morphological heterogeneity of BC

The presence of alveolar or trabecular structures in breast tumors was more frequently associated with a lack of response to NAC (a stable or progressive disease) compared to tumors lacking these structures (50.3 vs. 35.8%, $p = 0.0056$; 50.7 vs. 31.6%, $p = 0.0004$, respectively; *Fig. 3B*). Earlier, in a smaller sample of

patients, we described a relationship between alveolar and trabecular structures and the chemoresistance of BC and examined the possible mechanisms behind this relationship [8, 9]. Interestingly, a relationship between alveolar structures and chemoresistance was observed only in a group with lymph node metastases: 57.1 (patients with structures) vs. 36.2% (patients without structures; $p = 0.0089$, respectively; *Fig. 3D*).

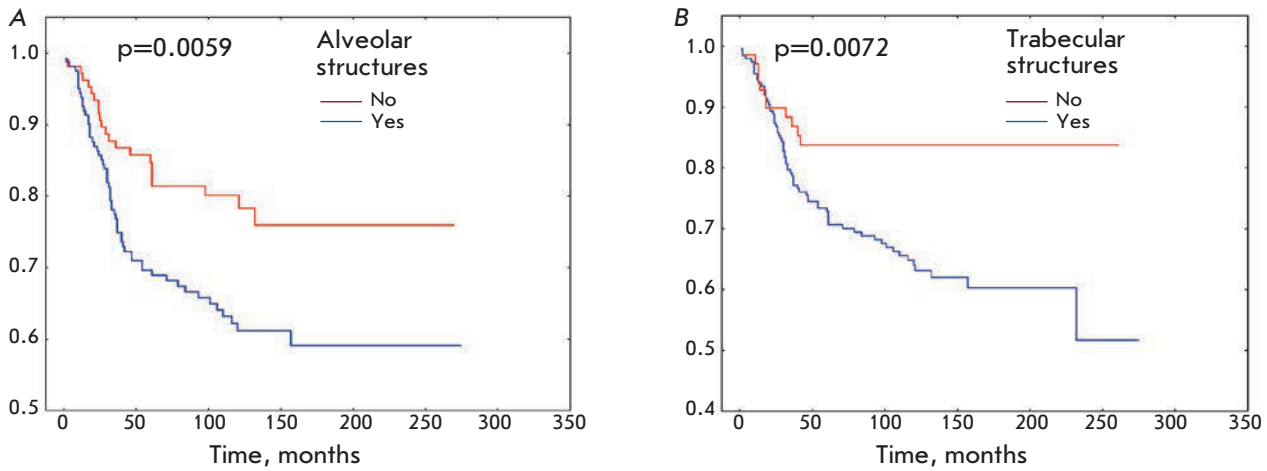


Fig. 4. Metastasis-free survival rate of BC patients with alveolar (A) and trabecular (B) structures in tumors

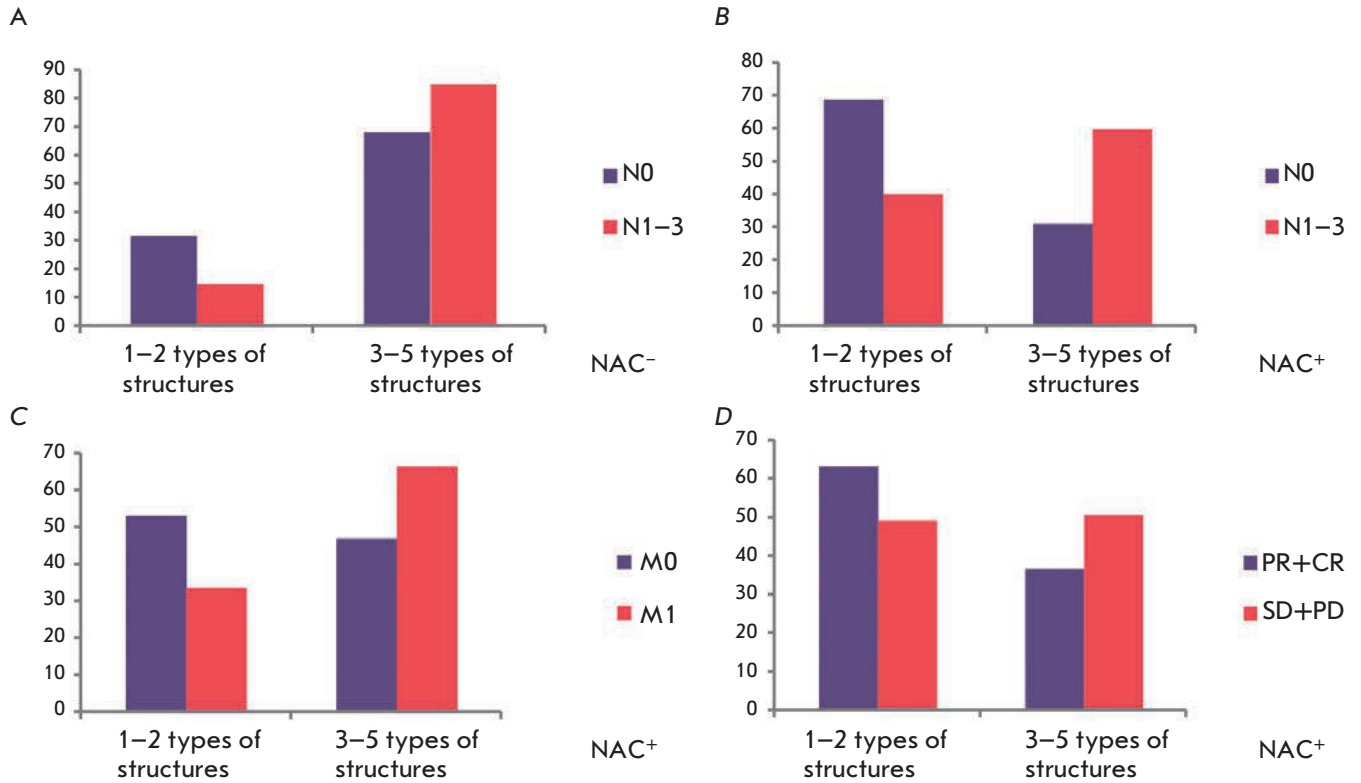


Fig. 5. The chemotherapy efficacy and metastasis rate depending on the number of different morphological structures in breast tumors. A – the rate (%) of lymph node metastasis in NAC-naive patients with low (1–2 types of structures) and high (3–5 types of structures) intratumoral morphological diversity. B, C – the rate (%) of lymph node and distant metastasis in NAC-treated patients with low (1–2 types of structures) and high (3–5 types of structures) intratumoral morphological diversity. D – the frequency (%) of a lack of response to NAC in patients with low (1–2 types of structures) and high (3–5 types of structures) intratumoral morphological diversity. NAC⁻ – NAC-naive patients; NAC⁺ – NAC-treated patients. Only statistically significant differences ($p < 0.05$) are shown

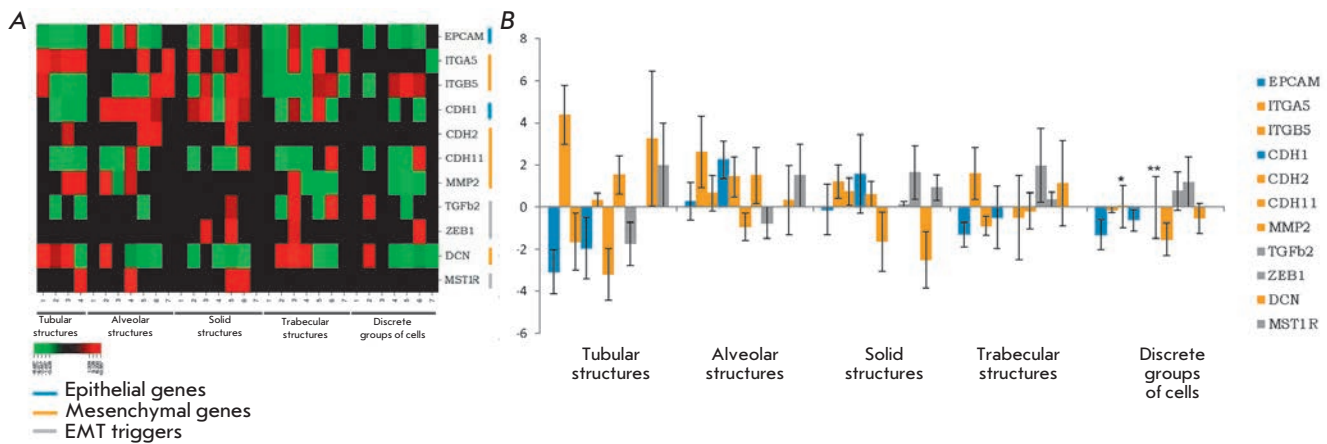


Fig. 6. Expression of EMT genes in different morphological structures of breast tumors. **A** – a heat map of the expression level. **B** – the mean log expression level. * – an expression level of 0.029. ** – an expression level of 0.016. The large standard error of the mean is due to the small sample size, significant variation in expression levels among patients, and the absence of gene expression in some samples of the morphological structure

At the same time, a relationship between trabecular structures and chemoresistance was found only in patients without lymph node metastases (45.8 vs. 28.0%, $p = 0.0117$, respectively; *Fig. 3D*). The relationship between structures and the NAC efficacy also depended on the menopausal status of BC patients. The presence of alveolar or trabecular structures or discrete groups of cells was associated with a lack of response to chemotherapy only in a subgroup of premenopausal patients (51.0 vs. 33.3%, $p = 0.0133$; 56.2 vs. 24.7%, $p = 0.0000$; 50.0 vs. 35.0%, $p = 0.0365$, respectively; *Fig. 3F*). The presence of solid structures was associated with a response to chemotherapy only in premenopausal patients (67.0 vs. 48.4%, $p = 0.0094$; *Fig. 3F*).

It should be noted that drug resistance and a high rate of lymph node and distant metastasis were in general more often observed in tumors with three to five types of morphological structures than in tumors with one or two types ($p = 0.0082$; $p < 0.0001$; $p = 0.0005$, respectively; *Fig. 5*).

An analysis of the association between intratumoral morphological heterogeneity and the metastasis rate and NAC efficacy, depending on chemotherapy regimens, molecular subtypes of BC, and tumor size, was not performed due to a disproportionate ratio of case numbers in subgroups.

Expression of EMT genes in different morphological structures of breast tumors

An expression analysis of the genes involved in EMT demonstrated that each of the structures was associated with a specific set of markers (*Fig. 6*). Expression of

epithelial genes, *EPCAM* and *CDH1*, was typical of all structures (*Fig. 6B*). However, tubular and trabecular structures and discrete groups of tumor cells had low expression levels (*Fig. 6B*). Expression of EMT triggers, *TGFb2*, *ZEB1*, and *MST1R*, was heterogeneous both in different breast tumors and in the structures (*Fig. 6A*). *ZEB1* and *MST1R* were more often expressed in solid structures, while *TGFb2* was more often expressed in trabecular structures. Mesenchymal genes (*CDH2*, *CDH11*, *ITGA5*, *ITGB5*, *MMP2*, and *DCN*) had variable expression levels. *CDH2* encoding a classical mesenchymal marker, N-cadherin, was not expressed in most of the structures. Expression of the integrin alpha 5 gene (*ITGA5*) was almost completely absent in discrete groups of tumor cells and was more pronounced in tubular and trabecular structures. On the contrary, the *ITGB5* gene, along with the decorin proteoglycan gene (*DCN*), was uniformly expressed in different structures. Interestingly, the matrix metalloproteinase 2 gene (*MMP2*) was not expressed solely in solid structures (*Fig. 6A*).

DISCUSSION

Our findings demonstrate the differential contribution of different morphological structures to chemoresistance and the progression of BC. A lymph node and distant dissemination of tumor cells is mainly associated with alveolar and trabecular structures. Interestingly, a contribution of alveolar and trabecular structures to distant metastasis, as well as an impact of discrete groups of cells on the rate of lymph node metastasis, was observed only in chemotherapy-treated patients.

Obviously, chemotherapy is a factor that modulates BC progression. Noteworthy, the presence of alveolar and trabecular structures in the tumors of NAC-treated patients was simultaneously associated with both the rate of lymph node and distant metastasis and chemoresistance, which suggests a relationship between these processes. The relationship between alveolar and trabecular structures and the rate of lymph node metastasis did not depend on the efficacy of chemotherapy. An association of alveolar structures with the rate of distant metastasis was observed only in non-responders, and an association of trabecular structures with the rate of distant metastasis was present in patients with a response to NAC. The dependence of a high rate of lymph node and distant metastasis and drug resistance on a greater morphological diversity of the tumor may also be explained by an increased proportion of alveolar and trabecular structures in the total amount of morphological components. Intratumoral morphological heterogeneity was demonstrated to significantly affect the clinical outcome of BC. This was evidenced in the observation that the survival rate of patients with alveolar or trabecular structures in tumors was significantly lower than that of patients without these structures.

We had previously suggested that different morphological structures could be correlated with invasive growth patterns: discrete groups of cells are associated with individual migration, while solid, alveolar, trabecular, and tubular structures are associated with different types of collective migration [8, 13]. During invasive growth, tumor cells migrate by means of intravasation from the primary site to the lymph and/or blood vessels, followed by dissemination to other organs. Neoplastic cells lack a programmed ability to migrate; they acquire the ability via a triggering of signaling cascades *de novo* or a response to cytokine stimulation or under the influence of antitumor therapy. EMT, as a central molecular program induced during mesenchymal cell migration, creates the preconditions for the development of at least three phenotypic states of tumor cells: the epithelial, mesenchymal, and intermediate epithelial-mesenchymal phenotypes [27, 28]. The most aggressive intermediate state is that where the cell has a hybrid phenotype, acquiring mesenchymal properties and partially preserving epithelial features [27–29]. Furthermore, a hybrid EMT state was shown *in vitro* to be associated with an increased formation of spheroids or tumor cell clusters (2–50 cells) capable of intravasation into blood vessels and associated with more severe metastasis [27, 28]. Interestingly, the shape and amount of cells in small alveolar structures are similar to those in the spheroids circulating in the blood of cancer patients, and according to our findings, the presence of alveolar structures in tumors is associated with an in-

creased rate of lymph node and distant metastasis. Alveolar structures, along with trabecular ones, are likely to be collective migration types with a hybrid epithelial-mesenchymal phenotype, which provides the structures with aggressive features and, as a consequence, high metastatic activity. Indeed, based on an evaluation of the expression of epithelial and mesenchymal state genes, alveolar and trabecular structures were found to be characterized by an intermediate EMT state, with the epithelial (*EPCAM*, *CDH1*) and mesenchymal features (*CDH11*, *ITGB5*, *MMP2*, *DCN*, etc.) preserved. Solid structures may also be considered as an intermediate state of EMT, but with a predominance of the epithelial features (*EPCAM*, *CDH1*). For example, solid structures may represent a type of collective migration with partial EMT in the invasive front area [13, 14]. The relationship between alveolar structures and increased distant metastasis may also be explained by an involvement of these morphological structures in the formation of premetastatic niches through a high production of cytokines and growth factors [30].

Interestingly, tubular structures were characterized by a low expression of epithelial genes, *EPCAM* and *CDH1*, along with an increased expression of mesenchymal genes, *DCN*, *ITGA5*, and *MMP2*. The morphology of tubular structures, which resembles that of normal breast ducts, rather points to the epithelial nature of these morphological structures. Furthermore, the presence of tubular structures is routinely used as a favorable prognostic indicator in the assessment of a tumor grade: the larger the number of tubular structures in the tumor, the lower grade it is, and vice versa [31]. Our previous findings likewise confirm the positive predictive value of tubular structures: an increased ratio of trabecular and tubular structures (Tr/Tub) in tumors is associated with a high rate of distant metastasis. For example, the risk of distant metastasis for a Tr/Tub ratio of 2 is 5-fold higher than that for Tr/Tub of 1 [32]. Probably, the expression of mesenchymal markers in tubular structures may be explained by the fact that part of the structures undergoes initial EMT. Furthermore, there is evidence suggesting that epithelial cells within a heterogeneous tumor may maintain the transition state of other tumor cells undergoing EMT through the secretion of stimulating factors [19].

Discrete groups of tumor cells as individual migration patterns are the most compositionally heterogeneous morphological components of a tumor; they may contain single cells or groups of cells likely capable of both mesenchymal and amoeboid motion. The phenotype of discrete groups of tumor cells has a variable expression portrait with a low representation of epithelial markers on the background of slightly increased mesenchymal features. This is somewhat surprising,

because single tumor cells or their small clusters arise likely due to EMT when cells lose their epithelial features and the ability to form multicellular clusters. At the same time, it is emphasized that the use of known markers of the mesenchymal phenotype, some of which we have used in our work, is not sufficient to judge about the presence or absence of mesenchymal features in tumor cells [33].

There is ample evidence that preoperative chemotherapy is able to modify the genome of tumor cells and affect the tumor population structure [23–25]. The molecular profile of primary tumor samples of triple-negative BC after NAC was shown to differ from the profile of biopsy samples of the same tumors before chemotherapy [34]. Chemotherapy was found to be able to initiate the development and/or expansion of cell populations resistant to treatment [24]. Under the influence of NAC, the morphological structures of breast tumors may acquire additional features that enhance tumor dissemination and promote a subsequent development of chemoresistance. Furthermore, drug resistance and invasion are closely interrelated processes that support each other during malignant growth [15, 35, 36]. This relationship is obvious in the case of the alveolar and trabecular structures associated simultaneously with both a high rate of lymph node and distant metastasis of the tumor and resistance to therapy. The point is that the signaling pathways common to invasion and chemoresistance are activated in migrating cells. The cascade triggered by integrins, cadherins, and small GTPases Rac and Rho intersects with PI3K, mTOR, Src, and MAP-kinase pathways [15, 35]. The EMT state of migrating cells reduces the sensitivity of the cells to antitumor therapy [18, 24]. Tumor cells undergoing EMT exhibit high resistance to radiotherapy and some chemotherapeutic agents [24]. In addition, EMT induces ABC-transporters and activates the al-

ternative oncogenic signaling pathways EGFR, RAF, and MEK, which promotes the development of resistance to therapy, in particular to targeted therapy [37, 38].

Therefore, the biological behavior of a tumor largely depends on the features of its invasive growth [14, 15]. We have demonstrated that the intratumoral morphological heterogeneity of BC, which is probably represented by invasive growth patterns at various EMT stages, may be a factor that determines the metastatic tumor potential and the ability of cells to respond to treatment and affect the clinical outcome of the disease.

CONCLUSION

The main obstacle to a successful diagnosis and treatment of cancers is the intratumoral heterogeneity. Because of significant intratumoral diversity, modern biopsy-based diagnostic techniques do not provide a full understanding of the further clinical manifestations of the tumor. We have demonstrated that the intratumoral morphological heterogeneity of BC probably represented by invasive tumor growth patterns is associated with the rate of lymph node and distant metastasis and the efficacy of preoperative therapy. Probably, the morphological diversity of a tumor may form the basis for the creation of an effective model for developing prognostic and predictive criteria for breast cancer, while alveolar and trabecular structures, as the key indicators of aggressive tumor growth, may become targets in the development of targeted therapy.

This study was supported by the Russian Science Foundation (# 14-15-00318). E.V. Denisov was supported by the Tomsk State University Competitiveness Improvement Program.

REFERENCES

- Virchow R. Cellular Pathology as Based upon Physiological and Pathological Histology. Philadelphia: JB Lippincott Co, 1863.
- Fisher R., Pusztai L., Swanton C. // Br. J. Cancer. 2013. V. 108. № 3. P. 479–485.
- Almendro V., Marusyk A., Polyak K. // Annu. Rev. Pathol. 2013. V. 8. P. 277–302.
- Ng C.K., Pemberton H.N., Reis-Filho J.S. // Expert. Rev. Anticancer Ther. 2012. V. 12. № 8. P. 1021–1032.
- Lakhani S.R., Ellis I.O., Schnitt S.J., Tan P.H., van de Vijver M.J. World Health Organization (WHO) classification of tumours of the breast. Lyon, France: IARC Press, 2012.
- Davydov M.I., Letyagin V.P. Breast cancer (Atlas). M.: ABV-print, 2006.
- Zavyalova M.V., Perelmuter V.M., Slonimskaya E.M., Vtorushin S.V., Garbukov E.Yu., Glyshenko S.A. // Siberian Journal of Oncology. 2006. № 1. P. 32–35.
- Denisov E.V., Gerashchenko T.S., Zavyalova M.V., Litviakov N.V., Tsyganov M.M., Kaigorodova E.V., Slonimskaya E.M., Kzhyshkowska J., Cherdyntseva N.V., Perelmuter V.M. // Neoplasma. 2015. V. 62. № 3. P. 405–411.
- Denisov E.V., Litviakov N.V., Zavyalova M.V., Perelmuter V.M., Vtorushin S.V., Tsyganov M.M., Gerashchenko T.S., Garbukov E.Y., Slonimskaya E.M., Cherdyntseva N.V. // Sci. Rep. 2014. V. 4. P. 4709.
- Zavyalova M.V., Perelmuter V.M., Vtorushin S.V., Denisov E.V., Litvyakov N.V., Slonimskaya E.M., Cherdyntseva N.V. // Diagn. Cytopathol. 2013. V. 41. № 3. P. 279–282.
- Zavyalova M.V., Denisov E.V., Tashireva L.A., Gerashchenko T.S., Litviakov N.V., Skryabin N.A., Vtorushin S.V., Telegina N.S., Slonimskaya E.M., Cherdyntseva N.V., et al. // BioRes. Open Access. 2013. V. 2. № 2. P. 148–154.
- Zavyalova M.V., Litvyakov N.V., Garbukov E.Y., Vtorushin S.V., Stakheeva M.N., Savenkova O.V., Kritskaya N.V., Perelmuter V.M., Slonimskaya E.M., Cherdyntseva N.V. //

- Siberian Journal of Oncology. 2008. V. 6. P. 30–34.
13. Krakhmal N.V., Zavyalova M.V., Denisov E.V., Vtorushin S.V., Perelmutter V.M. // *Acta Naturae*. 2015. V. 7. № 2. P. 17–28.
14. Friedl P., Alexander S. // *Cell*. 2011. V. 147. № 5. P. 992–1009.
15. Alexander S., Friedl P. // *Trends Mol. Med.* 2012. V. 18. № 1. P. 13–26.
16. De Craene B., Berx G. // *Nat. Rev. Cancer*. 2013. V. 13. № 2. P. 97–110.
17. Alexandrova A.Y. // *Biochemistry (Mosc)*. 2014. V. 79. № 9. P. 947–963.
18. Nieto M.A. // *Annu. Rev. Cell Dev. Biol.* 2011. V. 27. P. 347–376.
19. Neelakantan D., Drasin D.J., Ford H.L. // *Cell Adh. Migr.* 2015. V. 9. № 4. P. 265–276.
20. Hayward J.L., Carbone P.P., Heuson J.C., Kumaoka S., Segaloff A., Rubens R.D. // *Cancer*. 1977. V. 39. № 3. P. 1289–1294.
21. Denisov E.V., Skryabin N.A., Vasilyev S.A., Gerashchenko T.S., Lebedev I.N., Zavyalova M.V., Cherdyntseva N.V., Perelmutter V.M. // *J. Clin. Pathol.* 2015. V. 68. № 9. P. 758–762.
22. Pfaffl M.W. // *Nucl. Acids Res.* 2001. V. 29. № 9. P. e45.
23. Marusyk A., Almendro V., Polyak K. // *Nat. Rev. Cancer*. 2012. V. 12. № 5. P. 323–334.
24. Saunders N.A., Simpson F., Thompson E.W., Hill M.M., Endo-Munoz L., Leggatt G., Minchin R.F., Guminski A. // *EMBO Mol. Med.* 2012. V. 4. № 8. P. 675–684.
25. Litviakov N.V., Cherdyntseva N.V., Tsyganov M.M., Slonimskaya E.M., Ibragimova M.K., Kazantseva P.V., Kzhyshkowska J., Choinzonov E.L. // *Oncotarget*. 2016. V. 7. № 7. P. 7829–7841.
26. Perelmutter V.M., Zavyalova M.V., Vtorushin S.V., Slonimskaya E.M., Kritskaya N.V., Garbukov E.Y., Litviakov N.V., Stakheeva M.N., Babyshkina N.N., Malinovskaya E.A., et al. // *Advances in Gerontology*. 2008. V. 21. № 4. P. 643–653.
27. Grosse-Wilde A., Fouquier d'Herouel A., McIntosh E., Ertaylan G., Skupin A., Kuestner R.E., del Sol A., Walters K.A., Huang S. // *PLoS One*. 2015. V. 10. № 5. P. e0126522.
28. Huang R.Y., Wong M.K., Tan T.Z., Kuay K.T., Ng A.H., Chung V.Y., Chu Y.S., Matsumura N., Lai H.C., Lee Y.F., et al. // *Cell Death Dis.* 2013. V. 4. P. e915.
29. Bulfoni M., Gerratana L., Del Ben F., Marzinotto S., Sorrentino M., Turetta M., Scoles G., Toffoletto B., Isola M., Beltrami C.A., et al. // *Breast Cancer Res.* 2016. V. 18. № 1. P. 30.
30. Tashireva L.A., Denisov E.V., Savelieva O.E., Gerashchenko T.S., Zavyalova M.V., Perelmutter V.M. // *Biopolymers & Cell*. 2015. V. 31. № 6. P. 429–435.
31. Bloom H.J., Richardson W.W. // *Br. J. Cancer*. 1957. V. 11. № 3. P. 359–377.
32. Perelmutter V.M., Zavyalova M.V., Slonimskaya E.M., Vtorushin S.V., Garbukov E.Y. // *Siberian Journal of Oncology*. 2006. № 3. P. 29–33.
33. Westcott J.M., Prechtel A.M., Maine E.A., Dang T.T., Esparza M.A., Sun H., Zhou Y., Xie Y., Pearson G.W. // *J. Clin. Invest.* 2015. V. 125. № 5. P. 1927–1943.
34. Balko J.M., Giltane J.M., Wang K., Schwarz L.J., Young C.D., Cook R.S., Owens P., Sanders M.E., Kuba M.G., Sanchez V., et al. // *Cancer Discov.* 2014. V. 4. № 2. P. 232–245.
35. Häger A., Alexander S., Friedl P. // *Eur. J. Cancer Suppl.* 2013. V. 11. № 2. P. 291–293.
36. Alexander S., Weigelin B., Winkler F., Friedl P. // *Curr. Opin. Cell Biol.* 2013. V. 25. № 5. P. 659–671.
37. Mallini P., Lennard T., Kirby J., Meeson A. // *Cancer Treat. Rev.* 2014. V. 40. № 3. P. 341–348.
38. Holohan C., van Schaeybroeck S., Longley D.B., Johnston P.G. // *Nat. Rev. Cancer*. 2013. V. 13. № 10. P. 714–726.

Differentiation of Human Pluripotent Stem Cells into Mesodermal and Ectodermal Derivatives Is Independent of the Type of Isogenic Reprogrammed Somatic Cells

E. S. Philonenko^{1*}, M. V. Shutova^{1*}, E. A. Khomyakova^{1,2}, E. M. Vassina¹, O. S. Lebedeva², S. L. Kiselev^{1,2,3}, M. A. Lagarkova^{1,2,3*}

¹Vavilov Institute of General Genetics, Russian Academy of Sciences, Gubkina Str. 3, Moscow, 119333, Russia

²Scientific Research Center of Physical-Chemical Medicine, Pirogovskaya Str. 1a, Moscow, 119435, Russia

³Kazan State University, Kremlevskaya Str. 18, Kazan, 420008, Russia

*These authors made equal contribution to the paper

*E-mail: lagar@vigg.ru

Received April 22, 2016; in final form, June 01, 2016

Copyright © 2017 Park-media, Ltd. This is an open access article distributed under the Creative Commons Attribution License, which permits unrestricted use, distribution, and reproduction in any medium, provided the original work is properly cited.

ABSTRACT Induced pluripotent stem cells (iPSCs) have the capacity to unlimitedly proliferate and differentiate into all types of somatic cells. This capacity makes them a valuable source of cells for research and clinical use. However, the type of cells to be reprogrammed, the selection of clones, and the various genetic manipulations during reprogramming may have an impact both on the properties of iPSCs and their differentiated derivatives. To assess this influence, we used isogenic lines of iPSCs obtained by reprogramming of three types of somatic cells differentiated from human embryonic stem cells. We showed that technical manipulations *in vitro*, such as cell sorting and selection of clones, did not lead to the bottleneck effect, and that isogenic iPSCs derived from different types of somatic cells did not differ in their ability to differentiate into the hematopoietic and neural directions. Thus, the type of somatic cells used for the generation of fully reprogrammed iPSCs is not important for the practical and scientific application of iPSCs.

KEYWORDS induced pluripotent stem cells, human embryonic stem cells, transcription, hematopoiesis, neurons, methylation.

ABBREVIATIONS iPSCs – induced pluripotent stem cells, PSCs – pluripotent stem cells, hESCs – human embryonic stem cells, DAPI – 4',6-diamidino-2-phenylindole.

INTRODUCTION

Change in the epigenetic state of a cell using various external conditions fundamentally affects the program of the specialized somatic cell [1, 2]. The most commonly used viral integrative or integration-free methods of reprogramming to a pluripotent state do not substantially affect the genome of the somatic cells subjected to reprogramming [3]. Practical use of induced pluripotent stem cells (iPSCs) for medical or research purposes involves the application of differentiated derivatives of pluripotent cells. The protocols of directed differentiation are aimed primarily at modifying the epigenetic state of pluripotent stem cells (PSCs) by microenvironment conditions mimicking the processes (occurring during) of the individual development of an organism. Thus, the initial epigenetic state and the differences between iPSC lines established even from

the same source can have a significant impact on the final result of the differentiation. For example, a total of 25 cell lines was analyzed for the selection of iPSC line-derived retinal pigment epithelium most suitable for transplantation [4], which requires a lot of time and data. In order to study the contribution of the reprogramming process and somatic cell epigenome to the terminal state of iPSCs, as well as optimize the selection of the reprogrammed cell lines, we have developed a system of isogenic lines of pluripotent and somatic cells. The isogenic system of cell lines has allowed us to show that iPSC clones do not leave traces of their tissue-specific origin upon complete functional reprogramming. However, the reprogrammed cells acquired individual epigenetic marks specific to each iPSC clone, indicating that the establishment of pluripotency did not occur in the usual way but through mechanisms

different from germline pathways [5]. The appearance of these individual features not related to the reprogramming can be caused by technical manipulations *in vitro* such as cloning, cell sorting, etc.. There is no doubt that a directed influence of such manipulations on the genome can negatively affect further iPSCs application. For example, the possibility of creating banks of reprogrammed cell lines, both personal and immunologically universal lines of iPSCs that would be compatible with a large number of recipients has been widely discussed [6]. However, the question concerning which type of donor cells (skin fibroblasts, blood cells, hair follicle cells, etc.) should be used for reprogramming remains open. According to our results and other studies, isogenic iPSCs derived from different somatic cell types are functionally similar [5, 7]. However, taking into account the fact that they should be further differentiated into specialized types of cells *in vitro*, it is necessary to know how their ability to differentiate would vary.

In the present work, we studied the influence of genetic manipulations, clone selection, and cell sorting *in vitro* on the molecular and genetic properties of iPSCs. In order to do that, we used lines of isogenic somatic cells derived from human embryonic stem cells (hESCs) and their derivatives reprogrammed into iPSCs to compare the ability of isogenic lines of a iPSC line of three different somatic origins to differentiate into the neuronal and hematopoietic directions.

EXPERIMENTAL

Cell lines

We used the cell lines hESM01, hESM01n5 (hereinafter n5), fibroblasts, neurons, retinal pigment epithelial cells differentiated from hESM01n5 (F, N, R, respectively), and the iPSC lines iF, iN, iR obtained by genetic reprogramming of the lines F, N, R, respectively [5].

Human ESC lines HUES 9 [8], H9 [9], iPSC lines endo-iPS12 [10], and IPSRG2L were used in experiments on hematopoietic differentiation [11]. Lines endo-iPSS5 and endo-iPSS9 were obtained by the reprogramming of HUVEC cells using the Sendai virus. The lines of iPSCs were cultured according to [5].

Media for hematopoietic differentiation

Medium 1 for embryoid bodies (EB1): Stemline II (Sigma), penicillin-streptomycin ("PanEco", 5,000 U/ml penicillin and 5,000 U/ml streptomycin), 100 ng/ml VEGF (Prepro Tech), 50 ng/ml BMP-4 (Prepro Tech), and 20 ng/ml FGF (Prepro Tech).

Medium 2 for embryoid bodies (EB2): Stemline II (Sigma), penicillin-streptomycin ("PanEco", 5,000 U/ml penicillin and 5,000 U/ml streptomycin), 100 ng/ml

VEGF (Prepro Tech), 50 ng/ml BMP-4 (Prepro Tech), 20 ng/ml FGF (Prepro Tech), 100x cytokine cocktail CC110 (Stemcell Technologies) or 20 ng/ml SCF (Prepro Tech). Hemangioblasts were cultured in a semi-liquid medium (MHB): Methocult 4436 (Stemcell Technologies), 20 ng/ml FGF (Prepro Tech), 50 ng/ml VEGF (Prepro Tech), 20 ng/ml SCF (Prepro Tech), 20 ng/ml FLT3-L (Prepro Tech), 20 ng/ml TPO (Prepro Tech), 2 µg/ml recombinant HoxB4.

Hematopoietic differentiation of PSCs

PSCs cultured in a 35-mm Petri dish (Corning) coated with a Matrigel matrix (BD) were grown to 70% confluence and treated with a 0.05% Trypsin-EDTA solution to a single-cell state. Trypsin was inactivated by the addition of a DMEM medium ("PanEco") with 10% fetal bovine serum (FBS, Gibco). Embryoid bodies were formed in Aggrewell (Stemcell Technologies) for 24 hours in a mTeSR1 medium (Stemcell Technologies) supplemented with 10 µM Y-27632 (Stemgent). The embryoid bodies were transferred to a 24-well low-adhesion plate (Costar) in a 1-ml volume per well in a EB1 medium and incubated for 48 hours. A 500 µl aliquot was taken from the well, mixed with 500 µl of a EB2 medium and incubated for 48 hours. The embryoid bodies were treated with 0.05% Trypsin-EDTA for 4-6 minutes. Next, trypsin was inactivated by adding the DMEM medium supplemented with 10% FBS. The cells were centrifuged at 200 g for 5 min. The cells ($2-5 \times 10^5$ per volume of not more than 100 µl of a IMDM medium ("PanEco")) were added to the wells of a 6-well low-adhesion plate (Costar) with a GBS medium using syringes (Stem cell Technologies) with a blunt needle for methylcellulose. The cells were incubated for 6-8 days. Then, additional 2 ml of MHB was added and the cells were incubated for another 2-4 days. For a comparison of the differentiation efficiency, the number of hemangioblast colonies was counted on the 10th day after introduction into MHB.

The ability of hemangioblasts to differentiate into blood cells was tested by the introduction of hemangioblasts into the methylcellulose medium Methocult 4436 (Stemcell Technologies). The result was evaluated after 3 weeks.

Neuronal differentiation

Neuronal differentiation into neural progenitors and neurons was performed according to [11]. A FACS analysis of neural progenitors was performed using antibodies to CD56 PE Abcam cat # 2412540 (Sony Biotechnology) (1 : 25 dilution) and isotype control Mouse IgG1PE Abcam cat # 2600560 (1 : 166). For a fluorescence analysis, antibodies against βIII-tubulin in a 1 : 1000 dilution (Abcam) and the secondary antibodies

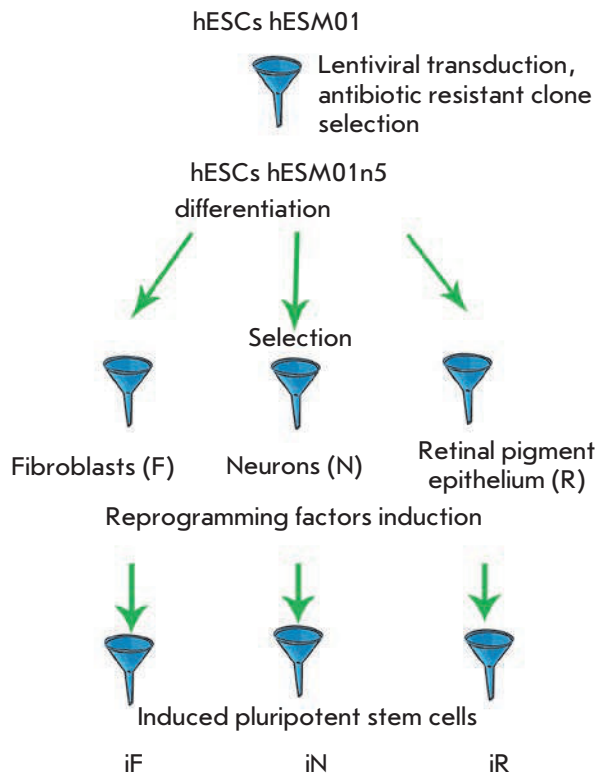


Fig. 1. General scheme of the creation of a human isogenic iPSC system depicting critical stages of the passage of cell populations through the bottleneck of selection and cloning.

Invitrogen Goat anti Rabbit IgG Alexa Fluor 488 in a 1 : 1000 dilution were used.

Isolation of total RNA from the cell cultures and real-time PCR were performed according to [5].

RESULTS AND DISCUSSION

Selection and screening of iPSCs do not cause systemic changes in methylation and gene transcription. Culturing of human PSCs and, especially, genetic manipulations with these cells are ultimately associated with cell selection and/or cloning. Previously, we established and described an isogenic cell system that allows one to study the molecular mechanisms of reprogramming and differentiation processes [5]. We performed a successive selection of clones and cell sorting several times during the creation of an isogenic system (Fig. 1). In relation to this, a question arose as to how manipulations of human PSC cloning in culture can have a systemic impact on gene expression and DNA methylation at the genome-wide level. Expression of certain genes and CpG methylation patterns might have been changed simply because the cells had passed through multiple

bottleneck selection procedures. Selective pressure can result in the overexpression of the genes associated with cell survival and confer them an advantage in growth without altering other properties [12]. In the system developed (fig. 1), reprogramming factor genes under the control of an inducible promoter were introduced into the cell line hESM01 and a hESM01n5 clone (hereinafter as n5) was selected which had the lowest level of transgene “leakage” and retained the property of pluripotency [5]. In the next round of the selection, we used magnetic sorting of differentiated n5 derivatives with antibodies to specific markers of the three types of human somatic cells. The last bottleneck happened after the induction of transgenes and selection of iPSC clones (Fig. 1). We analyzed the gene expression profile and the level of DNA methylation (database GSE70739) in each of the cell lines obtained at each stage of the system’s establishment. We hypothesized that selective pressure can lead to a successive change in gene expression and/or methylation, providing cells with survival and proliferation advantage. In order to identify the genes and CpG the expression and methylation levels of which gradually increased or decreased during cell selection procedures, the expression/methylation levels in iPSCs were compared between parental lines of somatic cells and isogenic hESC line n5. A gradual increase/decrease of 0.2 for CpG methylation and a 1.5-fold change in the case of gene expression were considered as significant. We analyzed data for 11 cell lines (two hESC lines, three lines of somatic cells, and six lines of iPSCs) the cells of which had been subjected to three bottleneck rounds. We found that transcription of a very small number of genes gradually decreases or increases during cell manipulations, with the transcription level of none of the gene changing in all of the cell lines simultaneously (Table 1). This is indicative of the fact that the applied approach, which was identical for all iPSC lines, did not introduce any systematic changes in the cell expression profile, and that the observed expression alterations were accidental. However, the analysis of the methylation profile of isogenic PSC lines and somatic cell lines demonstrated a gradual increase in

Table 1. Genes the expression level of which gradually decreases or increases in the process of hESC differentiation and subsequent reprogramming.

iPSCs	Upregulation	Down-regulation
iF	CTGF, TAGLN	SOX15
iN	ACSL4, DDIT4, TIMP1, LOC730278	LFNG
iR	MT1A	

Table 2. Genes the CpG methylation level of which gradually decreases or increases in the process of hESC differentiation and subsequent reprogramming.

Increased level of methylation			Decreased level of methylation		
iF	iN	iR	iF	iN	iR
IRX1	ZFP42	AJAP1	AJAP1	MSL3	LOC284661
AJAP1	BANK1	PAX8	CHL1		CD1C
REC8	ZNF454	ZFP42	MARCKS		RTKN
C19orf41	HIST1H1A	SIM1	ZNF311		RAET1L
CBLN4	LOC390595	DPP6	GCM2		GPNMB
ZNF542	ZNF829	GNA14	DPP6		CSMD1
ZFP28	ZNF626	ARHGAP22	TCERG1L		MGMT
LOC390595	ZNF568	FIGNL2	MGMT		TCERG1L
TMEM132C	ZFP28	TBX5	GALNT9		DNAH9
EBF3		A2BP1	TMEM121		BAHCC1
PTPRN2		CCDC102A	BAHCC1		
ZFP42		HS3ST4	SHISA6		
		ARHGAP23	C22orf34		
		SHISA6			
		TMEM200C			
		MYH14			
		AFF2			

the methylation level of the *Rex1* gene (also known as *ZFP42*) (Table 2). Currently, there is no definitive information on the function of this gene in early embryonic development. According to some researchers, this gene is considered as a marker of pluripotency [13]. However, mouse ESCs are capable of self-renewal and remain pluripotent even in its absence [14]. As shown earlier, *Rex1* is expressed in human ESCs even in the case of promoter 50% methylation [15]. Using real-time PCR, we analyzed the *Rex1* expression level and compared it with the methylation of the promoter region (Fig. 2). The expression level of *Rex1*, as well as the level of its promoter methylation, significantly varied in the analyzed pluripotent cell lines. However, we found no correlation between the *Rex1* methylation level and its expression. For example, the *Rex1* expression level was more than 3-fold higher in two iN clones (neuron-derived iPSCs) and one iR clone (iPSCs derived from the retinal pigment epithelium) than in all other PSC lines (Fig. 2). Thus, the culturing, reprogramming, and selection that led to the hypermethylation of the *Rex1* promoter region had no impact on gene expression in iPSC lines. This observation additionally confirms the assumption about the auxiliary role of *Rex1* in maintaining cell pluripotency and also indicates that *Rex1*

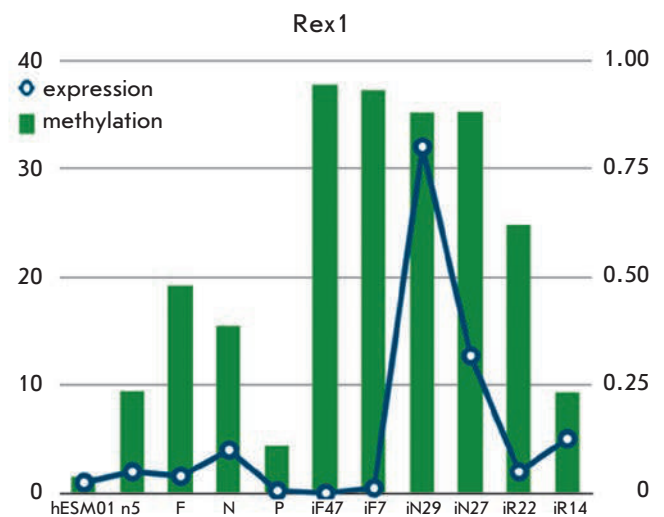


Fig. 2. Gradual increase (more than 0.2) of the *Rex1* methylation level does not correlate with its expression level. Beta-values based on Illumina 450K data were used for the evaluation of the methylation level ($p < 0.01$, $fdr < 0.05$), while real-time PCR was used to analyze gene expression. (*GAPDH* was used as the reference; the hESM01 line was used to assess the basal level).

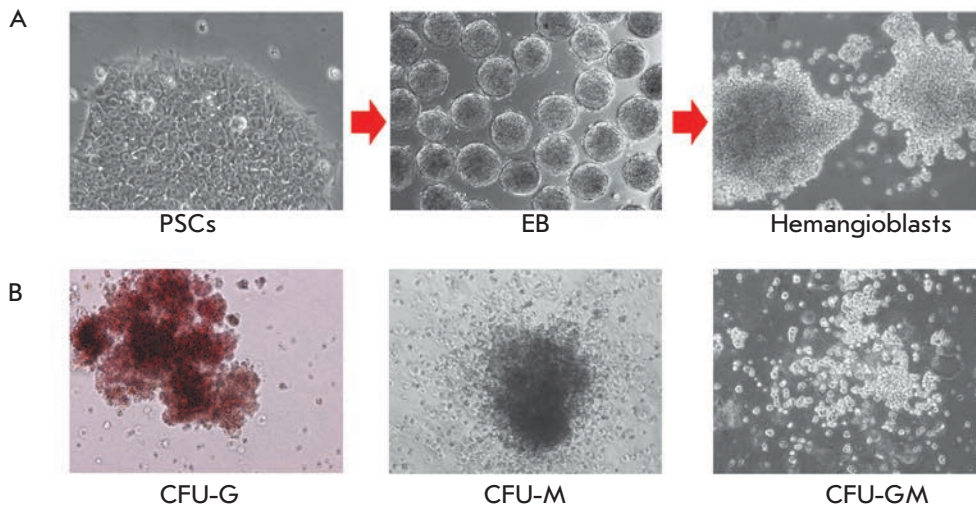
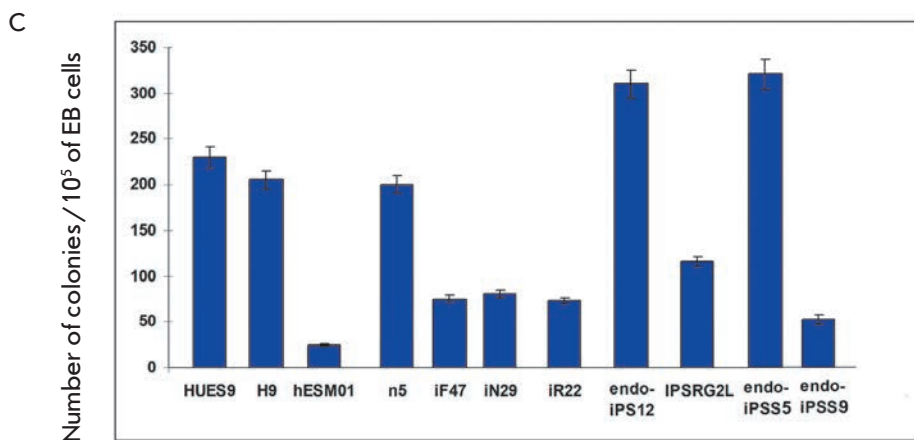


Fig. 3. Hematopoietic differentiation of iPSCs. *A* – PSCs, embryoid bodies and hemangioblasts obtained from PSCs. Line n5 is shown. *B* – Examples of hematopoietic colonies formed in methylcellulose. *C* – Comparison of the number of hematopoietic colonies formed in methylcellulose from different PSCs lines on day 10.



expression is not dependent on the methylation status and is extremely heterogeneous in different iPSC lines, as noted previously [12, 15].

Generally speaking, the obtained results indicate that the procedures of genetic modifications, clone selection, and cell sorting have no systemic impact at the genome-wide level of gene expression and DNA methylation in human PSCs. This conclusion is of serious practical importance due to the possible application of technologies using human PSCs in regenerative medicine.

Comparison of the ability of isogenic PSCs to differentiate into the hematopoietic direction

The established isogenic system of human PSC reprogramming and differentiation analysis allowed us to prove that one can use somatic cells of any type for reprogramming, since the type of the cells do not make any significant contribution to establishment and maintenance of the pluripotent state [5]. However, taking into account the fact that only differentiated deriva-

tives of PSCs have to be used further, the issue of how the somatic cell type the iPSCs are derived from would affect differentiation efficiency remains open. In order to evaluate this influence, we decided to examine the differentiation efficiency of isogenic human iPSCs derived from fibroblasts (iF), neurons (iN), and retinal pigment epithelium (iR) into hematopoietic cells and neurons. For the evaluation of the effectiveness of hematopoietic differentiation through the stage of embryoid bodies, PSCs were differentiated into early mesodermal derivatives (Fig. 3A). The mesodermal derivatives obtained earlier possessed the characteristics of hemangioblasts, since they could differentiate into blood cells (Fig. 3B) and endothelium (data not shown). Upon introduction of hemangioblasts into a semi-liquid methylcellulose medium containing hematopoietic cytokines and growth factors, the hemangioblasts formed different types of hematopoietic colonies: erythroid (CFU-E), macrophage (CFU-M), granulocyte (CFU-G), mixed granulocyte-macrophage (CFU-GM), as well as mixed-type colonies CFU-mix, which indicates that

hemangioblasts are hematopoietic cells. The examples of such colonies are shown in *Fig. 3B*. The ability of various iPSC lines to differentiate was assessed by the number of hemangioblast colonies formed in MHB on the 10th day. The performed calculation showed that the ability of PSCs to differentiate in the hematopoietic direction greatly varies between the lines but does not depend on their origin. For example, the hESM01 cell line showed the lowest efficiency of hematopoietic differentiation (*Fig. 3B*), while the n5 cell line derived from it was characterized by a significantly higher efficiency of hematopoietic differentiation. The isogenic iPSC lines did not differ in their ability to differentiate despite the fact that they were obtained from different germ layers. Fibroblasts and blood cells belong to the same germ layer. However, the efficiency of iF differentiation into hematopoietic cells was comparable to the isogenic iPSCs of other somatic cell types obtained alongside with them. Other lines that were included into the analysis exhibited different differentiation efficiencies. It should be noted that, in contrast to previously published data, we did not observe a reduced efficiency of human iPSC line differentiation in the hematopoietic direction compared to hESCs [16]. These results indicate that the ability of hematopoietic differentiation is an intrinsic characteristic of each particular PSC line, and that the optimal direction of differentiation can be chosen using, for example, gene cards [17]. The isogenic iPSC lines shared an almost identical ability to differentiate in the hematopoietic direction, since the similarity of the method and simultaneity of reprogramming and culturing, as well as other external conditions, apparently, made a greater contribution to the similarity of the lines than the differences established in their tissue origin.

Comparison of the ability of isogenic PSCs to differentiate in the neuronal direction

One of the most popular trends in using differentiated PSC derivatives is the study of the nervous system functioning and therapy of neurodegenerative diseases. In this context, a comparative analysis of the efficiency of the differentiation of isogenic PSCs in the neuronal direction becomes relevant. In order to do this, the original hESC line and iPSCs iN, iF, and iR, which are isogenic to it, were differentiated through the neuronal pathway (*Fig. 4A*). The differentiation efficacy was evaluated by immunocytochemical staining of the cells and flow cytometry at the stage of neuronal progenitors carrying the surface antigen CD56 (NCAM). The developed protocol allowed us to obtain neuronal precursors with high efficiency, with more than 90% of the cells being positive for NCAM (*Fig. 4B*). We found no difference in the differentiation efficiency until the

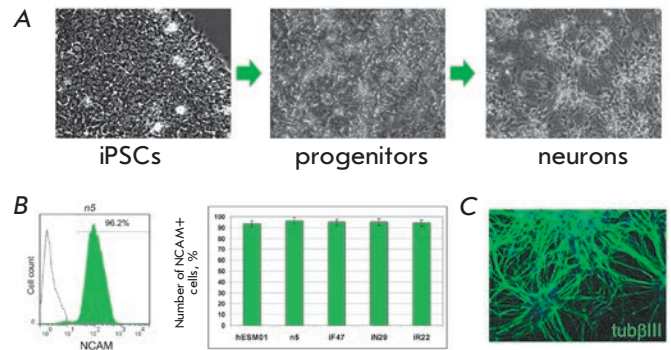


Fig. 4. The efficiency of differentiation in the neural direction does not depend on the tissue of origin of isogenic iPSCs. **A** – Scheme of PSC differentiation into neurons. iPSCs differentiate up to the stage of neuronal progenitors and further, in the presence of neurotrophic factors, into neurons. **B** – flow cytometry results of the NCAM+ neuronal progenitors obtained from isogenic hESCs and iPSCs. On the left are the results of flow cytometry of the neuronal progenitors obtained from the n5 line (green): isotype control is not colored. On the right is a summary of the results of flow cytometry of five lines presented as a diagram. **C** – immunohistochemical analysis of neurons differentiated from iPSCs. Green – antibodies to β III tubulin; nuclei are stained with DAPI (blue)

stage of neuronal precursors between PSC lines of different origins. Postmitotic neurons (*Fig. 4C*), which were analyzed by immunohistochemistry for the presence of β III-tubulin, were obtained during the subsequent differentiation. We also did not find any statistically significant differences between PSC lines in the efficiency of differentiation into postmitotic neurons (data not shown). Thus, as in the case of hematopoietic differentiation, the type of somatic cells used for reprogramming does not play a role in the effective differentiation of PSCs through the neuronal pathway. The obtained results demonstrate a number of important practical conclusions. First of all, the type of somatic cells used for reprogramming is not important in the creation of a bank of allogenic iPSCs for their further application as differentiated derivatives. Blood or skin cells can be obtained from one donor, while neuronal tissue (if available) can be obtained from another donor. Furthermore, fully reprogrammed iPSCs are identical in their differentiation potential. In addition, we have shown that neither genetic manipulations nor selection of PSC clones had a systemic impact on their properties. Undoubtedly, gene expression is more likely associated with changes in chromatin rather than the mutations affecting gene function. This is additionally confirmed by the recently published data on the high genetic sta-

bility of PSCs [18]. Despite the fact that there are significant variations in the epigenetic markers of human PSCs that have been identified [19, 20], recent research data suggest that the current methods of human PSCs cultivation allow one to maintain an epigenetic profile over a long period. Thus, PSC lines and their deriva-

tives can already present well-standardized cultures, which opens up the possibility of their practical use.

This work was supported by the RFBR grant № 15-04-05675 and the Russian Science Foundation grant № 14-15-00930.

REFERENCES

1. Takahashi K., Yamanaka S. // *Cell*. 2006. V. 126. № 4. P. 663–676.
2. Pang Z.P., Yang N., Vierbuchen T., Ostermeier A., Fuentes D.R., Yang T.Q., Citri A., Sebastiano V., Marro S., Südhof T.C., et al. // *Nature*. 2011. V. 476. № 7359. P. 220–223.
3. Bhutani K., Nazor K.L., Williams R., Tran H., Dai H., Džakula Ž., Cho E.H., Pang A.W., Rao M., Cao H., et al. // *Nat. Commun.* 2016. V. 7. № 10536. doi: 10.1038/ncomms10536.
4. Kamao H., Mandai M., Okamoto S., Sakai N., Suga A., Sugita S., Kiryu J., Takahashi M. // *Stem Cell Repts.* 2014. V. 2. № 2. P. 205–218.
5. Shutova M.V., Surdina A.V., Ischenko D.S., Naumov V.A., Bogomazova A.N., Vassina E.M., Alekseev D.G., Lagarkova M.A., Kiselev S.L. // *Cell Cycle*. 2016. V. 15. № 7. P. 986–997.
6. Andrews P.W., Cavagnaro J., Deans R., Feigal E., Horowitz E., Keating A., Rao M., Turner M., Wilmut I., Yamanaka S. // *Nat. Biotechnol.* 2014. V. 32. № 8. P. 724–726.
7. Kyttälä A., Moraghebi R., Valensisi C., Kettunen J., Andrus C., Pasumarthy K.K., Nakanishi M., Nishimura K., Ohtaka M., Weltner J., et al. // *Stem Cell Repts.* 2016. V. 6. № 2. P. 200–212.
8. Cowan C.A., Klimanskaya I., McMahon J., Atienza J., Witmyer J., Zucker J.P., Wang S., Morton C.C., McMahon A.P., Powers D., et al. // *N. Engl. J. Med.* 2004. V. 350. № 13. P. 1353–1356.
9. Thomson J.A., Itskovitz-Eldor J., Shapiro S.S., Waknitz M.A., Swiergiel J.J., Marshall V.S., Jones J.M. // *Science*. 1998. V. 282. № 5391. P. 1145–1147.
10. Lagarkova M.A., Shutova M.V., Bogomazova A.N., Vassina E.M., Glazov E.A., Zhang P., Rizvanov A.A., Chestkov I.V., Kiselev S.L. // *Cell Cycle*. 2010. V. 9. № 5. P. 937–946.
11. Nekrasov E.D., Vigont V.A., Klyushnikov S.A., Leb-edeveva O.S., Vassina E.M., Bogomazova A.N., Chestkov I.V., Semashko T.A., Kiseleva E., Suldina L.A., et al. // *Mol. Neurodegener.* 2016. V. 11. № 27.
12. International Stem Cell Initiative, Amps K., Andrews P.W., Anyfantis G., Armstrong L., Avery S., Baharvand H., Baker J., Baker D., Munoz M.B., et al. // *Nat. Biotechnol.* 2011. V. 29. № 12. P. 1132–1144.
13. Altarescu G., Renbaum P., Eldar-Geva T., Brooks B., Varshaver I., Avitzour M., Margalioth E.J., Levy-Lahad E., Elstein D., Epsztejn-Litman S., et al. // *Prenat. Diagn.* 2011. V. 31. № 9. P. 853–860.
14. Masui S., Ohtsuka S., Yagi R., Takahashi K., Ko M.S., Niwa H. // *BMC Dev. Biol.* 2008. V. 8. № 45.
15. Bhatia S., Pilquil C., Roth-Albin I., Draper J.S. // *PLoS One*. 2013. V. 8. № 2. e57276.
16. Feng Q., Lu S.J., Klimanskaya I., Gomes I., Kim D., Chung Y., Honig G.R., Kim K.S., Lanza R. // *Stem Cells*. 2010. V. 28. № 4. P. 704–712.
17. Bock C., Kiskinis E., Verstappen G., Gu, H., Boulting G., Smith Z.D., Ziller M., Croft G.F., Amoroso M.W., Oakley D.H., et al. // *Cell*. 2011. V. 144. P. 439–452.
18. Rouhani F.J., Nik-Zainal S., Wuster A., Li Y., Conte N., Koike-Yusa H., Kumasaka N., Vallier L., Yusa K., Bradley A. // *PLoS Genet.* 2016. V. 12. № 4. e1005932.
19. Lagarkova M.A., Volchkov P.Y., Lyakisheva A.V., Philonenko E.S., Kiselev S.L. // *Cell Cycle*. 2006. V. 5. № 4. P. 416–420.
20. Allegrucci C., Wu Y.Z., Thurston A., Denning C.N., Pridde H., Mummery C.L., Ward-van Oostwaard D., Andrews P.W., Stojkovic M., Smith N., et al. // *Hum. Mol. Genet.* 2007. V. 16. № 10. P. 1253–1268.

Voltage-Dependent Interaction of Capsaicin and Protons on TRPV1-Receptors

E.A. Tsvetkov^{1,2}, N.N. Potatieva¹, K.V. Bolshakov^{1,2*}

¹Sechenov Institute of Evolutionary Physiology and Biochemistry of the Russian Academy of Sciences (IEPhB RAS), pr. Torez 44, St. Petersburg, 194223, Russia

²Federal State Budgetary Educational Institution of Higher Professional Education «Saint-Petersburg State University», Universitetskaya nab. 7–9, St. Petersburg, 199034, Russia

*E-mail: k.bolshakov@biotechnologies.ru

Received May 31, 2016; in final form, November 21, 2016

Copyright © 2017 Park-media, Ltd. This is an open access article distributed under the Creative Commons Attribution License, which permits unrestricted use, distribution, and reproduction in any medium, provided the original work is properly cited.

ABSTRACT The interaction of TRPV1-receptors agonists (capsaicin and protons) has been studied on cultured CHO cells transfected by TRPV1-receptors. Using the whole-cell patch-clamp approach, it was shown that summation of the currents induced by agonist application was dependent on the membrane potential. The TRPV1-mediated currents induced by the pH and Capsaicin demonstrated arithmetical summation at potentials between 40–40 mV, while they were potentiated at potentials below -40 mV. Currents induced by the pH and Capsaicin combined were higher in comparison with the arithmetic sum of the currents induced by the pH and Capsaicin applied separately at such potentials. Such a potential dependence seems to be a base of the sensitization that is induced by inflammation or pain, when concentrations of proinflammatory mediators acting as TRPV1 agonists are increasing. Further depolarization induced by TRPV1 activation doesn't generate potentiation, which might serve as a protective mechanism to restrict their activity.

KEYWORDS TRPV1, Capsaicin, pH, Agonists of TRPV1-receptors, Interaction of agonists of TRPV1-receptors.

ABBREVIATIONS CHO – Chinese Hamster Ovary (cells of connective tissue of Chinese hamster ovary); TRPV1 – Transient Receptor Potential channel subfamily V member 1 (vanilloid receptor, type 1); GFP – Green Fluorescent Protein; MP – membrane potential.

INTRODUCTION

Capsaicin receptors (TRPV1) are complexly organized polymodal sensory systems that react to a variety of stimuli of both chemical and physical nature [1–12]. In most cases, these stimuli cause the opening of a pore of the channel-receptor complex and elicit a transmembrane ion current.

The polymodality of TRPV receptors allows them to react not only to the application of individual agonists, but also to their combinations. The latter generally causes a mutual potentiation of responses, and this phenomenon has been previously described for various combinations of agonists, including capsaicin, arachidonic acid derivatives, pH, as well as physical stimuli such as changes in temperature, membrane potential or pressure [1–13]. In particular, the data show that extracellular acidification of the environment increases TRPV1 receptors' sensitivity to capsaicin [4, 14, 15], while an increase in temperature shifts their activation by potential toward depolarization [16].

Since acidification of the environment is an important sign of a developing inflammatory response [17],

potentiation of TRPV1 receptors, when combined with the effect of other agonists (e.g. capsaicin), can be considered as part of the signaling mechanism triggered in a cell in response to inflammation. Elucidation of the phenomenology of such potentiation and its mechanism are of practical interest both for understanding the inflammatory process itself and for studying ways to attenuate it.

Nevertheless, an analysis of the published data reveals that understanding of the potentiation of TRPV1 receptors, observed after their simultaneous activation by two agonists, is incomplete. In particular, there are no data on whenever this interaction may depend on the membrane potential, which is an important parameter of a cell that affects both the signaling cascades and receptors themselves, including capsaicin receptors.

The aim of this work was to study the interaction of capsaicin and pH at different membrane potentials.

It has been demonstrated that nonlinear summation of TRPV1 receptor responses to combined exposure to protons and capsaicin is observed only at potentials

close to the resting potential. When the membrane is depolarized due to the development of an inflammation or various pathologies, the summation becomes linear. This property of TRPV1 receptors seems to be protective, limiting their hyperactivation in pathological conditions.

EXPERIMENTAL PART

The work was performed on recombinant TRPV1 receptors constitutively or transiently expressed in CHO cells. CHO cells were cultured under standard conditions in a DMEM/F12 medium (Dulbecco's modified Eagle's medium, Biotech) with 10% fetal bovine serum (Hyclone) and 1% gentamycin in a humidified incubator, at 5% CO₂ and 37°C. Transfection was performed with lipofectamine-2000 (Invitrogen, USA) according to the manufacturer's recommendations. For transfection, 0.5 µg of the plasmid encoding TRPV1 and 0.5 µg of the plasmid encoding the eGFP gene were added to a 35-mm Petri dish with the CHO culture. The plasmids were provided by Dr. Staruschenko and Dr. Medina, respectively. The experiments were performed on Days 2 to 5 after the transfection. The transfection efficiency was assessed by the fluorescence intensity of GFP, as measured by a MF-51 microscope. Part of the work was performed on constitutively transfected CHO cells, kindly provided by E.V. Grishin. There were no differences between the two types of transfection: therefore, the data were combined.

Agonist-evoked currents were recorded at different membrane potentials in the voltage clamp "whole cell" mode. The EPC10 amplifier (HEKA Elektronik, USA) and the PatchMaster v8.2 software package (HEKA Elektronik) were used in the study. The test solutions were applied using a NANION solution exchange system (Nanion, Germany) through a micro-manifold with an internal diameter of 250 µm; the time for replacing the solution was about 100 ms. To reduce the desensitization of the receptors due to repeated application of solutions, the frequency of their application did not exceed 1 time in 45 s. The recording pipettes were prepared on a P-87 microfuge (Sutter Instruments Co., USA) from borosilicate capillaries with a filament (Sutter Instruments Co.). The outer and inner diameters of the capillaries were 1.5 and 0.86 mm, respectively. The resistance of the filled pipettes was 3–6 MΩ. For electrophysiological tests, the cells were transferred to a solution with the following composition (mM): 140 NaCl, 5 KCl, 1 MgSO₄, 2.5 CaCl₂, 10 glucose; 10 HEPES, pH 7.4. The composition of the pipette solution (mM): 100 CsF, 40 CsCl, 5 NaCl, 0.5 EGTA, 10 HEPES, pH 7.2. Reagents from Sigma (USA) were used for the preparation of the solutions. Capsaicin was diluted according to the recommendations of the manu-

facturer (Sigma), in 96% ethanol to a concentration of 10 mM, and the required amount was added to obtain the indicated final concentrations.

Statistical processing of the data was performed in EXCEL. The comparison of mean values and assessment of their placement into one/different sets was carried out using the paired Student t-test, since the sets of means were obtained on the same cell. Since different cells had different amplitudes of responses to capsaicin and protons (due to differences in receptor density and cell size), for measurement of the potentiating effect we normalized the amplitudes of the current of each cell by the amplitude of the capsaicin response of that cell. The EC₅₀ and Hill coefficient were estimated using the ORIGIN package with approximation of the experimental data to the theoretical curve by Hill's equation: $I = I_{max} / (1 + (EC_{50}/[C])^s)$, where I_{max} is the current amplitude at the saturating concentrations of the ligands, capsaicin or pH; I is the current amplitude at the current ligand concentration $[C]$; EC₅₀ is the concentration of the half-maximum effect; and s is the Hill coefficient. EC₅₀ for proton concentration is indicated in the text in units of acidity, pH₅₀.

RESULTS AND DISCUSSION

To study the combined effect of the TRPV1 receptor agonists, we first assessed the range of the working concentration for the application of each agonist alone. For this purpose, dose-response curves were obtained for capsaicin and pH at a membrane potential of -80 mV. The results are shown in *Fig. 1*. The data show that responses to acidification of the environment start to appear at pH 6.5, and their amplitude subsequently increases with increasing acidity and reached saturation at pH 5.5 and above. Responses to capsaicin started to appear at a concentration of 0.01 µM and reached saturation at values close to 100 µM. However, as the concentration of capsaicin increased, the amplitude of the responses decreased. The drop in the response amplitude at high concentrations of capsaicin may be associated with its nonspecific action on the cell membrane. Therefore, concentrations of capsaicin above 100 µM were not used in the subsequent experiments. EC₅₀ calculated from these experiments for capsaicin was 2.2 ± 1.2 µM ($n = 10$), and pH₅₀ for TRPV1 receptors was 6.0 ± 0.05 ($n = 10$), which agrees well with the published data [4]. It should be noted that neither capsaicin nor pH in the studied concentrations elicited a current in non-transfected CHO cells. Responses to capsaicin and pH in transfected cells were blocked by 10 µM ruthenium red. This indicates that the currents recorded under these conditions are mediated by the TRPV1 receptors.

The following protocol was used to study the interactions of the proton and capsaicin effects at different

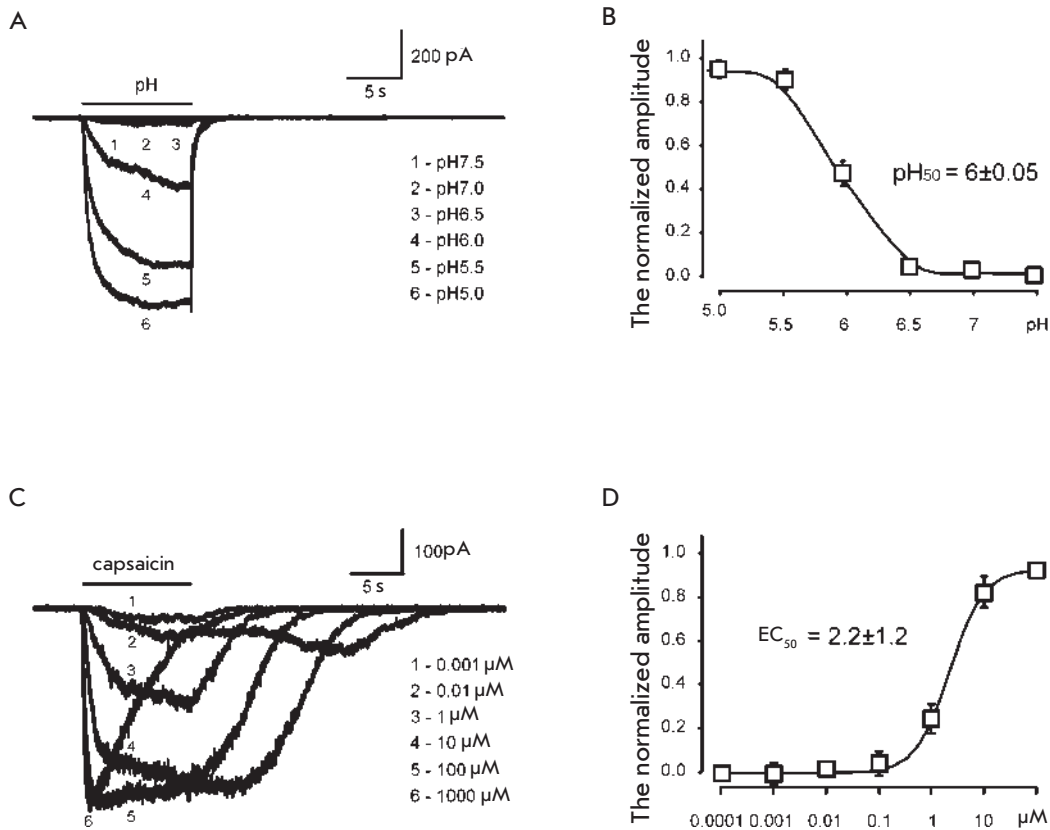


Fig. 1. The sensitivity of TRPV1 receptors to capsaicin and pH.

A: The responses of a representative cell elicited by the application of a solution with a different pH.

B: The dose-response curve, normalized to the amplitude of the current elicited by a solution with pH5.0; $pH_{50} = 6.0 \pm 0.05$; $n = 10$.

C: The responses of a representative cell elicited by the application of a solution with a different concentration of capsaicin.

D: The dose-response curve, normalized by the amplitude of the current elicited in a solution at a saturated concentration of capsaicin; $EC_{50} = 2.2 \pm 1.2 \mu$ M; $n = 10$.

potentials. First, we recorded the response to the application of a solution with a certain pH, then the response to a solution of capsaicin at a certain concentration; then, we applied the solution with both the pH and capsaicin concentrations as described above. In a separate series of experiments, we showed that a change in the order (sequence) of the application of agonists did not affect the amplitudes of the responses. The data analysis included a comparison of the response amplitude for a combined application of capsaicin and protons ($I_{(pH+Cap)}$) with the sum of the response amplitudes ($I_{pH} + I_{Cap}$) obtained when capsaicin (I_{Cap}) and proton (I_{pH}) were applied separately. The obtained data are shown in *Fig. 2*, where 0.1 μ M and pH 5.0 were taken as the test concentrations of capsaicin and protons, respectively. *Figure 2* demonstrates that the amplitude of the responses to the combined application of the agonists used ($I_{(pH+Cap)}$) can significantly exceed the sum of the response amplitudes ($I_{pH} + I_{Cap}$) obtained when capsaicin (I_{Cap}) and pH (I_{pH}) are applied separately. This potentiation depends on the level of the membrane potential and is most pronounced under conditions of hyperpolarization of the cell. At a potential of -40 mV, the current amplitude caused by 0.1 μ M capsaicin at pH 5.0 significantly exceeded the sum of the responses

caused by the application of 0.1 μ M capsaicin, followed by the lowering of pH to 5.0 ($p < 0.01$); at a potential of -120 mV, this difference was significant at $p < 0.001$. Displacement of the MP towards the depolarization lowers the value of potentiation and brings the amplitude of the response for a combined application of capsaicin and protons closer to the sum of the responses for their individual application. At 20 and -20 mV, the differences between the amplitudes of the response to a combined treatment and the sum of the amplitudes of the individual responses to agonists are unreliable.

For a more detailed characterization of the phenomenon of TRPV1 receptors potentiation, similar experiments were repeated at different concentrations of the agonists. The range of capsaicin concentration varied from 0.1 to 10 μ M; and pH levels, from 5.5 to 7.0. The ratio of the amplitude of the current elicited after a combined application of the agonists ($I_{(pH+Cap)}$) to the sum of the amplitudes of the currents elicited by an individual application of these agonists ($I_{pH} + I_{Cap}$) was used as a parameter for evaluating the potentiation. The values of $(I_{(pH+Cap)})/(I_{pH} + I_{Cap})$ are presented in *Fig. 3* in graphic form. In this figure, the columns present the data obtained at the same pH values, where the concentration of capsaicin was varied, while the rows

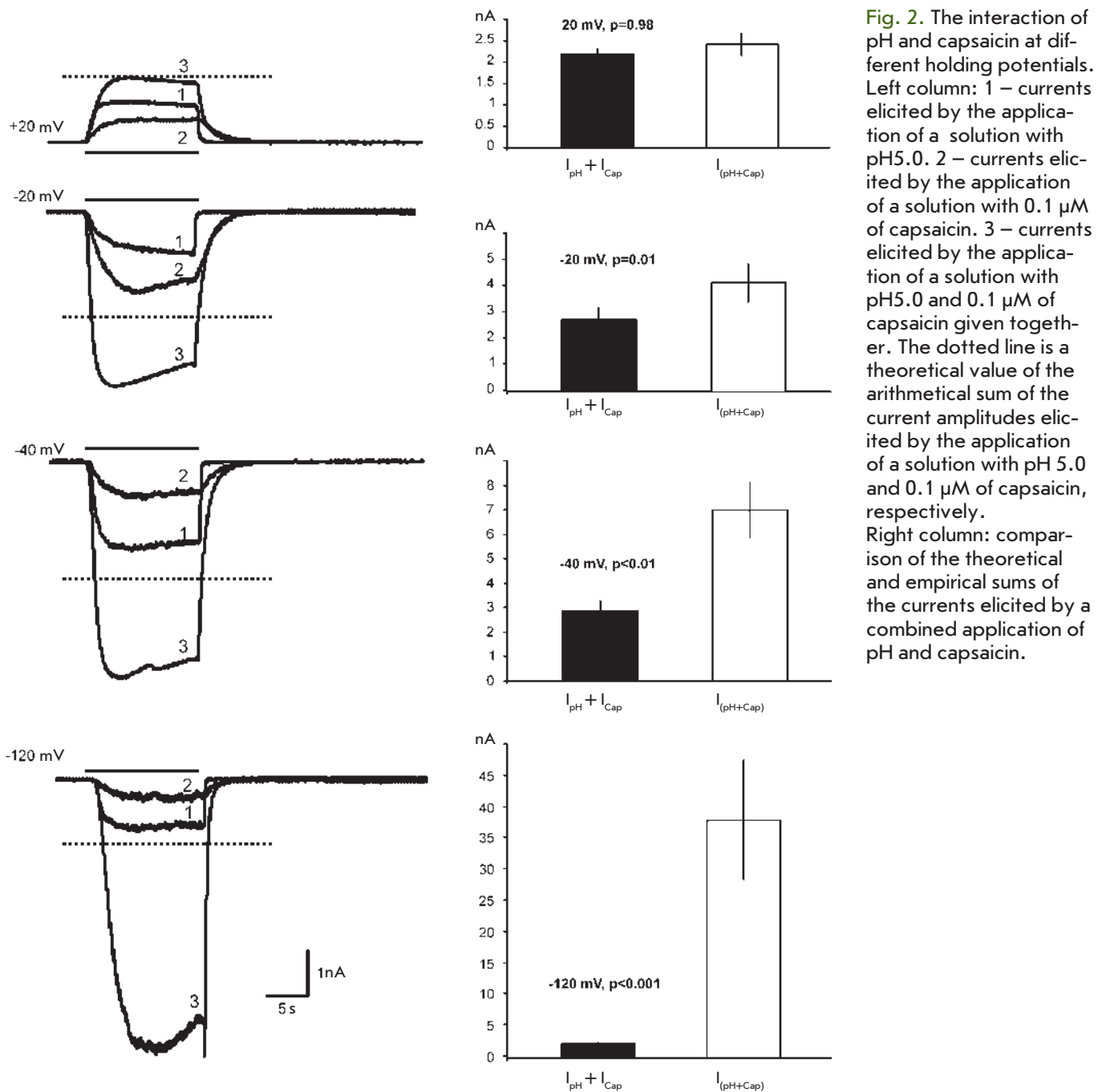


Fig. 2. The interaction of pH and capsaicin at different holding potentials. Left column: 1 – currents elicited by the application of a solution with pH5.0. 2 – currents elicited by the application of a solution with 0.1 μM of capsaicin. 3 – currents elicited by the application of a solution with pH5.0 and 0.1 μM of capsaicin given together. The dotted line is a theoretical value of the arithmetical sum of the current amplitudes elicited by the application of a solution with pH 5.0 and 0.1 μM of capsaicin, respectively. Right column: comparison of the theoretical and empirical sums of the currents elicited by a combined application of pH and capsaicin.

present the data obtained at the same concentrations of capsaicin, where the pH was varied. It should be noted that the potentiation effect was not observed at a capsaicin concentration greater than 10 μM ; therefore, no experiments with a higher concentration of the agonist were performed.

Figure 3 shows that the potentiation effect depends on all the parameters controlled in these tests. The greatest effect was observed under conditions of maximum cell hyperpolarization with maximum acidifica-

tion of the environment and the lowest concentrations of capsaicin (see upper left corner of the table in Fig. 3). It is clear that the extent of potentiation of TRPV1 receptors directly depends on the concentration of protons and increases with acidification at a constant concentration of capsaicin. The potentiating effect of pH better manifests itself at low concentrations of capsaicin and practically disappears when the concentration reaches 10 μM . Thus, there is an inverse relationship between the potentiation of the pH-response and the

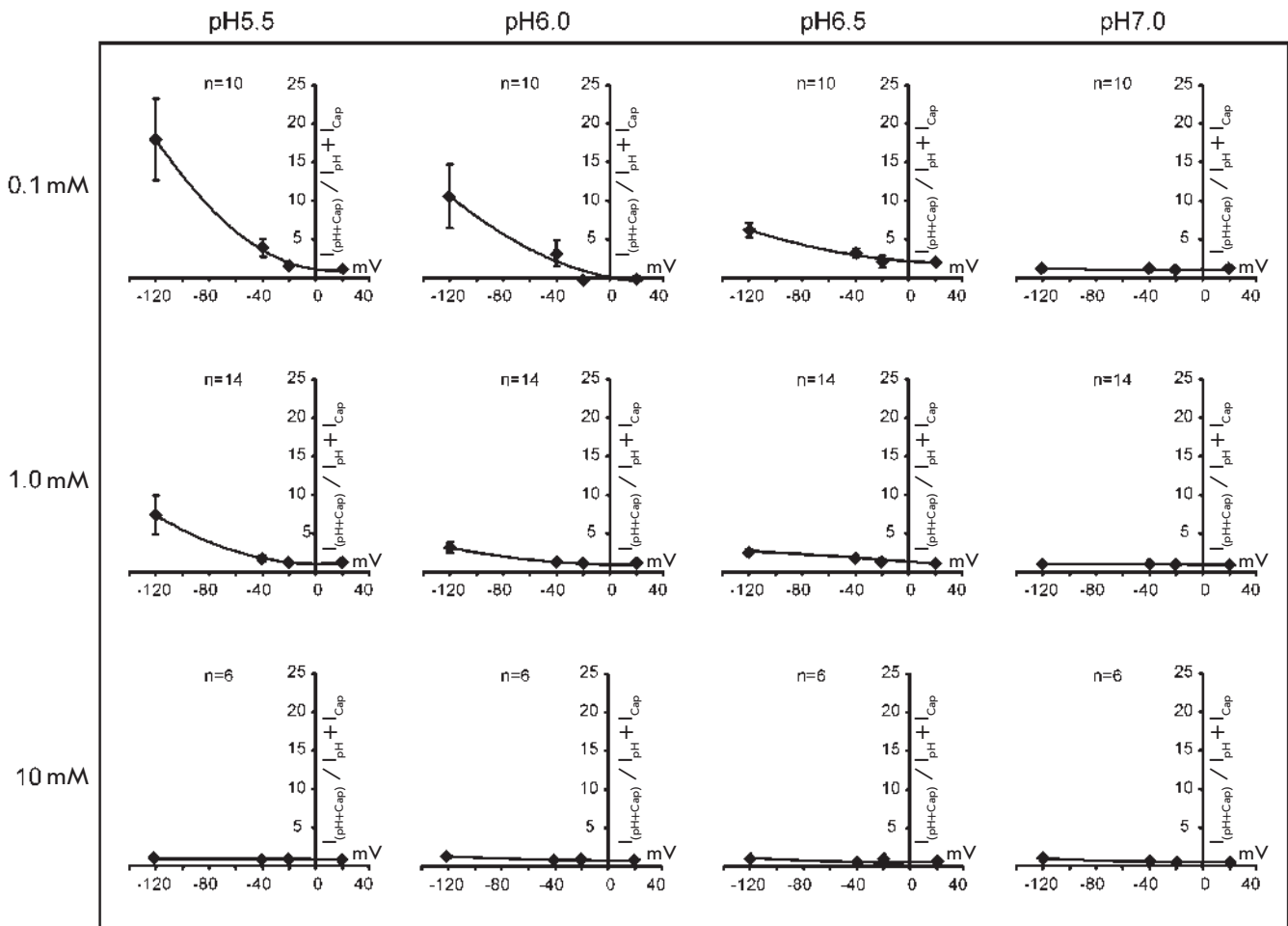


Fig. 3. The dependence of capsaicin receptors potentiation on the membrane potential at different pH and capsaicin concentrations. Explanation of the experimental protocol and the analysis procedure are given in the text.

capsaicin concentration, and an increase in the concentration of capsaicin results in a decrease in the potentiation.

The sensitivity of the potentiation of capsaicin receptors to the membrane potential of the cell suggests that the application of capsaicin in conditions of lower pH of the environment would lead to a change in the current-voltage relationship of the capsaicin receptor responses to the action of the agonists. To verify this assumption, we compared the current-voltage relationship of the channels obtained by activating the receptors with capsaicin, pH, and the combined application of these agents at concentrations which corresponded to the maximum value of the potentiation effect in the previous experiments. The result of these experiments is shown in *Fig. 4*. The responses to pH and capsaicin are characterized by inward rectification, which

agrees well with the published data [2, 14]. In the case of a combined application of protons and capsaicin, the degree of rectification decreases. The weakening of the rectifying properties of TRPV1 receptors can be considered as an element of the mechanism that regulates the signaling functions of the receptors during the development of inflammatory reactions, pain, thermoregulation, and other functions in which TRPV1 receptors are involved [1–12].

The data obtained is insufficient to draw a definite conclusion on the mechanisms of potentiation of capsaicin receptors in the case of a combined application of capsaicin and protons. However, considering the change in the rectifying properties of the channel observed when the agonists are applied together, the potential mechanism of this phenomenon can be both a voltage-dependent increase in the sensitivity of these

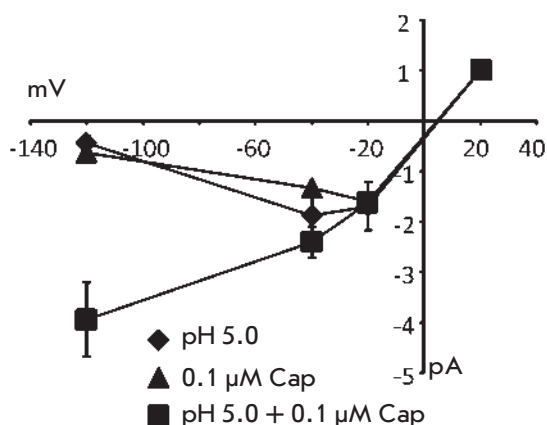


Fig. 4. I/V relationship of TRPV1-receptor responses elicited by the application of agonist. Triangles – I/V relationship of TRPV1-receptor responses elicited by the application of a solution with 0.1 μM of capsaicin. Rhombs – I/V relationship of the TRPV1-receptor responses elicited by the application of a solution with pH5.0. Rectangles – I/V relationship of the TRPV1-receptor responses elicited by the application of a solution with pH5.0. and 0.1 μM capsaicin given together.

receptors to one of the agonists in the presence of the other and a modification of the parameters of receptor inactivation under these experimental conditions. Verification of these assumptions and identification of

the mechanisms of interaction between the responses caused by the activation of the receptors by protons and capsaicin at different potentials, as well as the elucidation of the physiological significance of this interaction, requires further studies.

CONCLUSION

The identified relationships between the potentiating action of TRPV1 agonists when they are applied together and the membrane potential reveals another feature of TRPV1 receptors that allows them to fine-tune their response to a combination of external and internal factors. For example, the potentiation of TRPV1 responses under hyperpolarization conditions enables the involvement of these receptors in an early stage of inflammation, when the concentration of inflammatory agents is not yet too high. Since the triggering of these receptors can be associated with the initiation of apoptosis, the disappearance of a response potentiation to a combined application of the agonists under conditions of depolarization will serve as a protective mechanism. However, understanding of the functional significance of the amplitude of TRPV1 responses, as well as the elucidation of the molecular mechanisms that mediate the interaction of the different agonists of these receptors, requires further research.

This work was supported by the Russian Foundation for Basic Research (Grant No. 15-04-03957) and Presidium of RAS program Molecular and cell biology.

REFERENCES

- Zhu M.X. TRP channels. Boca Raton: Taylor & Francis, 2011.
- Caterina M.J., Schumacher M.A., Tominaga M., Rosen T.A., Levine J.D., Julius D. // *Nature*. 1997. V. 389. № 6653. P. 816–824.
- Blumberg P.M., Pearce L.V., Lee J. // *Curr. Top Med. Chem.* 2011. V. 11. № 17. P. 2151–2158.
- Vanilloid Receptor TRPV1 in Drug Discovery: Targeting Pain and Other Pathological Disorders / Eds Gomtsyan A., Faltynek C.R. Hoboken, New Jersey: John Wiley & Sons, Inc., 2010.
- Venkatachalam K., Montell C. // *Annu. Rev. Biochem.* 2007. V. 76. P. 387–417.
- Nilius B., Voets T. // *Pflügers Arch.* 2005. V. 451. № 1. P. 1–10.
- Pedersen S.F., Owsianik G., Nilius B. // *Cell Calcium*. 2005. V. 38. № 3–4. P. 233–252.
- Voets T., Talavera K., Owsianik G., Nilius B. // *Nat. Chem. Biol.* 2005. V. 1. № 2. P. 85–92.
- Ramsey I.S., Delling M., Clapham D.E. // *Annu. Rev. Physiol.* 2006. V. 68. P. 619–647.
- Nilius B. // *Biochim. Biophys. Acta*. 2007. V. 1772. № 8. P. 805–812.
- Nilius B., Owsianik G., Voets T., Peters J.A. // *Physiol. Rev.* 2007. V. 87. № 1. P. 165–217.
- Nilius B., Mahieu F. // *Mol. Cell*. 2006. V. 22. № 3. P. 297–307.
- Dhaka A., Uzzell V., Dubin A.E., Mathur J., Petrus M., Bandell M., Patapoutian A. // *J. Neurosci.* 2009. V. 29. № 1. P. 153–158.
- Tominaga M., Caterina M.J., Malmberg A.B., Rosen T.A., Gilbert H., Skinner K., Raumann B.E., Basbaum A.I., Julius D. // *Neuron*. 1998. V. 21. № 3. P. 531–543.
- Ryu S., Liu B., Qin F. // *J. Gen. Physiol.* 2003. V. 122. № 1. P. 45–61.
- Voets T., Droogmans G., Wissenbach U., Janssens A., Flockerzi V., Nilius B. // *Nature*. 2004. V. 430. № 7001. P. 748–754.
- Grivennikov S.I., Greten F.R., Karin M. // *Cell*. 2010. V. 140. № 6. P. 883–899.

Dual Active Site in the Endolytic Transglycosylase gp144 of Bacteriophage phiKZ

O.V. Chertkov¹, G.A. Armeev², I.V. Uporov³, S.A. Legotsky³, N.N. Sykilinda¹, A.K. Shaytan², N.L. Klyachko³, and K.A. Miroshnikov^{1*}

¹Shemyakin and Ovchinnikov Institute of Bioorganic Chemistry, Mikluho-Maklaya str. 16/10, Moscow, 117997, Russia

²Lomonosov Moscow State University, Biology department, Leninskie Gory 1, bld. 12, Moscow, 119991, Russia

³Lomonosov Moscow State University, Chemistry department, Leninskie Gory 1, bld. 11, Moscow, 119991, Russia

*E-mail: kmi@ibch.ru

Received April 01, 2016; in final form, June 10, 2016

Copyright © 2017 Park-media, Ltd. This is an open access article distributed under the Creative Commons Attribution License, which permits unrestricted use, distribution, and reproduction in any medium, provided the original work is properly cited.

ABSTRACT Lytic transglycosylases are abundant peptidoglycan lysing enzymes that degrade the heteropolymers of bacterial cell walls in metabolic processes or in the course of a bacteriophage infection. The conventional catalytic mechanism of transglycosylases involves only the Glu or Asp residue. Endolysin gp144 of *Pseudomonas aeruginosa* bacteriophage phiKZ belongs to the family of Gram-negative transglycosylases with a modular composition and C-terminal location of the catalytic domain. Glu115 of gp144 performs the predicted role of a catalytic residue. However, replacement of this residue does not completely eliminate the activity of the mutant protein. Site-directed mutagenesis has revealed the participation of Tyr197 in the catalytic mechanism, as well as the presence of a second active site involving Glu178 and Tyr147. The existence of the dual active site was supported by computer modeling and monitoring of the molecular dynamics of the changes in the conformation and surface charge distribution as a consequence of point mutations.

KEYWORDS bacteriophage phiKZ, endolysin, enzyme active site, molecular dynamics, site-directed mutagenesis, transglycosylase.

ABBREVIATIONS gp – gene product; NAM – *N*-acetylmuramic acid; NAG – *N*-acetylglucosamine.

INTRODUCTION

Bacteriophage phiKZ (vB_PaeM_KZ, GenBank NC_004629) belongs to the *Myoviridae* family and is a type representative of the genus of giant phages that infect the Gram-negative bacteria *Pseudomonas aeruginosa* and some close relatives [1]. PhiKZ-like phages are used as objects in various genomic [2], evolutionary [3], and structural [4–6] studies.

At the late stages of a phage phiKZ infection, the host bacteria are lysed by the peptidoglycan degrading enzyme (endolysin) gp144. This protein has a modular structure and consists of two domains: the *N*-terminal one responsible for primary binding to the substrate, and the *C*-terminal domain with catalytic properties [7]. The peptidoglycan binding function of the *N*-terminal domain of the polypeptide (amino acid residues 9–69) has been confirmed experimentally using a construction with a fused green fluorescent protein [8, 9]. The *C*-terminal domain of gp144 (amino acid residues 70–260) demonstrates strong homology to class

1 lytic transglycosylases. The catalytic mechanism has been proved by mass spectrometric analysis of peptidoglycan cleavage products [10]. Lytic transglycosylases are the enzymes that cleave the β -1,4-glycosidic bond between *N*-acetylmuramic acid (NAM) and *N*-acetylglucosamine (NAG), yielding the cyclic anhydride of *N*-acetylmuramic acid (the bond between O6 and C1 atoms) [11]. The phiKZ gp144 spatial structures of apoenzyme (3BKV) and the enzyme bound to a chitotetraose molecule (3BKH) were determined by X-ray crystallography with 2.6 Å resolution [12]. The *C*-terminal domain mostly consists of α -helices and is structurally homologous to the catalytic domain of class 1 lytic transglycosylases. According to the widely accepted model [11], the only amino acid residue in the active site is responsible for the catalytic properties: in phiKZ gp144, that residue is Glu115 [12]. However, the mutagenesis of this residue does not completely inactivate the enzyme, leaving ~30% of the activity for the mutant protein [8]. Hence, this study was aimed at

shedding light on the role of other amino acid residues in the phiKZ gp144 catalysis and refining the structural organization of the active site.

EXPERIMENTAL

Site-directed mutagenesis

The key manipulations involved in the molecular cloning in *Escherichia coli* were performed as described previously in [13]. Plasmid pKZ144 bearing gene 144 of bacteriophage phiKZ in a pQE30 (Qiagen) vector was used as the template for point mutagenesis [7]. The QuickChange Kit (Stratagene) was used for site-directed mutagenesis. The following primers were employed for polymerase chain reaction (PCR):

E115A Fw 5'-CATTGCTTCTATTG**C**ATCAGCAT-TCGATTAC-3',

E115A Re 5'-GTAATCGAATGCTAG**TG**CAATA-GAAGCAAATG-3',

H200L Fw 5'-GATCTTTAGCT**CT**CTTCTTTG-GGCCTGG-3',

H200L Re 5'-CCAGGCCCA**AAGAA**GA-GAGCTAAATAAAGATC-3',

Y197F Fw 5'-ACTGATACTGATCTTT**TTTT**TAGCT-CACTTCTTT-3',

Y197F Re 5'-AAAGAAGTGAGCTAA**AAAA**AGAT-CAGTATCAGT-3'.

E178A Fw 5'-GCGGAACTGATTA**AGCAA**ACAT-GAACATTCTG-3', and

E178A Re 5'-CAGAATGTT**CA**TGTT**TG**CTTAAT-CAGTTCCGC-3'.

After PCR, the plasmid carrying the gene encoding the wild-type enzyme was degraded using DpnI endonuclease specific to methylated DNA. The resulting material was used for electroporation of NovaBlue *E. coli* cells (Novagen) plated onto Petri dishes with a LB agar medium containing 100 µg/ml ampicillin, and cultured at 37°C for 16 h. The plasmids pKZ144-E115A, pKZ144-H200L, pKZ144-Y197F, pKZ144-E115A/H200L, pKZ144-E115A/Y197F, pKZ144-H200L/Y197F, pKZ144-E178A, and pKZ144-E115A/E178A were isolated from the individual clones using the Qia-Quick Spin kit (Qiagen), and sequenced to verify a target mutation.

Isolation and purification of the proteins

AD494(DE3) *E. coli* cells (Novagen) transformed with the corresponding plasmids were cultured in a 2xYT medium at 37°C until $A_{600} \sim 0.6$ rel. units; then, expression was induced by adding isopropylthio- β -D-galactoside to a final concentration of 0.5 mM. The cells were further incubated at 37°C under moderate aeration for 4 h. Then, the cells from 0.15 L of the culture were precipitated by centrifugation at 3,500 rpm for

15 min; the precipitate was re-suspended in 10 mL of buffer A (20 mM Tris-HCl 8.0, 100 mM NaCl, 1 mM o-phenylmethanesulfonyl fluoride (PMSF)). The cells were ultrasonically disintegrated (Techpan MD20); the insoluble fragments were separated by centrifugation at 15,000 rpm for 20 min. The supernatant was applied to a Ni-NTA-agarose column (Qiagen). The affine bound protein was eluted with 200 mM imidazole in buffer A and dialysed against 20 mM Tris-HCl pH 8.0, 50 mM NaCl buffer, then stored at -70°C. The protein concentration was determined spectrophotometrically by measuring the absorbance at 280 nm on a GENESYS 10 spectrophotometer (Thermo Electron). The extinction coefficient was calculated using the VectorNTI software based on the concentration of aromatic residues in a protein molecule. The alterations in the secondary structure of mutant proteins were estimated by circular dichroism spectroscopy on a JASCO J-500 spectropolarimeter in a 0.5 cm cell (Hellma) in sodium phosphate buffer, pH 6.2, at room temperature.

Activity determination

The enzyme activity of the protein samples was determined using a suspension of cell walls of *P. aeruginosa* PAO1, which were obtained by treating cells with chloroform to remove the outer cell membrane, as a substrate. In order to prepare the cell-wall suspension, PAO1 cells were cultured at 37°C in a 2xTY medium until $A_{500} \sim 0.6$ rel. units was achieved. The cells were precipitated by centrifugation at 4,000 rpm for 15 min. The cell precipitate was re-suspended in a 50 mM Tris-HCl buffer (pH 7.8) saturated with chloroform and incubated under stirring at room temperature for 45 min. The remaining cell walls were precipitated by centrifugation at 4,000 rpm for 15 min. The precipitate was re-suspended in a 10 mM sodium phosphate buffer (pH 6.2, 120 mM NaCl), and absorbance at 500 nm was adjusted to 0.6–1 rel. units. A 30 µl enzyme sample was added to the microplate containing 270 µl of the cell-wall suspension, and the decrease in absorbance was measured on a Victor spectrophotometric reader (Perkin Elmer) at room temperature for 1.5 h with a scan step of 1 min. We assumed that one unit of peptidoglycan lysing activity is the activity that causes a linear decrease in absorbance by 0.001 rel. units per minute. The measurement results were processed in the Activity Calculator software [14]. Three replica experiments were performed; the results were averaged and compared with the corresponding negative controls and the positive control containing hen egg-white lysozyme.

Molecular dynamics simulations

The substrate molecule was built and optimized in the Avogadro software [15]. Docking was applied for the

relaxed and subsequently frozen native structure using the SwissDock web service [16], and the resulting structure was selected based on an orientation and position similar to the 3BKV PDB structure [12]. The distribution of the electrostatic potential in the native protein molecule was calculated with the PDB2PQR [17, 18] and APBS software [19].

The conformational mobility of the protein was studied with molecular dynamics. The models based on the AMBER99 force field [20, 21] were built according to the crystal structure of 3BKH [12]. Modeling was carried out in the GROMACS software package [22–25] with the following parameters: simulation time, 100 ns; step, 2 fs; the cut-off radius of van der Waals interactions, 1 nm; the electrostatic interactions were taken into account by the PME method; temperature, 300 K; the protein and the solution were thermostated separately; the periodic boundary conditions with the cubic unit cell were used.

The data was analyzed by comparing the root-mean-square deviation of the structures of the mutants from that of the wild-type enzyme. The conformation of transglycosylase obtained by molecular dynamics simulation at 300 K was assumed to be a reference structure. Comparison was performed for the atoms of the protein backbone of only those amino acids that reside near the substrate (amino acids 110–116, 125–150, 168–185, 195–210, 220–230) and can affect its binding to the enzyme. Since the mobility of the molecule at room temperature was too high to draw any statistically valid conclusions about conformational changes at the available calculation times, we used the method of simulated annealing of the structures to lower the temperatures. The system was gradually frozen within 1 ns from 300 K to the temperature of liquid nitrogen (77 K).

RESULTS

An analysis of the X-ray diffraction data for phiKZ gp144 3BKV [12] demonstrated that the spatial arrangement of Glu115 in the active site with respect to the substrate molecule is not optimal and that there is a possibility that non-canonical amino acid residues are also involved in the catalysis. We suggest that His200 with a reduced electron density, and the highly conserved Tyr197 residue that coordinates a portion of the substrate at the –1 position, could possibly be such residues.

The spatial configuration of phiKZ gp144 3BKV shows that the catalytic domain is very similar to the analogous domain in *E.coli* transglycosylase Slt70 [26]. The position and orientation of the catalytic residue Glu115 in gp144 is similar to the position of Glu478 in Slt70. The mechanism of the catalysis of transglycosylase Slt70 was proposed earlier: it differs from the

conventional mechanism by the involvement of an additional Tyr597 residue that is located in the catalytic site of the enzyme and participates in the catalysis. The function of Tyr597 is to activate the catalytic residue Glu478 via the formation of a hydrogen bond, thus increasing the negative charge on Glu478 and facilitating the protonation of the *O*-glycosidic bond [27]. The phiKZ gp144 polypeptide contains a Tyr197 residue with a position and orientation similar to those of Tyr597 in Slt70. The high degree of spatial homology gives grounds for assuming that the mechanism of catalysis of phiKZ gp144 is similar to that of Slt70.

The key hypothesis explaining why enzyme activity is retained after the main catalytic residue is replaced suggests that there exist two catalytic sites: the principal one, Glu115/Tyr197, and a secondary active site, Glu178/Tyr147. The arrangement of amino acids in the putative secondary active site with respect to the chain of the peptidoglycan substrate is similar to that in the principal active site. Superposition of the side chains of the residues of the principal and secondary active sites by calculating the minimal root-mean-square deviation yields an almost identical position (*Fig. 1*).

A series of single and double point mutants of these amino acids was obtained to experimentally confirm the role of the residues partaking in the functioning of the active site of phiKZ gp144. Insertion of point mutation had no significant effect on the solubility or the secondary structure (as shown by the binding to the affinity column and circular dichroism spectroscopy). The mutant proteins were purified by Ni-chelate chromatography [7] without any significant modifications. The resulting specimens contained 3–6 mg of the mutant protein with > 90% purity.

The single point mutants E115A, E178A, and Y197F (with respect to each individual residue) had residual activities of 54, 63, and 51%, respectively, compared to the intact phiKZ gp144 protein (*Fig. 2, Table 1*). All the mutants exhibited maximum activity in a buffer with the same composition (pH 6.2 and *I* = 120 mM NaCl) as that for the wild-type enzyme. All subsequent reactions proceeded under the same conditions. Mutation in His reduced activity by 20–30%, thus supporting the hypothesis that histidine residues are involved in substrate coordination.

The fact that E115A/Y197F with mutations in both residues of the principal active site and the intact secondary site lost its activity lacks consistency under this hypothesis. In order to interpret this phenomenon, we had to study both the details of the spatial interplay between the protein and the substrate and the possible changes in protein conformation caused by mutations. Since the conformation of the chitotetraose used to emulate the substrate in phiKZ experiments on crystal-

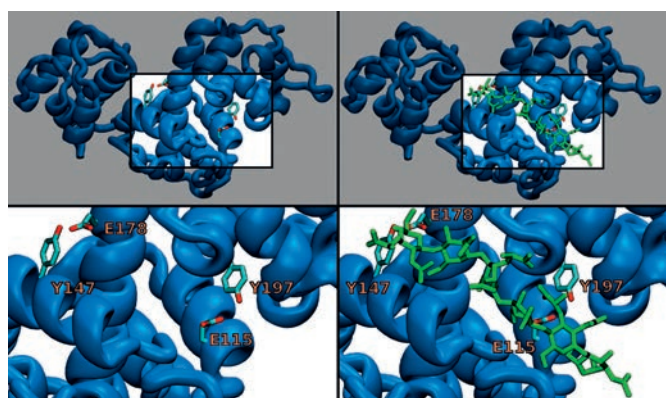


Fig. 1. The side chains of amino acid residues forming the active sites of phiKZ gp144 and the possible location of the NAM–NAG molecule. The top image shows the general view of the enzyme without (top left) and with the substrate (top right). Bottom images provide a close-up view of the binding sites of the enzyme without (bottom left) and with the substrate (bottom right).

lization of gp144 [12] differs rather significantly from that of the natural substrate (NAM–NAG)₃, molecular docking was carried out to compute the possible configurations of substrate binding to the protein molecule. The most plausible arrangement of the substrate in the active site groove is shown in *Fig. 1*.

In order to additionally evaluate the changes in protein conformations with various substitutions, we carried out a molecular dynamic analysis of the groove configuration by studying its appearance (*Fig. 3A*) and the distance between the C α atoms of the amino acid residues 126 and 229 (*Fig. 3B, Table 2*). It is most likely that some mutations disrupt the interaction network between the side chains of the residues forming the active site; so, the domain of the active side groove of phiKZ gp144 changes its conformation rather significantly. For example, mutations in amino acid residues in the principal active site change the shape of the groove where the substrate is packaged, which may reduce protein affinity to the substrate and, therefore, its reactivity. One can see that a double mutation in

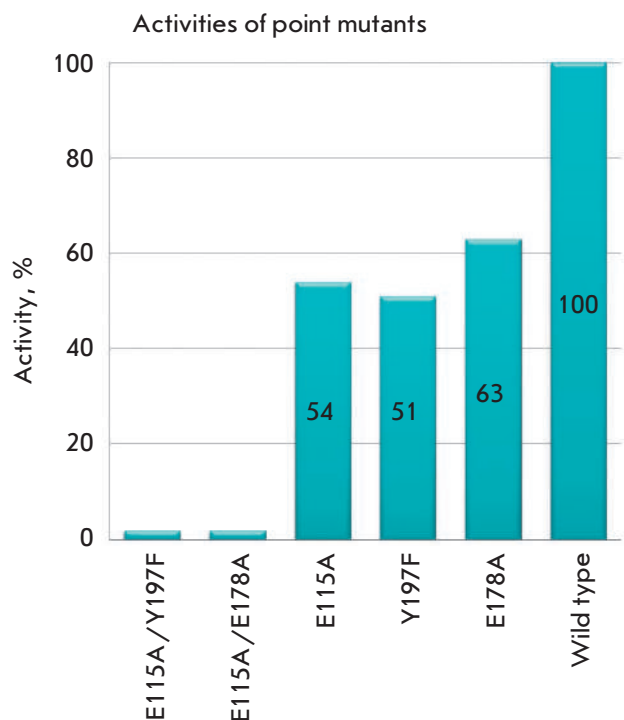


Fig. 2. Activities of single- and double-point phiKZ gp144 mutants compared to that of the wild-type enzyme taken as 100%.

the principal active site results in the most significant groove opening (*Fig. 4*).

Charge distribution over the surface of each mutant accessible to a solvent was calculated. The calculation of the surface charge of a phiKZ gp144 protein globule shows that the substrate-binding groove has a predominantly positive charge. Substitutions of amino acid residues in active sites also significantly change the charge distribution in a number of cases (*Fig. 5*). The E115A/Y197F mutant exhibited no activity, although one of the active sites remained intact. The double point mutation in the closely spaced amino acids drastically changed the conformation of the substrate-binding surface (*Fig. 4*) and altered the charge in this portion of the groove (*Fig. 5*). This change in surface

Table 1. Activities of single- and double-point mutants phiKZ gp144, and the wild-type enzyme.

Enzyme	Wild type	E178A	Y197F	E115A	E115A/ Y197F	E115A /E178A
Activity, U/mg	210000	132000	107000	113000	0	0

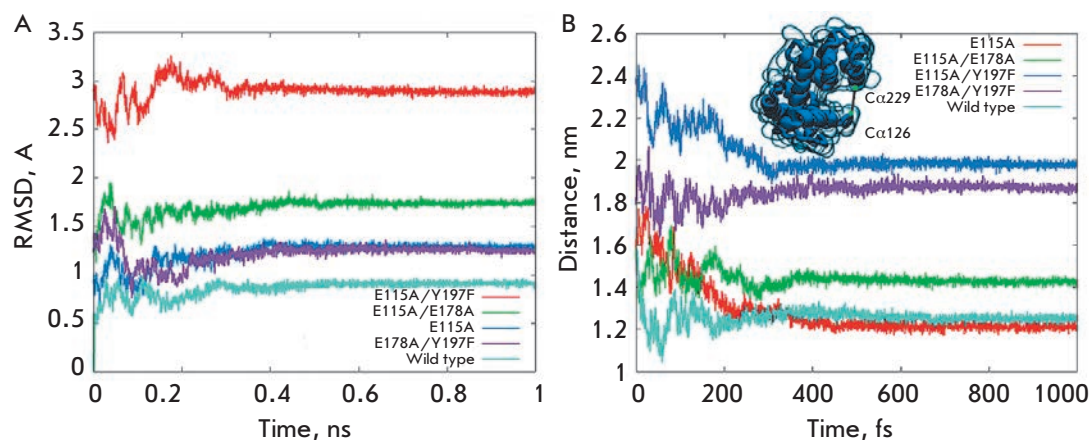


Fig. 3. A – The root-mean-square deviation of the protein backbone of transglycosylases frozen at 77 K. The deviation was calculated only for the area in contact with the substrate. B – Changes in spacing between the C α atoms of the amino acids 126 and 229 during freezing up to 77K.

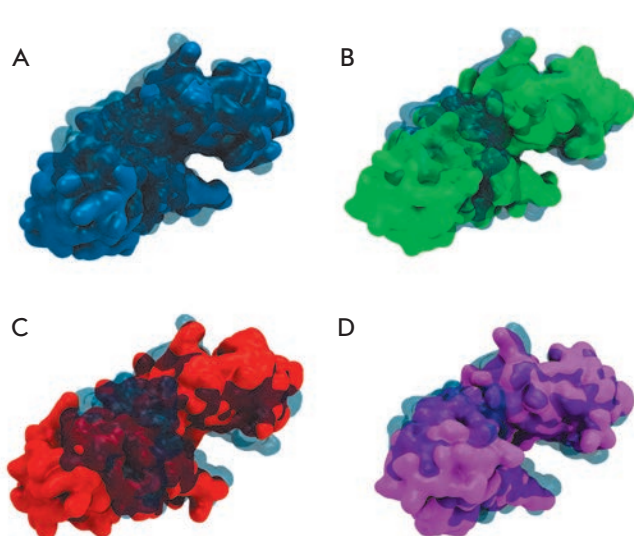


Fig. 4. Surface modeling of the phiKZ gp144 mutants compared to the native form: A – E115A, B – E115A/E178A, C – E115A/Y197F, and D – E178A/Y197F. The translucent surface belongs to the structure of the wild-type enzyme. The domain not involved in binding to the substrate is deleted in the images. The side view of the groove is provided.

properties has the potential to hinder substrate binding by this phiKZ gp144 mutant, thus completely inactivating the enzyme.

DISCUSSION

Lytic transglycosylases belong to the class of peptidoglycan lysing enzymes that play a crucial role in the life cycle of bacteria [28] and bacteriophages [29]. Transglycosylases affect the same peptidoglycan domain as lysozymes ([EC 3.2.1.17]; peptidoglycan-N-acetylmuramoylhydrolases, muramidases): the β -1,4-glycosidic bond between the NAM and NAG residues. The key difference between transglycosylases and muramidases is that transglycosylases contain no nucleophilic catalytic residue. The differences are also manifested in the binding of the oligosaccharide at the binding sites +1 and +2. The classical mechanism of action of transglycosylases suggests that there is one acidic catalytic residue that resides in the active site of the enzyme between the subsites +1 and -1. At the first stage of the

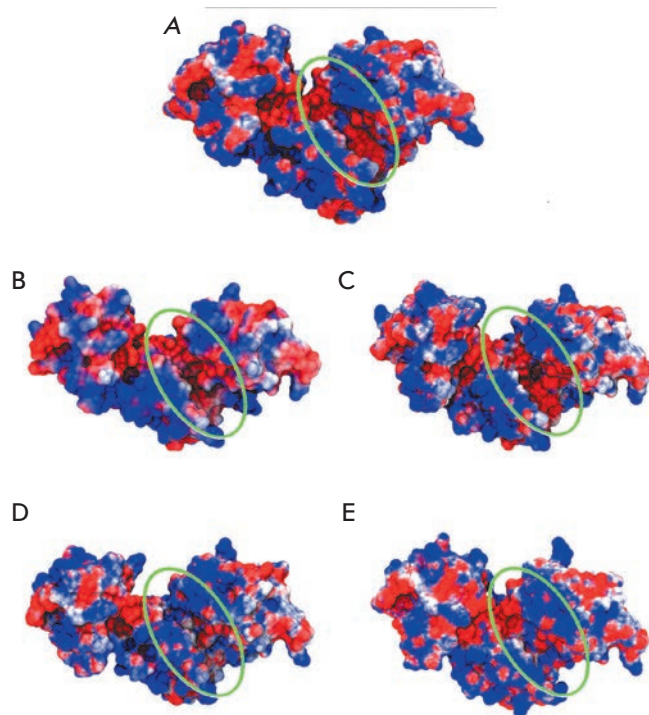


Fig. 5. Charge distribution on the surface of the mutant phiKZ gp144 isoforms. The substrate-binding site is shown with a circle. A) native structure, B) E115A, C) E178A/Y197F, D) E115A/E178A, and E) E115A Y197F.

ramoylhydrolases, muramidases): the β -1,4-glycosidic bond between the NAM and NAG residues. The key difference between transglycosylases and muramidases is that transglycosylases contain no nucleophilic catalytic residue. The differences are also manifested in the binding of the oligosaccharide at the binding sites +1 and +2. The classical mechanism of action of transglycosylases suggests that there is one acidic catalytic residue that resides in the active site of the enzyme between the subsites +1 and -1. At the first stage of the

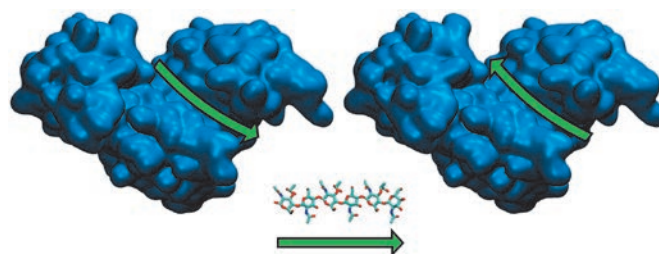
Table 2. Standard deviations of the protein structure during simulated annealing to the temperature of liquid nitrogen.

Enzyme	Mean, Å	Standard deviation, Å	Min, Å	Max, Å
Native	0.858	0.081	0.005	0.974
E115A	1.225	0.118	0.692	1.370
E115A /Y197F	2.895	0.104	2.366	3.249
E178A /Y197F	1.219	0.110	0.762	1.693
E115A /E178A	1.693	0.084	1.130	1.944

reaction, the catalytic amino acid residue protonates the glycosidic oxygen, resulting in the formation of an oxocarbenium cation and further rupture of the *O*-glycosidic bond between NAM and NAG. The second stage of the reaction involves the intramolecular nucleophilic attack of carbon C1 of the oxocarbenium cation by C6 hydroxyl, yielding the 1,6-oxazalone cycle of NAM. The catalytic residue Glu activates C6 hydroxyl by pulling a proton away from the hydroxyl [11].

We suggest that there are two active sites in the polypeptide chain of phiKZ gp144 transglycosylase : a principal one (E115/Y197) and a secondary (E178/Y147) one. A portion of a peptidoglycan molecule can be bound to the groove on the enzyme globule in two ways (*Fig. 6*). The direction of substrate packaging probably matters for the reaction and determines which active site will be responsible for the reaction of substrate degradation. Hence, the corresponding direction of substrate packaging will not be accompanied by enzyme-induced cleavage if one of the domains of the active site is inactivated.

Glu is the key residue that attacks the β -1,4-glycosidic bond. Its substitution results in complete inactivation of one of the active sites, thus reducing enzyme activity twofold. Single-point mutations at the Tyr residue also reduce enzyme activity. In the spatial model of the active site, Glu and Tyr face one another and form a hydrogen bond. They are coordinated in this fashion during almost the entire molecular dynamics simulation. One can suggest that Tyr immobilizes Glu in the spatial position most favorable for the reaction. The substitution of Tyr for Phe shifts the side chain of Glu away from the favorable position and changes the activity of the mutant site. No site activation was detected in the experiment with the double mutant E178A/Y197F. Although one of the active sites was switched off because of Glu substitution, the second one remained active even while lacking the Tyr residue. The double mutant E115A/E178A exhibited no activity, since the attacking Glu residues in both active sites had been substituted.

**Fig. 6.** The possible directions of substrate orientation in the groove of phiKZ gp144. The substrate (*N*-acetylmuramyl-*N*-acetylglucosamine) is shown above the arrow.

The mutant E115A/Y197F exhibits no activity despite the fact that one of the active sites remained in its native state. Double mutation in closely spaced amino acids deeply altered the conformation of the substrate-binding surface (*Fig. 4*) and the charge in this groove portion (*Fig. 5*). This alteration of surface properties probably prevents phiKZ gp144 from binding to the substrate; so, the enzyme becomes completely inactive.

CONCLUSIONS

Our findings support the hypothesis that phiKZ gp144 possesses two active sites and elucidate the catalytic mechanism of this enzyme. The dual active site probably appeared in the course of evolution, as indicated by the high homology between the active site structures.

Numerous strains of pathogenic and opportunistic bacteria resistant to synthetic antibiotics are currently emerging. Enzybiotics, enzymes toxic to bacteria (e.g., peptidoglycan hydrolases), can potentially be used as an alternative to antibiotics [29]. One of the most efficient approaches to designing enzybiotics that would be active with respect to Gram-negative pathogens involves combining enzymes and polycationic peptides [30] or constructing fusion proteins that comprise such peptides (artilysins) [31, 32]. Polycationic peptides fa-

cilitate enzyme penetration through the bacterial outer membrane. In this context, the catalytic domain of phiKZ gp144 is a suitable candidate for designing engineered enzymatic antimicrobial drugs due to its high activity and specificity. A thorough understanding of the mechanisms of action of peptidoglycan lysing en-

zymes would enable us to use them to design more effective agents for combating pathogenic bacteria.

This work was supported by the Russian Science Foundation (grant no. 16-16-00073).

REFERENCES

- Krylov V.N., Dela Cruz D.M., Hertveldt K., Ackermann H.W. // Arch. Virol. 2007. V. 152. № 10. P. 1955–1959.
- Cornelissen A., Hardies S.C., Shaburova O.V., Krylov V.N., Matheus W., Kropinski A.M., Lavigne R. // J. Virol. 2012. V. 86. № 3. P. 1844–1852.
- Krylov V.N., Miroshnikov K.A., Krylov S.V., Veiko V.P., Pletneva E.A., Shaburova O.V., Burkal'tseva M.V. // Genetika. 2010. V. 46. № 2. P. 159–167.
- Fokine A., Battisti A.J., Bowman V.D., Efimov A.V., Kurochkina L.P., Chipman P.R., Mesyanzhinov V.V., Rossmann M.G. // Structure. 2007. V. 15. № 9. P. 1099–1104.
- Aksyuk A.A., Kurochkina L.P., Fokine A., Forouhar F., Mesyanzhinov V.V., Tong L., Rossmann M.G. // Structure. 2011. V. 19. № 12. P. 1885–1894.
- Thomas J.A., Weintraub S.T., Wu W., Winkler D.C., Cheng N., Steven A.C., Black L.W. // Mol. Microbiol. 2012. V. 84. № 2. P. 324–339.
- Miroshnikov K.A., Faizullina N.M., Sykilinda N.N., Mesyanzhinov V.V. // Biochemistry (Mosc). 2006. V. 71. № 3. P. 300–305.
- Briers Y., Volckaert G., Cornelissen A., Lagaert S., Michiels C.W., Hertveldt K., Lavigne R. // Mol. Microbiol. 2007. V. 65. № 5. P. 1334–1344.
- Briers Y., Schmelcher M., Loessner M.J., Hendrix J., Engelborghs Y., Volckaert G., Lavigne R. // Biochem. Biophys. Res. Commun. 2009. V. 383. № 2. P. 187–191.
- Paradis-Bleau C., Cloutier I., Lemieux L., Sanschagrin F., Laroche J., Auger M., Garnier A., Levesque R.C. // FEMS Microbiol. Lett. 2007. V. 266. № 2. P. 201–209.
- Höltje J.V. // EXS. 1996. V. 75. P. 425–429.
- Fokine A., Miroshnikov K.A., Shneider M.M., Mesyanzhinov V.V., Rossmann M.G. // J. Biol. Chem. 2008. V. 283. № 11. P. 7242–7250.
- Sambrook J., Russell D.W. Molecular Cloning. Cold Spring Harbor Laboratory Press, 2001. 2231 p.
- Briers Y., Lavigne R., Volckaert G., Hertveldt K. // J. Biochem. Biophys. Methods. 2007. V. 70. № 3. P. 531–533.
- Hanwell M.D., Curtis D.E., Lonie D.C., Vandermeersch T., Zurek E., Hutchison G.R. // J. Cheminform. 2012. V. 4. № 8. P. 1–17.
- Grosdidier A., Zoete V., Michielin O. // Nucl. Acids Res. 2011. V. 39. Suppl. 2. P. 270–277.
- Dolinsky T.J., Nielsen J.E., McCammon J.A., Baker N.A. // Nucl. Acids Res. 2004. V. 32. № WEB SERVER ISS. P. 665–667. <https://www.ncbi.nlm.nih.gov/pubmed/15215472>
- Dolinsky T.J., Czodrowski P., Li H., Nielsen J.E., Jensen J.H., Klebe G., Baker N.A. // Nucl. Acids Res. 2007. V. 35. Suppl. 2. P. 522–525.
- Baker N.A., Sept D., Joseph S., Holst M.J., McCammon J.A. // Proc. Natl. Acad. Sci. USA. 2001. V. 98. № 18. P. 10037–10041.
- Sorin E.J., Pande V.S. // Biophys. J. 2005. V. 88. № 4. P. 2472–2493.
- DePaul A.J., Thompson E.J., Patel S.S., Haldeman K., Sorin E.J. // Nucl. Acids Res. 2010. V. 38. № 14. P. 4856–4867.
- Berendsen H.J.C., van der Spoel D., van Druenen R. // Comput. Phys. Commun. 1995. V. 91. № 1–3. P. 43–56.
- Lindahl E., Hess B., van der Spoel D. // J. Mol. Model. 2001. V. 7. № 8. P. 306–317.
- Van Der Spoel D., Lindahl E., Hess B., Groenhof G., Mark A.E., Berendsen H.J.C. // J. Comput. Chem. 2005. V. 26. № 16. P. 1701–1718.
- Hess B., Kutzner C., Van Der Spoel D., Lindahl E. // J. Chem. Theory Comput. 2008. V. 4. № 3. P. 435–447.
- van Asselt E.J., Dijkstra A.J., Kalk K.H., Takacs B., Keck W., Dijkstra B.W. // Structure. 1999. V. 7. № 10. P. 1167–1180.
- Thunnissen A.M.W.H., Isaacs N.W., Dijkstra B.W. // Proteins Struct. Funct. Genet. 1995. V. 22. № 3. P. 245–258.
- Scheurwater E., Reid C.W., Clarke A.J. // Int. J. Biochem. Cell Biol. 2008. V. 40. № 4. P. 586–591.
- Schmelcher M., Donovan D.M., Loessner M.J. // Future Microbiol. 2012. V. 7. № 10. P. 1147–1171.
- Legotsky S.A., Vlasova K.Y., Priyma A.D., Shneider M.M., Pugachev V.G., Totmenina O.D., Kabanov A.V., Miroshnikov K.A., Klyachko N.L. // Biochimie. 2014. V. 107. Pt B. P. 293–299.
- Yang H., Yu J., Wei H. // Front. Microbiol. 2014. V. 5. P. 542–548.
- Briers Y., Lavigne R. // Future Microbiol. 2015. V. 10. № 3. P. 377–390.

Search for Modified DNA Sites with the Human Methyl-CpG-Binding Enzyme MBD4

D. A. Yakovlev¹, A. A. Kuznetsova¹, O. S. Fedorova^{1,2*} and N. A. Kuznetsov^{1,2*}

¹Institute of Chemical Biology and Fundamental Medicine, Siberian Branch of the Russian Academy of Sciences, Lavrentieva ave. 8, Novosibirsk, 630090, Russia

²Department of Natural Sciences, Novosibirsk State University, Pirogova str. 2, Novosibirsk, 630090, Russia

*E-mail: fedorova@niboch.nsc.ru, nikita.kuznetsov@niboch.nsc.ru

Received May 12, 2016; in final form, July 04, 2016

Copyright © 2017 Park-media, Ltd. This is an open access article distributed under the Creative Commons Attribution License, which permits unrestricted use, distribution, and reproduction in any medium, provided the original work is properly cited.

ABSTRACT The MBD4 enzyme initiates the process of DNA demethylation by the excision of modified DNA bases, resulting in the formation of apurinic/apyrimidinic sites. MBD4 contains a methyl-CpG-binding domain which provides the localization of the enzyme at the CpG sites, and a DNA glycosylase domain that is responsible for the catalytic activity. The aim of this work was to clarify the mechanisms of specific site recognition and formation of catalytically active complexes between model DNA substrates and the catalytic N-glycosylase domain MBD4^{cat}. The conformational changes in MBD4^{cat} and DNA substrates during their interaction were recorded in real time by stopped-flow detection of the fluorescence of tryptophan residues in the enzyme and fluorophores in DNA. A kinetic scheme of MBD4^{cat} interaction with DNA was proposed, and the rate constants for the formation and decomposition of transient reaction intermediates were calculated. Using DNA substrates of different lengths, the formation of the catalytically active complex was shown to follow the primary DNA binding step which is responsible for the search and recognition of the modified base. The results reveal that in the primary complex of MBD4^{cat} with DNA containing modified nucleotides, local melting and bending of the DNA strand occur. On the next step, when the catalytically competent conformation of the enzyme-substrate complex is formed, the modified nucleotide is everted from the double DNA helix into the active center and the void in the helix is filled by the enzyme's amino acids.

KEYWORDS MBD4, DNA demethylation, DNA repair, pre-steady-state kinetics, conformational dynamics.

ABBREVIATIONS MBD4^{cat} – catalytic domain of methyl-CpG-binding enzyme MBD4; 5hmU – 5-hydroxymethyluracil; AP-site – apurinic/apyrimidinic site; F-site – (3-hydroxytetrahydrofuran-2-yl) methyl phosphate; aPu – 2-aminopurine; FAM – 6-carboxyfluorescein; BHQ1 – black hole quencher; FRET – Förster resonance energy transfer; PAGE – polyacrylamide gel electrophoresis.

INTRODUCTION

The processes of DNA methylation and demethylation are the basis for the epigenetic regulation of gene expression, which plays a major role in cellular differentiation, genome imprinting, carcinogenesis, and many age-related changes in organisms. It is known that different enzyme systems are involved in DNA demethylation: DNA methyltransferases, dioxygenases, and DNA glycosylases [1, 2]. DNA glycosylases initiate the process of demethylation through the excision of the methylated DNA base, and hence, other enzymes, such as AP-endonucleases (APE1), DNA polymerases, and DNA ligases, are necessary to restore the original nucleotide [3–5].

DNA glycosylase MBD4 [EC 3.2.2.-] contains two domains: a methyl-CpG-binding domain and a DNA gly-

cosylase domain. The catalytic N-glycosylase domain MBD4^{cat} consists of 138 amino acid residues (residues 437–574) that form nine α -helices to create a globular structure and the active site pocket [6]. Based on the MBD4^{cat} structure, the enzyme belongs to the helix-hairpin-helix family (HhH) and is so named due to the α 7-loop- α 8 motif, which is specific to different proteins of this family.

The main substrate of MBD4 is DNA that contains non-complementary G/T or G/U pairs [2]. MBD4 is also active on 5-hydroxymethyluracil (5-hmU) [7]. It is believed that 5-hmU is formed as an intermediate in a multistep pathway of active demethylation in which 5-mC is hydroxylated by TET-dioxygenases, with the formation of 5-hydroxymethylcytosine (5-hmC). Thereafter, 5-hmC is deaminated by deaminase AID

to form 5-hmU and is removed with MBD4 during the base excision repair pathway [8]. MBD4 is also active on several halogenated substrates: 5-ClU and 5-BrU produced during inflammatory processes and 5-FU, which can appear during chemotherapy [9]. Moreover, the enzyme is active towards 3,N⁴-ethenocytosine (ϵ C), which is formed during lipid peroxidation and vinyl chloride metabolism [10].

The structures of free MBD4^{cat} and MBD4^{cat} in complexes with DNA duplexes containing 5-hmU/G, T/G, and AP/G base pairs have been identified [11, 12]. As shown in *Fig. 1A*, in a complex with reaction products, the enzyme interacts preferably with five nucleotides of the damaged DNA strand. The formation of the enzyme-substrate complex does not lead to significant conformational changes compared to a free protein (*Fig. 1B*). Meanwhile, DNA duplexes, in complex with MBD4^{cat}, are bent in the region of the modified nucleotide, the nucleotide is everted from the double helix, and the nitrogenous base is inserted to the active center. MBD4^{cat} forms direct contacts with five phosphate groups located on the 5' and 3'-side of the everted nucleotide [12]. Two amino acid residues, Arg468 and Leu508, intercalate DNA through the minor groove and fill the void in the duplex, which is formed after

eversion of the modified nucleotide. It has been suggested that the hydrolysis of the N-glycoside bond occurs through a mechanism of nucleophilic substitution [7]. The C1'-atom is subjected to a nucleophile attack from either a water molecule coordinated in the active site of the enzyme or the carboxyl group of Asp560 [7, 12].

The pre-steady-state kinetics of product formation during the N-glycosylase reaction of the G/T-containing DNA substrate catalyzed by MBD4 in single-turnover conditions has been studied previously in [13] for the time range 15 s – 10 h. It has been shown that the reaction curve is biphasic with a rapid initial burst of product formation, followed by a slower phase; this is due to tight binding of the enzyme to the AP site reaction product.

The aim of this work was to study the mechanisms of specific site recognition by the enzyme in the substrate and formation of a catalytically competent state. The conformational dynamics of MBD4^{cat} and model DNA substrates at short time points ranging from 2 ms to 200 s under conditions corresponding to or close to single-turnover of the enzyme has been studied. The changes in the protein conformation were recorded from changes in the tryptophan (Trp) fluorescence intensity. The

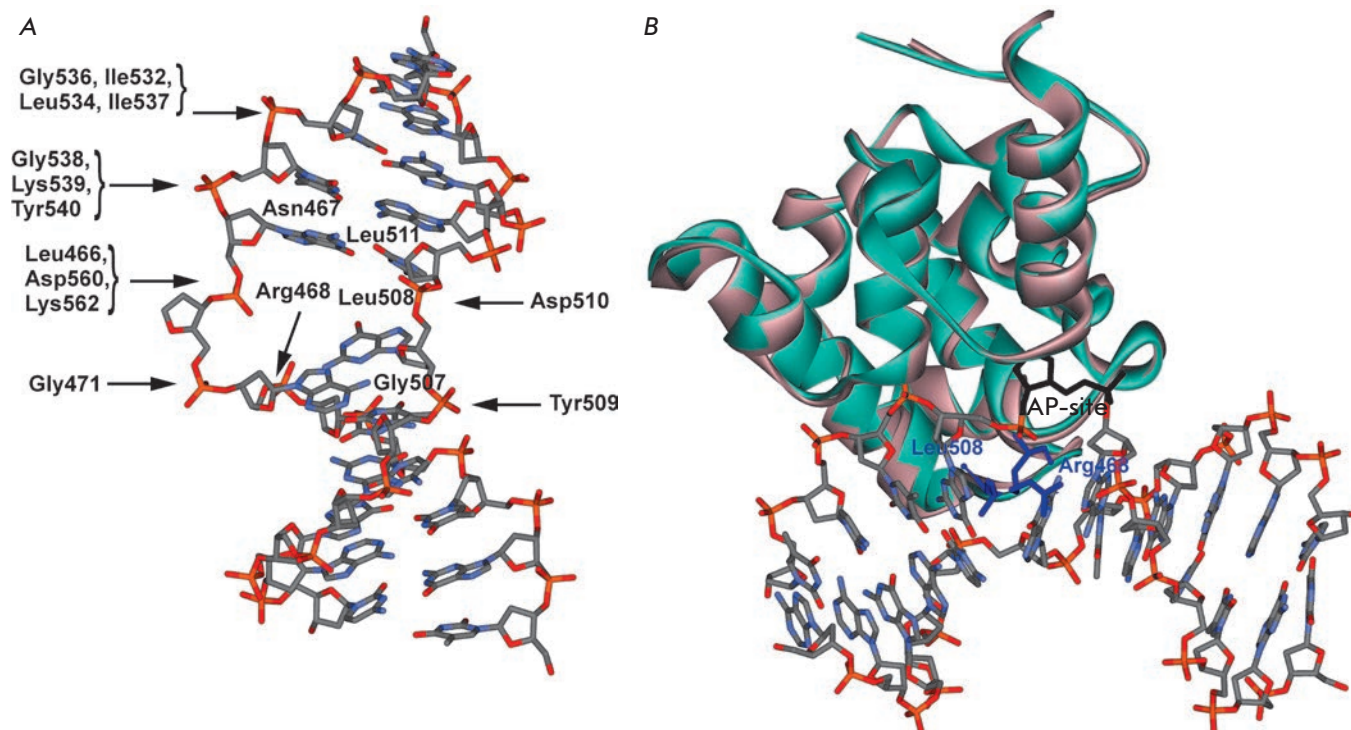


Fig. 1. (A) Schematic representation of specific contacts in the complex between MBD4^{cat} and DNA [12]. (B) Overall structures of free MBD4^{cat} (pink, PDB ID 4E9E, [11]) and MBD4^{cat} associated with damaged DNA (green, PDB ID 4DK9, [12]). AP-site (black) is flipped out of the double helix and inserted into the active site, Arg468 and Leu508 (blue) intercalate the DNA.

changes in DNA conformation were studied based on the 2-aminopurine (aPu) fluorescence intensity or from the efficiency of the fluorescence resonance energy transfer (FRET) using the FAM/BHQ1 dye pair. The substrates were duplexes containing an U/G pair. The product analogue was duplexes containing an uncleavable analogue of the AP-site – (3-hydroxytetrahydrofuran-2-yl) methyl phosphate residue (F-site). The influence of the duplex length on enzyme binding to DNA and its search for modified bases was studied using substrates of different lengths: 12, 17, and 28 base pairs (bp). Based on the findings, we determined the kinetic mechanism of conformational rearrangements of DNA glycosylase MBD4^{cat} and DNA substrates containing modified nucleotides during their interaction.

MATERIALS AND METHODS

These reagents manufactured by Sigma-Aldrich (USA) were used: acrylamide, N,N'-methylenebisacrylamide, dithiothreitol, urea, EDTA, acetonitrile, glycerol, tris-(hydroxymethyl)-aminomethane, and domestic reagents of extra-pure grade. All solutions were prepared in double-distilled water.

DNA-substrates

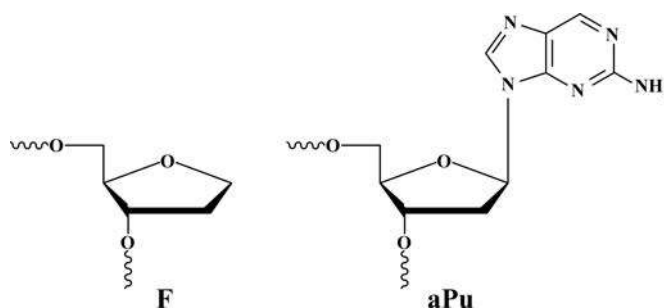
Oligodeoxyribonucleotides were synthesized at the Laboratory of Bionanotechnology, Institute of Chemical Biology and Fundamental Medicine, Russian Academy of Sciences, using an ASM-800 automated DNA/RNA-synthesizer (Biosset, Novosibirsk, Russia) with commercial amidophosphite derivatives of nucleosides and CPG carriers (GlenResearch, USA). Native and modified oligodeoxyribonucleotides were purified with HPLC using an Agilent 1200 chromatograph (USA) and a Zorbax SB-C18 column (5 μ m), 4.6 \times 150 mm, with a linear gradient of acetonitrile (0 \rightarrow 50%) in the presence of 20 mM triethylammonium acetate, pH 7, for 30 min at a flow rate of 2 mL/min. Fractions containing oligodeoxyribonucleotides were dried in vacuum, dissolved in water, and precipitated with 2% LiClO₄ in acetone. After washing with pure acetone and drying, the oligodeoxyribonucleotide precipitate was dissolved in water and stored at -20°C until usage. The homogeneity of purified oligodeoxynucleotides was evaluated by denaturing gel-electrophoresis (20% polyacrylamide gel, 8 M urea, 0.1 M tris-borate buffer, pH 8.3). The oligodeoxyribonucleotides were visualized with the Stains-All dye (Sigma, USA). The substrates and ligands of the enzyme were the 12-, 17- and 28-bp oligodeoxyribonucleotide duplexes presented in Table 1.

Enzyme MBD4^{cat}

The catalytic domain of human DNA glycosylase, MBD4^{cat} (amino acid residues 426–580), was isolated from

Table 1. Sequences of oligodeoxynucleotides and structure of the modified residues.

Short name	Sequence
U ₁₂ -substrate	CTCTC (U) CCTTCC GAGAG G GGAAGG
F ₁₂ -ligand	CTCTC (F) CCTTCC GAGAG G GGAAGG
FaPu ₁₂ -ligand	CTCTC (F) (aPu) CTTC GAGAG G C GAAGG
U ₁₇ -substrate	GCTCA (U) GTACAGAGCTG CGAGT G CATGTCTCGAC
UaPu ₁₇ -substrate	GCTCA (U) (aPu) TACAGAGCTG CGAGT G C ATGTCTCGAC
FAM-U-BHQ1-substrate	FAM-GCTCA (U) GTACAGAGCTG CGAGT G CATGTCTCGAC-BHQ1
U ₂₈ -substrate	GTGTCACTGCTCA (U) GTACAGAGCTG CACAGTGGTGACGAGT G CATGTCTCGAC



the cells of *Escherichia coli* Rosetta 2 transformed with the plasmid pET29b-MBD4^{cat} as described previously [11, 14]. The plasmid pET29b-MBD4^{cat} containing the MBD4^{cat} gene was kindly provided by M.K. Saparbaev (Groupe Réparation de l'ADN, Université Paris-Sud XI, Institut Gustave Roussy, France). The cell culture of *E. coli* Rosetta 2 was grown in a LB medium (1 L) containing 50 μ g/mL of kanamycin at 37°C to an optical density of 0.6–0.7 at 600 nm. Then, the temperature was lowered to 20°C and transcription was induced by the addition of isopropyl- β -D-thiogalactopyranoside to 0.2 mM. After induction, the cells were incubated during 16 h and then centrifuged (12,000 rpm, 10 min). A cell suspension was prepared in 30 mL of buffer solution I (20 mM HEPES-NaOH, pH 7.8) containing 50 mM KCl. The cells were lysed under pressure using a SIM AMINCO French Press. All subsequent procedures were performed at 4°C. The cell lysate was centrifuged (30,000 rpm, 40 min), and the supernatant was loaded on column I (Q-Sepharose Fast Flow, Amersham Biosciences, Sweden) and eluted with buffer solution I (20 mM HEPES-NaOH, pH 7.8, containing 50 mM KCl). Fractions containing the protein were collected and loaded on column II (HiTrap-Helating™, Amersh-

am Biosciences, Sweden) in buffer solution II (20 mM HEPES-NaOH, pH 7.8, containing 500 mM NaCl and 20 mM imidazole). Chromatography was performed in buffer solution II and a linear gradient of 20 → 500 mM imidazole. The solution's absorbance was detected at a wavelength of 280 nm. The protein purity was assessed using gel-electrophoresis. Fractions containing the MBD4^{cat} protein were dialyzed in buffer (20 mM HEPES-NaOH, pH 7.5, 1 mM EDTA, 1 mM dithiothreitol, 250 mM NaCl, 50% glycerol) and stored at -20°C. The protein concentration was calculated based on the optical density of the protein solution at 280 nm and a molar extinction coefficient of 54493 M⁻¹cm⁻¹ [15].

All the experiments in studying the enzymatic reaction were performed in a buffer solution: 50 mM Tris-HCl, pH 7.5, 50 mM KCl, 1 mM EDTA, 1 mM dithiothreitol, and 9% glycerol at 25°C.

PAGE product analysis

The reaction products were separated using polyacrylamide gel electrophoresis (PAGE) with 5'-end ³²P-labeled oligonucleotides containing a modified base. The oligonucleotides were labeled at the 5'-end according to [16]. The dependence of the substrate conversion extent on time was studied by mixing 10 μL of a buffer solution containing a ³²P-labeled oligonucleotide and an equimolar amount of a complementary oligonucleotide with 10 μL of 2.0–4.0 μM of the enzyme in the same buffer solution. The reaction mixture was rapidly mixed, and after periods of time, 2 μL aliquots were taken and transferred in prepared test tubes containing 2 μL of a 7 M urea solution, 0.1% bromophenol blue, and 0.1% xylene cyanol. Then, 1 μL of 1 M NaOH were added and incubated at 56°C for 15 min to hydrolyse phosphodiester bonds at the AP-sites. The solution was neutralized with an equivalent amount of hydrochloric acid and loaded on a polyacrylamide gel (PAAG). Electrophoresis was performed at a voltage of 50 V/cm. The gel was autoradiographed using the Molecular Imager FX phosphorimager (Bio-Rad, USA), and the data were processed using the Gel-Pro Analyzer 4.0 software package (Media Cybernetics, USA) to determine the amount of the formed product. The degree of product formation was defined as the ratio of the product peak areas to the overall product peak areas and original oligonucleotide peak areas. The measurement error commonly did not exceed 20%.

Study of the kinetics using the stopped-flow method

The kinetic curves of fluorescence were detected by a stopped-flow method using an SX.18MV spectrometer (Applied Photophysics, United Kingdom). The MBD4^{cat} protein contains eight Trp residues and seven Tyr residues. Fluorescence excitation of MBD4^{cat} was

performed at a wavelength of 290 nm, and the fluorescence was recorded at wavelengths longer than 320 nm (WG-320 filter, Schott, Germany). Under these conditions, Trp residues (> 90%) contributed most to the protein fluorescence. When using substrates containing aPu residues, the fluorescence was excited at wavelengths of 310 nm and detected at wavelengths longer than 370 nm (LG-370 filter, Corion, USA). To analyze the efficiency of FRET energy transfer using the FAM/BHQ1 pair, the fluorescence of the FAM dye was excited at 494 nm and the fluorescence of the FAM dye was detected at wavelengths longer than 515 nm using an OG-515 filter (Schott, Germany). The dead time comprised 1.4 ms. Each kinetic curve was derived by averaging at least three experimental curves.

Analysis of the kinetic data

To generate a minimal kinetic scheme that describes the interaction of the enzyme with the substrates and to assess the rate constants for conformational transitions during all the elementary steps of the reaction, a number of kinetic curves for different concentrations of the enzyme or substrate were obtained. The quantitative analysis was performed using the DynaFit software (BioKin, USA) [17] by fitting the parameters to the kinetic schemes as described previously [18–20].

RESULTS

Interaction of MBD4^{cat} with the 28-bp DNA-duplex

Figure 2A shows the kinetic curves of the changes in the Trp fluorescence intensity during the interaction of MBD4^{cat} with the 28-bp substrate U₂₈. Since MBD4^{cat} forms contacts only with five of the nucleotides of DNA, using the 28-bp DNA duplex as a substrate leads to the fact that the stage of the search for the uracil residue in DNA contributes significantly to the overall rate of the reaction. Indeed, it is seen in the kinetic curves (Fig. 2A) that the fluorescence intensity of Trp decreases within a wide time range 2 ms–10 s followed by a phase of Trp fluorescence intensity growth (10–100 s).

An analysis of the reaction product formation using electrophoretic separation of the reaction mixture in PAAG (Fig. 2B) has shown that the reaction is biphasic, with rapid (to ~200 s) and slow (to 1,600 s and longer) phases. At the initial region of the kinetic curves (to 200 s), a burst is observed, followed by slow growth. This type of curve indicates the presence of a rate-limiting step after the catalytic reaction. An increase in the concentration of U₂₈ from 0.25 to 1.0 μM increases the quantity of the cleaved substrate at the step of burst to 0.7 μM. However, with further increase in the concentration of the U₂₈-substrate to 2.0 μM, the quantity

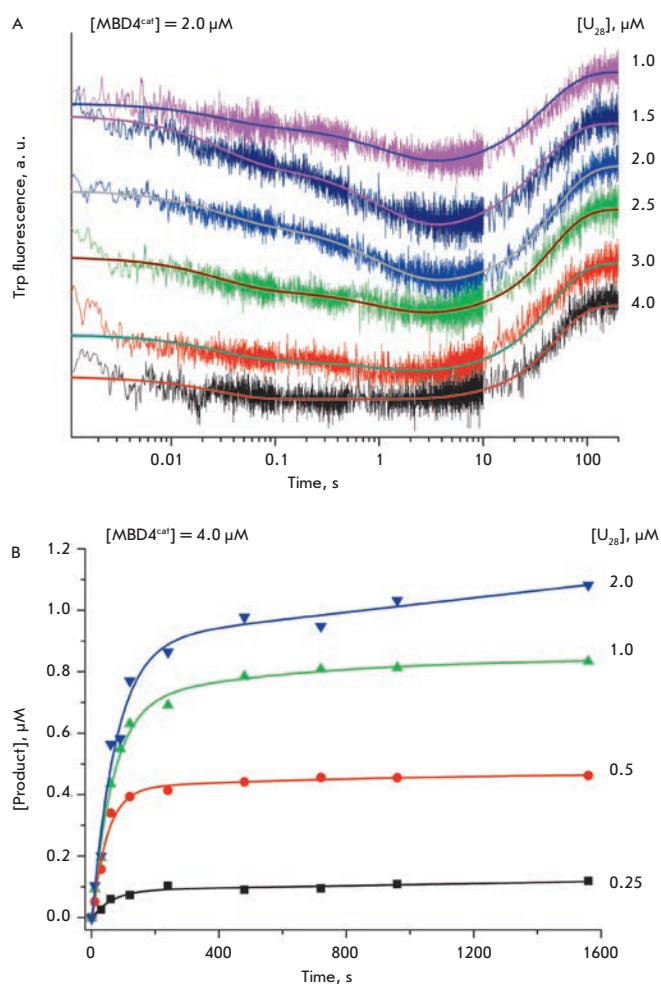
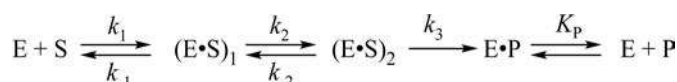


Fig. 2. Interaction of MBD4^{cat} with the U₂₈-substrate. (A) Changes in the Trp fluorescence intensity. Jagged traces represent the experimental data; smooth curves are the results of the fitting to Scheme 1. [MBD4^{cat}] = 2.0 μM, concentrations of U₂₈ (1.0–4.0 μM) are shown on the right side of the plot. (B) Accumulation of reaction product determined by PAGE. [MBD4^{cat}] = 4.0 μM, concentrations of U₂₈ (0.25–2.0 μM) are shown on the right side of the plot.

of the cleaved substrate increases insignificantly to 0.9 μM, indicating that the active form of the enzyme becomes saturated with the DNA substrate. Thus, data on the reaction product formation show that the concentration of the active form of the enzyme is about 1.0 μM. The relatively low activity of the MBD4^{cat} catalytic domain (~25%) is apparently linked to the features of the polypeptide assembly into a functional protein in the cells of *E. coli*, which is consistent with the data in [13].

Therefore, it is possible to suggest that the decrease in the Trp fluorescence intensity in the range of



Scheme 1. The kinetic mechanism of interaction between MBD4 and a DNA substrate, where E is MBD4; S is the substrate; (E · S)₁ и (E · S)₂ are enzyme–substrate complexes; (E · P) is a complex of the enzyme with the product; P is the product; k₁ and k₋₁ (i = 1 or 2) are the rate constants of equilibrium steps; k₃ is the rate constant of the catalytic reaction; and K_p is the equilibrium dissociation constant of the (E · P) complex.

2 ms– ~10 s characterizes the formation of a primary complex and the search for a modified base and growth in an interval of ~10–100 s indicates a reorganization of the enzyme globule into a catalytically competent conformation and onset of product formation. It is necessary to note that an increase in the fluorescence intensity of Trp at an interval of 10–100 s (Fig. 2A) coincides in time with the onset of reaction product formation (Fig. 2B). The dissociation step of the enzyme–product complex is probably the rate-limiting step of the enzymatic reaction, which is consistent with the conclusions made previously in [10].

Based on a quantitative analysis of the kinetic curves of the MBD4^{cat} interaction with the 28-bp DNA substrate (Fig. 2A), we propose the minimal kinetic Scheme 1 that satisfactorily describes the experimental data. Two equilibrium steps characterize the primary binding with DNA and the subsequent rearrangement of the enzyme conformation, leading to the formation of a catalytically competent complex in which the N-glycoside bond undergoes irreversible hydrolysis. The enzymatic cycle is terminated with the equilibrium dissociation step of the enzyme–DNA product complex. The rate constants and equilibrium constants characterizing the steps contained in Scheme 1 are presented in Table 2. Using the rate constants of elementary steps, steady-state parameter values of the enzymatic reaction were obtained (K_m and k_{cat}), which are in good agreement with the data in [11, 13].

Using equation (1) and the data (e₀ = 4.0 μM, s₀ = 0.5 μM, Fig. 2B), we evaluated the actual rate of steady-state phase of the reaction V_{st} ≈ (3.2 ± 1.2) × 10⁻⁵ μM/s. The expected value of the minimal catalytic reaction rate was estimated with a formula, V_{max} = k_{cat} × e₀, where e₀ – the initial enzyme concentration: it is 4.6 × 10⁻² μM/s taking into account 25% enzyme activity. This indicates that the dissociation of the enzyme/reaction product complex, rather

Table 2. The rate and equilibrium constants of the interaction between MBD4^{cat} and the DNA-substrates.

Substrates Constants	U ₂₈	U ₁₇	U ₁₂	F ₁₂
$k_1 \times 10^{-6}, \text{s}^{-1} \cdot \text{M}^{-1}$	7.0 ± 2.0	12.0 ± 3.0	0.5 ± 0.2	10.0 ± 4.0
k_{-1}, s^{-1}	30 ± 10	45 ± 20	3.3 ± 0.5	8.0 ± 4.0
${}^a K_1 \times 10^{-6}, \text{M}^{-1}$	0.2 ± 0.1	0.3 ± 0.1	0.15 ± 0.06	1.2 ± 0.8
k_2, s^{-1}	2.1 ± 0.3	3.0 ± 1.0	0.18 ± 0.04	0.08 ± 0.01
k_{-2}, s^{-1}	0.38 ± 0.05	0.23 ± 0.05	0.12 ± 0.01	0.03 ± 0.01
${}^a K_2$	5.5 ± 1.1	13.0 ± 5.0	1.5 ± 0.3	2.7 ± 0.9
k_3, s^{-1}	0.056 ± 0.007	0.046 ± 0.002	< 0.01	
K_p, M	$(1.0 \pm 0.2) \times 10^{-7}$	$(1.5 \pm 0.2) \times 10^{-7}$		
${}^b K_d, \text{M}$	6.6×10^{-7}	2.7×10^{-7}	2.6×10^{-6}	2.2×10^{-7}
${}^c K_m, \text{M}$	7.4×10^{-7}	3.2×10^{-7}		
${}^d k_{\text{cat}}, \text{s}^{-1}$	4.6×10^{-2}	4.2×10^{-2}		

$${}^a K_1 = k_1/k_{-1}, K_2 = k_2/k_{-2},$$

$${}^b K_d = 1/K_{\text{ass}}, K_{\text{ass}} = K_1 + K_1 \times K_2,$$

$${}^c K_m = (k_2 k_3 + k_{-1} k_{-2} + k_{-1} k_3)/k_1 (k_2 + k_{-2} + k_3),$$

$${}^d k_{\text{cat}} = k_2 k_3 / (k_2 + k_{-2} + k_3).$$

than the chemical step, is probably the rate-limiting step, which correlates with the presence of a burst on the kinetic curves of product formation:

$$V_{\text{st}} = \Delta[\text{P}]/\Delta t, \quad (1)$$

where $\Delta[\text{P}]$ – an increase in the product P concentration over time Δt .

Interaction of MBD4^{cat} with the 17-bp DNA-duplex

The kinetic curves obtained during the interaction of MBD4^{cat} with a shorter 17-bp DNA substrate have two phases of changes in the Trp fluorescence intensity, similar to the 28-bp duplex (*Fig. 3A*). An analysis of the reaction products using electrophoretic separation of the reaction mixture in PAAG (*Fig. 3B*) has shown that, in the case of the U₁₇-substrate, the products accumulate within a time interval of $< 1,000$ s. The kinetic curves have a marked burst of product formation in a time interval of up to 200 s, followed by a slow increase in the product concentration. The subsequent slowdown in the reaction product formation suggests that the dissociation of the enzyme–product complex is the rate-limiting step, similar to the U₂₈-substrate.

An analysis of the kinetic curves of fluorescence presented in *Fig. 3A* has shown that the kinetic curves are also described by minimal kinetic *Scheme 1*. The rate and equilibrium constants corresponding to this scheme are presented in *Table 2*. It is notable that the decrease in the non-specific region of the duplex U₁₇-substrate by 11 nucleotides does significantly change the rate constants of formation and decomposition of the (E · S)₁

primary complex compared to the U₂₈-substrate. However, a decrease in the length of the duplex resulted in an increase in the equilibrium constant K_2 , which characterizes the formation of the (E · S)₂ catalytic complex, 2.4-fold efficiently versus the U₂₈-substrate (13.0 and 5.5, respectively). This should be associated with a reduction in the search time for modified bases, which occurs through one-dimensional diffusion by means of both sliding and hopping [21–23] of the enzyme along the DNA chain and three-dimensional diffusion that involves multiple acts of association-dissociation.

Similar to the case of the U₂₈-substrate, the U₁₇-substrate is characterized by an actual steady-state rate of product formation V_{st} of $\sim (6.2 \pm 0.9) \times 10^{-5} \mu\text{M/s}$ at $e_0 = 4.0 \mu\text{M}$, $s_0 = 0.5 \mu\text{M}$ and a lower value $V_{\text{max}} = 4.2 \times 10^{-2}$ almost 1,000-fold. This difference, as well as the burst on the kinetic curves of reaction product formation (*Fig. 3B*), indicates that the dissociation of the enzyme–reaction product complex limits the rate of the enzymatic reaction.

Interaction of MBD4^{cat} with the 12-bp DNA-duplex

Figure 4 shows the curves of the changes in the Trp fluorescence intensity corresponding to the interaction of MBD4^{cat} with the 12-bp substrate U₁₂. *Figure 4A* reveals that the kinetic curves have two phases: a decrease in the intensity (10–500 ms) and growth reaching a plateau (0.5–10 s). The kinetics of product formation determined by electrophoretic separation of the reaction mixture in PAAG (*Fig. 4B*) suggests that the catalytic phase occurs at time points $\geq 1,000$ s, i.e., much slower than the steps corresponding to the change in the Trp

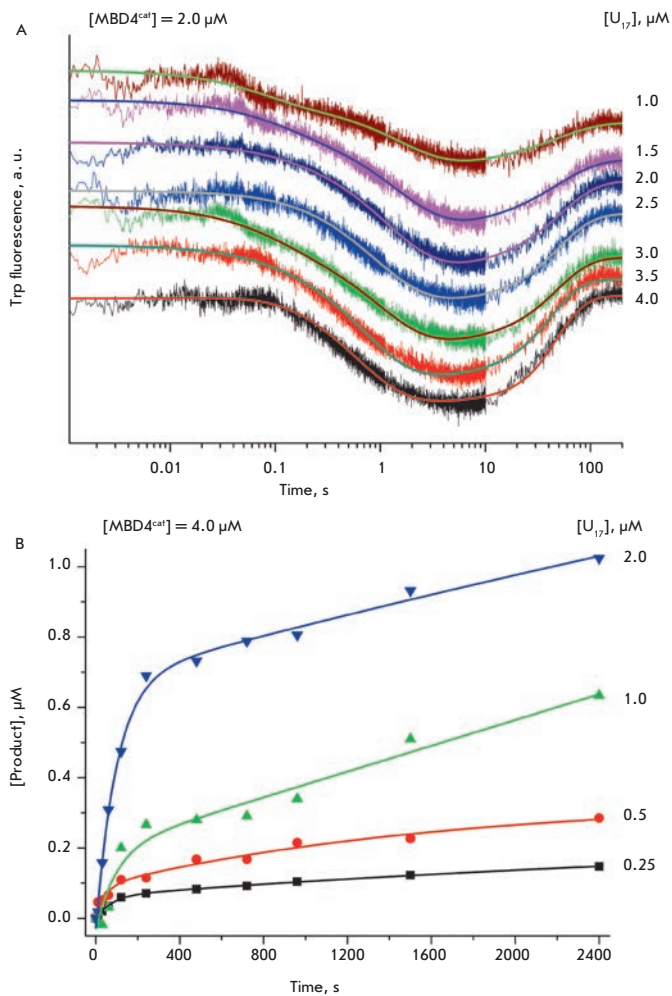


Fig. 3. Interaction of $MBD4^{cat}$ with the U_{17} -substrate. (A) Changes in the Trp fluorescence intensity. Jagged traces represent experimental data; smooth curves are the results of the data fitting to Scheme 1. $[MBD4^{cat}] = 2.0 \mu M$, concentrations of U_{17} (1.0–4.0 μM) are shown on the right side of the plot. (B) Accumulation of product determined by PAGE. $[MBD4^{cat}] = 4.0 \mu M$, concentrations of U_{17} (0.25–2.0 μM) are shown on the right side of the plot.

fluorescence intensity. Therefore, these changes that are detected in the time interval to 200 s most likely reflect the initial conformational changes in the enzyme during enzyme–substrate complex formation and further rearrangement in the enzyme conformation. In addition, a catalytically competent state is formed with poor efficiency, and the reaction of N-glycoside bond hydrolysis is significantly slowed down compared with the 17- and 28-bp substrates. Therefore, to analyze a series of kinetic curves, we used only the equilibrium steps of DNA binding that characterize the formation

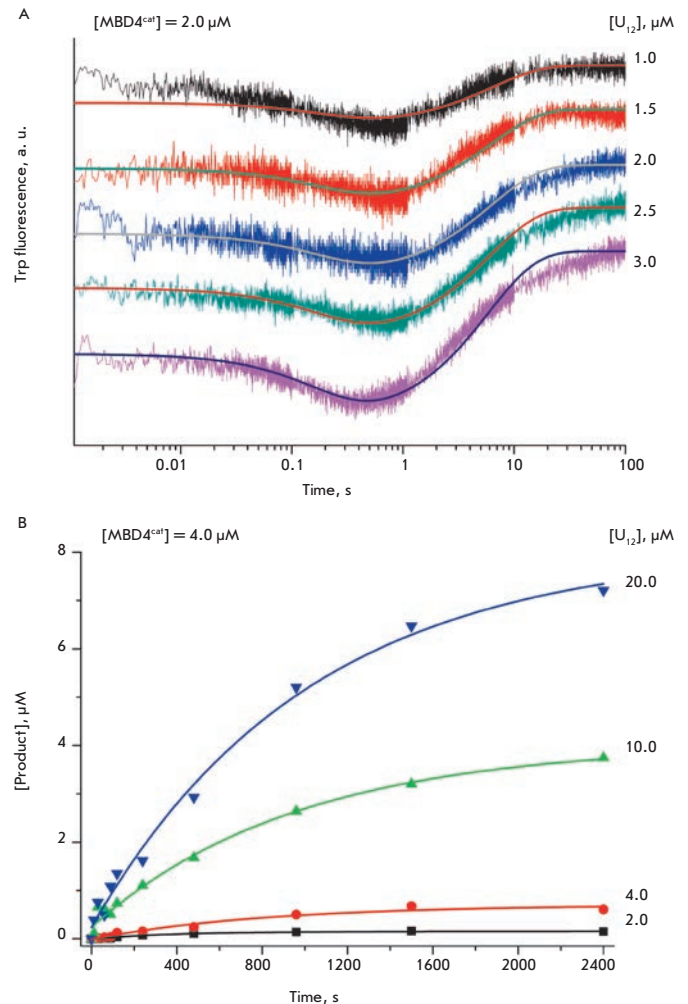


Fig. 4. Interaction of $MBD4^{cat}$ with U_{12} -substrate. (A) Changes in the Trp fluorescence intensity. Jagged traces represent experimental data; smooth curves are the results of the data fitting to Scheme 1 (steps 1 and 2). $[MBD4^{cat}] = 2.0 \mu M$, concentrations of U_{12} (1.0–3.0 μM) are shown on the right side of the plot. (B) Accumulation of product determined by PAGE. $[MBD4^{cat}] = 4.0 \mu M$, concentrations of U_{12} (2.0–20.0 μM) are shown on the right side of the plot.

of the $(E \cdot S)_1$ and $(E \cdot S)_2$ complexes on Scheme 1. The rate constants characterizing these steps and derived by analyzing the kinetic curves of fluorescence intensity changes of the enzyme (Fig. 4A) are presented in Table 2.

A comparison of the rate constants corresponding to $MBD4^{cat}$ interaction with the 12- and 17-bp substrates reveals that a decrease in the duplex length by five nucleotides reduced significantly both the rate of the $(E \cdot S)_1$ primary complex formation, which is characterized by the rate constant k_1 , and the rate of com-

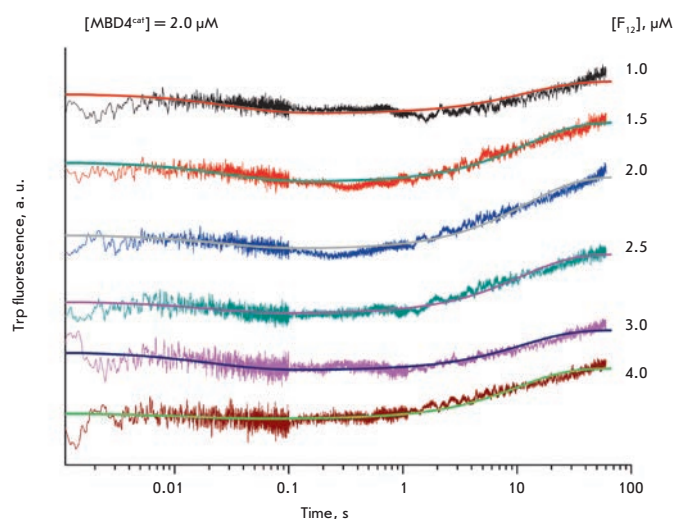


Fig. 5. Changes in the Trp fluorescence intensity during the interaction of MBD4^{cat} with F₁₂-ligand. Jagged traces represent experimental data; smooth curves are the results of the fitting to Scheme 1 (steps 1 and 2). [MBD4^{cat}] = 2.0 μM, concentrations of F₁₂ (1.0–4.0 μM) are shown on the right side of the plot.

plex decomposition, k_{-1} , 24- and 14-fold, respectively. Furthermore, the association constant of E with S, resulting in the (E · S)₁ complex formation, K_1 , decreases only 2-fold. It is suggested that the nonspecific region of the U₁₇-substrate is a template with which the primary complex (E · S)₁ is formed under conditions of rapid equilibrium that allows the enzyme to perform an effective search for a damaged site. In fact, the constant k_2 of formation of the catalytic complex (E · S)₂ in the case of the U₁₇-substrate is 17-fold higher than in the case of the U₁₂-substrate. Thus, an increase in the nonspecific region of the duplex by five nucleotides in the U₁₇-substrate compared to the U₁₂-substrate results in a 10-fold decrease in the total dissociation constant K_d (Table 2). Absence of a nonspecific region in the U₁₂-substrate, apparently, prevents the formation of a properly oriented active conformation of the enzyme.

Interaction of MBD4^{cat} with an analogue of the product

Excision of the modified base by the MBD4 enzyme leads to the formation of an AP-site in DNA. In order to identify the nature of the conformational changes in the enzyme and DNA that occur during binding of the reaction product containing the AP-site, we used a stable AP-site analogue, a (3-hydroxytetrahydrofuran-2-yl) methyl phosphate residue (F-site) without an OH-group in the C1' position of deoxyribose.

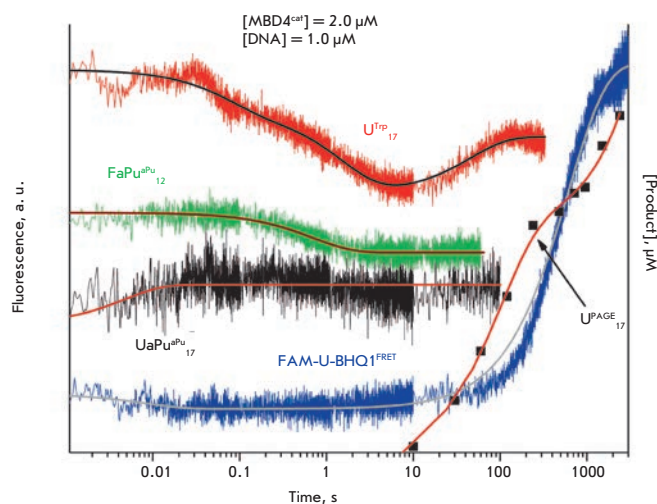


Fig. 6. Comparison of the product accumulation determined by PAGE and changes in the fluorescence intensity of the Trp and aPu residues and the FRET-signal during the interaction of MBD4^{cat} with U₁₇, UaPu₁₇, FaPu₁₂ and FAM-U-BHQ1. [MBD4^{cat}] = 2.0 μM, [DNA] = 1.0 μM.

An interaction of MBD4^{cat} with the F₁₂-ligand should lead to the formation of a complex that imitates the enzyme/product complex after the catalytic steps of the enzymatic reaction.

The kinetic curves of the changes in the Trp fluorescence intensity during the interaction of MBD4^{cat} and the F₁₂-ligand have a biphasic profile (Fig. 5), similar to the U₁₂-substrate (Fig. 4). It can be suggested that the decrease and subsequent increase in the Trp fluorescence intensity have the same nature as in the DNA duplex containing uridine. Thus, regardless of the nature of the modified nucleotide, primary binding and further rearrangement of the enzyme conformation during the interaction of MBD4^{cat} with DNA lead to the formation of a catalytically active complex (Fig. 5). The derived kinetic curves are described satisfactorily by a two-step equilibrium kinetic scheme. The rate constants characterizing these steps are presented in Table 2.

A comparison of the rate constants and equilibrium constants (Table 2) characterizing the interaction of MBD4^{cat} with the U₁₂-substrate and F₁₂-ligand has shown that a primary complex with a reaction product analogue is formed with about a 10-fold higher efficiency. It is noteworthy that the equilibrium constants for the second step differ less than 2-fold. Hence, we can conclude that the search for and binding of damaged DNA by the MBD4^{cat} enzyme occur with higher

efficiency in the case of a DNA duplex destabilized by an F-site.

Comparative analysis of conformational changes in the enzyme and DNA

In order to clarify the nature of the processes occurring during catalytic complex formation and detected from the changes in the Trp fluorescence intensity, we used model DNA duplexes carrying fluorescent residues (Table 1) as “sensors” of the conformational changes in DNA. It is known that the fluorescence intensity of aPu in DNA depends on the fluorophore microenvironment changes, for example, as a result of local melting of the duplex in the immediate vicinity of the fluorophore [24–26]. In double-stranded DNA structures, during stacking interaction with neighboring bases, the fluorescence intensity of aPu residues reduces significantly in comparison with single-stranded DNA. Using a UaPu₁₇-substrate carrying a aPu residue on the 3'-side of uridine allowed us to detect the conformational changes in DNA that occur during the interaction with MBD4^{cat}, probably, as a result of an eversion of the damaged nucleotide from DNA and insertion of the Arg468 and Leu508 residues into the resulting void. As seen in *Fig. 6*, the kinetic curve which characterizes the interaction of the MBD4^{cat} and UaPu₁₇-substrate has a phase of rapid growth (1–50 ms) of the aPu fluorescence intensity, indicating a destabilization of the central part of the duplex at the initial steps of enzyme-substrate interaction.

Additionally, a FRET technique was applied to study changes in the DNA-substrate structure. We used a FAM-U-BHQ1-substrate containing FAM and BHQ1 dyes at the 5'-ends of the oligonucleotides forming the duplex to track the conformational changes in the duplex linked to the changes in the distance between the donor and acceptor dye molecules. It is clear (*Fig. 6*) that a small decrease in the FRET-signal occurs at the initial region of the kinetic curve (1–50 ms) indicating a decrease in the distance between FAM and BHQ1 in the duplex. A comparison with a curve of the changes in the Trp fluorescence intensity has shown that at this time point (< 100 ms), the enzyme undergoes no significant conformational changes. Therefore, we can suggest that during the initial DNA binding the helix is bent and the central part of the duplex partially melts. Apparently, it is exactly these changes in the structure of the duplex induced by the enzyme that allow MBD4^{cat} to distinguish between the modified and non-modified bases during the sliding on the DNA duplex.

Interestingly, the growth phase of the Trp fluorescence intensity (10–100 s), coincident with the initial reaction product formation, does not correspond with the change in the FRET signal. However, the rate-lim-

iting step of the enzyme/reaction product complex dissociation causes a slow increase in the FRET signal in a time interval of 100–3,000 s and also leads to a slow accumulation of reaction products (*Fig. 6*).

The intensity of the aPu fluorescence upon binding with DNA-duplexes containing uracil (UaPu₁₇) and the F-site (FaPu₁₂) changes oppositely (an increase and a decrease, respectively) and in different time intervals ($t < 0.1$ s and 0.1 s $< t < 1$ s, respectively). The growth phase of the aPu fluorescence intensity when using the UaPu₁₇-substrate reflects a local melting of the duplex during primary complex formation. While this growth phase on the aPu fluorescence traces are not detected when using a FaPu₁₂-ligand, since the aPu residue located on the 3'-side from the F-site is already situated in a less hydrophobic environment than in canonical DNA. However, during the interaction of MBD4^{cat} with the FaPu₁₂-ligand, a well-marked decrease in the aPu fluorescence intensity is observed at later time points (up to 1 s). This decrease, associated with an increased hydrophobicity of the aPu residue environment, most likely indicates an insertion of the amino acid residues of MBD4^{cat} (Arg468 and Leu508) into the duplex at these time points.

DISCUSSION

X-ray crystallography findings [11, 12] allow one to suggest that in the primary complex, formed during the interaction of MBD4^{cat} with DNA in the initial time point, amino acid residues build a system of non-specific contacts with the ribose-phosphate backbone, allowing the enzyme, due to thermal motions, to move along the double helix in search of a damaged nucleotide. It is known that the search for specific sites by enzymes in a DNA molecule occurs by using both one-dimensional (1D) and three-dimensional (3D) diffusion: without dissociation of the enzyme-substrate complex by means of enzyme sliding and hopping along the DNA chain and by multiple acts of dissociation-association, respectively [21, 23]. The length of the 1D-diffusion region differs for different DNA-glycosylases. It was shown that uracil-DNA-glycosylase UNG can move by a length of about four nucleotides between acts of dissociation [27]. In 8-oxoguanine-DNA-glycosylase hOGG1, this distance may range from 60 [28] to 400 [29] nucleotides. DNA glycosylases Fpg, Nei, Nth, and hOGG1 [30–32] use certain residues as detectors for a damaged region of DNA during the search for a damaged site in the DNA molecule. If a modified nucleotide appears in the DNA-binding center of the enzyme, this leads to the formation of specific contacts, an eversion of the nucleotide from the DNA duplex, the insertion of a modified base into the active site of the enzyme, and movement of detector amino acid residues into the

void in the DNA duplex. These conformational rearrangements prevent the enzyme from moving from the specific site on the DNA and lead to the formation of a catalytically competent complex. It is interesting to note that the MBD4^{cat} enzyme, which belongs to the structural family of a HhH motif containing DNA-glycosylases together with hOGG1 and Nth, also inserts Arg468 and Leu508 into the DNA duplex during catalytic complex formation. Therefore, these amino acid residues can function as detectors during the search for a damaged nucleotide.

Comparison of fluorescence kinetics curves for the 12-, 17-, and 28-bp DNA substrates shows that with increasing duplex length, the phase of decrease in the Trp fluorescence intensity slows down, which characterizes the search for the modified base during sliding or hopping of MBD4^{cat} on the DNA chain. Using fluorescently labeled UaPu₁₇- and FAM-U-BHQ1-substrates, it has been shown that the DNA duplex bends and locally melts in the primary complex. In the subsequent time point, the damaged nucleotide is everted from the duplex and the amino acid residues of the enzyme are inserted in the void. The results obtained with a fluorescently labeled analogue of the reaction product FaPu₁₂- show that insertion of Arg468 and Leu508 in the DNA duplex is preceded by the growth phase of Trp fluorescence intensity. Insertion of amino acid residues into the DNA provides for specific recognition of the modified base. The growth phase of Trp

fluorescence intensity characterizes the formation of a catalytically active complex and ends in 100–200 s in all cases, which coincides with the initial burst of reaction product formation. Dissociation of the reaction product/enzyme complex is the rate-limiting step of the entire reaction. The observed rate of the catalytic reaction increases markedly with increased length of the duplex. This indicates the possible involvement of the non-modified DNA regions lying adjacent to the modified base in the formation of a properly oriented and active conformation of MBD4^{cat}.

Thus, conformational transitions in the MBD4 enzyme and DNA substrates during their interaction have been detected in real time for the first time. The kinetic mechanism has been established. The rate constants of formation and dissociation of intermediate enzyme-substrate complexes have been calculated, and the nature of the conformational rearrangements of the MBD4^{cat} and DNA substrates during modified base recognition and excision has been identified.

This study was supported partially by the SB RAS Comprehensive Scientific Program (No II.2II/VI.57-6 (0309-2015-0025)), grants of the Russian Foundation for Basic Research (No. 16-04-00037 O.S.F., № 15-34-20121 N.A.K.). A pre-steady-state kinetic analysis of the MBD4^{cat} enzyme interaction with DNA substrates was supported by a grant of the Russian Science No. 16-14-10038.

REFERENCES

- Zheng G., Fu Y., He C. // Chem. Rev. 2014. V. 114. P. 4602–4620.
- Sjolund A.B., Senejani A.G., Sweasy J.B. // Mutat. Res. 2013. V. 743–744. P. 12–25.
- Friedberg E.C., Walker G.C., Siede W., Wood R.D., Schultz R.A., Ellenberger T. DNA Repair and Mutagenesis. Washington: ASM Press, 2006. P. 1161.
- Barnes D.E., Lindahl T. // Annu. Rev. Genet. 2004. V. 38. P. 445–476.
- Gros L., Saparbaev M.K., Laval J. // Oncogene. 2002. V. 21. P. 8905–8925.
- Zhang W., Liu Z., Crombet L., Amaya M.F., Liu Y., Zhang X., Kuang W., Ma P., Niu L., Qi C. // Biochem. Biophys. Res. Commun. 2011. V. 412. P. 425–428.
- Hashimoto H., Zhang X., Cheng X. // Nucl. Acids Res. 2012. V. 40. P. 8276–8284.
- Hill P.W., Amouroux R., Hajkova P. // Genomics. 2014. V. 104. P. 324–333.
- Turner D.P., Cortellino S., Schupp J.E., Caretti E., Loh T., Kinsella T.J., Bellacosa A. // Cancer Res. 2006. V. 66. P. 7686–7693.
- Petronzelli F., Riccio A., Markham G.D., Seeholzer S.H., Genuardi M., Karbowski M., Yeung A.T., Matsumoto Y., Bellacosa A. // J. Cell Physiol. 2000. V. 185. P. 473–480.
- Morera S., Grin I., Vigouroux A., Couve S., Henriot V., Saparbaev M., Ishchenko A.A. // Nucl. Acids Res. 2012. V. 40. P. 9917–9926.
- Manvilla B.A., Maiti A., Begley M.C., Toth E.A., Drohat A.C. // J. Mol. Biol. 2012. V. 420. P. 164–175.
- Petronzelli F., Riccio A., Markham G.D., Seeholzer S.H., Stoerker J., Genuardi M., Yeung A.T., Matsumoto Y., Bellacosa A. // J. Biol. Chem. 2000. V. 275. P. 32422–32429.
- Kuznetsova A.A., Kuznetsov N.A., Ishchenko A.A., Saparbaev M.K., Fedorova O.S. // Biochim. Biophys. Acta. 2014. V. 1840. P. 3042–3051.
- Gill S.C., von Hippel P.H. // Anal. Biochem. 1989. V. 182. P. 319–326.
- Sambrook J., Fritsch E.F., Maniatis T. Molecular Cloning: A Laboratory Manual. Cold Spring Harbor, N.Y.: Cold Spring Harbor Lab., 1989. P. 1626.
- Kuzmic P. // Anal. Biochem. 1996. V. 237. P. 260–273.
- Kuznetsov N.A., Koval V.V., Zharkov D.O., Vorobiev Y.N., Nevinsky G.A., Douglas K.T., Fedorova O.S. // Biochemistry. 2007. V. 46. P. 424–435.
- Koval V.V., Kuznetsov N.A., Ishchenko A.A., Saparbaev M.K., Fedorova O.S. // Mutat. Res. 2010. V. 685. P. 3–10.
- Kuznetsov N.A., Vorobiev Y.N., Krasnoperov L.N., Fedorova O.S. // Nucl. Acids Res. 2012. V. 40. P. 7384–7392.
- Halford S.E., Szczelkun M.D. // Eur. Biophys. J. 2002. V. 31. P. 257–267.
- Friedman J.I., Stivers J.T. // Biochemistry. 2010. V. 49. P. 4957–4967.
- Lee A.J., Warshaw D.M., Wallace S.S. // DNA Repair (Amst.). 2014. V. 20. P. 23–31.
- Jean J.M., Hall K.B. // Proc. Natl. Acad. Sci. USA. 2001.

- V. 98. P. 37–41.
25. Rachofsky E.L., Osman R., Ross J.B.A. // *Biochemistry*. 2001. V. 40. P. 946–956.
26. Kuznetsov N.A., Kladova O.A., Kuznetsova A.A., Ishchenko A.A., Sapaebaev M.K., Zharkov D.O., Fedorova O.S. // *J. Biol. Chem.* 2015. V. 290. P. 14338–14349.
27. Schonhoft J.D., Stivers J.T. // *Nat. Chem. Biol.* 2012. V. 8. P. 205–210.
28. Rowland M.M., Schonhoft J.D., McKibbin P.L., David S.S., Stivers J.T. // *Nucl. Acids Res.* 2014. V. 42. P. 9295–9303.
29. Blainey P.C., van Oijen A.M., Banerjee A., Verdine G.L., Xie X.S. // *Proc. Natl. Acad. Sci. USA.* 2006. V. 103. P. 5752–5757.
30. Kuznetsov N.A., Bergonzo C., Campbell A.J., Li H., Mechetin G.V., de los Santos C., Grollman A.P., Fedorova O.S., Zharkov D.O., Simmerling C. // *Nucl. Acids Res.* 2015. V. 43. P. 272–281.
31. Nelson S.R., Dunn A.R., Kathe S.D., Warshaw D.M., Wallace S.S. // *Proc. Natl. Acad. Sci. USA.* 2014. V. 111. P. E2091–2099.
32. Kuznetsova A.A., Kuznetsov N.A., Ishchenko A.A., Sapaebaev M.K., Fedorova O.S. // *Biochim. Biophys. Acta.* 2014. V. 1840. P. 387–395.

Mapping the *D. melanogaster* En1A Enhancer Modules Responsible for Transcription Activation and Long-Distance Enhancer-Promoter Interactions

L. S. Melnikova*, E. A. Pomerantseva, V. V. Molodina, P. G. Georgiev

Institute of Gene Biology, Russian Academy of Sciences, Vavilova str. 34/5, Moscow, 119334, Russia

*E-mail: lsm73@mail.ru

Received June 23, 2015; in final form, November 08, 2016

Copyright © 2017 Park-media, Ltd. This is an open access article distributed under the Creative Commons Attribution License, which permits unrestricted use, distribution, and reproduction in any medium, provided the original work is properly cited.

ABSTRACT The structure of the new enhancer En1A of the 1A region of the X chromosome of *D. melanogaster* was investigated. Two distinct regulatory elements were found. The first element is responsible for transcription activation, and the second element provides specific interaction with the promoter of the *yellow* gene. The findings support the hypothesis of a modular structure for enhancers, including certain sequences that bind transcription activators and special communication elements providing long-distance enhancer-promoter interaction.

KEYWORDS *Drosophila melanogaster*, long-distance interactions, transcription activation, enhancer structure, *yellow* gene.

ABBREVIATIONS TF – transcription factors; En1A (Enhancer 1A) – enhancer of the 1A region of the X chromosome; Cm1A (Communicator 1A) – communication element of the En1A enhancer; TE (tethering element) – a regulatory element in the promoter responsible for long-distance enhancer-promoter interactions.

INTRODUCTION

One of the key properties of enhancers is their ability to specifically activate the transcription of the target gene that, in some cases, covers a distance of tens or even hundreds of kilobase pairs [1]. However, the mechanisms that are at play for maintaining specific long-distance interactions between enhancers and promoters remain elusive. In some cases, the *cis*-regulatory sequences found within the promoter regions of eukaryotic genes have been known to enable communication between an enhancer and a promoter [2–4]. Collected data [5] suggest that the specificity of some enhancers is due to the presence in them of binding sites for the said transcription factors (TF), which are responsible for transcription activation, and of proteins providing a stable long-distance enhancer-promoter interaction.

The aim of the current study was to investigate the new enhancer En1A found in the intron of the unexplored gene *CG3777* located on the X chromosome.

The En1A enhancer was shown to have a modular structure. We found the activation and communication elements in the structure of En1A. The activation element is able to functionally replace the *yellow* gene body and wings enhancers; i.e., stimulate transcription in the corresponding cuticular structures. The com-

munication element is necessary for the interaction between En1A and the *yellow* gene promoter and able to provide long-distance GAL4-dependent transcription activation.

EXPERIMENTAL PROCEDURES

All constructs are based on a pCaSpeR3 vector containing the *mini-white* gene. The plasmid vector pCΔ derived from pCaSpeR3, which contains a deletion of the *mini-white* gene, has been described previously [6].

For the constructs EcoRI–PstI–Y, PstI–PvuII–Y, and HindIII–y⁺–Y, the corresponding restriction fragments of the chimeric element from the y⁺ allele were used. The fragments were inserted upstream of the *yellow* gene promoter at position –343 bp (hereinafter, including figures, the numeration within the *yellow* locus is determined relative to the gene transcription initiation site) at the KpnI restriction site.

For (a1–a2)Y construct design, *yellow* cDNA lacking a bristle intron and an enhancer was used (pCaSpeR3–Yil). A fragment of 362 bp was amplified from the genomic DNA of a y⁺ fly line using the primers a1 (5'–CTTTTTGCATACACATCCAC–3') and a2 (5'–GCTGATGGAAGTTGCAGA–3') and cloned into a vector based on the pBlueScript plasmid between two

loxP sites at the EcoRV site (a1–a2/*lox*). Next, a a1–a2/*lox* fragment was cloned into the vector pCaSpeR3–Yil at the KpnI site at position –343 bp. All of the constructs had a deletion of the *yellow* regulatory sequence of up to –343 bp (XbaI–Eco47III fragment).

In order to obtain a vector lacking *yellow* body and wing enhancers, the XbaI–Eco47III fragment containing body and wing enhancers was deleted from the pCA vector, which contains a complete sequence of the *yellow* gene (CA–y (–890)). In the constructs YG4(Cm1A), eveYG4(Cm1A), and ΔeveYG4(Cm1A), a DNA fragment containing 10 binding sites for the yeast activator protein GAL4 (two copies of five binding sites from the pUAST plasmid vector) was inserted into a CA–y (–890) vector at the 3'–end of the *yellow* gene at the SmaI restriction site, while a a1–a2/*lox* fragment was inserted at the SacI restriction site. The procedures for the substitution of the –68 ... +130 bp sequence in the *yellow* promoter with the sequence of the *eve* promoter and how to obtain pre-promoter –69... –100 bp deletion have been described previously [2].

DNA constructs and a *P*-element with defective inverted *P25.7wc* repeats used as a source of transposase were injected into pre-blastoderm-stage embryos of *yacw*¹¹¹⁸. The survived flies were crossed with a *yacw*¹¹¹⁸ line. The transgenic flies were selected based on the phenotypic expression of the genes *white* and *yellow*. Lines with a single construct copy in the genome, which was confirmed by Southern blot analysis, were selected for further studies. Details of the cloning of *yellow* gene sequences into vectors, molecular methods of research, embryo transformation and production of transgenic lines of *Drosophila*, phenotypic analysis of *yellow* gene expression in transgenic lines, induction of site-specific recombination between *loxP* sites, and induction of GAL4-dependent activation in transgenic lines have been described in detail in previous studies [2, 5, 6].

Line *yw*¹¹¹⁸; *P[w+, tubGAL4]117/TM3, Sb* (Bloomington Center #5138) was used for the induction of the yeast protein GAL4. Line *y ac w*¹¹¹⁸; *Cyo, P[w+, cre]/Sco* was used for the induction of recombination between the *loxP* sites. The nucleotide sequence of the gene CG3777 and the structure and profile of its expression are presented in the FlyBase database (<http://flybase.org/reports/FBgn0024989.html>).

RESULTS AND DISCUSSION

In *Drosophila melanogaster*, gene *yellow* is responsible for the pigmentation of cuticular structures: the body, wings, and bristles. The enhancers that control *yellow* expression in the body and wing cuticle are located on the 5'–end of the gene, whereas the enhancer responsible for expression in bristles is located in the intron [7].

In wild-type flies, the body, wings, and bristles have a dark color.

The allele *y*² is often used as a model system in works that study transcriptional regulation in *D. melanogaster*. The *y*² allele has an incorporated retrotransposon, MDG4 (*gypsy*), between the promoter and enhancer of the body and wings of the *yellow* gene [8]. As a result, a Su(Hw) insulator comprising MDG4 blocks *yellow* activation through body and wing enhancers. Thus, the *y*² phenotype is characterized by a yellow color of the body and wings, while the bristles are dark-colored.

The superunstable allele *y*^{+s} (*Fig. 1A*) was obtained by induction of P–M hybrid dysgenesis in a line containing the *y*² mutation [9]. Allele derivatives *y*^{+s} – *y*^{2s1} and *y*^{2s2} containing a chromosome X region 1A duplication in the pre-promoter region of *yellow* have also been obtained [9, 10]. The study of the structure of the alleles *y*^{2s1} and *y*^{2s2} made it possible to identify the regulatory element 1A–RE, which activates long-distance *yellow* expression and is a *yellow*-specific insulator, within the duplicated fragment comprising the region 1A [10]. In the presented paper, we continued our thorough study of the structure of the *y*^{+s} allele.

The mutation *y*^{+s} was a result of the introduction of a chimeric 5,4 kb element at position –69 bp with simultaneous deletion of the *yellow* sequence between –146 and –70 bp. The chimeric element consists of 1,2 kb *P*-elements located “tail to tail” and a 3 030 bp sequence trapped between them, which presents a duplication of the region 1A of chromosome X and is located distal to the *yellow* locus in the genome (*Fig. 1A*) [9]. This duplication includes a fragment of the unexplored gene CG3777, which is expressed at the same stages of development as the *yellow* gene.

The body and wings of the flies carrying allele *y*^{+s} exhibit a dark color close in intensity to the color of wild-type flies. Hence, gene expression is activated in the body and wings in the case when the 1A region from chromosome X is shifted to the *yellow* gene, despite the fact that the Su(Hw) insulator blocks the corresponding enhancers. We managed to localize a 1748 bp enhancer, which was called enhancer 1A (En1A), in the relocated DNA sequence by using transgenic constructs (*Fig. 1B*).

First, we tested two restriction fragments which together cover most of the region 1A duplications: EcoRI–PstI of 771 bp and PstI–PvuII of 1748 bp (*Fig. 1A*). In the transgenic constructs EcoRI–PstI–Y and PstI–PvuII–Y, these fragments were located upstream of the *yellow* promoter at position –343 bp (*Fig. 1B*). Both constructs contained no body or wing enhancers. Among the lines carrying the EcoRI–PstI–Y construct, 19 flies out of 20 had an uncolored body and wings. The phenotype of the flies from transgenic PstI–PvuII–Y lines was similar to the wild-type phenotype in 23 out of 31 lines

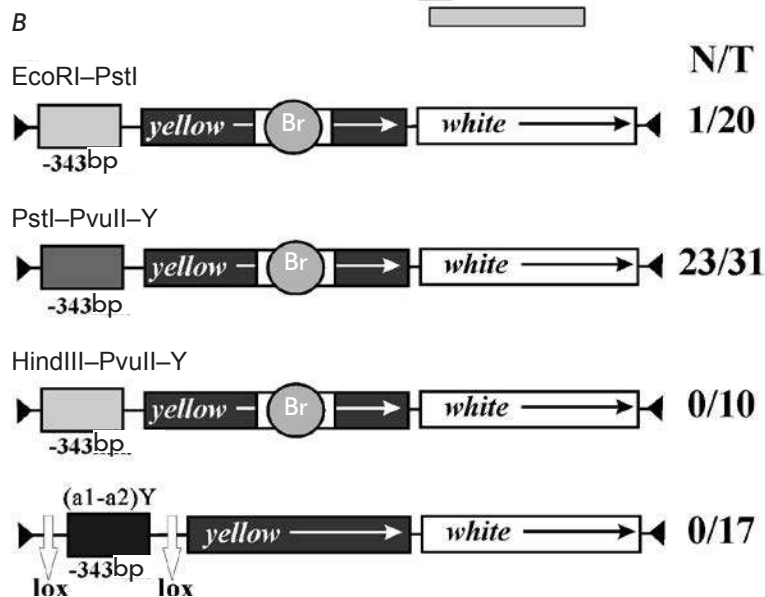
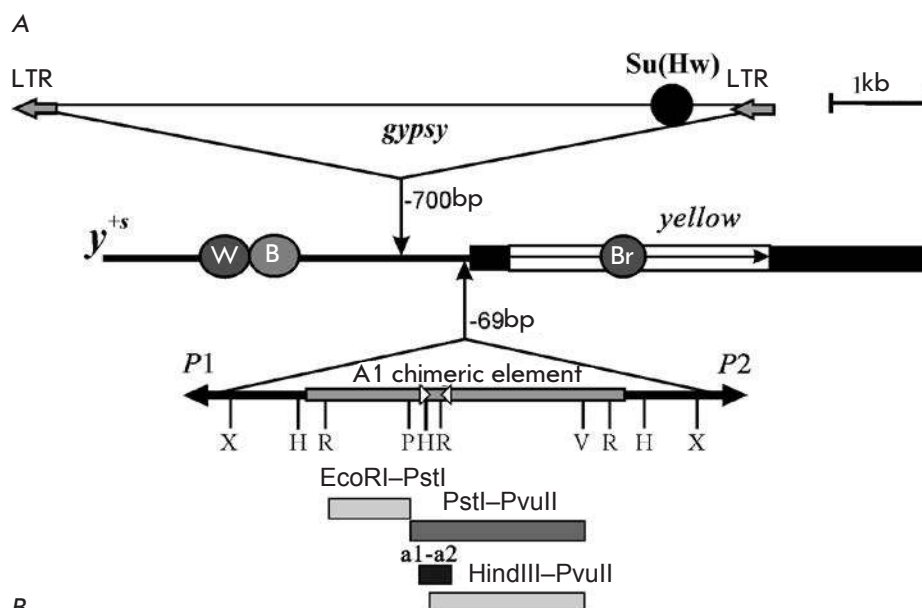


Fig. 1. Mapping of a new enhancer, En1A, of the 1A region of the X chromosome. **A** – schematic representation of the structures of the *yellow* locus and *y⁺* allele. The *Yellow* exons and intron are depicted by black and white boxes, respectively. The direction of transcription is indicated by an arrow. Grey circles represent the tissue-specific transcriptional enhancers responsible for *yellow* expression in the wings (W), body (B), and bristles (Br). Triangles indicate insertions of the *gypsy* retrotransposon and chimeric element. Long terminal repeats (LTR) at the ends of the retrotransposon are shown by gray arrows. Black arrows in the chimeric element indicate the size and orientation of *P*-element sequences. The internal region of the chimeric element corresponding to the sequence of gene *CG3777* is depicted by a gray rectangle. Abbreviations of the restriction sites are: R – EcoRI; X – XhoI; P – PstI; H – HindIII; V – PvuII. Localization and direction of PCR primers are shown by open triangles. The rectangles under the scheme of the chimeric element correspond to fragments comprising transgenic constructs.

B – schematic representation of transgenic constructs including fragments of the chimeric element. Arrows indicate the direction of *yellow* and *white* transcription. Ends of the *P*-element in the vector are shown by black triangles. White vertical arrows signed “*lox*” indicate *Cre* recombinase binding sites. N is the number of fly lines with a dark body and wings pigmentation. T is the total number of transgenic lines.

obtained, which is proof of the ability of the 1748 bp fragment to functionally replace the body and wing enhancers of the *yellow* gene. Hence, the En1A enhancer is localized within the PstI–PvuII region.

In order to accurately map En1A, two genetic constructs containing distinct PstI–PvuII fragments incorporated at position -343 bp were designed: HindIII–PvuII–Y and (a1–a2)Y (Fig. 1B). The HindIII–PvuII fragment, of 1 511 bp (Fig. 1A), had no enhancer properties: the body and wings of the flies were yellow in all 10 transgenic HindIII–PvuII–Y lines (Fig. 1B). A bio-

informatic analysis of the structure of the PstI–PvuII sequence revealed a 362-bp fragment comprising recurring motifs, which, possibly, could serve as binding sites for regulatory proteins. This DNA fragment was amplified by PCR using the primers a1 and a2 and then incorporated upstream of the *yellow* promoter as part of the (a1–a2)Y construct (Fig. 1B). Fragment a1–a2 is surrounded by the *Cre* recombinase recognition sites (*loxP* sites), which allow *in vivo* excision of the analyzed element [11]. It should be noted that *yellow* cDNA contained no bristle enhancer in the construct (a1–a2)Y

(Fig. 1B). We obtained 17 transgenic lines carrying the construct. Despite the absence of a bristle enhancer, the flies of all the lines had the y^2 phenotype. Excision of the a1–a2 sequence resulted in the disappearance of pigmentation in bristles in 12 out of 15 lines. Thus, the studied 362 bp fragment within the (a1–a2)Y construct interacted with a promoter and stimulated *yellow* expression in bristles but was incapable of functionally substituting body and wing enhancers.

The obtained results allowed us to suggest that enhancer En1A has a heterogeneous structure. One part of the enhancer, (a1–a2) of 362 bp, named the “communication part” (hereinafter Cm1A), alone stimulates *yellow* expression only in the bristles. However, it is necessary for the stimulation of *yellow* expression by the full-length En1A in the body and wings. Another part of the PstI–PvuII sequence of 1,386 bp is capable of inducing a high level of *yellow* expression in the body and wings only in combination with the communication part (Fig. 1A, B). Full-length En1A of 1,748 bp activates *yellow* transcription in all cuticular structures. Apparently, the 1,386-bp fragment contains binding sites for *yellow* transcription activators in the body and wings, but their interaction with the promoter is provided by Cm1A-binding proteins.

To further explore the communication properties of the Cm1A element, we used a model system based on the properties of the yeast activator GAL4. This activator is known to stimulate promoters of various genes in the *Drosophila* genome [2]. However, GAL4, located at the 3’-end of the gene, is incapable of transcription activation [12]. In the construct YG4(Cm1A), the protein GAL4 binding sites and a potential communicator, Cm1A, surrounded by *loxP* sites were incorporated at the 3’-end of the *yellow* gene. In addition, the 5’ sequence of *yellow* containing body and wing enhancers (up to -890 bp) was deleted (Fig. 2). In seven transgenic lines carrying the YG4(Cm1A) construct, the flies had a y^2 phenotype. Thus, in the absence of GAL4 activation, the Cm1A fragment is incapable of activating the transcription of *yellow* in the body and wings. Then, we crossed YG4(Cm1A) transgenic lines with a line expressing the GAL4 protein. As a result of GAL4 activation, the body and wings of the flies in all the lines acquired a darker color (Fig. 2). Deletion of Cm1A led to a decrease in *yellow* expression to its initial level. Therefore, the Cm1A element, indeed, has communication properties. It provides stable long-distance interaction with the GAL4 activator and *yellow* promoter.

Earlier, we had localized TE at -69 ... -100 of *yellow*, which provides long-distance interaction of body and wing enhancers with the *yellow* promoter, as well as the heterologous promoter of the gene *eve* [2]. We hypothesized that the Cm1A communicator functionally

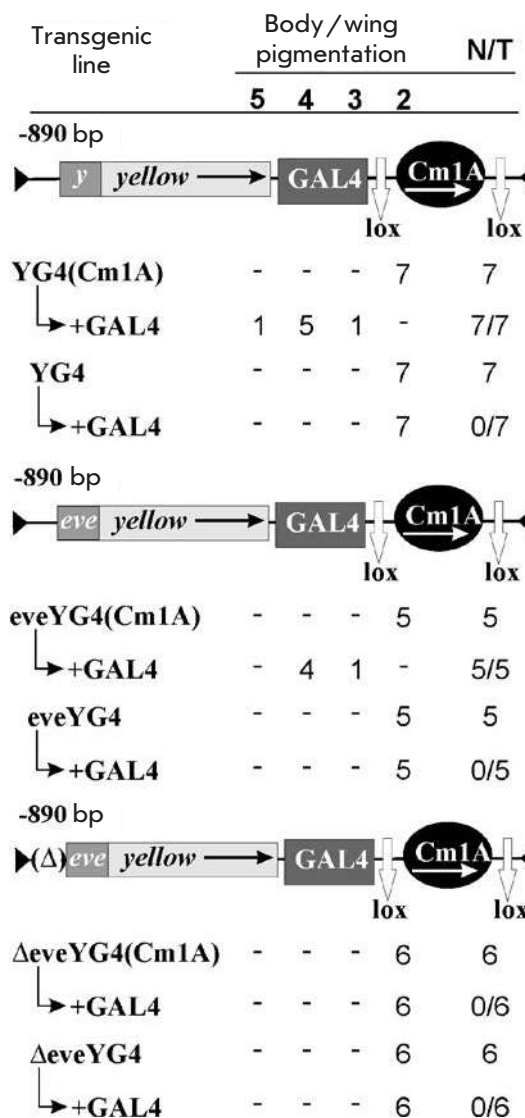


Fig. 2. Screening of the communication properties of the Cm1A fragment. Results of the phenotypic analysis of the flies in transgenic lines are presented under construct schemes. Designations: *y* – *yellow* gene promoter; *eve* – *even skipped* gene promoter; black ellipse – Cm1A communicator. The arrow inside an ellipse indicates the transcription direction. Deletion of the *yellow* gene sequence of -69 to -100 bp (TE) is marked by Δ. Pigmentation of the body and wings is numbered from 5 (dark color, as in the wild-type) to 2 (yellow color corresponding to the phenotype of the y^2 allele). The designation “+ GAL4” refers to the derivatives obtained after GAL4 activation in transgenic lines of the corresponding genotype. N is the number of lines of flies that acquired a new phenotype after Cm1A deletion or by crossing with the line expressing GAL4. T is the total number of lines examined for each particular construct. For other designations, see Fig. 1.

interacts with TE of the *yellow* gene. In order to test this hypothesis, the constructs *eveYG4(Cm1A)* and Δ *eveYG4(Cm1A)* were obtained (Fig. 2). In both constructs, the *yellow* gene promoter was replaced by a heterologous promoter of the *eve* gene (-68 ... +130 bp) (Fig. 3). Moreover, the TE sequence of the *yellow* gene was deleted in the Δ *eveYG4(Cm1A)* construct (Figs. 2, 3). The results obtained during a phenotypic analysis of five *eveYG4(Cm1A)* transgenic lines were similar to the results of a *YG4(Cm1A)* line analysis. As in the previous case, the communicator provided GAL4-dependent transcription activation of *yellow*. Since the structures of the *yellow* and *eve* promoters are different (Fig. 3), one can assume that the core elements of the promoter are not involved in the functional interaction with Cm1A. In six transgenic lines carrying the Δ *eveYG4(Cm1A)* construct, GAL4 activation did not lead to changes in the initial y^2 phenotype (Fig. 2). Hence, the communicator Cm1A is incapable of supporting long-distance interaction between the transcription activator and the promoter of the gene in the absence of *yellow* gene TE. Apparently, the proteins binding the communication element Cm1A can interact with the proteins recruited to TE of the *yellow* gene. Such interaction brings the GAL4 activator and promoter spatially together in the described model system, which enables contact between the activation complex recruited to the GAL4 sequences and the transcriptional complex of the promoter.

CONCLUSION

The presented data allow us to conclude that the new enhancer *En1A* has a modular structure. In a previous study, we showed that the regulatory system of *white* also includes elements that do not affect transcription but provide long-distance enhancer-promoter interaction. The pre-promotor region and the eye enhancer of gene *white* contain binding sites for the Zeste protein. The Zeste protein is not involved in transcription activation but allows the *eye* enhancer to activate a long-distance promoter through binding to its target sites [5]. The results of the current study support the hypothesis that the regulatory regions of various genes have a modular structure and include activation elements that bind to transcription factors, initiating and providing efficient transcription and communication elements that bind proteins, providing spatial contact between an enhancer and a promoter. The described model

```
(-118) ccgaatcactaaaacca
ccgaagtggcgcgcccttcgtttcatttt
catggccgtgcttcgtcttcggagaaaaaa
aacttCATATAAacgcggccgacata
ttaggccACCAGTcgttaccgcgcca
ggtccacagaagaggattaaaaaatat
cacacagccgaaggctagagaagaacc
ccctatagctgaacatatataaacaatat
atTTTTTTattgccaacacactttggcttaag
tgtaagagtgattgtcagcttagagcta
agtgcaATG(+173)
```

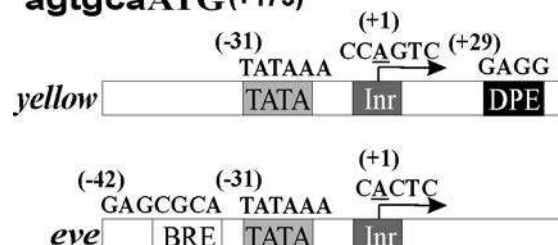


Fig. 3. Promoter regions of the *yellow* and *eve* genes. The upper part of the figure depicts the sequence of the *yellow* promoter region. The TATA promoter, initiator, and translation start site are designated by capital letters. The 198-bp *yellow* region substituted in the *eveYG4(Cm1A)* and Δ *eveYG4(Cm1A)* constructs is shown in italic. The transcription initiation site is indicated by an asterisk. Partially duplicated sequences (a putative tethering element) upstream of TATA are underlined. The sequence of -69 to -100 bp including TE of the *yellow* gene is boxed. Figures in parentheses indicate the relative distance from the transcription start site. The core promoter elements of the *yellow* and *eve* promoters are shown schematically. Arrows indicate the transcription direction. Previously reported sequences of the TATA box (TATA), initiator (Inr), downstream promoter element (DPE), and the putative sequence of the TFIIIB binding element (BRE) are shown. The sequences of core promoter elements are designated by capital letters.

systems can be used to study the enhancer structure and identification of the sequences involved in long-distance interactions between the regulatory elements of the genome.

The authors would like to express their gratitude to E.K. Koryagina for technical input. This work was financially supported by a grant of the Russian Science Foundation (project № 14-14-01067).

REFERENCES

1. Erokhin M., Vassetzky Y., Georgiev P., Chetverina D. // Cell Mol. Life Sci. 2015. V. 72. № 12. P. 2361–2375.
2. Melnikova L., Kostuchenko M., Silicheva M., Georgiev P.

- // Chromosoma. 2008. V. 117. № 2. P. 137–145.
3. Calhoun V.C., Levine M. // Proc. Natl. Acad. Sci. USA. 2003. V. 100. № 17. P. 9878–9883.
4. Calhoun V.C., Stathopoulos A., Levine M. // Proc. Natl.

SHORT REPORTS

- Acad. Sci. USA. 2002. V. 99. № 26. P. 9243–9247.
5. Kostyuchenko M., Savitskaya E., Koryagina E., Melnikova L., Karakozova M., Georgiev P. // *Chromosoma*. 2009. V. 118. № 5. P. 665–674.
6. Savitskaya E., Melnikova L., Kostuchenko M., Kravchenko E., Pomerantseva E., Boikova T., Chetverina D., Parshikov A., Zobacheva P., Gracheva E., et al. // *Mol. Cell. Biol.* 2006. V. 26. № 3. P. 754–761.
7. Geyer P.K., Corces V.G. // *Genes Dev.* 1987. V. 1. № 9. P. 996–1004.
8. Geyer P.K., Spana C., Corces V.G. // *EMBO J.* 1986. V. 5. № 10. P. 2657–2662.
9. Georgiev P., Tikhomirova T., Yelagin V., Belenkaya T., Gracheva E., Parshikov A., Evgen'ev M.B., Samarina O.P., Corces V.G. // *Genetics*. 1997. V. 146. № 2. P. 583–594.
10. Pomerantseva E., Biryukova I., Silicheva R., Savitskaya E., Golovnin A., Georgiev P. // *Genetics*. 2006. V. 172. № 4. P. 2283–2291.
11. Siegal M.L., Hartl D.L. // *Methods Mol. Biol.* 2000. V. 136. P. 487–495.
12. Erokhin M., Davydova A., Kyrchanova O., Parshikov A., Georgiev P., Chetverina D. // *Development*. 2011. V. 138. № 18. P. 4097–4106.

Antiretroviral Activity Of a Novel Pyrimidyl-Di(Diazaspiroalkane) Derivative

E.A. Novoselova^{1*}, O.B. Riabova², I.A. Leneva³, V.G. Nesterenko¹, R.N. Bolgarin¹, V.A. Makarov²

¹«NEARMEDIC PLUS» LLC, Aviakonstruktora Mikoyana str. 12, Moscow, 125252, Russia

²A.N. Bach Institute of Biochemistry, Federal Research Centre «Fundamentals of Biotechnology» of the Russian Academy of Sciences, Leninskiy pr. 33-2b, Moscow, 119071, Russia

³I. Mechnikov Research Institute of Vaccines and Sera, Malyj Kazennyj per. 5, Moscow, 105064, Russia

*E-mail: helen.novoselova@gmail.com

Received February 01, 2017; in final form, February 16, 2017

Copyright © 2017 Park-media, Ltd. This is an open access article distributed under the Creative Commons Attribution License, which permits unrestricted use, distribution, and reproduction in any medium, provided the original work is properly cited.

ABSTRACT A novel compound, 3,3'-(5-nitropyrimidine-4,6-diyl)bis-3,12-diaza-6,9-diazoniadispiro[5.2.5.2]hexadecane tetrachloride dihydrochloride, was synthesized. The compound was found to inhibit the replication of various viral families by blocking specific heparan sulfate receptors on the host cell's surface. In experiments, the compound was found to be highly effective against several strains of HIV retroviruses.

KEYWORDS antiviral activity, dispiro compounds, heparan sulfate, HIV.

INTRODUCTION

Searching for compounds that could block the interaction between a pathogen and the host cell is one of the promising directions in designing both antiviral and antimicrobial drugs. This approach has several advantages, especially in the case of antiviral drugs, since there is no need for the active compound to penetrate into the cells, which dramatically reduces both the cytotoxicity and overall toxicity of the substance used.

At the first stage of viral infection development, the virus adheres to the cell through the binding of specific viral proteins to specific molecules on the cell surface. Most often, adhesion occurs through specific binding to heparan sulfate proteoglycans (HSPG), which are located on the cell surface. It is known that this mechanism is used by various viral families, such as type 1 and 2 herpesviruses (HSV-1, HSV-2) [1], papillomaviruses (HPV) [2], human cytomegalovirus (HCMV) [3], some strains of the human immunodeficiency virus (HIV) [4], human respiratory syncytial virus (HRSV) [5], the hepatitis B and C viruses (HBV and HCV) [6], and others.

Previously we synthesized N,N-bis(1-oxido [1,2,5]oxadiazolo [3,4d]pyrimidin-7-yl)-3,12-diaza-6,9-diazonium (5,2,5,2) dispirohexadecane dichloride **1** (Figure), the most well known and most extensively studied inhibitor of the adhesion process. It was shown that compound **1** and its analogues, including dispirotripiperazine,

are characterized by effective reversible binding to cellular HSPG and, thus, prevent virus binding [7]. Dispiro compound **1** inhibits replication in herpes viruses [8], as well as other viral families that use HS as a receptor or co-receptor [3]. However, the metabolic instability of compound **1** that is due to a degradation accompanied by the formation of nitric oxide prohibited an investigation of its biological properties [9].

Therefore, we attempted to obtain a novel dispirotripiperazinium derivative. We designed an optimal compound capable of binding to known HSPG with allowance for a potential metabolic stability of the target compound and synthesized 3,3'-(2-methyl-5-nitropyrimidine-4,6-diyl)3,12-bis-6,9-diaza-diazoniadispiro [5.2.5.2] hexadecane tetrachloride dihydrochloride **2**. It was assumed that dispiropiperazine **2**, which is represented in a more chemically stable structure, would be a similarly effective blocker of cellular HSPG and, thereby, would inhibit cell adhesion of the virus, leading to a disruption of the life cycle and reduced titer of the virus.

In this paper, we report on the high antiviral activity of the novel dispirotripiperazinium derivative **2**, which fully confirms our hypothesis. Currently, dispiro compound **2** is undergoing in-depth preclinical studies.

EXPERIMENTAL

Our studies were carried out at the National Cancer Institute (National Cancer Institute, Bethesda, Mary-

Antiviral activity of dispiro piperazine **2** against different viral strains

Viral strain	Cell line	CC ₅₀ , μM	IC ₅₀ , μM	TI (CC ₅₀ /IC ₅₀)
HIV-1 6S	MT-2	98.2	1.4	71.4
HIV-1 IIIB	MT-4	200.0	5.7	35.0
HIV-1 RF	CEM-SS	197.0	150.0	1.3
HIV-1 N119	MT-4	200.0	31.7	6.3
HIV-1 DPS	MT-4	200.0	1.2	170.0
HIV-1 A-17	MT-2	79.1	4.7	16.7
HIV-1 A-17	MT-4	200.0	33.7	5.9
HIV-2 ROD	CEM-SS	200.0	13.3	15.0
SIV MAC 251	MT-4	200.0	6.3	31.5

Note: CC₅₀ – cytotoxic concentration; IC₅₀ – half-maximal inhibition concentration; TI – therapeutic index.

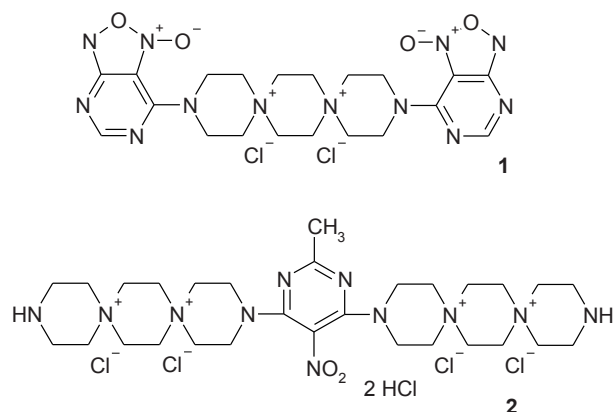


Fig. 1. The structure of *N,N'*-(bis-1-oxido[1,2,5]oxadiazolo[3,4d]-nitropyrimidine-7-yl)-3,12-diaza-6,9-diazonia(5,2,5,2)dispirohexane dichloride (**1**) and 3,3'-(5-nitropyrimidine-4,6-diyl)bis-3,12-diaza-6,9-diazoniadispiro[5.2.5.2]hexadecane tetrachloride dihydrochloride (**2**).

land, USA). Antiviral activity was assessed using the XTT test [10] with various concentrations of the compound and incubation of cells (CEM-SS, MT-2, MT-4) in the presence of serial dilutions of dispiropiperazine **2** (dissolved in dimethyl sulphoxide, DMSO) for 6 days at a temperature of 37°C and humidified atmosphere with 5% CO₂, followed by addition of XTT reagents. The method is based on a spectrometric measurement of the level of formazan transformed by living cells from a water-soluble tetrazolium salt, XTT.

The following HIV strains were used: the reference HIV-1 IIIB strain; the AZT-sensitive HIV-1 6S, HIV-1 RF strains; the drug-resistant HIV-1 N119 strains (resistant to nevirapine, Y181C mutation), HIV-1 DPS (resistant to diphenyl sulfone, Y181C mutation), and HIV-1 A-17 (resistant to nevirapine, K103N and Y181C mutations). We also used the HIV-2 ROD strain and simian immunodeficiency virus SIV MAC 251.

RESULTS AND DISCUSSION

The results, summarized in *Table*, show that dispirotripiperazine **2**, which we synthesized, effectively inhibits the replication of HIV-1, HIV-2, and SIV. At the same time, in contrast to the previously obtained data on the activity of compound **1** against herpes viruses, we observed a fairly wide range of sensitivity of HIV and SIV.

HIV-1 and HIV-6S 1 DPS were the most sensitive to the inhibitory effects of dispiro compound **2** among the tested strains, IC₅₀ = 1.37 and 1.17 μM, respectively. In contrast to these strains, HIV-1 RF was 100-fold less sensitive to the test compound (IC₅₀ = 150 μM).

Unlike HSV viruses, wherein the IC₅₀ values were within the same range, as well as the values for all tested strains (8.2 to 20.4 μM), inhibition of HIV replication heavily depended on the used strains, where the IC₅₀ values varied from 150 μM (HIV-1 RF, CEM-SS cell line) to 1.4 μM (HIV-1 6S, MT-2 cells). In the case of the HIV-1 A-17 strain, IC₅₀ values were determined for different cell lines and they ranged from 33.7 μM for the MT-4 line to 4.7 μM for the MT-2 line.

Such a significant difference in IC₅₀ values (both within a single cell line for different HIV strains, and within a single strain for different cell cultures) may be due to two reasons. First, different cell lines may have a different surface concentration of heparan sulfate proteoglycans. Second, it has been reliably shown that HIV strains differ significantly from each other in the efficiency of co-receptor use (CCR5 and CXCR4) at the stage of target cell binding [11].

Unlike the herpes viruses, the structure of HIV binding mediated by heparan sulfate has not yet been confirmed by an X-ray analysis, and the possibility of interaction between HIV and the host cell, mediated by heparan sulfate proteoglycans, has only been reported in the literature.

We believe that the new class of pyrimidyl-di(diazodispiroalkane) derivatives can be used as antiviral agents. Our belief is rooted in several factors, such as the specificity of the inhibitory effect with respect to viral strains, as exemplified by dispiro tripiperazinium **2**; the ability of dispiro compounds to form very stable bonds with some viral receptors or co-receptors; and

the composition with a chemically defined low molecular weight [7].

It should be noted that this mechanism of action is very promising in terms of overcoming the resistance

shown by viruses toward officinal medicines, since it acts on the cell rather than on the virus itself. Owing to these properties, this class of compounds can be a valuable tool in studying virus-cell interactions.

REFERENCES

1. Shukla D., Spear PG // *J. Invest.* 2001. V. 108. № 4. P. 503–510.
2. Selinka HC, Giroglou T., Sapp 2002. V. 299. № 2. P. 279–287.
3. Paeschke R., Woskobochnik I., Makarov Agents Chemother. 2014. V. 58. № 4. P. 1963–1971.
4. Patel V., Ferguson M., Minor 1993. V. 192. № 1. P. 361–364.
5. Hallak LK, Spillmann D., Collins 2000. V. 74. № 22. P. 10508–10513.
6. Jiang YF, He B., Ma Belg. 2012. V. 75. № 3. P. 316–321.
7. Schmidtke M., Wutzler P., Makarov Drug Design & Discovery. 2004. V. 1. Number 4. P. 293–299.
8. Artemenko AG, Muratov EN, Kuz'min 2007. V. 60. № 1. P. 68–77.
9. Kaminka M.E, Kalinkina M.A., Pushkina, T.V., Tupikina S.M., Ryabova O.B., Makarov V.A., Granik V.G. // *Eksp. i Klin. Farmakol.* 2004. V. 67. No 3. P. 30–33.
10. Weislow OS, Kiser R., Fine Cancer Inst. 1989. V. 81. № 8. P. 577–586.
11. O'Brien SJ, Moore JP // *Immunol Rev.* 2000. V. 177. P. 99–111.

GENERAL RULES

Acta Naturae publishes experimental articles and reviews, as well as articles on topical issues, short reviews, and reports on the subjects of basic and applied life sciences and biotechnology.

The journal is published by the Park Media publishing house in both Russian and English.

The journal *Acta Naturae* is on the list of the leading periodicals of the Higher Attestation Commission of the Russian Ministry of Education and Science. The journal *Acta Naturae* is indexed in PubMed, Web of Science, Scopus and RCSI databases.

The editors of *Acta Naturae* ask of the authors that they follow certain guidelines listed below. Articles which fail to conform to these guidelines will be rejected without review. The editors will not consider articles whose results have already been published or are being considered by other publications.

The maximum length of a review, together with tables and references, cannot exceed 60,000 characters with spaces (approximately 30 pages, A4 format, 1.5 spacing, Times New Roman font, size 12) and cannot contain more than 16 figures.

Experimental articles should not exceed 30,000 symbols (approximately 15 pages in A4 format, including tables and references). They should contain no more than ten figures.

A short report must include the study's rationale, experimental material, and conclusions. A short report should not exceed 12,000 symbols (8 pages in A4 format including no more than 12 references). It should contain no more than four figures.

The manuscript and the accompanying documents should be sent to the Editorial Board in electronic form:

- 1) text in Word 2003 for Windows format;
- 2) the figures in TIFF format;
- 3) the text of the article and figures in one pdf file;
- 4) the article's title, the names and initials of the authors, the full name of the organizations, the abstract, keywords, abbreviations, figure captions, and Russian references should be translated to English;
- 5) the cover letter stating that the submitted manuscript has not been published elsewhere and is not under consideration for publication;
- 6) the license agreement (the agreement form can be downloaded from the website www.actanaturae.ru).

MANUSCRIPT FORMATTING

The manuscript should be formatted in the following manner:

- Article title. Bold font. The title should not be too long or too short and must be informative. The title should not exceed 100 characters. It should reflect the major result, the essence, and uniqueness of the work, names and initials of the authors.
- The corresponding author, who will also be working with the proofs, should be marked with a footnote *.
- Full name of the scientific organization and its departmental affiliation. If there are two or more scientific organizations involved, they should be linked by digital superscripts with the authors' names. Ab-

stract. The structure of the abstract should be very clear and must reflect the following: it should introduce the reader to the main issue and describe the experimental approach, the possibility of practical use, and the possibility of further research in the field. The average length of an abstract is 20 lines (1,500 characters).

- Keywords (3 – 6). These should include the field of research, methods, experimental subject, and the specifics of the work. List of abbreviations.

• INTRODUCTION

• EXPERIMENTAL PROCEDURES

• RESULTS AND DISCUSSION

• CONCLUSION

The organizations that funded the work should be listed at the end of this section with grant numbers in parenthesis.

• REFERENCES

The in-text references should be in brackets, such as [1].

RECOMMENDATIONS ON THE TYPING AND FORMATTING OF THE TEXT

- We recommend the use of Microsoft Word 2003 for Windows text editing software.
- The Times New Roman font should be used. Standard font size is 12.
- The space between the lines is 1.5.
- Using more than one whole space between words is not recommended.
- We do not accept articles with automatic referencing; automatic word hyphenation; or automatic prohibition of hyphenation, listing, automatic indentation, etc.
- We recommend that tables be created using Word software options (Table → Insert Table) or MS Excel. Tables that were created manually (using lots of spaces without boxes) cannot be accepted.
- Initials and last names should always be separated by a whole space; for example, A. A. Ivanov.
- Throughout the text, all dates should appear in the “day.month.year” format, for example 02.05.1991, 26.12.1874, etc.
- There should be no periods after the title of the article, the authors' names, headings and subheadings, figure captions, units (s – second, g – gram, min – minute, h – hour, d – day, deg – degree).
- Periods should be used after footnotes (including those in tables), table comments, abstracts, and abbreviations (mon. – months, y. – years, m. temp. – melting temperature); however, they should not be used in subscripted indexes (T_m – melting temperature; T_{pt} – temperature of phase transition). One exception is mln – million, which should be used without a period.
- Decimal numbers should always contain a period and not a comma (0.25 and not 0,25).
- The hyphen (“-”) is surrounded by two whole spaces, while the “minus,” “interval,” or “chemical bond” symbols do not require a space.
- The only symbol used for multiplication is “×”; the “x” symbol can only be used if it has a number to its

right. The “.” symbol is used for denoting complex compounds in chemical formulas and also noncovalent complexes (such as DNA·RNA, etc.).

- Formulas must use the letter of the Latin and Greek alphabets.
- Latin genera and species' names should be in italics, while the taxa of higher orders should be in regular font.
- Gene names (except for yeast genes) should be italicized, while names of proteins should be in regular font.
- Names of nucleotides (A, T, G, C, U), amino acids (Arg, Ile, Val, etc.), and phosphonucleotides (ATP, AMP, etc.) should be written with Latin letters in regular font.
- Numeration of bases in nucleic acids and amino acid residues should not be hyphenated (T34, Ala89).
- When choosing units of measurement, SI units are to be used.
- Molecular mass should be in Daltons (Da, KDa, MDa).
- The number of nucleotide pairs should be abbreviated (bp, kbp).
- The number of amino acids should be abbreviated to aa.
- Biochemical terms, such as the names of enzymes, should conform to IUPAC standards.
- The number of term and name abbreviations in the text should be kept to a minimum.
- Repeating the same data in the text, tables, and graphs is not allowed.

GUIDENESS FOR ILLUSTRATIONS

- Figures should be supplied in separate files. Only TIFF is accepted.
- Figures should have a resolution of no less than 300 dpi for color and half-tone images and no less than 500 dpi.
- Files should not have any additional layers.

REVIEW AND PREPARATION OF THE MANUSCRIPT FOR PRINT AND PUBLICATION

Articles are published on a first-come, first-served basis. The members of the editorial board have the right to recommend the expedited publishing of articles which are deemed to be a priority and have received good reviews.

Articles which have been received by the editorial board are assessed by the board members and then sent for external review, if needed. The choice of reviewers is up to the editorial board. The manuscript is sent on to reviewers who are experts in this field of research, and the editorial board makes its decisions based on the reviews of these experts. The article may be accepted as is, sent back for improvements, or rejected.

The editorial board can decide to reject an article if it does not conform to the guidelines set above.

The return of an article to the authors for improvement does not mean that the article has been accept-

ed for publication. After the revised text has been received, a decision is made by the editorial board. The author must return the improved text, together with the responses to all comments. The date of acceptance is the day on which the final version of the article was received by the publisher.

A revised manuscript must be sent back to the publisher a week after the authors have received the comments; if not, the article is considered a resubmission.

E-mail is used at all the stages of communication between the author, editors, publishers, and reviewers, so it is of vital importance that the authors monitor the address that they list in the article and inform the publisher of any changes in due time.

After the layout for the relevant issue of the journal is ready, the publisher sends out PDF files to the authors for a final review.

Changes other than simple corrections in the text, figures, or tables are not allowed at the final review stage. If this is necessary, the issue is resolved by the editorial board.

FORMAT OF REFERENCES

The journal uses a numeric reference system, which means that references are denoted as numbers in the text (in brackets) which refer to the number in the reference list.

For books: the last name and initials of the author, full title of the book, location of publisher, publisher, year in which the work was published, and the volume or issue and the number of pages in the book.

For periodicals: the last name and initials of the author, title of the journal, year in which the work was published, volume, issue, first and last page of the article. Must specify the name of the first 10 authors. Ross M.T., Grafham D.V., Coffey A.J., Scherer S., McLay K., Muzny D., Platzer M., Howell G.R., Burrows C., Bird C.P., et al. // Nature. 2005. V. 434. № 7031. P. 325–337.

References to books which have Russian translations should be accompanied with references to the original material listing the required data.

References to doctoral thesis abstracts must include the last name and initials of the author, the title of the thesis, the location in which the work was performed, and the year of completion.

References to patents must include the last names and initials of the authors, the type of the patent document (the author's rights or patent), the patent number, the name of the country that issued the document, the international invention classification index, and the year of patent issue.

The list of references should be on a separate page. The tables should be on a separate page, and figure captions should also be on a separate page.

The following e-mail addresses can be used to contact the editorial staff: vera.knorre@gmail.com, actanaturae@gmail.com, tel.: (495) 727-38-60, (495) 930-87-07

NANOTECHNOLOGIES

in Russia

Peer-review scientific journal

Nanotechnologies in Russia
(*Rossiiskie Nanotekhnologii*)

focuses on self-organizing structures and nanoassemblages, nanostructures including nanotubes, functional nanomaterials, structural nanomaterials, devices and facilities on the basis of nanomaterials and nanotechnologies, metrology, standardization, and testing in nanotechnologies, nanophotonics, nanobiology.

—> **Russian edition:** <http://nanoru.ru>

—> **English edition:** <http://www.springer.com/materials/nanotechnology/journal/12201>

Issued with support from:



The Ministry of Education and Science of the Russian Federation

Science and Technologies in Russia – STRF.RU



40% of scientists agree that the publication of research results helps the enlightenment of the society, leads to the growth of authority of scientific work

34% believe that wide communicating of research results helps to rise the foundation

12% hope that media communications helps them to stand out in public opinion...
...but

17% never speak to journalists*

Open your work to the world!

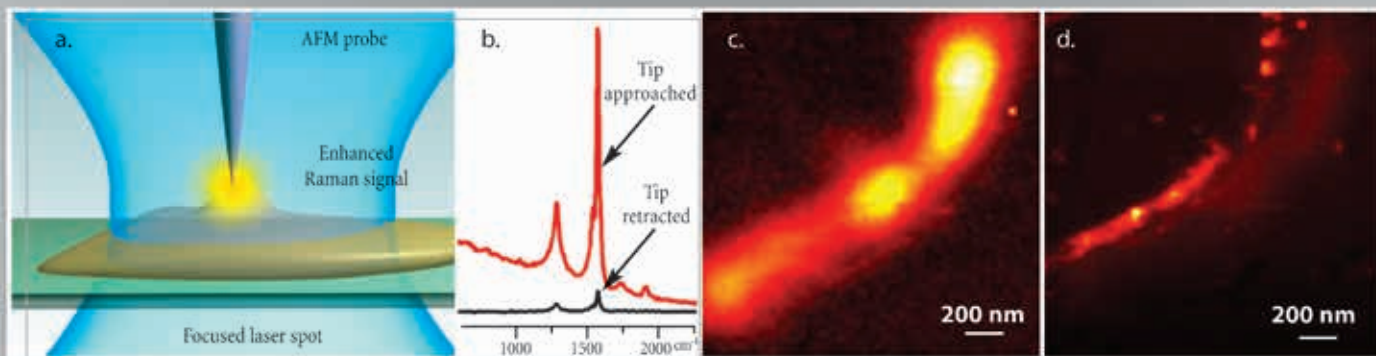
Colours do not play at nanometer scale

But you can colour molecules by their Raman spectra.



Raman mapping by TERS with ultra-high resolution

NTEGRA Spectra



a — a specially prepared AFM probe (metal coated cantilever or etched metal wire) is precisely positioned inside a tightly focused laser spot. b — intensity of carbon nanotube G- and D- Raman bands increases by several orders of magnitude when the special AFM probe is landed and positioned over a small (5 nm height) nanotube bundle - the effect of Tip enhanced Raman scattering (TERS). c — "conventional" confocal Raman image of the nanotube bundle, the observed width of the bundle is ~250 nm (diffraction limit of confocal microscopy, laser

wavelength - 633 nm). d — TERS image of the same bundle - now the observed width is ~70 nm.

Note, in this example, TERS provides more than 4-times better spatial resolution as compared to confocal microscopy. Resolution down to 10 nm and less is theoretically possible. Measurements are done with NTEGRA Spectra in Inverted configuration.

Data courtesy of Dr. S. Kharintsev, Dr. J. Loos, Dr. G. Hoffmann, Prof. G. de With, TUE, the Netherlands and Dr. P. Dorozhkin, NT-MDT Co.

* Enter the Gift code at www.nt-mdt.com and get a present from NT-MDT Co. Attention: limited quantity! Be in time to get your gift!



NT-MDT Co., building 100, Zelenograd,
124482, Moscow, Russia
tel: +7 (499) 735-0305, +7 (495) 913-5736
fax: +7 (499) 735-6410, +7 (495) 913-5739
e-mail: spm@ntmdt.ru; www.ntmdt.com

NT-MDT Europe BV, High Tech Campus 83
5656 AG Eindhoven, the Netherlands
tel: +31(0) 88 338 99 99
fax: +31(0) 88 338 99 98
e-mail: info@ntmdt.eu, www.ntmdt.com